Sheffield Hallam University

A Sheffield Hallam University thesis

ProQuest Number: 10695700

ProQuest 10695700

ProQuest LLC.
789 East Eisenhower Parkway
P.O. Box 1346
Ann Arbor, MI 48106 – 1346

THE INFLUENCE OF VISCO-ELASTIC PROCESSES

ON THE GENERATION OF THERMAL STRESSES IN

QUENCHED LOW ALLOY STEEL PLATES

BY

F. ABBASI

A THESIS SUBMITTED TO THE COUNCIL FOR
NATIONAL ACADEMIC AWARDS IN PARTIAL
FULFILMENT FOR THE DEGREE OF
DOCTOR OF PHILOSOPHY

COLLABORATING ESTABLISHMENT:-   SPONSORING ESTABLISHMENT:-

Atomic Energy Research   Department of Metallurgy,
          Establishment,   Sheffield City
Harwell,   Polytechnic.
Didcot, Oxon.

                                       December, 1983.
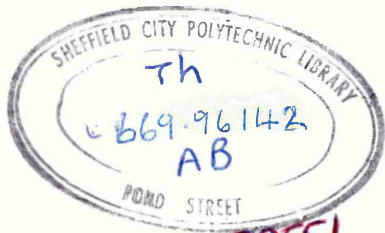
PREFACE

All the work reported in this thesis was carried out at the Sheffield City Polytechnic during the period April 1980 to April 1983.

The candidate has not, during the period of registration for the CNAA degree of PhD, been a registered candidate for any other CNAA award or for any University degree.

The results presented in the thesis are, to the best of my knowledge, original except where reference and acknowledgement has been made to other authors. No part of this thesis has been submitted for a degree at any other University or College.

The following courses were attended during the work:-

   (i)   "Process Metallurgy", Part of Module 1 of the MSc
         in Metallurgical Process Management, October 1980 -
         February 1981, Sheffield City Polytechnic.

  (ii)   "Numerical Methods and Programming", Part of
         Module 2 of the MSc. in Metallurgical Process
         Management, October 1980 - February 1981, Sheffield
         City Polytechnic.

 (iii)   "Heat Treatment", Advanced Topic in Module 3 of the
         MSc in Metallurgical Process Management Feb-June
         1981, Sheffield City Polytechnic.

  (iv)   "High Strength Steels", Advanced Topic in Module 3
         of the MSc in Metallurgical Process Management,
         May-June 1981, Sheffield City Polytechnic.

ACKNOWLEDGEMENTS

THE INFLUENCE OF VISCO-ELASTIC PROCESSES ON THE GENERATION OF THERMAL STRESSES IN QUENCHED LOW ALLOY STEEL PLATES

F. Abbasi

Abstract

The visco-elastic effect in quenched specimens of 835M30 steel was described quantitatively by the use of the standard linear solid, which allowed the calculation of the thermal stress and strain during quenching in water, oil and in a martempering situation. The introduction of viscous flow into the calculation produced a marked improvement in the degree of agreement between the calculated and experimental residual stresses after an oil quench, although this was accompanied by a small reduction in the corresponding agreement in the case of water quench. The use of isothermal stress relaxation data in a continuous cooling situation was dealt with by the use of several models that cover a range of situations that varied from progressive hardening during the quench to one where recovery was predominant at all times. The use of martempering was of limited value, although an air cool following an intermediate salt bath treatment above the Ms temperature prevented the generation of thermal stresses during the formation of martensite. The use of an oil quench following the salt bath treatment was of no value, and none of the combinations of heat treatment possible during martempering significantly reduced the distortions to a lower level than was obtained by a conventional oil quench from 850°C. The mathematical model was also extended to include the effect of transformation plasticity, viz. the effect of an applied stress on the volume change that accompanied a phase transformation, as a consequence of heterogeneous plastic flow. This led to an excellent level of agreement between calculation and experiment in the case of residual stresses: it also produced a deterioration in the case of residual strains. Although some further work is required, the mathematical model has been developed sufficiently for it to be of practical value.

A)		Parameters used in the standard
B)		linear solid equation.
CF_N	=	Correction factor for levelling at position N during through thickness measurement.
C_N	=	Distance between the reference axis and position N on the plate at inclination.
F_o	=	Fourier number
G	=	Shear modulus, MPa
H	=	Quantity of heat generated, used in equation 2.4.1.1, Joules.
I)		Coordinates, used to define stress and
J)		strain components.
K	=	Steady state creep rate used in equation 2.3.4, s^{-1}.
L	=	Length, mm.
M)		Constants used in equation 2.3.7
P)		
N	=	Position number at which through thickness is obtained.
Q	=	Activation energy, KJ/mole
R	=	Gas constant, $J/mol\,^{O}K$.
T	=	Temperature, ^{O}K.
% ΔV	=	Percent volume change associated with the structure change from ferrite and carbide to martensite.
V_α	=	Volume fraction of martensite.
V_γ	=	Volume fraction of austenite.
W	=	Strain hardening coefficient $\left(\dfrac{d\,\sigma_f}{d\,\varepsilon_p}\right)$, MPa.
Y_Q	=	Width of plate after quench, mm.
Y_S	=	Width of plate in softened condition, mm.
TH_{NQ}	=	Thickness of plate after quench, mm.
TH_{NS}	=	Thickness of plate in softened condition, mm.
a)		Constants relating linear variations of E and
b)		v with temperature, according to $E/(1-v) = a - b\theta$
f	=	ratio of transient creep rate to the transient creep strain used in equation 2.3.5.

h	=	surface heat transfer coefficient, $W/m^2 \, ^\circ C$.
i	=	Node positional subscript
j	=	Number of elements in half thickness of plate.
m	=	Constant used in equation 2.3.4.
n	=	node time subscript.
s_{IJ}	=	Stress tensor.
e_{IJ}	=	Strain tensor.
t	=	time, s.
Δt	=	time interval, s.
t^{n+1}	=	total elapsed time in the n+1 interval.
v	=	Rate of relative movement of grains, cm/s, equation 2.3.8.
Δx) Δz)		Thickness of elements in plate.
p) q)		Thickness of plate at positions 1 and 11, figure 88.
α_{ex}	=	Coefficient of linear thermal expansion, $^\circ C^{-1}$
α_{td}	=	Thermal diffusivity, m^2/s.
α_{TRIP}	=	Coefficient of expansion due to transformation plasticity, $^\circ C-1$.
	=	Constant used in equation 2.3.4.
δ_{IJ}	=	Kronecker's delta.
ε	=	Strain
$\dot{\varepsilon}$	=	Strain rate, s^{-1}.
ε_E	=	Elastic strain.
ε_{creep}	=	Creep strain
$(\dot{\varepsilon})_{creep}$	=	Rate of creep strain from equations 4.2.7 and 4.2.9, s^{-1}.
ε^o	=	Instantaneous strain.
ε_p	=	Plastic strain.
$\varepsilon_{thermal}$	=	Strain due to thermal expansion only.
ε_{TRIP}	=	Strain due to transformation plasticity.
ε_t	=	Limiting transient creep strain used in equation 2.3.5.
ε_{tot}	=	Total creep strain shown in figure9
$\dot{\varepsilon}_s$	=	Steady state creep rate used in equation 2.3.5, $s-1$.
$\dot{\varepsilon}_d$	=	Strain rate due to dislocation movement, s^{-1}.

$\dot{\varepsilon}_{gb}$ = Strain rate due to grain boundary sliding, s^{-1}.

ε_{xx})
ε_{yy} } Strains in x, y and z directions.
ε_{zz})

$(\Delta\varepsilon)_{creep}$ = Amount of creep strain in time Δt.

ε_m = Hydrostatic strain.

η = Coefficient of viscosity of the mechanical models, MPa.s.

Θ = Temperature, ^{o}C.

λ = Thermal conductivity, W/m ^{o}C.

ν = Poissons' ratio.

ρ = Density, kg/m^3

σ = Stress, MPa.

$(\sigma)_r$ = Stress when edges of plate are restrained, MPa.

σ_f = Flow stress with uniaxial stress system, MPa.

$(\sigma)_{av}$ = Average stress during a time interval t, used to calculate the amount of stress relaxation and creep in that interval, MPa.

σ_m = Hydrostatic stress, MPa.

$(\bar{\sigma})$ = Average stress level in half thickness of plate, MPa.

$(\dot{\sigma})_{Relaxed}$ = Rate of stress relaxation from equation 4.2.6 and 4.2.8, MPa s^{-1}.

$(\Delta\sigma)_{Relaxed}$ = Amount of stress relaxation in time Δt, MPa.

σ_{xx})
σ_{yy} } Stress in x, y and z directions.
σ_{zz})

τ = Shear stress term used in equation 2.3.8, kg/cm^2.

ϕ = Material parameter used in standard linear solid equation, s^{-1}.

CONTENTS

1. INTRODUCTION

Heat treatment of steel components may result in the initiation of cracking and cause changes in dimensions above the allowable tolerances. These are caused frequently by the generation of thermal stress during the quenching process. The development of thermal stresses in steel components during quenching is a complex phenomenon that has been subjected to a great deal of both experimental and theoretical investigation although the traditional approach to this problem has been an emperical one, based on previous experience or experimental trials. The experimental investigation of residual stresses and distortion after quenching, is a laborious and difficult task. The large number of experimental variables involved are difficult to control and standardize, which makes it difficult to correlate the results of different investigations.

Considerable effort has been directed to the experimental determination of the physical properties of the quenchant and the physical and mechanical properties of the material under consideration, so that the data used in the mathematical models, developed to simulate the stress generation process, is as realistic as possible. However, the generation of thermal stress and strain involve the complex interaction of several processes, while the mathematical models tend to use simplifying assumptions that ignore many of these complexities.

Although this simplifies the calculations it results in a reduction in the level of agreement between the calculated and experimentally determined residual stress and strain. A realis tic appraisal of the thermal stress and strain generated during quenching requires that simplifications introduced into the calculation should be minimum possible and all relevant processes should be included.

The process of viscous flow, which is dependent upon both temperature and time, has been ignored by most of the mathem atical models that simulate the stress generation process, probably on account of the complex relationships between stress, creep strain and time. Dubious assumptions have often been made and most attempts to resolve this problem have been empirical. This particular study arises from the need to incorporate viscous flow processes into one particular mathematical model which ignored this important process.

The combination of viscous flow and elastic strain are represented by a suitable arrangement of dashpots and springs, which provide a set of equations governing the stress relaxation and creep processes. The data relating to these viscous processes has been obtained from isothermal stress-relaxation tests. Subsequently this isothermal data has been introduced into models that represent the continuous cooling situation actually present in a quenched plate. In order to test the model in a wide range of conditions, where the importance of viscous flow varies considerably, the predicted residual stresses and strains have been

compared to experimental data obtained from plates quenched in water, oil and in those subjected to a martempering operation.

It has been observed that the presence of stress has a significant effect on the transformation characteristics of the material, which in turn influences the stress generation process during the quench. In the present work an attempt has also been made to incorporate experimental data of this effect, termed transformation plasticity into the mathematical model.

The introduction of viscous and transformation plasticity effects into the calculation is a major step towards the development of a realistic model of thermal stress and strain during quenching. Even so, the present analysis has been simplified by the choice of an infinite plate of an air hardened steel (835M30), which is completely martensitic after being quenched. Only when the stress generation processes are well understood and it is possible to make an accurate prediction of residual stresses and strains in this comparatively simple case will it be realistic to introduce the complexities associated with other shapes and non-martensitic transformations. It is, of course the more complex situations that are of greatest industrial relevance, and the present work is part of a long-term investigation whose objective is the understanding or control of distortion in commercial components.

2. LITERATURE SURVEY

2.1 Definition of Residual Stresses

Residual stresses or internal stresses may be defined as those stresses that exist in bodies which are at a uniform temperature, and which are not subject to any external force[1,2]. Several different terms have been used to describe residual stresses, these include 'thermal stresses' [3,4] and 'internal stresses' [5,6]. The term 'thermal stresses' indicates those stresses in a body which are due to external restraints which prevent its expansion and contraction under the influence of a change in temperature. This term also refers to stresses resulting from thermal gradients in a material whilst the term 'internal stress' refers to those stresses existing in bodies upon which no external forces are acting. They are also referred to as 'locked up' stresses[7].

Residual stresses are broadly classified into two groups[8], Microstresses (also termed as tessellated[5] or textural stresses[9]) and Macrostresses. Microstresses, as the name implies, are stresses extending over short distances and occur at mircostructural inhomogeneities in the material. The distances involved are such that variation in microstresses cause x-ray line broadening.

Macrostresses operate over much larger distances than microstresses, and are also termed body stresses. They may be due to external (mechanical, thermal, chemical) factors, which may affect different parts of a body

differently[5]. Measurement of such stresses may be carried out by both mechanical and x-ray diffraction techniques. In the present investigation, only the macrostresses produced during the hardening of steel are considered.

2.2 Development of Residual Stresses During Quenching

Three types of stresses are induced during the quenching process[10]:

(i)   thermal stresses due to thermal contraction, which depend on the temperature distribution.

(ii)   transformation stresses due to the expansion that accompanies the transformation of austenite to other phases during quenching.

(iii) stresses caused by differences in the specific volumes of the induced structure.

Andrews[7] has illustrated the stress pattern developed by thermal contraction in quenched cylinders. At the onset of quenching, a temperature gradient is developed rapidly within the body. Initially, the surface, which is in contact with the quenching media, cools and contracts rapidly, which produces a tensile stress in this part of the specimen. As the forces within the material are in balance, a compensating compressive stress is developed at the centre. The magnitude of these stresses vary with the temperature difference between the surface and the centre. As shown in figure 1, the stress at any particular point attains a peak value when this temperature difference reaches a maximum. Subsequently, the

rate of cooling at the centre exceeds that at the surface, and the stresses begin to decrease until the temperature gradient in the body falls to zero. If the stresses produced during cooling are always within the elastic range then once the temperature gradient has disappeared there will be no residual stresses left in the body. However, if there has been any plastic flow at any point, there will be a compressive residual stress at the surface and a corresponding tensile stress at the centre.

The transformation of austenite is accompanied by an expansion of the material. The degree of expansion depends upon the type of phase change, e.g. austenite ⟶ ferrite or pearlite, austenite ⟶ bainite, austenite ⟶ martensite. In the case of the austenite ⟶ martensite transformation the expansion is shown by the dialatometric curve in figure 2. An extension of Andrews' analysis to the case of such a phase transformation indicates an initial change in structure at the surface will produce a compressive stress at this point followed by a stress reversal. This is because the expanding martensite at the surface is restrained by the untransformed centre and will undergo compression and the subsequent transformation at the centre will cause this surface stress to be replaced by one of opposite sense. Thus at the end of the transform-ation process the surface will have a tensile stress and the centre will be in compression, providing that plastic flow has occurred at some point in the transformation process.

A steel specimen may contain various phases, the formation of which are accompanied by different expansion. In addition to stress generation by unequal rates of transformation at different points the presence of these phases will cause residual stresses within the component, on account of the difference in their specific volumes. Hence, even if there is no plastic flow the misfit caused by the difference in specific volumes of the various phases produces residual stresses in the specimen after quenching.

The inelastic behaviour of a metal at high temperature and stress levels is considerably more complex than that of the idealized elastic body. Creep, a phenomenon in which stress and strain are time dependent, may become significant even when the stress is below the elastic limit. Furthermore, at stress levels in excess of the elastic limit time-independent plastic flow will occur with the increase in strain, a non linear function of the loading system. In most cases where thermal stresses are produced during quenching, creep and plastic flow will be present and must be considered simultaneously, even though this greatly increases the complexity of the stress analysis.

2.3 Creep and Stress Relaxation

A material behaves in an elastic manner when there is a linear relation between the components of stress and components of strain. In real solids such a behaviour is only followed at relatively low temperature

and stress levels. At higher temperatures and stresses a real solid deviates from the idealized elastic behaviour, and shows a more complex relationship between stress and strain which must take into account inelastic behaviour, such as creep, stress relaxation, yielding and work hardening. During the heat treatment of materials the high temperatures involved and the subsequent stress levels generated make it necessary to take creep and stress relaxation into consideration.

Several general texts are now available on the subject of creep[11,12,13,14,15,16]. This process may be defined as the time-dependent plastic flow of metals under conditions of constant load. The creep behaviour of a material may be assessed by a creep test, which relates strain to the four externally modifiable parameters, i.e. stress, temperature, time and environment. Although creep data can be displayed in various forms, the one which presents most fundamental interest is the curve that relates the strain produced to the time of test. The shape of the curve depends upon both stress level and temperature. Upto four distinct sections can be distinguished on the strain-time curve as shown in figure 3, viz:

   (i)   The region of instantaneous strain, which occurs on loading.

  (ii)   The primary or transient region (stage I) where the strain rate is continuously decreasing.

(iii)   The secondary or steady state region (stage II) where the strain rate is constant.

(iv) The tertiary region (stage III) where the strain rate increases until fracture occurs.

The occurrence of all these stages together, in any one test, requires the use of a suitable combination of temperature, stress, and duration of test. Thus stress, temperature and time are the major factors affecting the creep behaviour of a material.

When a metal or alloy, loaded under static, dynamic or creep conditions, is prevented from changing its shape, the load it supports decrease with time[12]. This phenomena is called stress relaxation and is shown in figure 4.

In a stress relaxation test the total strain is held constant:

$$\varepsilon_p + \varepsilon_E = \text{constant} \qquad \ldots 2.3.1$$

As the stress supported by the specimen relaxes, the elastic strain also relaxes,

$$\dot{\sigma} = E \; \dot{\varepsilon}_E \qquad \ldots 2.3.2$$

Re-writing equation 2.3.1

$$\dot{\varepsilon}_E = -\dot{\varepsilon}_p$$

Substituting in equation 2.3.2

$$\dot{\sigma} = -E \; \dot{\varepsilon}_p$$

Integrating between limits $\varepsilon_p, \varepsilon_p^{\,o}$ and σ, σ^o

$$\varepsilon_p - \varepsilon_p^{\,o} = \frac{\sigma^o - \sigma}{E} \qquad \ldots 2.3.3$$

It may be noted thus, that, during stress relaxation the elastic strain is converted to plastic strain; hence creep occurs under conditions of decreasing stress.

Both the phenomena described above are significant at the higher end of the temperature range relevant to the quenching of steel components, so it is desirable to include both in any mathematical model of thermal stress and strain generation. However creep phenomena are normally determined when the material is free to deform under a constant load, while in the case of thermal stress the material is constrained, and creep has the effect of reducing the stress generated by these constraints. Generally there are no test data available which can be directly applied to this more complex situation, although theoretical laws have been proposed which relate creep data at constant stress and temperature to the non-steady conditions of stress and temperature developed during quenching. These are reviewed in the next section.

2.3.1 Description of creep behaviour by means of empirical relationships

The first attempts to describe creep deformation were empirical e.g. the equations of Andrade[17,18], Kennedy[19], Graffalo[20]. Theoretical interpretation of the creep process concentrated on the relationship between creep strain and time[17,18,19]. Andrade[17] proposed an equation

$$\varepsilon_{creep} = \varepsilon^o + \beta t^m + kt \qquad \dots 2.3.4$$

21.

which fitted most experimental curves reasonably well in spite of the improbable initial creep rate predicted. Graffalo[20] proposed a slight modification to the above equation:

$$\varepsilon_{creep} = \varepsilon^0 + \dot{\varepsilon}_t \{1 - \exp(ft)\} + \dot{\varepsilon}_s t \qquad \dots 2.3.5$$

By varying the stress only, a family of creep curves can be obtained, which can, once again, be described by various mathematical equations. Between 0.5 and 0.7 T_m the relationship between applied stress and the secondary creep rate was represented by three different expressions, which depend upon the level of stress involved[21,22,23], i.e.

(i)   Low Stress $\dot{\varepsilon}_{creep} \, \alpha \, \sigma$

(ii) Medium Stress $\dot{\varepsilon}_{creep} \, \alpha \, \sigma^p$

(iii) High Stress $\dot{\varepsilon}_{creep} \, \alpha \, \exp(M\sigma)$

To cover the whole range Graffalo[20] suggested the relation

$$\dot{\varepsilon}_{creep} = \text{Sin } h \, (M\sigma)^0$$

which reduces to the power or exponential form for the appropriate value of $M\sigma$.

As the temperature increases the secondary creep rate is also increased, but the extent of this effect is limited until, at a sufficiently high temperature, stage II can become a point of inflection between the decreasing rate of primary creep and the accelerating rate of tertiary creep[22]. It has been established that creep involves

thermally activated processes[24] and creep behaviour has been described by the following equation,

$$\dot{\varepsilon}_{creep} = \text{Constant} \quad \text{x} \quad \exp(-\frac{Q}{RT}) \qquad \ldots 2.3.5$$

Combining the above relationships, Sellars and Tegart[25] proposed an equation to include the stress and temperature dependence of creep rate as:

$$\dot{\varepsilon}_{creep} = \text{Constant} \quad \text{x} \quad \text{Sin h} \ (\ M\sigma\ )^p \ \text{x} \exp(-\frac{Q}{RT}) \quad \ldots 2.3.6$$

A variety of equations have so far been presented which have sought to relate the externally modifiable parameters viz stress, temperature, strain rate and time. One difficulty in analysing the effect of time on the creep process is that the relationship is very sensitive to the previous history of the sample; e.g. prestraining the sample alters the shape of the creep curve. These relationships may provide a useful qualitative description of the creep process, but do not generate a quantitative understanding of creep behaviour. Because the relationships obtained are also so sensitive to the structure of the material, it is difficult to derive from them the atomistic mechanism which controls creep[26].

2.3.2 Theories of creep

In order to obtain an understanding of the creep mechanism on an atomic scale, it is necessary to know the mode of deformation during creep. The models proposed differ from one another significantly and each

shows individual features[27]. These models include:

(i)   Gliding of dislocations within the grain,

(ii)   Subgrain formation,

(iii) Diffusion of point defects in the crystal lattice,

(iv)   Flow of grain boundaries.

The gliding of dislocations through the crystal lattice is observed at relatively low temperatures and when a constant stress is applied at relatively low temperatures this movement is impeded by work hardening effects. In certain cases the most favourably placed dislocation will be able to proceed as a consequence of thermally activated climb. However, as these most easily moved dislocations are progressively removed from the lattice, further movement becomes more difficult, with a consequent fall in the strain rate. This would explain the observed shape of the creep curve at low stresses[28].

Subgrain or cell formation, is the mechanism whereby the grains of the sample become fragmented into a number of smaller subgrains. In order to accommodate the slip processes occurring in different slip planes in neighbouring grains, bending is expected to occur near grain boundaries, as shown in figure 5[29], which leads to the formation of excess dislocations of one sign. With time these dislocations will adjust themselves by climb to form stable arrays of dislocation at right angles to the original slip plane. Breakdown of grains into subgrains

24.

during high temperature creep has been attributed to polygonization by Cahn[30]. Since the important thermal controlling process during polygonization and subgrain formation is the rate of dislocation climb, which involves diffusion, the diffusion rate is directly related to the rate of polygonization.

Diffusion of vacancies as the main mechanism of creep at high temperatures was observed by Nabarro and Herring[31,32]. Under uniaxial stress conditions grain boundaries perpendicular to the stress axis can act as sources for vacancies and boundaries parallel to the stress axis can act as sinks. In this way an elongation of the grain in the direction of the applied stress would be obtained at temperatures where the diffusion of vacancies is sufficiently easy. However this mechanism predominates only at temperatures near the melting point and at extremely low stresses.

Deformation mechanisms that can operate in poly-crystalline materials depend upon the stress applied and the temperature of deformation. A useful representation of such mechanisms can be displayed on a deformation map as suggested by Ashby[33], (see figure 6). These use the axes of stress and temperature to indicate the dominant deformation mechanisms, at a given grain size.

The fields of Nabarro creep and Coble creep are both diffusion controlled processes and have been shown to be dominant at high temperature and low stresses.

Grain boundary flow is an important factor in the creep of metals at high temperature[34,35,42]. Rosenhain[36] was possibly the first to produce evidence of relative grain movements. It was observed that, when pure iron was strained at 900°C, differences in levels of the grains occurred on the originally flat polished surface, which indicated that relative translation of the grains had taken place. Hanson and Wheeler[37] made similar observation on aluminium subjected to creep deformation at 250°C. The absence of slip bands, at high temperature was indirect evidence that some other mechanism of deformation might be operative. McLean[38] has demonstrated that the total creep strain in poly-crystalline aluminium at 473°K was due to microscopically detectable slip, subgrain tilting, and grain boundary shearing. Whereas microscopically detectable slip was associated with dislocations that move within the grains, subgrain tilting was due to entrapment of dislocations of like sign in subgrain boundaries. Consequently, creep in polycrystalline aggregates appeared to be the resultant of two mechanisms, namely, migration of dislocations and grain boundary shearing.

The process of grain boundary sliding as a factor controlling creep is discussed in section 2.3.3. It is this process around which the subsequent modelling of the creep behaviour is obtained, for the quantification of creep and stress relaxation occurring at high temperatures during the heat treatment operation.

26.

2.3.3 Grain boundary sliding

The deformation characteristics of poly-
crystalline materials at high temperature are considerably
different from their behaviour at low temperatures.
Experimental observations of low temperature deformation by
many investigators have revealed the following features
during plastic flow, (i) deformation bands, (ii) well
defined slip, (iii) twinning. On the other hand high
temperature deformation is characterised by (i) breakdown
of grains into subgrains (ii) grain boundary shearing and
grain boundary migration, (iii) fine slip which is
difficult to resolve using microscopic techniques.

Low temperature deformation occurs essentially by
the deformation of the grains. At these temperatures the
deformation in the vicinity of the grain boundary is less
than the average deformation of the grains, which indicates
that the grain boundaries are a source of strength at low
temperatures[45]. When the temperature of testing is
increased to approximately 0.5 T_m significant sliding
occurs along the grain boundaries. Under these conditions,
the grain boundaries are a source of weakness rather than
strength. Siegfried[46] indicated an equicohesive temper-
ature beyond which the strength of the grain boundary
material became less than that of the crystal structure,
as shown in figure 7.

Quantitative measurements of grain boundary sliding
in a number of polycrystalline metals and alloys have

been investigated[47,48,49,50,51,52]. The aim has been
to evaluate the nature of the sliding at individual
boundaries and to determine the contribution of the
sliding to the total deformation of the specimen.

McLean and Farmer[43] showed that the grain boundary
displacement 'ε_{gb}' was directly proportional to the
total elongation 'ε_{tot}' of the specimen. The proportion-
ality between grain boundary displacement and total
elongation give

$$\frac{\varepsilon_{gb}}{\varepsilon_{tot}} = \text{constant}$$

The ratio of $\frac{\varepsilon_{gb}}{\varepsilon_{tot}}$ was found to increase with
temperature as shown in figure 8. The work of McLean and
Farmer[43] indicated that grain boundary sliding may
account for as much as 50% to 80% of the total creep strain
for aluminium and aluminium alloys. Gifkins[52] has
tabulated the values of $\varepsilon_{gb}/\varepsilon_{tot}$ for various metals and
alloys, and found that values range form 2.7 to 93 percent
depending on the material and test conditions. Raschinger
[53] compared the values of ε_{gb} from measurements of
sliding on the surface of an aluminium specimen with
those determined from changes in grain shape in the
interior. It was found that $\varepsilon_{gb}/\varepsilon_{tot}$ was approximately
90 to 95 percent for the interior grains as compared to
20 percent of the surface grains; thus indicating that the
predominant deformation mechanism in the interior was the

sliding or rotation of the grains over one another, with
attendant grain boundary migration. Hence, interior grains
generally remain unchanged in shape. The excessive sliding
in the interior grains led to the suggestion that co-
incident with sliding considerable deformation of the
grains occurs in the immediate vicinity of the boundary.
This localised deformation and boundary migration would
permit appreciable deformation of the specimen without
alteration of grain shape.

McLean[38] observed that the total creep curve
results from the sum of three factors - slip, subgrain
tilting and grain boundary shearing, as shown in figure 9.
Both, slip and grain boundary tilting were associated
with the migration of dislocations, whereas grain boundary
shearing was believed to be a quasi-viscous phenomenon.
Thus the total creep rate might arise from the sum of
two contributions such that

$$\dot{\varepsilon}_{tot} = \dot{\varepsilon}_d + \dot{\varepsilon}_{gb}$$

Although McLean's data revealed that the grain
boundary contribution was small (about 10% of the total),
the percentage depended very much on such variables as
temperature, rate of straining and grain size. Figure 10
shows that grain boundary displacement increases with
decreasing grain size and increasing stress for a given
temperature[39]. Furthermore grain boundary shearing
exhibited the same primary and secondary stages of creep

as the total creep strain, as shown in figure 11[41,44].

The mechanism of grain boundary sliding is determined by the structure of the boundary. Consequently any model of grain boundary sliding will be governed by the model chosen to describe the structure of the boundary. Conrad[45] proposed a model of grain boundary sliding that was as follows:-

(i) At high temperature the boundary behaves as a viscous film which has a lower strength than the conjugate crystals:

(ii) Upon application of a stress the boundary yields viscously in localized regions where it is relatively flat or smooth. The sliding is, however, soon blocked by projections in the boundary, resulting in stress concentrations at these points.

(iii) The stress concentrations cause the projections to yield plastically, permitting additional sliding. To maintain continuity of stress and strain, deformation of the grains in the vicinity of the boundary occurs.

(iv) The plastic deformation of the projections and associated material produces work hardening at low temperatures. This limits the sliding to small displacements, which may not be visible under the microscope.

(v) At intermediate and high temperatures recovery can occur in the deformed zone, allowing additional sliding to take place.

(vi) As the amount of sliding increases, the deformed material in the vicinity of the boundary may accumulate sufficient energy to allow migration

of the boundary to take place. This migration
then makes available relatively weaker grain
material where enhanced sliding may proceed.

(vii) If the stresses are sufficiently high to
produce significant deformation in the interior
of the conjugate grains, dislocations will
pile up at the boundary. The stress fields
and orientation of some of these dislocations
will be such as to produce a shearing stress
in the boundary and contribute to the sliding.

Quantitative information about grain boundary sliding
was established by Ke[54,55,56,57]. By the comparison
of certain anelastic phenomena in aluminium, he demon-
strated that for small displacements of the grains
($\sim 10^{-5}$ cms), the material at the grain boundary behaved
like a viscous fluid. According to Ke[54,55], the rate
of relative movements of the grains could be expressed
as:-

$$v = \text{constant} \cdot \tau \cdot \exp(-Q/RT) \qquad \ldots 2.3.7$$

Making the assumption that the boundary layer be
about one atom thick, Ke[54] obtained an expression for
the viscosity which, when extrapolated to the melting
point, gave fair agreement with the experimentally
determined viscosity of the liquid metal.

Ke's [55,56] experiment to establish viscous
behaviour of grain boundaries were conducted at very low
stress values. However the activation energies for low
amplitude sliding and large scale sliding are equal.
Besides this the ratio $\varepsilon_{gb}/\varepsilon_{tot}$ is approximately a

constant during creep[43], which indicates that the rate
controlling process for both low amplitude sliding and
large scale sliding is the same[45].

2.3.4 <u>The relationship between creep and thermal
stress generation during quenching</u>

If a part is subjected to repetitive appli-
cations of thermal stress, with or without external load,
it may in time fracture in the same manner as in mechanical
fatigue. This is known as thermal fatigue. The possible
importance of thermal stress was emphasised by Brophy and
Furman[58]. There was a 70 fold increase in creep rate in
temperature-cycled stainless steels compared with static
temperature conditions. The results were attributed to
temperature gradients induced by the rapid temperature
changes inducing thermal stresses. It was further shown
that the accelerated creep rates could be greatly diminished
if more uniform temperature distributions were maintained
across the body.

Lubahn et al[59] demonstrated the effect of varying
stress and temperature on the creep rate of high purity
lead. As shown in figure 12, the stress was suddenly
increased to 468 psi after a steady state creep had been
established at 456 psi. The strain rate increased very
rapidly, initially, but then fell gradually until it
reached a value appropriate to a stress of 468 psi. When
the stress was reduced to 456 psi again, the strain rate
fell to zero for a period of 20 minutes, and then built

to a value characteristic of 456 psi.

The effect of sudden change of temperature was also observed in lead wire specimens. When the specimen reached a steady strain rate at 29.5°C the temperature was rapidly increased to 54°C, which produced an immediate large increase in strain rate which then fell gradually until it reached the value characteristic of 54°C. When the temperature was again reduced to 29.5°C no measurable creep was observed until after 57 hours. In these tests the net effect was an increase in elongation over that of the steady state under average load or temperature conditions.

The simultaneous action of both load and temperature variation has been demonstrated by Guarnieri[60], Shepard et al[61] and Daniels et al[62]. Guarnieri, working with various aircraft alloys in sheet metal form, found that load and temperature cycling produced a wide variety of effects, rupture being sometimes accelerated and at other times retarded.

The creep behaviour of materials is usually obtained under constant or steady conditions of stress and temperature. However, during the quenching process, both the stress and temperature vary with time. This would result in unsteady creep conditions. Theoretical predictions of this more complicated situation from the simpler steady state constant stress and constant temperature creep behaviour have been presented[11,27]. The most widely

used examples are the 'strain hardening' and 'time hardening' theories, the validity of which has been tested on many occasions[63,64,65,66,67]. It was found that these theories do not predict the unsteady creep case exactly, but gave approximations that formed a good basis for consideration of unsteady creep behaviour.

In the case of plastic flow without creep, the incremental stress is a function of incremental strain, and the strain history or loading path. When creep occurs the strain path becomes time dependent, i.e., if the stress is changed after a certain amount of creep has been produced at a given constant stress, it is then necessary to determine the strain - time path at the new stress level.

Creep data obtained at constant stress and temperature are presented in figure 13. The time-hardeing rule states that the principal factor governing the creep rate is the length of time at the particular temperature involved, regardless of the stress history. The path followed under transient stress conditions is shown in figure 13a.

When the strain-hardening rule is applied the principal factor governing the creep rate is the strain, regardless of the stress history required to produce that strain. The path followed, under the strain hardening rule, with transient stress conditions, is shown in figure 13b.

2.4 Prediction of Thermal Stress during Quenching

The prediction of thermal stresses, during quenching requires consideration of the following:-

(i)   Temperature field across the component.

(ii)   Phase transformation characteristics.

(iii)   Mechanical properties of the material at various temperature.

The temperature field is influenced by the quenching severity of the cooling medium and the thermal properties of the material, the former being proportional to the surface heat transfer coefficient. The steeper the overall temperature gradient the greater will be the tendency for high thermal stresses to be developed, although these stresses may be limited by the yield stress of the material.

Phase transformations are accompanied by volume changes which affect the coefficient of expansion used to determine the change in the unrestrained length of a body with temperature. In an isotropic material both temperature changes and transformations will cause only a uniform dilation in an element free to expand. Hence, the coefficient of thermal expansion and volume changes due to phase transformations are all modelled as a function of temperature. The change in length per degree fall in temperature is obtained from the dilato-metric curve (figure 2), which represents the coefficient of thermal expansion and also the length change due to

the phase transformation.

The mechanical properties of interest in the prediction of thermal stresses are, the elastic moduli, the yield stress, Poissons' ratio, the work hardening coefficient and the coefficient of viscosity for the grain boundary in the case of high temperature creep and stress relaxation. All these properties are temperature dependent and also vary with the proportion of the different phases present at any particular instant during the cooling cycle.

The essential steps required in the calculation of quenching stresses have been described by Denton[8] and Andrews[7]. Firstly, the temperature distribution within the body at different times during the quench must be calculated. Secondly, the elastic stress distribution that results from the change in temperature distribution during each time increment is found, using the elastic moduli and the coefficient of thermal expansion. The above step assumes that external loads and moments are applied to constrain completely each element within the body. Thirdly, the applied forces and moments are removed, thus allowing the different elements in the body to deform (elastically or plastically) in such a way that there is complete compatibility and that in any section the residual stresses are in force and moment equilibrium with themselves. The above process is repeated after each time increment during the quench and a complete

analysis of the stress and strain behaviour is obtained.
It is the possibility of plastic flow during the third
step of this procedure that creates the greatest difficulty.

2.4.1. The calculation of the temperature distribution in the body

The temperature distribution at all stages
of the cooling process may be determined by the solution
of the differential heat conduction equation[68]:

$$\frac{\partial}{\partial x}\left[\frac{\lambda \partial \Theta}{\partial x}\right] + \frac{\partial}{\partial y}\left[\frac{\lambda \partial \Theta}{\partial y}\right] + \frac{\partial}{\partial z}\left[\frac{\lambda \partial \Theta}{\partial z}\right] + H = C_p\left[\frac{\rho \partial \Theta}{\partial t}\right] \qquad \ldots 2.4.1.1$$

The above equation may be solved analytically[68,69]
or numerically[70]. The versatility of analytical
solution is restricted by the requirement of non-variant
initial and boundary conditions. In such cases it is also
necessary that the thermal properties and the heat transfer
coefficient, used in the equation be constant or vary as some
simple function of the variable concerned. This does not
actually happen during the quenching process, which greatly
reduces the value of the analytical method in the present
problem.

Solution by numerical methods involve the calculation
of the temperature at preselected, discrete points[71].
The temperature at a certain point is taken as representative of a certain region which includes the point,
and the heat flow at a boundary is taken as the summation

37.

of the flows from the appropriate regions. In the present work, the solution of heat conduction equation is obtained by the finite difference technique.

The finite difference solution to the heat conduction equation have been given by Croft and Liley[70], Dusinberre[71] and Adams and Rogers[72]. The partial differential equation has been replaced by finite difference equations in terms of partial quotients, which have then been solved to obtain the values of temperature at a finite set of points within the body. For the unsteady state problem the following boundary conditions are required to be specified:

(i) Temperature Θ at all points within the body at time $t = 0$

(ii) The heat flow from the surface governed by the convective heat transfer coefficient equation

$$\frac{\partial \Theta}{\partial n} = -\frac{h}{\lambda} (\Theta_s - \Theta_A)$$

Two types of finite difference solutions have been outlined, called the explicit and the implicit formulation respectively. In the case of uniaxial heat flow the formulations were reduced to:-

(a) Explicit formulation

$$\frac{\Theta_1^{n+1} - \Theta_1^n}{\Delta t} = \alpha_{td} \left[\frac{\Theta_{i+1}^n - 2\Theta_1^n + \Theta_{i-1}^n}{\Delta x^2} \right]$$

(b) Implicit formulation

$$\frac{\Theta_1^{n+1} - \Theta_1^n}{\Delta t} = \alpha_{td} \left[\frac{\Theta_1^{n+1} - 2\Theta_1^{n+1} + \Theta_{i-1}^{n+1}}{\Delta x^2} \right]$$

The derivation of these solutions was also obtained by the expansion of Taylor series[73]. The replacement of differentials by finite difference terms gave an error resulting from the truncation of the Taylor series and was of the order of Δx^2 [74].

The explicit formulation was reduced to the well known Sch midt formulation, by maintaining the Fourier's number $\dfrac{\alpha_{td} \Delta t}{\Delta x^2} = \frac{1}{2}$

$$\Theta_i^{n+1} = \left(\frac{\Theta_{i+1}^n + \Theta_{i-1}^n}{2} \right)$$

To obtain an accurate temperature field across the body by numerical methods it is required that the temperature dependence of heat transfer coefficient and the thermal diffusivity be known.

The dependence of heat transfer coefficient on the surface temperature of a quenched plate has been established by Price and Fletcher[75]. Heat transfer coefficients were estimated by the lumped parameter approach and were used in an explicit finite difference solution to obtain an estimate of the surface temperature. A plate with thermocouple located at a point just below the surface was quenched and the temperature profile for that position was determined experimentally. The calculated temperature at any instant was then compared with its corresponding experimental value. Successively more accurate estimates of the heat transfer coefficient were used to predict

temperatures after a small time interval, at the point
where experimentally determined temperatures were available.
The correct value of heat transfer coefficient was assumed
to be that which gave a discrepancy of less than a
specified amount between the experimental and predicted
temperatures. The variations of surface heat transfer
coefficient in the case of oil and water, as established
by Price and Fletcher[75], and in the case of a 46.6%
Nitrate-Nitrite salt bath and subsequent oil quenching by
Cuicas[102] are shown in figure 14.

The temperature dependence of thermal conductivity
and the specific heat in a $3\frac{1}{2}$%Ni, 1.55%Cr, 0.45%Mo, 0.3%C,
0.1%V steel, is obtained from the work of Atkin's et al[76]
and is shown in figure 15.

2.4.2 Calculation of thermal stresses during quenching

Thermal stress problems have been analytically
solved in various texts[77-80]. Perhaps the most author-
itative text covering the analytical solution is due to
Boley and Weiner[78]. Assuming that there be no thermo-
mechanical coupling and that the temperature distribution
across the body was known, the thermal stress problem
may be reduced to the following 15 equations:

3 equilibrium equations

$$\frac{\partial \sigma_{xx}}{\partial x} + \frac{\partial \sigma_{xy}}{\partial y} + \frac{\partial \sigma_{xz}}{\partial z} + X = 0$$

$$\frac{\partial \sigma_{xy}}{\partial x} \quad \frac{\partial \sigma_{yy}}{\partial y} \quad \frac{\partial \sigma_{yz}}{\partial z} + Y = 0$$

40.

$$\frac{\partial \sigma_{xz}}{\partial x} + \frac{\partial \sigma_{yz}}{\partial y} + \frac{\partial \sigma_{zz}}{\partial z} + Z = 0.$$

6 stress-strain relations

$$\varepsilon_{xx} = \frac{1}{E} \{\sigma_{xx} - \nu(\sigma_{yy} + \sigma_{zz})\} + \alpha_{ex}\theta$$

$$\varepsilon_{yy} = \frac{1}{E} \{\sigma_{yy} - \nu(\sigma_{zz} + \sigma_{xx})\} + \alpha_{ex}\theta$$

$$\varepsilon_{zz} = \frac{1}{E} \{\sigma_{zz} - \nu(\sigma_{xx} + \sigma_{yy})\} + \alpha_{ex}\theta$$

$$\varepsilon_{xy} = \frac{\sigma_{xy}}{2G}, \quad \varepsilon_{yz} = \frac{\sigma_{yz}}{2G}, \quad \varepsilon_{zx} = \frac{\sigma_{zx}}{2G}$$

6 strain-displacement relations

$$\varepsilon_{xy} = \frac{1}{2} \left(\frac{\partial u}{\partial y} + \frac{\partial v}{\partial x}\right) \qquad \varepsilon_{xx} = \frac{\partial u}{\partial x}$$

$$\varepsilon_{yz} = \frac{1}{2} \left(\frac{\partial v}{\partial z} + \frac{\partial \omega}{\partial y}\right) \qquad \varepsilon_{yy} = \frac{\partial v}{\partial y}$$

$$\varepsilon_{zx} = \frac{1}{2} \left(\frac{\partial \omega}{\partial x} + \frac{\partial u}{\partial z}\right) \qquad \varepsilon_{zz} = \frac{\partial \omega}{\partial z}$$

Classical calculus techniques may be used to solve the above equations for the following 15 unknowns:

6 stress components $\sigma_{xx}, \; \sigma_{yy}, \; \sigma_{zz}, \; \sigma_{xy}, \; \sigma_{yz}, \; \sigma_{zx}$

6 strain components $\varepsilon_{xx}, \; \varepsilon_{yy}, \; \varepsilon_{zz}, \; \varepsilon_{xy}, \; \varepsilon_{yz}, \; \varepsilon_{zx}$

3 displacement components $u, \; v, \; \omega$

Boley and Weiner[78] have established solutions for some simple cases and have taken into account elastic, plastic and viscoelastic effects. However in most of the analyses, the mechanical and thermal properties were assumed to be constant. Boley[81] has outlined an analytical solution to the linear partial differential equations to obtain a solution of the two dimensional heat and thermal stress problem. An attempt was made to incorporate a temperature dependent modulus of elasticity and coefficient of thermal expansion, using empirical relationships between each of these properties and temperature. Phase transformations were not considered. Considerable doubt can be thrown on the correctness of the empirical relationships used. Furthermore, no attempt was made to include viscoelastic effects in this final version of the mathematical model.

Landau et al[82] have presented a thermal stress analysis for a quenched plate which took into account elastic, plastic and viscoelastic effects and which used similar analytical solutions to those of Boley and Weiner[78]. A temperature dependent von-Mises yield criterion was used and the viscoelastic effect was expressed by a Maxwell type relationship, incorporating a temperature-dependent coefficient of viscosity. A finite difference technique was used to calculate the transient temperature distribution across the plate. The stress system was assumed to be plane stress with equal values of this quantity in the true in-plane principal directions

and a step by step procedure was used to calculate the values of temperature and stress and the location of the plastic regions at time t+ Δt, from the values already obtained at time t. Initially, an elastic strain estimate was obtained and the consequent elastic stress was used in a Maxwell-type relationship to give an estimate of the visco-elastic strain. The original elastic strain was then adjusted, to take into account the viscoelastic effect. The new stress level was then compared with the yield stress and the von-Mises yield criterion was applied to check whether any plastic flow had been produced at this stage in the process. From the analysis of the results, it was found that the viscoelastic effect had an insignificant effect on the residual stresses. However the temperature dependence of the yield stress was of much greater importance. One of the main criticisms of the above model is the method by which the stress relaxation factor has been obtained. Though the creep strain was evaluated from a Maxwell-type relationship, the corresponding stress relaxation was related to the strain by the elastic constant. The model also suffers from the drawback that it does not consider the effect of temperature on various physical and mechanical properties data. Phase transformations were ignored and a constant coefficient of thermal expansion was used in the analysis, and an arbitrary relationship between the yield stress and temperature and between the coefficient of viscosity and temperature was considered: the predicted results were

not verified experimentally.

Atkins et al[83] have proposed a method by which
stress relaxation may be introduced into a thermal stress
calculation involving rotors. Owing to the three
dimensional stress system at the centre and two dimensional
stress system at the surface, the plastic flow due to
creep was assumed to occur only at the surface. A dubious
relationship was used to obtain the sub surface depth
below which stress relaxation was assumed to be effective.
A finite difference method was used to compute the temper-
ature and stress across the section of the rotor. The
percentage stress reduction at the surface was obtained
from isothermal stress relaxation curves established
experimentally. No attempt was made to redistribute the
elastic stresses over the unrelaxed portion of the cylinder,
which was necessary if force and moment equilibrium were
to be maintained within the rotor.

Toshioka et al[84] have developed a model to
calculate the stresses during quenching of 0.45%C steel
cylinders. The temperature distribution was calculated by
fitting an empirical equation, which gave a relationship
between the temperature at the centre (experimentally
obtained) and the temperature at any point within the cross
section. The quenching severity was altered by changing
the value of a parameter which was used in the empirical
equation, to obtain the temperature distribution across the
cylinder at any instant. The effect of martensite and

bainite transformations on the overall stress distribution was included in the model. The progress of the martensite and bainite transformations was approximated as a quadratic function of temperature. The distribution of martensite and bainite was determined from hardness measurements. The strains induced by both the structures were assumed to be constants: these had not been determined experimentally. The flow stress of austenite was assumed to be zero, so that internal stresses were produced only after the transformation was initiated at the surface. A differential elastic-plastic calculation was carried out using a computer program. The residual stresses estimated were compressive at the surface and tensile at the centre with a low quenching severity. No attempt was made to compare the predicted stress distribution with experimental results. The model did not take into account the temperature dependence of physical properties, and the transient temperature distribution obtained from an empirical relationship did not take into account the relevant physical properties of the material or the quenchant. Furthermore the yield strength of austenite becomes significant as the temperature falls towards M_S. Though it was not the purpose of this assumption, it may have resulted in an exaggerated stress relaxation effect above the transformation temperature.

Fletcher[85] proposed a numerical method for the analysis of stress and strain, in a plate of low alloy

steel that had been quenched under various quenching conditions. The choice of steel was such that it transformed completely to martensite after quenching. Heat transfer was considered to take place only through the thickness of the plate, so that the subsequent stress system produced stresses only in the plane of the plate. The temperature distribution was calculated by the finite difference solution of the law of unsteady heat conduction with the relevant boundary conditions. This information was used to calculate the stress arising from the combination of that due to temperature alone and that produced by the transformation of austenite to martensite. It was found that the type of residual stress distribution present on the completion of the quench was dependent upon the cooling rate. Thus, at high quenching rates the residual stress at the surface was tensile, while the corresponding stress at the centre was compressive. However, the reverse stress pattern was produced by the slowest quench. No attempt was made to verify the predicted results by experimental analysis. The quenching severity or the heat transfer coefficient, which is temperature dependent, was either assumed to be constant or else was made to vary in steps within each of which it remained constant. Plastic flow was accounted for by the use of Von-Mises criterion, without due consideration of work hardening, which may have influenced the flow stress of the material. Stress relaxation effects, which may be significant in the case of the slower quenchants, were not included.

Thermal stresses in quenched steel specimens have
also been analysed by the finite element method. By this
method the structure is approximated to an assemblage of
elements, interconnected at a discrete number of nodal
points at the element boundaries. The stress at these
nodal points is computed by relating the nodal displace-
ments and the elastic properties of the material. Matrices
of the relevant equations are prepared for all the elements
in the structure and solved, which take into account
the following basic factors[86]:

  (i)   the equilibrium of forces

 (ii)   the compatibility of displacements

(iii)   the laws of material behaviour.

The finite element method is now well documented
[87-89]. Although it originated in structural engineering,
it has been widely accepted as an extremely valuable method
of analysis in several other areas[90]. Toshioka[91],
Inoue[92], Fujio et al[93], Archambault et al[94] have
used the finite element method for thermal stress analysis
in quenched specimens.

Toshioka[91] used the finite element technique to
calculate both the transient temperature distributions
and the consequent distortions produced in quenched steel
bars; these calculations included the use of temperature
dependent heat transfer coefficient, thermal conductivity
and specific heat capacity (see tables 1 and 2). The
effect of martensite, bainite and pearlite transformations

47.

were also taken into account. The predicted residual strain values obtained at the end of the quench were compared with those determined experimentally, (see figure 16). Reasonable agreement was found in the case of the change in diameter, but the length changes did not show good agreement. Although the specimens were of such a size (200mm diameter) that the effect of creep strain is likely to be quite significant, the contribution of creep strain to the overall residual strain was not included in the mathematical model.

Inoue and Tanaka[92] presented a finite element formulation of the elastic-plastic stress analysis during quenching of 0.43%C steel cylinders. The surface and centre temperatures were experimentally determined and were used as boundary conditions in the basic equations of thermal conduction, which were used to determine the temperature field at any stage in the cooling process. The coefficient of thermal expansion was modelled as a function of temperature and cooling rate and phase transformations, that were governed by the cooling rate, were subject to a critical rate criterion. Graphical relationships between temperature and dilation pertaining at the relevant cooling rates were used to obtain the coefficient of thermal expansion. Tension tests were carried out at elevated temperatures to determine the yield stress and the work hardening coefficient as a function of temperature, and the von-Mises yield criterion

was used to test for the onset of plastic flow. The predicted residual stress distribution in the cylinder showed good agreement with the experimental values, which were obtained by the Sach's boring out technique, (see figure 17). The determination of the yield stress and work hardening coefficients were carried out without due consideration of the actual structure present during the quench, so that the method by which the results from these tests were applied to the thermal stress calculation was inappropriate. Further, the assumption that the maximum cooling rate determines the structural change within the material is far from real, because it does not take into consideration the continuous cooling transformation diagrams, which are more representative of the volume of phase transformation occurring at any instant during the quench.

Inoue et al[93] in a later work observed a reduction in residual stresses in quenched cylinders of 12%Cr after they have been subjected to tempering. This was attributed to the process of creep during the time that the specimen was held at the tempering temperature (i.e. 2 hours and 50 hours at 400°C). The specimen considered was completely transformed to martensite during quenching. A finite element method was used to determine the temperature distribution, but no information was given about the thermal property data used. A heat generation term was

used to incorporate the heat evolved due to martensite transformation: by so doing, very large increases in temperature were observed during the transformation, which temporarily halted the cooling process. The creep strain was represented as an empirical function of stress, temperature and time. The results, shown in figure 18, indicate that the maximum change in stress occurs at the beginning of the tempering process and the stresses approach their final level asymptotically after the initial period of stress change. The results of these calculations were compared only with measurements of the stresses at the surface of a quenched cylinder, although good agreement was found at this point.

Fujio et al[94] have calculated the stresses developed when 50mm diameter cylinders of 0.45%C steel are quenched in water. The transient temperature distribution within the cylinders was obtained by means of a classical method employing the physical properties of the material pertaining to the mean temperature of the specimen during quenching. A constant heat transfer coefficient was calculated by comparing curves obtained with this property with the experimental cooling curves: iteration was continued until an acceptable agreement was obtained. Hardness measurements on experimentally quenched cylinders were used to determine the volume fraction of martensite present at different depths below the surface. The form of dilatometer curve used to represent dimension changes at a point in the specimen depended on the fraction of

martensite present at that point, as shown in figure 19. The yield stress data was obtained by interpolation which involved the use of the yield stress of the material at room temperature in either the martensite or annealed conditions, and a single high temperature value of the yield stress at 900°C, as shown in figure 20. The residual stress distribution in a quenched cylinder was determined experimentally using the Sach's boring method. A close correlation between the predicted and experimental values was obtained, as shown in figure 21 and it was concluded that a considerable effect was imparted on the residual stress distribution by the martensitic transformation. Fujio et al[95] extended the application of the model to obtain the distortion and residual stress in a gear tooth which involved the use of the finite element method to calculate the temperature distribution. A subsequent stress analysis by the finite element technique was then carried out. A good quantitative correlation was found between the predicted and experimental distortion values of the tooth profile, as shown in figure 22, but there were discrepancies between both the calculated diameter change of the cylinder at the tip and the calculated tooth height, and the corresponding values as obtained by experiment, as shown in figure 23.

Archambault et al[96], have presented a theoretical study of the formation of residual stresses in aluminium alloy cylinders of 20-120mm diameter that had been quenched

in water. The severity of the quench was altered by
either raising the temperature of the water or by coating
the specimens with a thermally non-conductive coating.
An attempt was made to find the optimum quench condition
which would increase the strength of the part, while
keeping the distortion at a minimum. A finite element
method was used to calculate the variation of internal
stresses and the residual stresses developed during
and after the quench. No mention was made as to the
physical and mechanical data used and the method for
determining the temperature distribution and subsequent
stress analysis was not outlined. It was observed that
higher cooling rates were accompanied by more plastic
deformation leading to residual stresses at the end of the
quench, while a reverse effect was observed at lower cooling
rates. Thus a quenching window, which gave the optimum
combination of strength, distortion and quenching conditions
was indicated as shown in figure 24. The application of
the model was extended further, and a qualitative analogy
was established for a very complex shape without due
consideration to the geometry of the part.

Denis et al[97] examined the effect of stress on the
decomposition of austenite and then included her results
in a mathematical model of the thermal stress generation
process in a cylinder of tool steel (60NCD11). The
temperature distribution was obtained experimentally,
by measuring the temperature along the median plane of
the cylinder at different points below the surface.

A thermo-elastic-plastic stress analysis was carried out by a method that involved successive approximation with temperature-dependent yield stress and strain hardening parameters. The effect of stress on the transformation was considered to be two-fold. Firstly, it displaced the M_s temperature to a higher value and secondly it induced transformation plasticity. These effects were observed by conducting dialatometric tests at various applied stresses. A tensile stress of 270 MPa raised the M_s temperature by $+15^\circ$C. This effect was incorporated in the calculation by shifting by the required amount the transformation start point on the dialatometric curve used to model the coefficient of thermal expansion. Also the dilations generated at any specific point during the transformation were increased by the appropriate amount as the level of applied stress was raised. The modelling of this effect in the thermal stress calculation was carried out by reducing the apparent yield stress at that point in the calculation, thus enhancing the amount of plasticity obtained during the transformation. The reduction in the flow stress was made arbitrarily without due consideration of the transformation characteristics of the material. Although later in the work an attempt was made to compare the plastic strains associated with the reduction in flow stress, to the enhanced dilation observed experimentally. The transformation plasticity is anisotropic phenomenon[98], which should be modelled by the actual transformation characteristics of the

material from a stress dilatometer test under both compression and tension. The effect of transformation plasticity brought about a reversal in the residual stress profiles calculated from the model, but this predicted stress pattern was not verified experimentally.

Fletcher and Price[99,100] have recently proposed a numerical method for the determination of the stresses and strains in plates of low alloy steels that transformed completely to martensite during quenching. The technique was first proposed by Fletcher[85] but has been extended to include temperature dependent physical and mechanical properties of the quenching media and the material. It is this model that has been used as a basis for the current work. The relationship between surface heat transfer coefficient and surface temperature was experimentally established for the cases of water, oil and polymer quenchants. The flow stress of austenite between M_s and $800^{\circ}C$ was determined and strain hardening was represented by two linear coefficients that were dependent upon the temperature and previous plastic strain. The increase in flow stress, produced during each time increment by the plastic flow, was added to the flow stress in the previous step and was used in the subsequent application of the yield criterion. The relationship between specimen length and temperature during cooling was established from dialatometric tests. The results of the calculation suggested that all three quenchants

produced plastic flow, which was confined to temperatures above M_s. This flow gave rise to a complex residual stress distribution which, in the case of the water or polymer quenchant, involved a maximum tensile stress just below the surface and a compressive stress towards the centre, as shown in figure 25a. The oil quench produced a reverse stress distribution (figure 25b). A comparison was also made between the residual stress and strain distributions predicted by the mathematical model and the corresponding results obtained by experiment using a surface grinding technique. The degree of agreement was dependent on the type of quenchant employed; in the case of water the agreement was good (figure 25a), but as the severity of the quench was reduced the discrepancy between the two results became progressively greater. The discrepancy was worst in the case of oil (figure 25b). Attempts that were made to explain the discrepancy in the results, included the suggestion that stress relaxation might occur to a significant extent in the case of an oil quench. A crude method was used to include stress relaxtion effects which involved the reduction in the flow stress of austenite and martensite, with a consequent reduction in the level of stresses developed these manipulations, in the case of oil, resulted in a slight improvement, but impaired the existing correlation in the case of water.

2.5 Transformation Induced Plasticity

It has been shown that austenite, when transformed to martensite under tensile stress, exhibits an elongation which is in excess of that expected from the associated volume expansion. This phenomenon has been called transformation induced plasticity[103].

Attempts have been made to explain this transformation induced plasticity on a crystallographic scale in the case of thermally activated transformations proceeding by nucleation and growth (e.g. the $\gamma \rightleftharpoons \alpha$ transformation in iron and steel)[104]. Porter and Rosenthal[105] have supposed that increased rates of nucleation result from the stress fields of dislocations which pile up at grain boundaries and other barriers during deformation and as a reaction to internal stresses. When the nucleus looses its coherency with the austenite matrix the advancing interfaces act as sinks for the piled up dislocations and additional plastic deformation takes place under the influence of external stress.

Greenwood and Johnson[98] have suggested that phase transformations under conditions where an external stress was applied, will be anisotropic in nature. A theoretical analysis of stress-induced phase transformation have suggested that such anisotropy may lead to localised plastic flow within regions of the weaker phase, which give a transformation plasticity strain proportional to the applied stress.

The description of transformation-induced plasticity made by Wasserman[106] suggested that the characteristics of such transformations were, firstly, that the yield point which must be exceeded in order to induce deformation was lowered briefly for the duration of the transformation process. Experimental verification of this has been obtained from the work of Bolling et al[107], Tamura[108] and later by Beck et al[109].

The transformation plasticity effect during martensite transformations have been observed by many workers[110,111, 112]. Beck et al[110] have observed an enhancement in the dilation during transformation when the specimen was subjected to tensile stresses. The amount of dilation was proportional to the applied stress. However, their work did not show the effect of compressive stresses on the dilation produced during transformation. The sign of the applied stress during transformation influences the sign of the associated transformation plasticity. Hence experiments of Desalos et al[111] and recently by Fletcher[112] have shown a reduced overall dilation and even contraction of a dilatometric specimen transforming under compressive stresses. Desalos et al[111] have conducted a finite element analysis of the effect of stress on an austenite grain during transformation into martensite. They assumed that the part of the structure most likely to transform was the one which had the greatest tendency to shear or where the second invariant of the stress tensor was a maximum. Further-

more, a linear relationship was established between the transformation plasticity strain and the applied stress.

The onset of martensite transformation requires a critical chemical driving force, obtained from the difference of free energies of austenite and martensite, which is achieved at the M_s temperature (see figure 26). However, it is possible to obtain martensite above the M_S temperature by the application of external stress. From the thermodynamic point of view the applied stress may be considered to provide a mechanical potential or driving force additional to the chemical driving force thus making available, at temperatures above the M_S temperature, a total driving force equal to that required for the transformation of austenite to martensite (see figure 26)[108].

2.6 <u>Conclusion from the Survey of Previous Work</u>

Steady progress in the modelling of thermal stress generation during quenching has taken place over the last thirty years. In the early stages classical stress analysis was used[77-80] which necessarily involved the use of temperature distributions that could be represented by a simple equation, usually a quadratic. Only a few workers incorporated plastic deformation into the calculations. The subsequent introduction of numerical methods allowed the use of temperature-dependent mechanical and physical properties[91-95], and also permitted the introduction of realistic temperature

distributions[70-72]. It was also now possible to introduce the effect of phase changes on the generation of thermal stress by modelling the linear coefficient of thermal expansion, either as a function of temperature alone[99], or as a function of both temperature and cooling rate[92].

However, much of the work that has been published prior to the last five years may be criticized on the grounds that at least some of the data used is an over-simplification and therefore not appropriate to some part of the thermal stress generation process. The more recent work, such as that of Fletcher and Price[99,100] is a big improvement on the earlier models, but there are still some significant properties that have been ignored.

Of these neglected properties, creep strain and stress relaxation are of particular relevance. Mendelson et al[57], Landau et al[82] and Inoue et al[93] have all attempted to incorporate creep effects into thermal stress calculations, but the actual mechanism of creep has not been taken fully into consideration.

3. STRESS RELAXATION AND CREEP DATA

3.1 Experimental Procedure used in the determination of Rates of Stress Relaxation and Creep in a Specimen of 835M30 Steel

(a) Stress relaxation test

The stress relaxation tests were carried out in an Instron tensile testing machine. The specimen was mounted in the grips between a load cell and a moving cross head. The load cell was connected to a chart recorder which registered the applied load and the extension in the specimen.

The cross head speed controlled the strain rate, which varied from 0.005/minute to 50/minute. The use of the mechanical property data obtained by Fletcher[85] in the thermal stress calculation indicated that the strain rate may vary during the quenching between the limits shown by the equations given below[100]

$$\varepsilon_{min} = 0.14 \times 10^{-3} s^{-1}$$

$$\varepsilon_{max} = 7.1 \times 10^{-3} s^{-1}$$

The stress relaxation tests at temperatures below 400°C required the use of a rapid cool and a rapid test, in order to minimise the possibility of decomposition of the austenite into non-martensitic phases. Temperature stabilization at these temperatures was obtained in about 3 minutes and the tests were carried out at the strain rate of $5.8 \times 10^{-3} s^{-1}$ which was nearer to

the maximum strain rate quoted above.   Although

the strain rate varied in a complex manner during the

course of the quench, as shown in figure 27, it was not

possible to incorporate, in the thermal stress model, the

stress relaxation effect as a function of both temper-

ature and strain rate.

Stress relaxation tests involved the application

of the desired load to the specimen at the specified

strain rate, after which the strain was held at a

constant value. This was achieved by maintaining the

cross head at a fixed point during the test. The

relationship between load, time was then obtained from

the chart recorder. The stress data obtained was then

expressed as a fraction of the initial stress i.e. P/P_o,

which made it possible to use the data independently of

the critical stress level.

Initially, it was decided to conduct stress relax-

ation tests at temperatures between 850^oC and 300^oC, as

it was assumed that at the onset of transformation (i.e.

below 300^oC) the hard martensitic structure would

reduce further stress relaxation to negligible levels.

However the results obtained showed that this was not

the case and the lower limit of temperature range

was then extended to 136^oC. Below this temperature

the specimens were subject to failure during loading.

The original arrangement did not allow the use of

high temperature stress relaxation tests on the Instron

machine. Therefore a moveable furnace, mounted on the front panel of the machine, was installed as shown in plate 1. The furnace could be moved out of the test zone, to allow the insertion of the grips and the specimen assembly, after which the furnace could be returned to its original position. The grips were attached to the load cell and the cross head by universal joints.

A resistance wound furnace coupled with a variable transformer was used to raise the specimen temperature. The furnace was packed with Kaol wool, at the top and the bottom, to prevent heat losses and control the specimen temperature to the desired level of accuracy. A temperature variation of $\pm 5^{\circ}C$ was observed at a specimen temperature of $850^{\circ}C$, which was within the specified British Standards[113]. A Chromal-Alumel thermocouple was attached to the specimen surface to monitor the specimen temperature. The furnace was cal- ibrated and the relationship between temperature and voltage was obtained, as shown in figure 28.

A cylindrical tensile specimen, as shown in figure 29 was selected from BS 3500. The specimen was nickel plated to prevent it from oxidizing while at high temperature. Metallographic inspection was carried out after the test for traces of surface oxidation, and the nickel flash was found to be sufficiently protective.

During the test the specimen was first austenitized at $850^{\circ}C$ and then cooled to the test temperature. The

cooling rates used were critical, on account of the possibility of the transformation of austenite to bainite at temperatures between 400°C and 300°C, (see figure 30). Mean cooling rates of 32.5°C/second, were obtained in the specimen, by cooling with a stream of argon. By the use of such cooling rates the specimen was able to cool from 850°C to 200°C in 20 seconds. However the cooling of the mass of the furnace and the grips took considerably longer. Hence during a test the specimen was quickly brought down to the test temperature by introducing argon into the furnace, but as soon as the test temperature was reached the argon was withdrawn from the interior and directed on the exterior of the furnace and the grips. This enabled the specimen temperature to be maintained at a constant value and at the same time increased the cooling of the mass of the furnace and the grips. This procedure took a maximum time of 10 minutes to stabilize temperatures as low as 200°C. At 400°C and 300°C the time taken to produce stabilization was not more than 3 minutes. Care was necessary to avoid the stressing of the specimen during the quench, by adjusting the cross head, so that no load was generated on the specimen at any time.

Using this arrangement stress relaxation tests were carried out at temperatures between 850°C and 136°C. A test was also conducted at 90°C but it resulted in the brittle fracture of the specimen.

(b) Creep tests

Creep tests were carried out on a Denison creep and stress rupture machine, as shown in plate 2. The specimen was loaded by means of a lever arm which carried a weight pan on one end and a specimen/grip assembly, attached to the base of the machine through a capstan, on the other end. The rotating capstan enabled the weight pan to be raised or lowered when loading and unloading the specimen, while the movement of the lever arm corresponded to the extension of the specimen. A dial gauge was fitted to monitor the movement of the lever arm. Alternatively a pen and drum mechanism (strain-time recorder) which revolved once every 24 hours was provided, which produced a continuous record of extension against time. A furnace capable of moving vertically on guide rods was used to heat the specimen.

The specimen was inserted into the furnace and heated to the austenitization temperature. Again the accuracy of the temperature measurement was $\pm 5^{\circ}C$ at $850^{\circ}C$. The temperature was lowered to the test temperature by switching off the furnace for a short period of time, after which the furnace controller was reset to give the required test temperature. The appropriate load was carefully placed in the load pan and the load applied gradually to avoid shock loading, by means of the clock-wise rotation of the capstan.

Creep data obtained over a long period of time did

not give reliable information about the properties of
metastable austenite below 750°C on account of the
structural instability of the phase. However creep
tests were carried out at 850°C, 800°C and 750°C under
loads of 38kg, 50kg and 75kg respectively.

3.1.1 Results of stress relaxation tests

        The results of stress relaxation tests
obtained at temperatures between 850°C and 136°C are
presented in figure 31. The results are plotted for a
time duration of 26 seconds, after which a constant
rate of stress relaxation was obtained in all the tests.
The initial rate of stress relaxation was observed to be
high at high temperatures; thus the stress level
reduced to 70% of its initial value after 1.8 seconds
at 850°C, wheras during the same time interval it reduced
to only 98% of the initial value at a temperature of
136°C.

3.1.2 Results of creep tests

        Creep tests were conducted at temperatures
of 850°C, 800°C and 750°C by the procedure described
in section 3.1. The creep tests were continued for a
period of time in excess of 24 hours in order to be able to
obtain a graph of creep strain versus time from the
chart recorder provided on the creep machine (described
in secion 3.1). All the results show a significant
period during which steady state creep occurred so that
it was possible in all cases to evaluate steady state
creep rate. A graph of steady state creep rates versus

65.

temperature is shown in figure 32.

3.2 The Representation of the Viscoelastic Effect by the use of Mechanical Bodies

Metallic materials subject to loads at elevated temperatures exhibit both elastic and anelastic behaviour, the latter produced by creep effects involving either intra-granular processes or the viscous flow of the grain boundaries. This type of behaviour may be represented by mechanical models (figure 33) involving combinations of the following

i) a perfectly elastic spring for elastic deformation

ii) a dashpot consisting of a perforated piston moving in a cylinder containing a viscous liquid for inelastic deformation.

These elements can be combined in different ways so that the model behaves in a way that approximates to the observed mechanical behaviour of real materials.

Three of the extensively used mechanical models, shown at figure 33, are:

i) Maxwell body,

ii) Kelvin or Voigt body,

iii) Standard linear solid.

The Maxwell body has a spring and dashpot connected in series, wheras the Kelvin body has these elements in parallel. The standard linear solid is a three element body with a Maxwell body connected in parallel with a spring.

In terms of stress-strain tensors the following relationships have been outlined by Boley and Weiner[78].

$$\dot{e}_{IJ} = \frac{\dot{s}_{IJ}}{2G} + \frac{s_{IJ}}{2\eta}$$
Maxwell body

$$2\eta\dot{e}_{IJ} + 2Ge_{IJ} = s_{IJ}$$
Kelvin body

$$\dot{e}_{IJ} + \phi e_{IJ} = \frac{\dot{s}_{IJ}}{2G} + \frac{s_{IJ}}{2\eta}$$
Standard linear solid

3.3 Theoretical Equations Representing Stress Relaxation and Creep

The relationships between stress and strain obtained from the mechanical bodies described in section 3.2 can be rearranged to represent both stress relaxation and creep effects. In the three dimensional case it is necessary to split the stress and strain into the mean and deviatoric portions.

Mean stress and strain are given by:

$$\sigma_m = \frac{\sigma_{II}}{3} \qquad\qquad \ldots 3.3.1$$

$$\varepsilon_m = \frac{\varepsilon_{II}}{3} \qquad\qquad \ldots 3.3.2$$

Deviatoric stress and strain tensors are given by

$$s_{IJ} = \sigma_{IJ} - \delta_{IJ}\,\sigma_m \qquad\qquad \ldots 3.3.3$$

67.

$$e_{IJ} = \varepsilon_{IJ} - \delta_{IJ}\, \varepsilon_m \qquad\qquad \dots\ 3.3.4$$

By employing the above equations, the expressions for creep strain and stress relaxation for uniaxial conditions (derived in Appendix 1) are as follows:

Maxwell body

Stress relaxation

$$\frac{\sigma}{\sigma^0} = \exp\left(-\frac{Gt}{\eta}\right) \qquad\qquad \dots\ 3.3.5$$

Creep strain

$$\dot{\varepsilon}_{creep} = \frac{\sigma}{2\eta(1+\nu)} \qquad\qquad \dots\ 3.3.6$$

Kelvin body

Stress relaxation

$$\sigma = 2G(1+\nu)\,\varepsilon^0 \qquad\qquad \dots\ 3.3.7$$

Creep strain

$$\varepsilon_{creep} = \frac{\sigma^0}{2G(1+\nu)}\left[1 - \exp\left(-\frac{Gt}{\eta}\right)\right] \qquad \dots\ 3.3.8$$

Standard linear solid

Stress relaxation

$$\frac{\sigma}{\sigma^0} = \left[1 - \frac{2\eta\,\phi}{E}(1+\nu)\right]\exp\left(-\frac{Gt}{\eta}\right) +$$

$$\frac{2\eta\phi\,(1+\nu)}{E} \qquad \dots\ 3.3.9$$

Creep strain

$$= \frac{\sigma^0}{E}\left[\frac{E}{2\eta\phi\,(1+\nu)} - 1\right]\left[1 - e^{\phi t}\right]$$

$$\dots\ 3.3.10$$

Consideration of the mechanical bodies shown in figure 33 in conjunction with equations 3.3.5-3.3.10 leads to the following description of the operation of the viscous models in a visco-elastic situation.

Maxwell body

(a) Stress relaxation

On the sudden application of strain the viscous element is initially zero and the immediate response comes from the elastic behaviour of the spring. With the total strain held constant the subsequent extension of the viscous element causes the load to decrease and the spring to contract.

(b) Creep

The applied stress is carried directly by the viscous element which gives the subsequent viscous response after the spring has produced an initial elastic strain. Under conditions of constant stress, the relationship between creep strain and time indicate Newtonian flow.

Kelvin body

(a) Stress relaxation

This model suggests no stress relaxation, because the spring which is in parallel with the dashpot is held at a constant strain, which prevents any movement in the dashpot.

(b) Creep

From the expression for creep, the creep strain increases, at a reducing rate as the time increases. The creep strain approaches a limiting value of $\frac{\sigma_o}{2G(1+\nu)}$ as the time approaches infinity. This is expected from the model, because the spring is restrained by the viscous element during the initial loading and then is allowed to extend as the viscous element extends.

The Standard linear solid

The Standard linear solid is a three element model that contains the features of both the Kelvin and Maxwell model. In one arm the spring and dashpot combination allows stress relaxation to occur by the replacement of elastic strain in the spring by viscous strain in the dashpot. However, unlike the Maxwell body, this process is partially restrained by the spring in the other arm of the combination (see figure 33). Thus the stress relaxation process essentially ceases at some finite level of stress. As is shown below, this model represents more closely than the Maxwell body the actual stress relaxation results obtained in this investigation.

3.4 Selection of a Mechanical Body to Represent the Viscoelastic Behaviour of 835M30 Steel

In the Maxwell body, stress relaxation is represented by a single exponential decay term, which suggests that the stress decays to zero at longer times. Experimental stress relaxation curves indicated that the

70.

stress approaches a positive final value asymptotically.
However it was not possible to fit an expression of the
Maxwell type to the experimental stress-relaxation curves
without varying the ratio G/η with time. Even so
attempts to model the stress relaxation behaviour by
arbitary choosing the best value of G/η gave a very
poor correlation with the experimentally observed
behaviour as shown in figure 34. Furthermore, the use of
such G/η ratios in the calculation of creep strains by
means of the Maxwell body gave values that could not be
reconciled with the experimentally determined creep values.
Indeed, the latter implied that G/η should be constant
with time. Therefore the Maxwell model was considered
unsuitable as a method by which stress-relaxation behaviour
could be described. The Kelvin body could also be
immediately discarded, because of its inability to predict
any stress relaxation.

The standard linear solid allows the stress relaxation
curve to approach a final finite stress level asymptot-
ically. However, the shape of curve obtained is dependent
upon the values of two constants η and ϕ , which are a
part of an exponential constant and an equation constant
in the stress-relaxation and creep strain expressions.
They are both dependent upon the type of material and
may be made to vary with temperature in order to model
the stress relaxation rates pertinent to a specific
temperature over a wide range of temperatures. The use

of two factors allows a much better fit between the calculated and experimental curves to be obtained than is possible with the single factor used in the Maxwell body, (see figure 34). Hence the standard linear solid has been selected to quantify the viscoelastic effect in 835M30 steel.

3.4.1 Comparison of calculated and experimental stress relaxation and creep curves

The relationships between σ/σ^0 and time obtained from stress relaxation tests at temperatures between 850°C and 136°C are shown in figure 31. According to the standard linear solid model these relationships are governed by:

$$\frac{\sigma}{\sigma^0} = (1 - A) e^{-Bxt} + A$$

The expression shows that the value of A lies between 1 and 0. If A =1, $\sigma = \sigma^0$ and the behaviour of the material is that of the Kelvin body. If A = 0, $\sigma = \sigma^0 e^{-Bxt}$ which is the same equation as that obtained from the Maxwell body. When time becomes infinite σ/σ^0 becomes equal to A, which is thus shown to be the limiting stress attained during the stress-relaxation test. The parameter B is an exponential rate constant which governs the rate of decay and influences the shape of the stress relaxation curve. An increase in B increases the rate of decay.

Once the value of A had been fixed as the limiting stress observed during the stress relaxation test the

72.

value of B was obtained to give the best fit between
the experimental and calculated curves. Hence a set of
values of A and B were obtained, which were functions of
temperature but not time. Figure 35 shows a comparison of
the predicted and experimentally obtained stress relax-
ation curves at temperatures between $850^{\circ}C$ and $136^{\circ}C$
together with the values of A and B that gave the best
fit at each temperature.

The values of A and B obtained from the stress
relaxation data may also be used to predict creep strain.
Thus creep strain may be obtained from the standard linear
solid by the use of the equation:

$$\varepsilon_{creep} = \frac{\sigma^{o}}{E} (\frac{1}{A} - 1) \left[1 - \exp(-A.B.t) \right]$$

which suggests a reduction in creep rate with time and an
assymptotic creep strain value which is characteristic
of the constants A and B. The only experimental creep
curves (those obtained at $850^{\circ}C$, $800^{\circ}C$ and $750^{\circ}C$) showed
a steady state creep rate, and a comparison of the theo-
retical creep curves with the experimentally obtained
curves show fundamental differences in the shape of the
two types of curve (see figures 36a,b,c). The standard
linear solid initially predicts high creep rates, but in
each case it was found that the creep rate predicted
after 10 seconds was very similar to the observed steady
state creep rate. Even at lower temperatures some check
on the experimental and calculated creep strains could

be obtained from the stress relaxation data. This check
depends on the assumption that the elastic strain lost
during the relaxation of stress was converted into
viscous flow on account of the constant total strain in
the specimen during the test. Thus the stress relaxation
values provided a direct measure of the creep strain
associated with the stress relaxation process. The amount
of elastic strain lost due to relaxation was calculated
by dividing the stress relaxation by the modulus of
elasticity. A comparison of the creep strain information
at temperatures between 850°C and 150°C calculated by these
two methods is presented in table 3, at temperatures where
the results are available a good correlation is observed
between the two methods.

3.4.2 The effect of temperature on the parameters A and B used in the standard linear solid equation.

A regression analysis provided the following
relationships between the parameters A and B and temper-
ature (see figure 37)

$$A = 1.038475 - 0.000816 \times \theta$$

$$B = 0.04959 + 0.000658 \times \theta$$

The parameter A, which increases linearly as the
temperature rises, is proportional to η and ϕ. Thus the
results obtained are in contradiction to the suggestion
that η is an exponential function of temperature[78].

4. Prediction of Thermal Stress and Strain

The thermal stresses generated during quenching were calculated by a technique first established by Fletcher[85], and then expanded by Price[100] to incorporate the effect of strain hardening and temperature-dependent physical and mechanical properties. Thermo-mechanical coupling was neglected so that the equations governing the transient heat conduction (see section 2.4.1) provided data that could be used directly in the calculation of thermal stress and strain. An infinite plate model with heat flow only in a direction perpendicular to the longitudinal plane of the plate was used which enabled the assumption of plane stress conditions to be made, with two equal principal stresses acting in directions parallel to the edge of the plate, as shown in figure 38. In the case of the calculation of the temperature distribution the distance between the surface and centre was split into 40 elements, but in the subsequent stress calculation the number of elements was reduced to 10. The temperature in these larger elements was obtained by averaging the temperatures of the smaller elements of which each larger element was composed. The whole quenching period was divided up into a series of small time intervals. The time steps were determined from the stability criterion:

$$\frac{\alpha_{td} \, \Delta t}{(\Delta z)^2} = \frac{1}{2}$$

75.

The calculation technique consisted of the following
steps

(i)   Determination of the temperature distribution
      across the plate, at a series of time points
      using an explicit finite difference method.

(ii) Determination of the change in thermal strain
      introduced in each element during the intervals
      between each time point.

(iii) Calculation of the associated elastic thermal
      stress assuming complete restraint at the edges
      and elastic conditions in the material.
      Subsequent modification of these stresses, to
      take into account the free edge boundary conditions.

(iv) Modification of the thermal stresses as a consequence
      of the application of the yield criterion.

(v)   Modification of the elastic strains as a consequence
      of the change in stress levels introduced subse-
      quent to stage (iii).

Stage (iv) required an iteration process until the
final stress distribution satisfied the free edge boundary
condition.

4.1   Calculation of Thermal Stress and Strain without considering Stress Relaxation

The temperature distribution was calculated using
the explicit formulation of the finite difference solution
to the transient heat conduction equation together with
the Schimidt assumption that $\Delta F_o = \frac{1}{2}$

then $\Theta_i^{n+1} = \dfrac{\Theta_{i+1}^n + \Theta_{i-1}^n}{2}$ ... 4.1.1

when $\quad \Delta F_o = \dfrac{\alpha \ td \ \Delta \ t}{(\Delta z)^2} = \tfrac{1}{2} \quad$ ... 4.1.2

The boundary conditions used were discussed in section 2.4.1. The surface heat transfer coefficients are presented in table 5 as a function of temperature.

According to Fletcher[85], the change in thermal stress in each part of the plate due to thermal contraction and transformation, assuming complete edge restraint and fully elastic conditions was:

$$(\Delta \sigma_i^{n+1})_r = \dfrac{E \ \alpha \ ex}{1 - \nu} \ (\theta_i^{\ n} - \theta_i^{\ n+1}) \quad ... 4.1.3$$

The total stress in each element at the new time was

$$(\sigma_i^{n+1})_r = \sigma_i^{\ n} + (\Delta \sigma_i^{n+1})_r \quad\quad ... 4.1.4$$

The removal of edge restraint required the condition of force and moment equilibrium to be met. This was achieved by the use of the equation

$$(\overline{\sigma}^{n+1})_r = \sum_{i=1}^{i=j} \dfrac{(\sigma_i^{\ n+1})_r}{j} \quad\quad ... 4.1.5$$

$$\sigma_i^{\ n+1} = (\sigma_i^{n+1})_r - (\overline{\sigma}^{n+1})_r \quad\quad ... 4.1.6$$

The application of the von Mises yield criterion was then carried out. In a uniaxial stress system, plastic deformation can occur only if,

$$\sigma_i^{\ n+1} \ \geqslant \ \sigma_{fi}^{\ n+1}$$

Then if $\sigma_i^{n+1} > \sigma_{fi}^{n+1}$, $\sigma_i^{n+1} = \sigma_{fi}^{n+1}$

and if $\sigma_i^{n+1} < \sigma_{fi}^{n+1}$, $\sigma_i^{n+1} = \sigma_i^{n+1}$

In the case of plastic flow, the replacement of elastic stress by a flow stress unbalanced the forces within the plate after the application of yield criterion: the elastic stresses were now modified by a constant amount, so that the overall force on the plate after the application of the yield criterion became zero.

The initial estimate of the strain increment produced during a time interval gave the first estimate of the elastic stress, prior to the application of the yield criterion. During the iterative procedure, used to determine the effect of plastic flow on the element, this initial estimate of the elastic stress was changed, until the subsequent application of the yield criterion produced zero net force on the plate. This was considered to have been attained when $\bar{\sigma}^{n+1} \leq 0.1$ MPa. A change in the elastic strain corresponding to the change in the estimate of elastic stress was then made to the initial estimate of the former.

Thus $\Delta\varepsilon_i^{n+1} = \dfrac{\sigma_i^n}{a-b\,\theta_i^n} - \dfrac{\sigma_i^{n+1}}{a-b\,\theta_i^{n+1}}$ ... 4.1.7

The flow stresses were adjusted as plastic flow occurred, in order to take into account the strain hardening effect. To this end a strain hardening coefficient was used which was dependent upon temperature

78.

and the amount of previous plastic deformation. The strain hardening rates were represented by two linear coefficients as:

$$\left(\frac{d\sigma_f}{d\varepsilon_p}\right) \quad \varepsilon_p = 0 \rightarrow 0.5\% \quad = \quad W_1$$

$$\left(\frac{d\sigma_f}{d\varepsilon_p}\right) \quad \varepsilon_p = 0.5 \rightarrow 1.0\% \quad = \quad W_2$$

The values of W_1 and W_2, as calculated by Price, are presented in table 4 and illustrated in figure 39.

4.2 Calculation of Thermal Stress and Strain when Stress Relaxation Occurs During the Quench

The uniaxial stress relaxation tests on the steel 835M30 at temperatures between $850^{\circ}C$ and $100^{\circ}C$ (described in section 3.1.1) showed a significant reduction in stress during a relatively short period of time. Since the thermal stresses generated during the quenching process were liable to be affected by this stress relaxation behaviour, the procedure used to calculate thermal stress was modified to incorporate these time dependent changes in stress. To achieve this it was necessary to determine the amount of stress relaxation and the associated creep strain during a series of small time steps, which could then be used to modify the thermal stress generated by the procedure described above (section 4.1).

The amount of stress relaxation and creep was repre-

sented by the standard linear solid model (section 3.4.1), which gave the following expressions for stress relaxation and creep, under plane stress conditions (derived in section 4.3.5).

$$\frac{\sigma}{\sigma^0} = \frac{2 \phi \eta (1+2\nu)(1-\nu)}{E} + \left[1 - \frac{2 \phi \eta (1+2\nu)(1-\nu)}{E} \right]$$

$$\exp \left(\frac{- Gt}{\eta} \right) \qquad \ldots 4.2.1$$

$$\varepsilon_{creep} = \frac{\sigma^0 (1-\nu)}{E} \left[\frac{E}{2 \phi \eta (1+2\nu)(1-\nu)} - 1 \right]$$

$$\left[1 - \exp(- \phi t) \right] \qquad \ldots 4.2.2$$

The parameter A in the uniaxial formulation of the stress relaxation equation must be modified to take into account the plane stress conditions (compare the expression for A in the uniaxial case, section 4.3.5). The new value of A is 0.82 of that obtained in the uniaxial case. The temperature dependence of A and B has already been established in section 3.4.2 and is shown in figure 37.

Creep and stress relaxation effects were entered into the calculation of thermal stress and strain at the point where the initial elastic stress estimate has been adjusted to provide equilibrium.

$$\text{viz.} \qquad \sigma_i^{n+1} = (\sigma_i^{n+1})_r - (\sigma^{n+1}) \qquad \ldots 4.1.6$$

The initial stress applicable to the stress relaxation

80.

process during any time interval was obtained from the average stress during that time period.

$$\text{viz.} \qquad (\sigma_i^{n+1})_{av} = \frac{\sigma_i^{n+1} + \sigma_i^{n}}{2} \qquad \ldots 4.2.3$$

Thus from equation 4.2.1

$$\sigma^0 = (\sigma_i^{n+1})_{av}$$

The stress relaxation curve at the relevant temperature was then used to obtain the proportion of σ^0 that was relaxed during the time interval in question. A knowledge of σ^0 thus allows the determination of the magnitude of the stress reduction introduced in time Δt, (i.e. $(\Delta \sigma_i^{n+1})_{Relaxed}$). Several different methods have been used to obtain the rate of stress relaxation on account of the uncertainty over the effect of the thermal and stress history of the specimen on subsequent viscous flow. These are discussed fully in section 4.2.1.

The initial elastic stress estimate given by equation 4.1.6 was then adjusted to take into account this stress relaxation

$$\sigma_i^{n+1} = \sigma_i^{n+1} - (\Delta \sigma_i^{n+1})_{Relaxed} \qquad \ldots 4.2.4$$

after which the new stress distribution was readjusted for equilibrium (as described in section 4.1).

The remaining steps in the calculation followed the procedure described in section 4.1 until the elastic strain was calculated. In the absence of stress relaxation this is given by:

81.

$$\varepsilon_i^{n+1} = \varepsilon_i^n + \frac{\sigma_i^n}{a-b\,\Theta_i^n} - \frac{\sigma_i^{n+1'}}{a-b\,\Theta_i^{n+1}}$$

$$\dots 4.1.7$$

To this elastic strain estimate there was now added the creep strain associated with the stress relaxation process obtained from equation 4.2.2.

Thus the new strain estimate was

$$\varepsilon_i^{n+1} = \varepsilon_i^n + \frac{\sigma_i^n}{a-b\,\Theta_i^n} - \frac{\sigma_i^{n+1'}}{a-b\,\Theta_i^{n+1}} + (\Delta\varepsilon_i^{n+1})_{creep}$$

$$\dots 4.2.5$$

A flow chart of the computer program for the complete thermal stress calculation is shown in figure 40.

4.2.1 The introduction of stress relaxation and creep rates into the thermal stress and strain calculation

The derivation of stress relaxation and creep rates from equations 4.2.1 and 4.2.2 were not straight-forward. Difficulties arose because:

(a) Even though the standard linear solid model gave the best overall fit with the experimental relationships there were nevertheless still certain discrepancies, thus the rates predicted by this theoretical model fell to zero after a relatively short time, when in practice viscous processes continued at a small but steady rate for a prolonged period.

(b) The isothermal experimental data did not take into account the prior thermal and stress history of the material during the earlier stages of the quench.

Thus the rates of stress relaxation and creep obtained by the differentiation of equations 4.2.1 and 4.2.2 were only realistic at shorter times and there was an absence of information about the use of isothermal data relating to viscous flow in a continuous cooling situation. There was no obvious method by which these difficulties could be overcome in a completely satisfactory manner, so several methods were initially used, each of which has advantages and disadvantages, viz:

(i)   Rates of stress relaxation and creep as a function of temperature only (method 1).

(ii) Rates of stress relaxation and creep as a function of time and temperature with a steady rate used after 20 seconds (method 2).

(iii) Rates of stress relaxation and creep as a function of time and temperature throughout the quench (method 3).

As mentioned above the rates of stress relaxation and creep obtained by the differentiation of equation 4.2.1 and 4.2.2 respectively approach zero after a relatively short time. Hence in the case of method 3 and method 2 (for the first 20 seconds) the average rates obtained from these equations between the start of the process and the time under consideration were used to represent the stress relaxation rate at the latter time.

Method 1 was based on the assumption that the rate

of stress relaxation was a function of temperature only
so that the initial rate of relaxation obtained in a
stress relaxation test at relevant temperature was used
whenever the material reached this temperature, irres-
pective of the time that had elapsed before the temper-
ature was attained. Thus during a time interval Δt
the average rate of stress relaxation and creep from
equation 4.2.1 and 4.2.2 was given by

$$(\dot{\sigma}_R)_i^{n+1} = \frac{(\sigma_i^{n+1})_{av} \, (1-A_i^{n+1}) \, \left\{1-\exp(-B_i^{n+1}\Delta t)\right\}}{\Delta t}$$

$$\ldots 4.2.6$$

$$(\dot{\varepsilon}_{creep})_i^{n+1} = \frac{(\sigma_i^{n+1})_{av} \, (1-A_i^{n+1}) \, \left\{1-\exp(-A_i^{n+1}B_i^{n+1}\Delta t)\right\}}{(a-b\,\theta_i^{n+1}) \, A_i^{n+1} \, \Delta t}$$

$$\ldots 4.2.7$$

Method 2 included the effect of hardening of the
material up until the time reached a value of 20 seconds,
whereafter a steady rate pertaining to 20 seconds was used.
Thus the average rates of stress relaxation and creep for
this method from equation 4.2.1 and 4.2.2 were given by:

$$(\dot{\sigma}_R)_i^{n+1} = \frac{(\sigma_i^{n+1})_{av}(1-A_i^{n+1}) \, \left\{1-\exp(-B_i^{n+1}t^{n+1})\right\}}{t^{n+1}}$$

$$\ldots 4.2.8$$

84.

$$(\dot{\varepsilon}_{creep})_i^{n+1} = \frac{(\sigma_i^{n+1})_{av} (1-A_i^{n+1}) \left\{1-\exp(-A_i^{n+1}B_i^{n+1}t^{n+1})\right\}}{(a-b\,\theta_i^{n+1})\,A_i^{n+1}\,t^{n+1}}$$

$$\ldots 4.2.9$$

where $t^{n+1} \leqslant 20$ seconds.

The use of a steady rate after 20 seconds was in line with both the experimentally observed rate of stress relaxation at later times during the test and the steady state creep rate obtained by experiments as shown in figure 41.

Method 3 was similar to method 2 except that the average rates of stress relaxation and creep were allowed to reduce with time throughout the quench. Thus a progressive hardening of the material was carried out during the quench by the use of this method. The average rates of stress relaxation and creep were obtained from equation 4.2.8 and 4.2.9, except that the restriction $t^{n+1} \leqslant 20$ seconds no longer applied.

A comparison was carried out between the stress relaxation rates obtained from expression 4.2.6 and 4.2.8 (methods 1 and 2), where the times used in expression 4.2.8 were representative of the cooling of the surface of a 20mm oil quenched plate (see figure 42). As would be expected method 1 (equation 4.2.6) gave a higher stress relaxation rate than method 2 (equation 4.2.8), although in both cases the rate of stress relaxation was found to

fall as the temperature was reduced (see table 6).

4.3 Data used in Thermal Stress Calculation

In order to carry out the thermal stress analysis
the following data was necessary:

(i) The relationships between temperature and thermal
diffusivity, thermal conductivity, and surface
heat transfer coefficient, in order to calculate
the temperature distribution (thermal property
data, see below).

(ii) The relationship between temperature and length
of a dilatometer specimen of 835M30 during cooling
from $850^{\circ}C$.

(iii) Uniaxial tensile test and Poissons ratio data
of 835M30 in the austenitic condition at temper-
atures from $850^{\circ}C$ to M_s, plus the corresponding
data for the material in the martensitic but
untempered condition (Mechanical property data,
see below).

(iv) The overall increase in volume accompanying the
transformation of ferrite $+ Fe_3C$ structure to
martensite in 835M30, in order to compare the
experimentally determined distortions with those
predicted by calculation.

The data used for the determination of stress relaxation
and creep under uniaxial conditions has already been des-
cribed in section 3.4.2. In the mathematical model,
however, the data was adapted for plane stress conditions.

4.3.1 Thermal Property data

The effect of temperature on the thermal diff-
usivity and surface heat transfer coefficient is shown in

figures 15 and 14 respectively. In the case of water and oil the data was obtained by Price and Fletcher[75] and in the case of the martempering salt bath, by Cuicas[102]. The thermal diffusivity was obtained from unpublished data provided by the British Steel Corporation. The equations relating the above data to the temperature are presented in tables 5 and 7.

4.3.2 The relationship between temperature and length of a dilatometer specimen of 835M30 during cooling from 850°C.

The relationship between temperature and length of a dilatometer specimen of 835M30 during cooling from 850°C was determined by Price and Fletcher[99] and is shown in figure 43. The equations representing these relationships were as follows:

$$\theta > 300°C \qquad \varepsilon_{thermal} = 2.1407 \times 10^{-5} \theta - 0.01066$$

$$288°C < \theta < 300°C \qquad \varepsilon_{thermal} = -0.00422$$

$$90°C < \theta < 288°C \qquad \varepsilon_{thermal} = \frac{(Y^1 - 1.4435)}{581.23}$$

$$\theta < 90°C \qquad \varepsilon_{thermal} = 0.6133 \times 10^{-5} \theta - 0.0015$$

where
$$Y^1 = 1.0102 + 0.1804(x^1) - 0.35024(x^1)^2 - 1.0244(x^1)^3 - 0.824(x^1)^4$$

$$x^1 = 0.0080193 \theta + 1.3079$$

The value of the thermal expansion coefficient, α_{ex} used in equation 4.1.3 to calculate the elastic stress

produced in each element under conditions of full restraint when the element was cooled from θ_i^n to θ_i^{n+1}, was obtained from

$$\left[\overline{\alpha.ex}\right]_{\theta_i^n \rightarrow \theta_i^{n+1}} = \frac{\left[\overline{\varepsilon_{thermal}}\right]_{\theta_i^{n}} - \left[\overline{\varepsilon_{thermal}}\right]_{\theta_i^{n+1}}}{\theta_i^n - \theta_i^{n+1}}$$

The values for the thermal expansion coefficient of each element were than obtained directly from the relevant part of the dilatometer curve. This allowed the expansion due to martensitic formation to be included in the calculations.

4.3.3 Mechanical property data

Uniaxial tensile tests were conducted at temperatures between 850°C and 200°C, on an Instron tensile testing machine as described in section 3.1. The flow stress of specimens of 835M30 which contained metastable austenite were determined and checked against the flow stress values obtained by Price[100], but the test range was extended to a lower temperature than had been possible with the equipment used in the earlier work. A good correlation was found as shown in figure 44. The relationship between austenite flow stress and temperature used in the present calculation is presented in table 4.

The flow stress used in the thermal stress calculations at temperatures lower than the M_s temperature were a function of the volume fraction of martensite and austenite and their respective flow stresses[85,99],

viz:

$$\sigma_f = V_\alpha (\sigma_f)_\alpha + V_\gamma (\sigma_f)_\gamma$$

The volume fraction of the austenite and martensite present at different temperatures were calculated from the relationship between temperature and the length of the dilatometer specimen, using the method shown in figure 43. A value of 1600MPa was used for the flow stress of the material that possessed a 100% martensitic structure. This value was obtained from published data on 835M30, since all room temperature tests carried out in the present investigation were suspect, on account of premature failure outside the specimen gauge length.

The relationships between temperature and the strain hardening coefficients used in the thermal stress calculation (section 4.1) are shown in figure 39 and table 4.

The data for the variation of Young's modulus and Poisson's ratio during a rapid cool designed to produce martensitic structure in a low alloy steel was given by Aitken et al[114]. The variation of $E/(1-\nu)$ with temperature derived from the above data is shown in figure 45. A linear approximation was used in the thermal stress calculation[99], viz:

$$\frac{E}{1-\nu} = 2.935 \times 10^5 - 141.77\,\theta \quad \text{MPa}$$

89.

4.3.4 Overall volume change accompanying the hardening of 835M30

The structure of the plates prior to hardening consisted of a mixture of ferrite and carbide, but after the austenitization and quenching treatment the structure contained only martensite. This structural change was accompanied by an increase in volume. The calculation procedure in the prediction of thermal stress and strain considered only the dimensional changes produced during the quench and did not take into account the additional volume change associated with the change from ferrite + Fe_3C to martensite. Thus when a comparison was made of the predicted residual strain with those obtained by experiment the change in dimensions produced by this change in structure was added to those predicted by the thermal stress calculation.

The net volume change accompanying the heating to $850^{\circ}C$ and subsequent quenching of a cylindrical specimen of 835M30, with an initial structure of ferrite and carbide (heat treated for 3 hours at $630^{\circ}C$ prior to the quenching operations) was 0.381%[99]. This represented a linear isotropic change of 0.127%.

4.3.5 Stress relaxation and creep equations for standard linear solid under plane stress conditions

The calculation of the generation of thermal stress assumed a state of plane stress. However the stress relaxation and creep information, as outlined in section

3.3, was obtained under uniaxial stress conditions. Hence the standard linear solid expressions (equations 3.3.9 and 3.3.10) were redetermined with plane stress conditions, viz:

$$\dot{e}_{IJ} + \phi\, e_{IJ} = \frac{\dot{s}_{IJ}}{2G} + \frac{s_{IJ}}{2\eta}$$

$$s_{IJ} = \sigma_{IJ} - \delta_{IJ}\, \sigma_m$$

$$e_{IJ} = \varepsilon_{IJ} - \delta_{IJ}\, \varepsilon_m$$

Thus by substitution

$$(\dot{\varepsilon}_{IJ} - \delta_{IJ}\, \dot{\varepsilon}_m) + \phi\, (\varepsilon_{IJ} - \delta_{IJ}\, \varepsilon_m) = \frac{1}{2G}\, (\dot{\sigma}_{IJ} - \delta_{IJ}\, \dot{\sigma}_m) + \frac{1}{2\eta}\, (\sigma_{IJ} - \delta_{IJ}\, \sigma_m)$$

$$\ldots 4.3.5.1$$

For the plane stress condition

$$\varepsilon_{IJ} = \varepsilon_{xx} = \varepsilon_{yy} \qquad\qquad \varepsilon_{zz} = -\nu\,(\varepsilon_{xx} + \varepsilon_{yy})$$

$$\sigma_{IJ} = \sigma_{xx} = \sigma_{yy} \qquad\qquad \sigma_{zz} = 0$$

Mean strain $\qquad \varepsilon_m = \dfrac{2(1-\nu)}{3}\, \varepsilon_{xx}$

Mean stress $\qquad \sigma_m = \dfrac{2}{3}\, \sigma_{xx}$

Substituting in equation 4.3.5.1 and rearranging

$$(1+2\nu)\, \dot{\varepsilon}_{xx} + \phi\,(1+2\nu)\, \varepsilon_{xx} = \frac{\dot{\sigma}_{xx}}{2G} + \frac{\sigma_{xx}}{2\eta}$$

$$\dot{\varepsilon}_{xx} + \phi\, \varepsilon_{xx} = \frac{\dot{\sigma}_{xx}}{2G\,(1+2\nu)} + \frac{\sigma_{xx}}{2\eta\,(1+2\nu)} \qquad \ldots 4.3.5.2$$

Simplification of equation 4.3.5.2 to represent stress relaxation and creep was now carried out by the same method as has been described in the case of uniaxial tension in Appendix 1 (equation 1.17). In the case of stress relaxation

$$\frac{\sigma_{xx}}{\sigma_{xx}^{o}} = \left[1 - \frac{2\,\phi\,\eta\,(1+2\nu)(1-\nu)}{E} \right] \exp\left(-\frac{G\,t}{\eta}\right) + \frac{2\phi\eta(1+2\nu)(1-\nu)}{E}$$

$$\ldots 4.3.5.3$$

In the case of creep strain

$$(\varepsilon_{xx})_{creep} = \frac{\sigma_{xx}\,(1-\nu)}{E} \left[\frac{E}{2\,\phi\,\eta\,(1+2\nu)(1-\nu)} - 1 \right] \left[1 - \exp(-\,\phi\,t) \right]$$

$$\ldots 4.3.5.4$$

These equations are analogous to those derived for uniaxial conditions (equation 3.3.9 and 3.3.10)

Let $\quad C = \dfrac{2\phi\eta\,(1+2\nu)(1-\nu)}{E}$

From equations 3.3.9 and 3.3.10

$$A = \frac{2\phi\eta\,(1+\nu)}{E} \qquad\qquad B = G/\eta$$

Comparing parameters C and A, and selecting a value of ν as 0.33

$$C = 0.82 \times A$$

The temperature dependence of A and B was established in section 3.4.2. Equations 4.3.5.3 and 4.3.5.4 were used in the mathematical model to represent stress relaxation and creep in the quenched plate under plane stress conditions.

4.4. Transformation Plasticity

4.4.1 Reduction in flow stress below M_s

As described in section 2.5, the presence of a stress changed the magnitude of the dimensional change associated with a phase transformation, due to the occurrence of transformation induced plasticity. Many workers [107,108,109] have suggested that a reduction in the flow stress of the material occurs during stress-assisted transformation, which allows the plastic flow of the material at stress levels where normally only an elastic strain occurs. Unfortunately experimental evidence for such a reduction has not been forthcoming and those, such as Beck et al[119] who have used this approach, have had to resort to an arbitary flow stress reduction which happens to agree approximately with the enhanced dilation produced during dilatometry experiments[97]. The usual explanation for the absence of direct evidence of a yield stress reduction is that the transformation plasticity effect only occurs during quenching while the phase change is taking place. It would therefore not be observed during isothermal tensile tests. Provided this explanation is accepted than the dilatometer data produced by Beck[110]

can be used to obtain both a reduced yield stress and a work hardening rate during the early stages of plastic flow, although Beck[97] himself appears to have made use of an arbitary reduction in yield stress. The procedure used in the present work aims to make greater use of a similar stress-dilation data obtained by Fletcher[112] using 835M30 steel (figure 46). The enhanced dilation observed when an applied stress in excess of 40MPa was used, has been attributed to plastic flow and the applied stress present at a given temperature and strain has been assumed to be the flow stress generated at that temperature as a consequence of the work hardening produced by the strain. For example at 300°C the plastic strain attributable to applied stress levels of 125MPa and 250MPa is 0.1% and 0.175% respectively (see figure 46). These stress and strain values provide two points on the stress-strain diagram (figure 47), and when extrapolated back to the elastic line, gave the value of both the yield stress and the strain hardening coefficient. This procedure has been repeated to obtain the values of flow stress and strain hardening coefficients for the range of temperatures where the transformation plasticity effect has been found to be prominent (300°C to 260°). The reduction in flow stress obtained from the dilation data, has been modelled as a function of temperature, as shown in figure 48(table 4). Temperature had no effect on the strain hardening coefficient, which remained constant during the transformation. The yield stress and work hardening data

94.

thus obtained from the dilatometer curves for 835M30 steel specimens has been subsequently introduced into the mathematical model of the thermal stress generation.

4.4.2 Transformation plasticity as an additional strain

The expansion produced by the asustenite martensite transformation is enhanced by the presence of transformation plasticity that occurs when the applied stress is positive. Conversely, this expansion is reduced and may even be replaced by a contraction when the applied stress is negative (see section 2.5). Such a situation was observed recently by Fletcher[112], who measured the relationship between dilatometric specimen length and temperature when an austenitic specimen of 835M30 was cooled in the presence of a compressive stress. In this case almost all of the transformation plasticity effect occurred during the first 40°C of the transformation i.e. between 300°C and 260°C (figure 46). Fletcher's data was obtained at stress levels of either -250MPa or -125MPa and showed that the transformation plasticity effect was smaller at low stress levels.

The value of the transformation strain used in the thermal stress calculation was obtained from the dilatometer curves produced when an initially austenitic specimen was cooled under stress-free conditions. In order to incorporate the effect of transformation plasticity in this model, an additional strain (either negative or

positive depending on the sense of the stress), has been obtained from Fletcher's data, the value of this additional strain being obtained by a comparison of the dilation curve obtained under stress free condition with that obtained when an applied load was present (figure 49). The temperature between 300°C and 260°C was divided up into temperature intervals of 5°C, as shown in figure 49: at the end of each temperature interval a value of $\frac{\Delta L}{L_o}$ was obtained from both the curves and added together to give the net transformation plasticity strain at the relevant temperature and stress level. In this way a set of transformation plasticity strain values within the temperature range 300°C to 260°C was obtained at each level of external stress (see figure 50). It was assumed that the transformation plasticity strain under tensile conditions was equal in magnitude but opposite in sign to the corresponding strain obtained by a compressive stress.

From figure 50 the following relationships were assumed:

(i)   The value of transformation plasticity strain at stress levels above |125| MPa were those pertaining to |250| MPa in the figure.

(ii) The value of transformation plasticity strain for stress levels between |125| MPa and 80 MPa were those pertaining to |125| MPa in the figure.

(iii) The transformation plasticity strain was equal to the transformation strain at stresses between 80 MPa and |40| MPa. In the case of compressive stresses within this range the net strain produced

96.

by the martensitic transformation was zero.

(iv) Zero transformation plasticity strain occurred at stresses below $|40|$ MPa.

The relationships between temperature and transformation plasticity strain within the various stress ranges as obtained from figure 50 are:

$\sigma > 125$MPa

$$\varepsilon_{TRIP} = -0.3135147 + 2.463707 \times 10^{-3} \theta - 4.698153 \times 10^{-6} \theta^2$$

$$\dots \ 4.4.2.1$$

$\sigma < -125$ MPa

$$\varepsilon_{TRIP} = -\left\{ -0.3135147 + 2.463707 \times 10^{-3} \theta - 4.698153 \times 10^{-6} \theta^2 \right\}$$

$$\dots \ 4.4.2.2$$

$\sigma > 80$ MPa

$$\varepsilon_{TRIP} = -0.126751 + 1.006846 \times 10^{-3} \theta - 1.93378 \times 10^{-6} \theta^2$$

$$\dots \ 4.4.2.3$$

$\sigma < -80$ MPa

$$\varepsilon_{TRIP} = -\left\{ -0.126751 + 1.006846 \times 10^{-3} \theta - 1.93378 \times 10^{-6} \theta^2 \right\}$$

$$\dots \ 4.4.2.4$$

$\sigma > 40$ MPa

$$\varepsilon_{TRIP} = \varepsilon_{Thermal} \qquad \dots \ 4.4.2.5$$

$\sigma < -40$ MPa

$$\varepsilon_{TRIP} = -\varepsilon_{Thermal} \qquad \dots \ 4.4.2.6$$

$$- 40MPa \quad < \quad \sigma \quad < \quad + 40MPa$$

$$\varepsilon_{TRIP} = 0.0 \qquad \ldots 4.4.2.7$$

The component of transformation plasticity strain generated for each degree fall in temperature, when the element cooled from $\Theta_i{}^n$ to $\Theta_i{}^{n+1}$ was obtained by the use of the following equation

$$\left[\alpha_{TRIP}\right]_{\Theta_i{}^n \to \Theta_i{}^{n+1}} = \frac{\left[\varepsilon_{TRIP}\right]_{\Theta_i{}^n} - \left[\varepsilon_{TRIP}\right]_{\Theta_i{}^{n+1}}}{\Theta_i{}^n - \Theta_i{}^{n+1}}$$

$$\ldots 4.4.2.8$$

The estimate of elastic stress given by equation 4.14 in the mathematical model was modified to take into account the stress component associated with the transformation plasticity strain given by equation 4.4.2.8. Equation 4.14 thus becomes:

$$(\sigma_i{}^{n+1})_r = \sigma_i{}^n + (\Delta\sigma_i{}^{n+1})_r + \frac{E \alpha_{TRIP}}{(1-\nu)} (\Theta_i{}^n - \Theta_i{}^{n+1})$$

$$\ldots 4.4.2.9$$

The remainder of the procedure was the same as that described in section 4.1 and 4.2. Consequently the additional transformation strain due to the presence of a stress was treated as an elastic strain.

4.5. <u>Results of Thermal Stress and Strain Calculations</u>

The results from the mathematical model which was used to calculate the thermal stresses and strains generated in plates quenched under various conditions have been divided into the following sections:

(i) Results of calculations that ignored stress relaxation.

(ii) Results of calculations that considered stress relaxation, which have been subdivided into those obtained under the following conditions:

a) Stress relaxation and creep rates as a function of temperature only (method 1).

b) Stress relaxation and creep rates as a function of both temperature and time, with steady state conditions after 20 seconds (method 2).

c) Stress relaxation and creep rates as a function of both temperature and time throughout the duration of the quench (method 3).

(iii) Results obtained from the model where a reduction in flow stress has been used to represent transformation plasticity during the formation of martensite.

(iv) Results obtained from the model with transformation plasticity included as an additional strain.

Both the later models (i.e. (iii) and (iv)) were used in conjunction with the stress relaxation consider-ations as represented above, by (a) and (b).

The values of physical and mechanical properties used are summarised in table 4,5 and 7. Each calculation has been

99.

defined by the abbreviations described in table 8, which
also refers to the numbers of the figures that contain
the results of each calculation.

4.5.1 <u>Water quenching</u>

Calculation CD1 predicts the generation of
thermal stress and strain in a 20mm plate quenched in
water, without taking into account the effect of viscous
flow on the stress generation process. Figure 51 shows
the relationships between stress and strain at the surface
and centre during the course of such a quench. At the
onset of quenching the surface cooled faster than the
centre, which developed a tensile stress in this part of
the plate, that was balanced by a compressive elastic
stress towards the centre. As the temperature difference
between the surface and centre became greater, the surface
tensile stress increased until plastic deformation occurred.
Similarly, the compressive stress at the centre increased
until it also produced plastic deformation. The stresses
at the surface and the centre then increased at a rate
dependent on the change in flow stress. At $398^{\circ}C$, as the
centre began to cool faster than the surface the surface
stress began to unload and then reversed. This reversal
was assisted later by the transformation of austenite to
martensite, at $300^{\circ}C$, which generated an expansion at
the surface, and increased the level of compressive stress
at this point. However during the transformation a rapid
rise in the flow stress of the material prevented further

plastic flow at the surface. At this stage the centre was at a higher temperature (567°C) and the associated tensile stress at the centre did generate plastic flow. A maximum compressive stress of -1175MPa was developed at the surface at a temperature of 244°C. An unloading of the compressive stress at the surface was brought about by the martensite transformation that was now taking place towards the centre of the plate. The arrival of the transformation front at the centre caused the tensile stress to unload at 286°C and then to become compressive.

The relationships between stress and strain predicted by calculations CD4 and CD5, with stress relaxation represented by method 1 and method 2 respectively are shown in figures 52 and 53 respectively. Method 3 gave similar results to method 2 on account of the rapidity of the water quench which reduced the temperature of the surface to 125°C in 20 seconds. Significant differences between methods 2 and 3 only occur at longer times than this. During the initial stages of the cooling process viscous flow had no significant effect on the relation-ships between stress and strain so that the results were very similar to those reported in the case of calculation CD1. Thus a tensile stress developed initially at the surface and a corresponding compressive stress developed towards the centre. Later unloading and stress reversal again led to a compressive stress at the surface as this part of the structure reached the M_s temperature. At lower temperatures the longer time interval involved

allowed the viscous flow to have some effect, since the maximum compressive stress at the surface was now lower than the -1175 MPa developed in calculation CD1 (-1075MPa for CD4 and -1125MPa for CD5). The effect of viscous flow was even detected at temperatures below 244°C at which temperature the unloading of the compressive stress began at the surface. The viscous flow caused an increase in the slope of the curve showing the relationship between stress and strain at this stage in the quench, with the steepest slope associated with calculation CD4. This increase in slope led to a final stress at the surface that was tensile rather than compressive. At the centre of the plate, plastic flow was produced as a consequence of the formation of martensite at the surface. The subsequent transformation of the centre, unloaded the tensile stress and produced a compressive stress at the end of the quench. In the case of calculation CD4 only (figure 52) a further unloading of the stresses occurred at a temperature of 137°C at the surface and at 194°C at the centre. This was due to the presence of viscous processes at very low temperatures, which only occurred in the case of method 1.

The residual stress and residual strain distribution across the plate obtained from calculations CD1, CD4 and CD5 are presented in figures 54 and 55. The general pattern of the residual stress and strain distribution obtained from these calculations were all very similar.

However the levels of residual stress and strain predicted were lower in the case of CD4 than was the case in CD1, with the results of calculation CD5 intermediate between those of CD1 and CD4.

4.5.2 Oil quenching

Figure 56 shows the relationship between stress and strain predicted by calculation CD2 at the surface and centre of an oil quenched 15mm plate not subject to viscous flow. During the initial stages of the quench these relationships showed a similar configuration to that of the water quench i.e. the surface was subjected to a tensile stress and the centre was subjected to a compression, which was associated in both cases with plastic flow. However the amount of plastic flow was now smaller, on account of the low values of the heat transfer coefficient associated with a prolonged vapour blanket stage. The stresses at the surface began to unload at $747^{\circ}C$, because at this point the centre began to cool at a faster rate than the surface. A similar effect took place at the centre. The surface now changed from a tensile state into one of slight compression, whereas the centre became less compressive. However, at $545^{\circ}C$ there was a rapid reversal of the surface stress, due to the onset of the nucleate boiling stage, which produced a steeper temperature gradient between the surface and centre. The stress at the surface now became tensile and eventually produced more plastic flow. A maximum tensile stress of 145MPa was produced at

the surface, at which point the temperature had fallen to $441^{O}C$. Another reversal of stress now occurred as the cooling rate at the centre again exceeded that at the surface. At the onset of the martensite transformation the surface was subjected to a compression which rose as the transformation continued, to a maximum value of -375MPa Unloading of the surface compressive stress now occurred as the martensite transformation began towards the centre of the plate. At the end of the quench the surface was subjected to a residual stress of -175MPa and a residual strain of 0.035%, while the centre was subjected to a residual stress of 65MPa and a residual strain of -0.004%.

The relationships between stress and strain in the presence of viscous effects, which are predicted by calculations CD6, CD7 and CD8 (associated with methods 1, 2 and 3 respectively) are shown in figures 57, 58 and 59 respectively. In the case where the viscous flow was most prominent (CD6, method 1) the first unloading of the surface stress (during the vapour blanket stage at $782^{O}C$) occurred at an earlier point than that predicted by calculation CD2, which did not show viscous flow (compare figures 56 and 57). At both the surface and the centre, viscous processes were pronounced throughout the vapour blanket stage, on account of the comparatively long period of time associated with the slow cooling produced at this stage in the quench. This showed itself as a very marked departure from the Hooke's law relation-

ship during the first unloading of the thermal stress at temperatures between $782^{O}C$ and $545^{O}C$. Indeed, at one point the slope of the curve is actually negative.

At the onset of nucleate boiling (at $545^{O}C$) a tensile stress was generated at the surface, but the level of stress developed was not high enough to produce plastic flow, as had been the case during the same stage of the calculation CD2(compare figures 56 and 57). A maximum tensile stress of 135MPa was produced at the surface, at $452^{O}C$, before the unloading of these stresses, as a consequence of the combined effects of viscous flow and a reduced temperature gradient between the surface and the interior. It is interesting to compare the slope of the curve showing the relationship between stress and strain at the surface as the stress rises between $545^{O}C$ and $452^{O}C$ and as it falls between $452^{O}C$ and $386^{O}C$. The presence of viscous flow has caused the slope of the curve in the former case to be lower than that demanded by Young's modulus, while the slope of the curve in the later case was correspondingly greater, than that obtained under elastic conditions. The effect of viscous flow was even more apparent between $321^{O}C$ and $300^{O}C$, at which stage there was sufficient time for the stress to relax slightly.

As the surface began to transform to martensite the stress at this point became more compressive, but the maximum level attained (-235MPa) was smaller than that predicted by calculation CD2 (no viscous processes). The

subsequent unloading of the surface stress, as the centre began to transform to martensite, was aided by the stress relaxation associated with viscous flow. Thus, unlike the case of calculation CD2 the unloading was continued until a stress reversal occurred, so that at 190°C a tensile stress of 30 MPa had been attained at the surface. However, even at these low temperatures viscous flow was significant, so that this tensile stress subsequently relaxed and gave, at the end of the quench, a stress free material.

The corresponding relationships between stress and strain at the centre of the plate were a mirror image of those developed at the surface, although the temperature at which particular events occurred were, of course, usually different from those pertaining to the surface.

The relationships between stress and strain predicted by calculations CD7 (method 2) and CD8 (method 3), figures 58 and 59, lie between those predicted by calculation CD2 (without viscous flow) and calculation CD6 (method 1). Both methods 2 and 3 gave identical results while the initial tensile stress was present at the surface and the corresponding compressive stress was present at the centre. However, the amount of viscous flow was very small and the plastic strain present after the unloading of these initial stresses was smaller than that produced in calculation CD6 (method 1). The smaller amount of viscous flow in the later stages of the quench

led to a higher maximum compressive stress at the surface than was the case with CD6 (compare figures 57, 58 and 59). During the unloading of this compressive surface stress virtually no viscous flow occurred in the case of method 3, and only a moderate amount was predicted by method 2. As a consequence the final surface stress predicted by methods 2 and 3 were compressive since the unloading process was never completed. However the magnitude of these residual surface stresses was lower than that predicted by CD2, which ignored stress relaxation.

The residual stress and residual strain distribution across the plate determined from calculations CD2, CD6, CD7 and CD8 are presented in figures 60 and 61 respectively. The residual stress distribution predicted by CD2 showed a compressive stress of -175MPa at the surface and a tensile stress of 65MPa at the centre. On the other hand calculation CD6 predicted a stress-free plate at the end of the quench. Calculation CD7 predicted a residual stress of -20MPa at the surface and 10MPa at the centre whereas calculation CD8 predicted a residual stress of -108MPa at the surface and 50MPa at the centre. Generally the greater the overall level of viscous flow during the quench the lower was the residual stress at the end of the cooling process. The pattern of residual strains predicted from all the calculations showed no significant differences, except that the level of residual strains predicted by calculation CD6 was slightly lower than that predicted by the others.

4.5.3 Martempering (Salt bath treatment at 400°C followed by an oil quench at 20°C).

The relationship between stress and strain predicted by calculation CD3 (without stress relaxation) is shown in figure 62. During the salt bath treatment, the surface was subjected initially to a tensile stress while the stress at the centre was compressive. The very high heat transfer coefficient at the start of the quench, associated with the use of a salt bath, caused plastic flow at both the surface and the centre of the plate. The maximum tensile stress developed at the surface was 75MPa (at a temperature of 711°C). At this point an unloading of the tensile stress occurred due to the increase in the rate of cooling at the centre relative to that at the surface. The stress at the centre now became tensile and that at the surface became compressive. When the surface temperature reached 465°C the specimen was transferred from the salt to the oil bath. Since the latter was at 20°C there was an immediate increase in the temperature gradient in the specimen, which caused a reduction in the compressive stress that already existed at the surface. Once the surface temperature fell below 428°C the centre began to cool faster than the surface, which caused a build up of the compressive stress still present at this point in the specimen. Later the martensite transformation which began at the surface, intensified this process. The remaining relationships between stress and strain were similar to the relevant

relationships between stress and strain predicted by calculation CD2 (oil quench without viscous flow), figure 56.

Calculations CD9, CD10 and CD11 which included viscous flow effects as modelled by methods 1, 2 and 3 respectively generated the relationships between stress and strain shown in figures 63, 64 and 65 respectively. The relationship between stress and strain predicted by calculation CD9 (figure 63) showed a significant effect of viscous flow on the results obtained at both the surface and the centre of the plate. This effect was more prominent in the later stages of the treatment in the salt bath, when the temperature lay between $733^{\circ}C$ and $465^{\circ}C$ at the surface and $832^{\circ}C$ and $469^{\circ}C$ at the centre. As the temperature approached the lower end of these ranges of temperature the stress relaxation due to viscous flow produced a negative gradient to the stress-strain curve, and at the end of the salt bath treatment both the surface and the centre possessed virtually zero internal stress. The subsequent treatment in oil introduced a tensile stress at the surface and a compressive stress at the centre. Unloading of the stress at the surface occurred, at $443^{\circ}C$, on account of the magnitude of the stress relaxation associated with creep, followed by the appearance of a compressive stress at this point in the plate, as the austenite began to transform to martensite. The maximum compressive stress of -180MPa was lower than that predicted by calculation CD3 (martempering without viscous flow

processes, figure 62). The remaining relationships between stress and strain were identical to those predicted by calculation CD6 (oil quench method 1), figure 57.

The most significant differences between the predictions of methods 1, 2 and 3 during the salt bath part of the martempering treatment was the progressive change in the amount of viscous flow in the later stages and the consequent differences in the level of internal stress present when the specimens were removed from the salt bath. As would be expected the method which permitted the greatest amount of viscous flow showed the lowest internal stress at this point in the quench. During the subsequent quench in oil the same effects were apparent although there was sufficient time in the cases of both methods 1 and 2 for the internal stress to fall to zero by the end of the quench. It should be noted, however, that in these two cases the stresses approached the stress axis from different directions, since a significant tensile surface stress was predicted towards the end of the quench by method 1. In the case of method 3 the maximum compressive stress at the surface was significantly higher than was the case of the other two methods, and the final residual stress at this point in the specimen was compressive. At all stages the relationships between stress and strain at the centre were a mirror image of those found at the surface.

The residual stress and residual strain distributions

across the plate predicted by calculations CD3, CD9, CD10 and CD11 are shown in figures 66 and 67. The residual stress distribution predicted by CD3 (without viscous flow processes), showed a compressive stress of -160MPa at the surface, and a tensile stress of 120MPa at the centre. Calculations CD9 and C10 (viscous flow modelled by methods 1 and 2 respectively) predicted a stress free plate at the end of the quench, whereas calculation CD11 (method 3) predicted a residual stress distribution intermediate between those predicted by calculations CD3 and CD9 or CD10. The residual strain patterns predicted by all the calculations were similar except that calculations CD9 and CD10 predicted slightly higher residual strains than those predicted by CD3 and CD11.

4.6   Reduction in Flow Stress to Simulate Transformation Plasticity

4.6.1   Water quenching

Calculation CD12 incorporated stress relaxation by method 2 into the calculation of thermal stress and strain during a water quench together with a reduction in the flow stress between M_s and $265^\circ C$ to simulate transformation plasticity. The relationship between stress and strain at the surface and the centre is shown in figure 68. The initial part of the stress generation process i.e. before the transformation of the surface, was identical to that predicted by calculation

111.

CD5 (water quench method 2, figure 53). At the onset of transformation of the austenite to martensite an expansion occurred at the surface which subjected it to plastic flow, as a consequence of the low flow stress at this stage in the process. The stresses, thereafter, increased in compression at a rate dependent upon the increase in flow stress. The plastic flow ceased at $265^{\circ}C$ when the flow stress rapidly increased and the surface stress became highly compressive. The centre was subjected to tensile plastic flow as a consequence of the phase transformation at the surface, but the extent of this plastic flow was less than that predicted by calculation CD5. At the onset of transformation the centre, was subjected to a tensile stress which was much higher than the value of the reduced flow stress at that point. Hence there was a sharp fall in the stress level, in correspondence with the flow stress value. Between $300^{\circ}C$ and $286^{\circ}C$ a small amount of plastic flow occurred before the stress reversal occurred. Below $286^{\circ}C$ the stress at the centre reversed elastically and became compressive, the level of which was sufficient to cause further plastic flow at temperatures between $273^{\circ}C$ and $265^{\circ}C$. At lower temperature the flow stress increased rapidly so that below $265^{\circ}C$ the increasing compressive stress was elastic.

Calculation CD13, incorporated stress relaxation effects by method 1. The relationships between stress and strain at the surface and the centre as predicted by this model are presented at figure 69. The only significant

difference between the results of calculations by methods 1 and 2 was the unloading of the internal stress during the final stages of the quench (below about 200°C).

The residual stress and strain distributions predicted by calculation CD12 and CD13 are presented in figures 70 and 71 respectively. Calculation CD13, with high rates of stress relaxation (method 1) predicted lower stress levels at all points than those predicted by calculation CD12 (method 2). Furthermore the residual stress pattern was similar to that predicted by the corresponding calculations which ignored the transformation plasticity effect (i.e. CD4 (method 1) and CD5 (method 2)), except that the overall level of stresses was slightly higher when transformation plasticity was included. The residual strain pattern predicted by calculation CD13 was lower than that predicted by calculation CD12 and the general trend was similar to that predicted by calculations CD5 and CD4, except that the residual strains were reduced by the introduction of transformation plasticity.

4.6.2 Oil quenching

Calculation CD14 incorporated into the mathematical model both stress relaxation effects by method 2 and the simulation of transformation plasticity by a reduction in flow stress at temperatures between M_s and 265°C. The quenchant in the case of calculation CD14 was oil with characteristics similar to that used in calculation CD7 (method 2 oil quench). Prior to trans-

formation the predicted relationships between stress and
strain at the surface and centre (presented in figure 72)
were the same as those predicted by calculation CD7
(figure 58). At the onset of the martensite transform-
ation at the surface, plastic flow occurred until the
surface temperature reached 271°C, at which stage the
stress began to unload, due to the start of the martensite
transformation at the centre. Owing to plastic flow
during transformation, the maximum compressive stress at
the surface was -109MPa and the maximum tensile stress
at the centre was 90MPa, which were significantly lower
than the values predicted by CD7 (figure 58). Eventually
the unloading of the stress at the surface, which began
at 271°C, caused a stress reversal, so that at the end
of the quench the surface was in tension and the centre
was in compression.

Calculation CD15, incorporated stress relaxation
effects by method 1. The relationships between stress and
strain at the surface and the centre predicted by this
model are presented in figure 73. The effect of high
stress relaxation rates, obtained from method 1, on these
relationships was more prominent towards the end of the
quench, where the tensile stress produced at the surface
and a compressive stress at the centre were relaxed to
a zero stress level at the end of the quenching process.

The residual stress and residual strain distributions
across the plate predicted from calculations CD14 and CD15

are shown in figures 74 and 75 respectively. Calculation CD15, which was similar to calculation CD6 (method 1, figure 60) except that it incorporated transformation plasticity, predicted a stress free plate at the end of the quench. Calculation CD14 (method 2), predicted a tensile stress of 36MPa at the surface and a compressive stress of -15MPa at the centre. The residual strain patterns were similar for both these cases and were in general agreement with calculations CD6 (method 1) and CD7 (method 2), which did not incorporate transformation plasticity (figure 61).

4.7 Thermal Stress Calculation with Transformation Plasticity included as an additional Strain Component

4.7.1 Water quenching

Figure 76 shows the relationships between stress and strain at the surface and the centre of a water quenched plate predicted by calculation CD16 with the effect of stress relaxation modelled by method 2. The transformation plasticity strain, which depended upon the sign and magnitude of the stress, has been included in the calculation at temperatures between $300^{\circ}C$ and $260^{\circ}C$ (described in section 4.4.2). Transformation plasticity only affects the calculation at temperatures below M_s, so the following confines itself to the later stages in the quenching process.

The surface was subjected to a compressive stress of -15MPa when the transformation to martensite began.

The expansion associated with the transformation produced a compressive strain that in turn generated a compressive stress. However simultaneously a strain component was introduced as a consequence of the transformation plasticity, which opposed the compressive strain created by the expansion of the structure. Therefore the stress generated was less compressive than would have been the case had there been no additional strain due to transformation plasticity. However, once the temperature fell below $260^{\circ}C$ there was no longer a positive strain component due to the transformation plasticity effect, so that there was now a rapid rise in the level of compressive stress. This was due to the normal expansion associated with the martensitic transformation. A maximum compressive stress at the surface of -892MPa was obtained at $220^{\circ}C$, which was similar to that produced by calculation CD12 (transformation plasticity simulated by a reduction in flow stress between M_s and 265 (figure 68)). The surface stress now, unloaded due to transformation of the interior of the plate to martensite and at the end of the quench was in a state of tension. Due to the transformation plasticity effect on the surface elements, the centre was subjected to less plastic flow than that predicted by calculation CD5 (water quench, method 2 without transformation plasticity, figure 53), but the amount was similar to that predicted by calculation CD12 (figure 68). Finally the stress at the centre unloaded and attained a negative value at the end of the quench.

Calculation CD17 incorporated the stress relaxation effect by method 1, and the relationships between stress and strain at the surface and the centre are presented in figure 77. The only significant difference between the results of the calculations by methods 1 and 2 was the unloading of the internal stress during the final stages of the quench (below about 200°C).

The residual stress and residual strain distribution predicted by these calculations are presented in figures 78 and 79 respectively. The residual stress pattern predicted by both calculations were similar, except that the level of stress at all points was lower in the case where stress relaxation was represented by method 1 (CD17). The shape of the curves showing the residual stress distribution in the plate were in general agreement with those predicted by calculation CD4 (method 1 without transformation plasticity) and CD5 (method 2 without transformation plasticity), figure 54, and calculations CD12 and CD13 (transformation plasticity simulated by a reduction in flow stress between M_s and 265°C), figure 70. The residual strain pattern predicted by both the calculations CD16 and CD17 showed a significantly larger difference between the residual strains at the surface and centre, than had been predicted by the corresponding calculations that did not consider transformation plasticity as additional strain (compare figures 79 and 55).

4.7.2 Oil quenching

Figure 80 shows the relationship between

stress and strain predicted by calculation CD18, in the
case of an oil quenched plate with stress relaxation
modelled by method 2 and transformation plasticity
included as an additional strain. Again differences
from the previous calculations occur after the martensite
transformation has begun at the surface.

The surface was subjected to a compressive stress
of -95MPa when the transformation to martensite began,
so at this high stress level the strain component
generated by the transformation plasticity effect countered
the compressive strain component associated with the
expansion due to the normal transformation of austenite
to martensite. Thus an immediate unloading of the
compressive stresses was brought about at the surface.
As the compressive stress level decreased, the transform-
ation plasticity effect was reduced and there was a
slight increase in the compressive stress, before the
transformation front reached the interior of the plate
and so brought about the normal unloading of the
compressive stress at the surface. The level of comp-
ressive surface stress present at this stage in the
cooling process was lower, due to the occurrence of
transformation plasticity, which opposed the normal
expansion due to martensitic transformation (compare
figures 80 and 58). The unloading of the surface
compressive stress is followed by the development of a
slight tensile stress at the surface at 260°C, where the

transformation plasticity effect ceased. Effectively,

transformation plasticity had become insignificant at a

rather higher temperature since the unloading process

reduced the surface stress to a point where it did not

produce this phenomenon. The unloading process, was, of

course a consequence of the martensitic transformation

occurring in the interior of the plate. Towards the end

of the quench the rate of tensile stress build up fell

and was exceeded by the rate of stress relaxation

associated with the high tensile stress developed at this

stage. This caused yet another unloading of the surface

stress which still, however, maintained a small tensile

value at the end of the quench. The relationships between

stress and strain at the centre were a mirror image of

the behaviour observed at the surface.

The relationships between stress and strain at the

surface and the centre predicted by calculation CD19

(oil quench, method 1, transformation plasticity) are

presented in figure 81. The effect of high rates of stress

relaxation, obtained from method 1, had a much pronounced

effect on the stress generation process towards the end of

the quench; whereby the tensile stresses at the surface

and the compressive stresses at the centre were relaxed

to zero.

The residual stress and strain patterns predicted

by the above calculations are presented at figures 82 and

83 respectively. In the case of calculation CD19, which

incorporates high viscous flow rates, a stress free state was predicted, whereas in the case of calculation CD18 (viscous flow rate incorporated by method 2) a tensile stress of 45MPa was predicted at the surface, and a compressive stress of -25MPa was predicted at the centre. The residual strain pattern was similar for both the calculations with a strain of 0.27% at the surface and 0.06% at the centre.

5. MEASUREMENT OF RESIDUAL STRESS AND RESIDUAL STRAIN IN QUENCHED PLATES

5.1 Introduction:

The experimental work was designed to measure residual stress and strain in plates of 835M30 steel after quenching, so as to allow a comparison between these results and the predicted residual stress and strains obtained from the mathematical model described in section 4.2. The plate specimens used had dimensions 120mmx120mm x15mm. The residual stress and distortion measurements involved two cases of heat treatment i.e. plates that had been either oil quenched or martempered. In order to achieve the condition of unidirectional heat flow, as was assumed in the mathematical model, the edges of the plate specimen were insulated with a 6mm thick layer of Kaol wool ceramic fibre insulation which was lightly held in position by a nickel frame around the plate as shown in figure 84. Care was taken to keep the tension from the nickel frame as low as possible so as to minimize the constraining forces applied to the edges of the plate. All the plate specimens were electroplated with a 0.05mm layer of nickel to prevent the oxidation of the surface during transfer from the furnace to the quenching tank.

The experimental work in the present treatise involved the following stages

> i)   Heat treatment of plates
>
> ii) Distortion measurements
>
> iii) Residual stress measurements

5.2 Heat Treatment Procedure

5.2.1 Stress relieving and softening of plates

This treatment was done prior to the quenching operation, to ensure that the material was in the ferritic condition and that any residual stresses introduced during the earlier treatment of the plate were removed. This closely coincides with the situation represented in the mathematical model, which assumes a zero stress initial condition prior to quenching. The plates were heated in a muffle furnace to a temperature of $630^{\circ}C$ for 2 hours and were allowed to cool to room temperature in the furnace, which was flushed with argon, to prevent surface oxidation of the specimen. The dimensions of the plates were measured using the techniques described later in section 5.3, and then were used together with the dimensions of the plate after quenching, to obtain measurements of the distortion introduced by this operation.

5.2.2 Quenching of the plates

The quenching of specimens was carried out in a tank, the dimensions of which are shown in figure 85. In order to ensure that the specimens were always quenched in the same manner a fixture was used which incorporated a pair of channel guides (shown in figure 85). The quenchant was agitated by means of two variable speed stirrers which were set up on the fixture (figure 85). This ensured a fresh supply of the quenchant at the specimen surfaces throughout the cooling operation. Prior to quenching

122.

the edges of the plate were insulated as described in section 5.1 and shown in figure 84. The plate contained, on one of the sides, an eyebolt (also shown in figure 84) to facilitate its transportation between the furnace and the quenching tank. They eyebolt was made of the same material as the plate (i.e. 835M30) to prevent the generation of any localized stress due to differential expansion and/or contraction in the threaded portion within the plate.

The plate was austenitized at $850^{\circ}C$ for 1.5 hours in a muffle furnace with an argon atmosphere and the quenching was carried out in RDN 175 oil (properties given in table 11). The temperature of the quenchant at the start of each quench was always within $\pm 1^{\circ}C$ of $20^{\circ}C$. Owing to the large volume of quenchant used the temperature remained virtually the same after the quench. In the case of martempering a Nitrate-Nitrite salt of eutectic composition was used as a heat treatment medium prior to the oil quench. The salt bath treatment was carried out in a standard pot type furnace heated externally by electric windings, the dimensions of the pot being 200mm diameter and 240mm deep with the salt 160mm deep. The bath temperature was $400^{\circ}C$. The holding time of 80 seconds in the salt bath was selected on account of the practical situation where a compromise between a small temperature gradient and a high productivity is desirable. In addition, longer holding times were undesirable due to the possibility of bainite formation in 835M30 steel between

the temperatures of 400°C and 300°C (see TTT diagram in figure 30). After this heat treatment, the plate was thoroughly cleaned with a soap solution and alcohol, to remove the grease and tarnish which appeared as a consequence of the quenching operation. It was then remeasured for dimensional changes, as described in section 5.3.

5.3 Distortion Measurement Technique

The distortion in the plate after the heat treatment was obtained by measurements of both the distances between the opposite edges and the thickness of the plate, prior to and after the quenching operation. The plates were first left in the metrology laboratory for 24 hours which allowed them to acclimatise to the conditions in the laboratory where the measurements were to be made, although no such remeasurements were made later than 48 hours after the plate had been quenched. The procedures adopted for making the various measurements were as follows.

5.3.1 Measurements along the opposite edges of the plate

After quenching, the changes in dimension between the opposite edges of the plate were found to be very small (a maximum of 0.12mm for a dimension of 120mm in an oil quenched plate). The measurement of such small changes in dimensions required a very accurate measuring system. The use of a micrometer for example gives an accuracy of only ± 0.025mm while the use of a Societe

Genevoise Universal measuring machine gave an accuracy
better than ± 0.0001mm.

This measuring machine comprises a horizontal bed,
capable of moving laterally, on which the plate was laid
with one face in contact with the bed. A steel probe
positioned above the bed was attached to a vertical head,
capable of vertical and transverse movements, the position
of which were measured by eye pieces with cross wires.
The positions at which the dimensions of the specimen
were measured are shown in figure 86. The probe was
brought into contact with each side of the plate at the
desired position by the combined movement of the horizontal
bed and the vertical head and the plate dimension, at any
point, was determined from the positions occupied by the
probe when in contact with each edge of the plate.

The percentage strain in the plate at the points
shown in figure 86, were obtained using the expression:

$$\% \, \Delta \, Y \;=\; (\frac{Y_Q - Y_S}{Y_S}) \;\; \text{x} \; 100 \qquad \ldots 5.3.1$$

In order to check the confidence level of the
measurements a set of readings were obtained from a slip
gauge, and analysed statistically.

5.3.2 Measurement of the thickness of the plate

The Societe Genevoise machine could only
measure the thickness of the plate at points within 10mm

of the edge of the plate. Consequently a more complicated method was required to obtain measurements at other points. This technique was adapted from the standard test used to check the flatness of a surface[115]. The test in its original form involves a comparison of the relative position of the surface, at various selected points, to a reference point, by means of spirit levels or a dial gauge. The plate was positioned with its faces inclined at a very small angle to a reference axis which was parallel to the surface on which the plate was placed. This was achieved by using lumps of plasticine under the plate corners and pressing the plate over on one side to give the desired angle of inclination. An electronic comparator positioned as shown in figure 87 was traversed across the centre of the face from one edge to another and a reading obtained after every 10mm of travel. The first and the last positions on the plate surface (1 and 11 in figure 87) was marked at points 10mm from the plate edges. The thickness of the plate at these points was known (measured by the Societe Genevoise Universal measuring machine). Thus the plate was divided into 11 equispaced positions and the comparator reading at the first and the last positions denoted by C_1 to C_{11} respectively as shown in figure 88. The level of the comparator was set at zero while at position 11 (towards the highest edge on the plate). Assuming that the plate surface was not parallel to the central axis, the true value of C_1 (at point 1), when this parallel condition

was obtained, was given by:

$$C_{1\ true} = C_1 - \frac{p-q}{2} \quad \text{(see figure 88a)} \quad \ldots 5.3.2$$

If the central axis of the plate was made parallel to the line of measurement (O-O), the distance between point 1 and the reference line O-O was given by

$$CF_1 = C_1 - C_{1\ true} \quad \text{(see figure 88b)} \quad \ldots 5.3.3$$

Since position A (point 11) was made to lie on the reference line, the half thickness at position B (point 1) was given by

$$\tfrac{1}{2}TH_1 = \frac{p}{2} - C_1 - (C_1 - \frac{p-q}{2}) \quad \ldots 5.3.4$$

The measurements at intermediate points were made at equal spacings (see figure 88), therefore by the symmetry of triangles (see figure 88a), the true values of the comparator readings at these points were related to the true value of C_1 by:

$$C_{N\ true} = \frac{11-N}{10} (C_1 - \frac{p-q}{2}) \quad \ldots 5.3.5$$

Therefore

$$CF_N = C_N - \frac{(11-N)}{10} (C_1 - \frac{p-q}{2}) \quad \ldots 5.3.6$$

Thus the corresponding half thicknesses at these points was given by

$$\tfrac{1}{2}TH_N = \frac{p}{2} - C_N - \frac{(11-N)}{10} (C_1 - \frac{p-q}{2}) \quad \ldots 5.3.7$$

The half thicknesses at the opposite side of the plate were calculated in a similar way. The half thicknesses obtained from either sides of the plate, at relevant points, were then added together to give the total thickness of the plate at those points. Thus the percent change in thickness at any point was given by

$$\% \; \Delta \varepsilon_{zz} = \left(\frac{TH_{NQ} - TH_{NS}}{TH_{NS}} \right) \times 100 \qquad \ldots 5.3.8$$

The distortion measurements in the direction through the thickness of the plate at various points, gave the extent to which the edge effect influenced the final shape of the plate. It also allowed measurements to be made at points where the edge exerted no influence i.e. towards the centre of the plate. Since plane stress conditions existed at such points the strain in the thickness direction arose solely from stresses in the plane of the plate. Hence the changes in the thickness dimensions at these points were directly related to the mean changes in the length or breadth which were known to be unaffected by the edge effect and were useful for comparison purposes to the strains predicted by the theoretical model. However, the measured strains were adjusted for the volume change which accompanied the change of ferrite + carbide structure to martensite as a consequence of the austenitising and quenching process viz:

$$\% \ \Delta\varepsilon_{xx} \text{ calculated} = \% \ \Delta\varepsilon_{xx} \text{ measured} - \% \frac{\Delta V}{3}$$

$$\% \ \Delta\varepsilon_{zz} \text{ calculated} = \% \ \Delta\varepsilon_{zz} \text{ measured} - \% \frac{\Delta V}{3}$$

$$\% \ \Delta\varepsilon_{xx} \text{ calculated} = -\tfrac{1}{2}\% \ \Delta\varepsilon_{zz} \text{ calculated}$$

Therefore

$$\% \ \Delta\varepsilon_{xx} \text{ measured} - \% \frac{\Delta V}{3} = -\tfrac{1}{2}(\% \Delta\varepsilon_{zz} \text{ measured} - \% \frac{\Delta V}{3})$$

$$\dots 5.3.9$$

5.4 Measurement of Residual Stress

A destructive mechanical method was used to measure the residual stress distribution across the thickness of the plate. The method involved the removal of surface layers which brought about a dimensional change in the remaining material due to the readjustment of the residual stress. The change in dimension was then measured by means of a strain gauge attached to the opposite surface of the plate; using the procedure documented by Andrews[7], although certain modifications were made by Price[99] to the relevant equations presented in appendix 2.

A Burdett grinding machine was used to remove the layers of the material and the strain measurements were made by means of a strain gauge attached at the centre of the plate surface, as shown in figure 89. The strain gauges used were rossettes of the Tokyo Sokki Kenkyujo

129.

FRA-6-11 type, which contained three arms. A control box
with a multiway toggle switch enabled each gauge to be
connected to the Wheatstone bridge one at a time. The
three inactive arms of the bridge were formed from a
separate strain gauge, attached to a steel strip, with
its arms connected in series (the bridge circuit is shown
in figure 90). Initially, the bridge was energised by
an AC carrier wave system using a Sangamo type C-52 direct
reading transducer meter, but this system was found to
give erratic fluctuation due to the stringent earthing
requirement associated with it. The long times involved
during the stress measurement experiment make it difficult
to maintain the stability of such a system. A more
stable arrangement was achieved by the use of a DC bridge
supply unit and transducer amplifier of the type
FYLDE492BBS and 251GA. The output from the amplifier was
connected to a digital voltmeter capable of reading 10
microvolt which corresponds to 0.33 microstrain in the
strain gauge (supply voltage 6 volts and gauge factor of
2.1). It was important to match the polarity of the
bridge supply to the output fed into the voltmeter. A
reversed polarity at the output would reverse the sense
of the strain gauge reading at the voltmeter.

In order to minimize machining stresses, the removal
of the material was accomplished at a very slow rate
(1mm per hour), accompanied by cooling of the specimen
with large quantities of coolant. To achieve the

experimental residual stress at points identical to the ones obtained from the calculation model, the total plate thickness of 15mm was divided into 20 stress elements. Thus a stress measurement was carried out after the removal of layers 0.75mm thick, which was achieved by a series of cuts 0.05mm deep.

The oscillation of the bed of the surface grinding machine introduced spurious signals not connected with the strain in the plate. This was removed by means of a second strain gauge attached to a recessed spacing plate which supported the plate specimen on the surface grinding machine. Both strain gauges were read each time a strain measurement was made and the difference between the readings was used to calculate the residual stress in the layer removed. The strain gauge measurements were found to be independent of the orientation of the device i.e. all the stresses in the plane of the plate were equal at the plate's surface, and the mean of the results obtained from the three arms of the rosette was used in the subsequent calculation of stress.

The use of large quantities of coolant in the vicinity of the strain measuring devices, required the proper insulation of the strain gauges. This was achieved by coating them with polyurethane. The recess between the plate and the supporting spacing plate was then filled with wax. The steel strip containing the inactive arms of the bridge was also placed on the grinder bed, along-

side the plate specimen, so as to be in a similar condition to the other gauges.

It was observed that the magnetic clamp of the grinder bed affected the gauge reading so that the magnets were switched off when the bridge was zeroed and then when each strain gauge reading was taken. After each 0.75mm layer had been removed the plate was allowed to stand until the small amount of heat generated by grinding had been dissipated and the strain gauge readings had stabilized.

The use of the grinding technique is known[116,117] to induce additional stresses into the component due to the heat generation and the force associated with the tool feed. These stresses could be minimised by the use of the proper grinding parameters (tool feed, cooling, wheel dressing)[118]. In the present study, it was felt necessary to check the level of grinding stresses induced in the plate by the use of the technique described above. Thus the determination of the residual stresses was conducted by this method on a plate specimen in a stress relieved condition. The experimental residual stresses found in the plate were negligible, so it has been concluded that no stresses were induced in the plate as a consequence of the grinding operation on a softened plate. However it was still possible that some grinding stresses may be induced in a plate which has been hardened. In such cases it was considered necessary

to dress the wheel after every 0.75mm removal of the surface layer, to minimize any such effects.

5.5 Results of the Measurements of the Residual Stresses and Strains Present in Quenched Plates

5.5.1 Oil quenched plates

The oil quenching of the plate specimen shown in figure 84 was carried out in the manner described in section 5.2.2, and the results of the change in length between reference points A to K on the opposite edges of the plate (as shown in figure 86) are given in table 9. The mean distortions obtained from these measurements are presented in figure 91, and the change in the through thickness dimensions along the length and width of the plate are presented in figure 92. The average distortion in the plane of the plate obtained from the change in thickness at the centre of the plate is shown as a horizontal broken line in figure 91: these values, which were obtained by the use of equation 5.3.9, are unaffected by the edge effect. The discrepancy between the average strain determined from the thickness measurements and the strains obtained directly from length measurements was very small, which indicated a minimum effect of the edge on the overall distortion found in the length of the plate. The average strain found in the plate after the oil quench was 0.074%.

The residual stresses present in the plate after the oil quench were determined using the procedure described

in section 5.4. Grinding was used to remove 8.25mm of
the material which represented more than half the plate
thickness. The residual stress in the remainder of the
plate was evaluated from consideration of the symmetry
of the stress distribution about the centre of the plate.
The experimental residual stress distribution showed a
tensile stress of 98 MPa at the surface which becomes
compressive towards the centre of the plate, as shown in
figure 93.

5.5.2 Martempered plate

Martempering of the plate specimen (shown in
figure 84) was carried out at 400°C in a mixture of
Potassium Nitrate and Sodium Nitrite of eutectic composition,
with a holding time of 80 seconds, followed by quenching
in RDN175 oil at 20°C. The quenching procedure was the
same as that described in section 5.2.2. Table 10 shows
the distortions which were generated in the plate during
the heat treatment and figure 94 shows the distribution of
distortion obtained from the measurements of the change
in length of the plate, and the average result calculated
from the change in thickness at its centre (shown as a
horizontal broken line). The measurements between the
edges of the plate were affected by the roughness of the
edge surface after the quench, which had been aggravated
by the salt bath treatment. However, the edges were
thoroughly cleaned with a dilute soap solution and alcohol,
to remove any residue left on the plate after the quenching

treatment. The unsymmetrical appearance of the width
changes shown in figure 94 was indicative of the presence
of slight warpage of the plate. Nevertheless, the change
in thickness at the centre of the plate was considered
free from any warpage. The average distortion found in
the martempered plate (0.05%) was similar to that
observed in the oil quenched plate.

The results of the residual stress determination
are shown in figure 95. Once again, the residual stress
distribution for a martempered plate was similar to that
observed in an oil quenched plate (figure 93).

5.5.3 <u>Water quenched plates</u>

In the previous investigation by Price[99],
the measurements of residual stress and strain in oil
quenched plates of 835M30 were not altogether satisfactory
and no results were obtained from martempered material.
Consequently the experimental programme described above
was necessary during the present investigation. However
in the case of water quenching of the same material the
corresponding data was very reliable. Therefore Price's
water quenching experiments have not been repeated;
instead the results reported in figures 96 and 97 have
been compared in chapter 6 with the calculated results
obtained in the present work.

6. DISCUSSION

6.1 Prediction of the Thermal Stress and Strain Developed during Quenching

(i) Mathematical model without viscous processes:

The mathematical model developed by Fletcher and Price[99] has been used as a basis for the present work. These elastic-plastic calculations included experimentally obtained data on the surface heat transfer coefficients of the quenchant used, and the mechanical and physical properties of the steel involved at various temperatures during quenching from the stable high temperature austenitic condition, but did not include consideration of viscous effects. The characteristics of the stress and strain generation process as predicted by this model are exhibited at figure 98. At the onset of the quench, the surface cools faster than the centre, and a tensile stress is developed in the former. Consequently the centre is subjected to compression. As the temperature gradient between the surface and the centre increases, both the surface and central portions are subjected to plastic flow with an elastic region in between. However at later stages during the quench the rate of cooling at the surface decreases, and unloading of the tensile stresses occurs at this point in the specimen, this is followed by a stress reversal. Simultaneously unloading and subsequent reversal of the compressive stresses is produced at the centre. Shortly afterwards the surface

begins to transform into martensite, which is associated with an expansion of that part of the specimen. This causes a marked increase in the compressive stress, which is not curtailed by the onset of plastic flow, on account of increase in flow stress associated with the formation of martensite. The centre, which is still untransformed and at a higher temperature is subjected simultaneously to tensile plastic flow. The compressive stresses produced at the surface begin to unload as the transform- ation front travels into the interior regions of the plate, and the tensile plastic flow at the centre is terminated as the martensitic transformation begins at the centre. Unloading and subsequent reversal of the tensile stresses now occurs towards the centre of the plate. The model used gives a better understanding of the stress generation process in quenched steels, but the absence of any consideration of the time-dependent viscous processes is a serious omission, especially in the case of the least severe quenchants, such as oil. The significance of the viscous processes is further supported by the poor level of agreement found between the predicted and experimental residual stress distributions in the case of an oil quenched plate (figure 25b). The experimental results show a tensile residual stress at the surface and compressive stress at the centre, while the predicted results show the opposite stress distribution. However a good level of agreement is found in the water quench

situation where there is much less time for viscous processes to occur (figure 25a). Therefore it is considered necessary to incorporate the viscous process into the existing model, and to observe its effect on the stress generation process during the quenching operation.

(ii) The effect of viscous processes on the characteristic stages of the stress generation process:

The introduction of stress relaxation and creep into the mathematical model discussed above has been found to be significant, particularly when the least severe quenchants are used. The extent to which viscous processes affect the stress generation process depends in a complex fashion on the temperature, the magnitude of the stress and the time available for viscous flow. Thus during any time interval the stress increment prior to the use of the yield criterion consists of two parts, viz:

a) that which is directly due to the elastic strain

b) that which is due to the inelastic processes, when a tensile stress produces a negative stress increment and vice versa.

The relative size of these two factors varies during the course of the quench. When the second is predominant a marked departure from the elastic Hooke's Law relationship is obtained and in extreme cases the slope of the stress-strain curve may even become negative. The viscous processes are most prominent when the rate of cooling is relatively small and the temperature is relatively high e.g. in the later stages of the vapour blanket stage in

an oil quench (see figure 57) or when the level of internal
stress is high e.g. during the martensitic transformation.
This is discussed in detail below.

6.2 Representation of Viscous Processes in the Stress Generation Model

(i) Use of the experimental stress relaxation and creep data obtained under isothermal conditions.

The relationships between stress, strain and time
at high temperatures is predicted by the use of mechanical
models made up from a combination of springs and dashpots,
in which the latter represents the time dependent and the
former the time independent processes. The selection of
the most appropriate model is made by a comparison of the
experimental stress relaxation curves obtained at different
temperatures, with the corresponding data predicted by the
various models. It is found that the standard linear
solid which generates the following equation

$$\frac{\sigma}{\sigma^0} = (1 - A) \exp(-B.t) + A$$

gives a satisfactory description of the experimentally
derived results. The establishment of this good correlation
under all combinations of time and temperature is aided by
the use of two physical parameters η and ϕ that are
dependent on the material under consideration. The
parameters A and B in the equation includes these material
parameters in the following combinations.

$$A = \frac{2 \phi \eta (1+v)}{E}$$

$$B = G/\eta$$

Although η and ϕ are dependent upon the physical condition of the material they have not been determined experimentally, but have been given values that produce the best possible representation of the experimental relationships over the complete ranges of time and temperature under consideration. The functional relationships, of A and B, with temperature thus obtained are presented in figure 37. With such relationships the degree of agreement between the stress relaxation data and that predicted by the standard linear solid is as shown in figure 35.

It may be argued that the experimental stress relaxation data can also be modelled by the use of polynomial regression, but the advantage of the mechanical model is its ability to give also an estimate of the creep strain associated with the stress relaxation, so that the viscous process is completely described. The relationship between creep strain stress and time in the case of the standard linear solid is given by

$$\varepsilon_{creep} = \frac{\sigma^o}{E} (\frac{1}{A} - 1) \{ 1 - \exp(-A.B.t) \}$$

In view of the high level of agreement between the

140.

experimental and predicted data, it is the standard
linear solid model with the data given in figure 37 that
has been used to represent the processes of stress
relaxation and creep strain generation. The only drawback
to the standard linear solid is that at most temperatures
a state of zero stress relaxation is obtained after a
relatively short time, whereas the experimental curves
indicate that such processes continue for somewhat longer
periods, particularly when steady state creep is established.

(ii) Application of isothermal data to an athermal
       situation:

The use of stress relaxation and creep data
obtained under isothermal conditions in the model of stress
and strain generation during quenching is made difficult
by the complex relationships between the viscous flow
processes, temperature and time that occur during
continuous cooling. Thus the stress relaxation rates
obtained at a particular stage in the cooling process are
influenced by the thermal and mechanical history of the
specimen during the earlier stages of the quench. This
arises because the rate of work hardening varies with
temperature, so that the degree of work hardening induced
at a particular point during a quench will differ from
that obtained during an isothermal treatment for an
equivalent time. To deal with this situation the
isothermal stress relaxation data has been introduced
by a number of different methods, each of which has

particular merits and drawbacks. These methods are discussed below:

(a) Method 1:

The stress relaxation rate produced at a particular temperature is that obtained from the initial slope of the stress relaxation test. In this case the effect of work hardening from the previous strain history has been ignored and the recovery processes are considered to be the dominating feature. However the rate of stress relaxation reduces with the decreasing temperature, in the manner indicated by the isothermal stress relaxation tests: this represents the most severe case of stress relaxation. It is most relevant at the start of the quench (at high temperatures where there is the greatest possibility of rapid recovery) or when a sudden increase in stress level has just been produced, (e.g. just below M_s). At other points in the process it will be an over-estimate.

(b) Method 2:

The stress relaxation rate at a particular temperature and time is the mean obtained at that temperature during the whole period up to the time in question. However, at higher temperatures, in particular the creep rate becomes steady at a value above zero. To simulate this process the stress relaxation rate is reduced as described above for the first 20 seconds, but the rate obtained after this time is then maintained until

142.

the end of the test. This method assumes that the
material becomes progressively more resistant to creep
during the first 20 seconds, after which steady state
conditions are reached. As mentioned earlier, the
standard linear solid assumes a state of zero stress
relaxation after a relatively short time, which is
overcome by the approach used in this method.

(c) Method 3:

This method is similar to method 2, except that
the rate of stress relaxation is continuously reduced
throughout the quench. Like method 2 at times of less
than 20 seconds the rate of stress relaxation at a given
point is the mean rate obtained during the quench to this
time. Thus progressively increased creep resistance is
assumed until the end of the quench. This simulates a
situation when the stress has been introduced at a constant
rate during the whole quench so that this model assumes
a gradual stress generation process - although this model
takes into account the change in stress relaxation and
creep processes as time increases, it does not take into
account the athermal nature of the stress generation
process during a quench.

The experimental stress relaxation tests are
influenced by the presence of grips and mechanical joints
in the equipment, which tend to lower the modulus of
elasticity of the mechanical system. This effect means

that the stress relaxation rates experimentally observed
are underestimates. However, the incorporation of
viscous flow into the mathematical model probably
involves an overestimate in all cases of stress relaxation,
because either the maximum rate (method 1) or an average
rate (methods 2 and 3) are used. Both these rates will
be greater than the instantaneous value obtained by the
differentiation of the relevant equation. Hence these
two possible sources of error will tend to be in opposition.

Although all of the methods used can be criticized,
they do, nevertheless, represent a very wide range of
possible situations which could occur in a real quench
and the following study, taken in conjunction with the
experimentally determined residual stresses and strains
does suggest possible ways by which these methods may be
modified to represent better the actual situation present
during a quench.

6.3 Thermal Stress and Strain in Quenched Plates

6.3.1 Oil quench

(i) Method 1 ; stress relaxation and creep rates
determined from the initial slope of the curves
obtained under isothermal conditions:

The influence of viscous processes on the generation
of thermal stress is most prominent in this model (figure
57). This is due to the high rates of stress relaxation
and creep which are at all times that appropriate to a
particular temperature at the start of the relaxation
process.

144.

A comparison of the relationships between stress and
strain (of figure 57), to the one predicted by the
earlier model due to Fletcher and Price[100] (when viscous
processes were excluded figure 56), shows that during the
initial stages of the quench, the stress generation
process is unaffected by the viscous flow. This is
because the time interval during which there is a rapid
rise in the stress at the surface and the centre is very
small. Nevertheless the rate of stress relaxation
pertaining to these high temperatures is high, so that a
reduction in the rate of stress generation at a slightly
later stage allows the viscous processes to become
significant and eventually predominant, (i.e. during
the latter part of the vapour blanket stage). This
causes unloading of the stresses at the surface to occur
at an earlier point than was the case in the calculations
of Fletcher and Price[100] (1.8 seconds compared to 4
seconds). Despite the earlier unloading in the presence
of stress relaxation the final stress and strain values
at the end of the vapour blanket stage (as shown in
figure 57) are not significantly different from those
suggested by the calculation of Fletcher and Price[100].
This is because the viscous flow produced while the surface
stress is positive is balanced by that produced at the
end of the vapour blanket stage, when the surface stress
is negative. At the onset of nucleate boiling the rate
of cooling at the surface begins to increase, with a
consequent increase in the tensile stresses at this point

in the plate. At these lower temperatures the stress
builds up to a higher level, with a consequent increase
in viscous flow and stress relaxation. This obviously
tends to counteract the build up of thermal stress and
eventually causes the tensile stress to unload at an
earlier stage than would be the case were viscous
processes absent (compare figure 57 to figure 56).
Subsequently the cooling rate at the surface drops off
considerably relative to that at the centre so that the
generation of compressive stress occurs at the surface.
The rate of thermal stress buildup is now low but the
temperature still sufficiently high to allow a substantial
rate of stress relaxation, this leads to an unloading of the
compressive stress at temperatures between $321^{\circ}C$ and $300^{\circ}C$.
At the onset of the martensitic transformation the surface
is at a lower compressive stress than when stress
relaxation is absent and the maximum compressive stress
subsequently produced is like-wise lower. The eventual
unloading of these compressive stresses as the martensitic
transformation occurs in the interior regions of the
plate is aided by the high rates of stress relaxation
associated with the very high level of these compressive
stresses. This unloading is eventually followed by the
generation of a tensile stress at the surface, but the
rate at which thermal stress is generated is very low,
while the rate of stress relaxation remains significant,
even at temperatures below $200^{\circ}C$. Consequently by the
time the surface has reached ambient this tensile stress

has been reduced to virtually zero. As has already been pointed out in section 6.1, Young's modulus does not generally determine the relationshiip between stress and strain when the former is below the yield stress, since the presence of viscous flow affects the slope of the stress-strain curve.

The significance of the predicted final stress and strain distribution in relation to the experimentally determined values is discussed below.

(ii) Method 2 and Method 3: stress relaxation and creep rates determined from isothermal tests at relevant times;

The relationships between stress and strain at the surface and centre predicted by these methods are illustrated at figures 58 and 59. Both these methods incorporate a gradual increase in the creep resistance of the material as the time increases. However, method 2 assumes a steady state condition after 20 seconds whereas method 3 involves a gradual hardening of the material throughout the quench. With either method the combined effects of temperature and time on the rate at which viscous process occurs leads to a reduction in the influence of either stress relaxation or creep as the quench continued. Method 2 simulates a situation where a primary creep stage is eventually replaced by secondary creep, while method 3 is appropriate in the case where primary creep persists at all times.

The use of methods 2 and 3 in the mathematical model

of thermal stress generation produced identical relationships
between stress and strain during the first 20 seconds
of the quench. This arose because the same viscous
flow rates were used by these methods during this time
interval (compare figure 58 to figure 59). Due to the low
viscous flow rates predicted by these methods the
unloading of stress at the surface during the later parts
of the vapour blanket stage, occurs at a slightly later
time (2.4 seconds compared to 1.8 seconds) than that
shown in figure 57 (method 1 with a high viscous flow rate).
Furthermore the tensile stress build up at the surface
produced by the fast cooling rate associated with the
nucleate boiling stage produces a small amount of tensile
plastic flow, which is absent in figure 57 (method 1 with
high viscous flow rate). The difference in the relation-
ship between stress and strain predicted by methods 2 and
3 becomes more significant during the martensite trans-
formation and the later stages of the quench, where the
viscous flow rates pertaining to method 2 are higher than
those predicted by method 3. However the viscous effect
is not pronounced in comparison to the results shown in
figure 57 (method 1 with high viscous flow) so that the
stress reversal present in figure 57 towards the end of
the quench is absent when methods 2 and 3 are used. Also
the final tensile stage at the surface predicted by
method 1 is absent when methods 2 and 3 are used so that
both these methods show a compressive stress at the surface
and a tensile stress at the centre. However the magnitude

148.

of these stresses is smaller than that predicted at a
corresponding point in the plate by Fletcher and Price's
model (where viscous flow was excluded, figure 56).

Due to the complex nature of the relationships
between temperature, time and stress generation during
quenching, previous attempts to apply isothermal creep
data to such a situation have been based on empirical
approaches that involves the concept of either "time
hardening" or "strain hardening"[101]*. The former
approach represented in the present work by method 2 and
method 3 shows that viscous flow has a relatively small
effect on the stress generation process, at least in
comparison with method 1 which ignores the prior thermal
history of the quenched specimen. The strain hardening
rule has been found to produce even less effect[101],
since the viscous flow depends here on the previous strain
history. Thus the greater the cumulative creep strain
from earlier time, the harder it is for further creep to
occur.

(iii) Comparison of predicted and experimental residual
       stresses and strains

Figure 99 shows the experimental residual stress
distribution adjusted for the edge effects, along with the
residual stress distributions predicted by each of the
methods discussed above. The experimental residual stress
pattern shows a tensile stress at the surface which

---

* For the explanation of these terms see page 34.

149.

becomes compressive towards the centre. None of the
models discussed above, show a residual stress pattern
that resembles closely   that found experimentally.
Nevertheless they do show an improved agreement over that
obtained from the calculations of Fletcher and Price,
which omitted all viscous processes (also shown at figure
99) Method 1 which employs the highest amount of viscous
flow, shows the closest agreement but there is still a
significant discrepancy between calculated and experiment-
ally determined stresses. In the case of the other
methods, the smaller the viscous effect the worse the
agreement with the experimental results.

The greater the amount of viscous flow the greater
is the probability that a stress reversal will occur
during the later stages of the martensite transformation
to produce a tensile stress at the surface and a
compressive stress at the centre, (see figure 57). This
is essential if close agreement with the experimental
results is possible. However the presence of viscous
flow after this final stress reversal causes relaxation
of the thermal stress. Hence method 1, which produces
tensile stress at the surface at 198°C, also predicts
zero residual stress at all points at the end of the
quench, on account of the significant viscous flow at
these low temperatures. It would appear, therefore,
that the experimentally determined stress distribution
requires significant viscous flow at temperatures above
about 200°C, but an absence of this effect below this

temperature. Obviously an abrupt change is not possible, but a steady increase in the influence of work hardening as the temperature falls towards 200°C could produce such an effect. None of the methods of introducing stress relaxation and creep used in the present work take such processes into account.

Comparison of the predicted and experimentally measured distortion in an oil quenched plate (figure 100) show that the distortion predicted by all the models are slightly greater than that determined experimentally. However there is a very little difference in the level of distortion predicted by individual models.

6.3.2 Water quench

(i) Influence of viscous processes on the predicted relationships between stress and strain:

Figures 52 and 53 show the relationships between stress and strain at the surface and centre of a water quenched plate, as predicted by the mathematical model with the viscous effect incorporated according to the methods described in section 6.2. These results remain largely unaffected by viscous flow during the initial stages of the quench. This is because of the rapidity of the water quench, which does not allow time for the viscous processes to produce a significant effect at these high temperatures. However all the methods predict that appreciable viscous flow occurs during transformation of the surface to martensite, on account of the high level

151.

of compressive stresses produced at this point in the quenching process. Hence the maximum compressive stresses generated at this stage are lower than those predicted by the earlier model that ignored viscous processes (compare figures 52 and 53 to figure 51).

Methods 2 and 3 with a progressive reduction in the viscous flow rates, at least during the first 20 seconds of the quench, produce identical relationships between stress and strain, as illustrated by figure 53. As already described in section 6.2, the difference between the stress relaxation rates obtained by these methods begins after a duration of 20 seconds. In a water quench 20mm plate the surface reaches a temperature of $130^{o}C$ after this time, at which stage the viscous flow rates obtained by both these methods have an insignificant effect on the stress generation process. However, in both cases, the viscous flow processes present at higher temperature assist the unloading of compressive stresses at the surface, thus producing a tensile stress at this point at the end of the quench.

The high viscous flow rates associated with method one, has a pronounced effect on the generation of thermal stress and strain during the formation of martensite and towards the end of the quench when an unloading of tensile stress occurs at the surface.

(ii) Comparison of predicted and experimental
      residual stresses and strains

Figure 54 shows the residual stress distribution predicted by the mathematical model that include consideration of viscous processes. In order to compare the experimental with the calculated results, the former have to be adjusted to account for the edge effect[100]. The adjusted experimental residual stress distribution along with the calculated distributions, using different methods of viscous flow in the mathematical model, are shown in figure 101. The inclusion of viscous flow into the mathematical model reduces the level of agreement between the calculated and experimental residual stress distribution, which is in contrast to the better level of agreement achieved by the earlier model which did not include viscous processes (also shown at figure 101). With the introduction of viscous flow, the general level of stress obtained by calculation is reduced at all points, and the level of this reduction is increased as the magnitude of the viscous effect becomes more pronounced (method 1). The only common feature in the set of predicted stress distributions is the overall shape of the curves which show a maximum tensile stress just below the surface. In a similar way the level of predicted strains obtained from the mathematical model that includes viscous process, show an overall reduction when compared to that obtained in the absence of viscous process. This however improves the level of agreement with the

experimentally obtained distortions shown in figure 102.

6.3.3 Method 4. Stress relaxation and creep rates as per method 1, above 230°C, whereafter the viscous flow stopped:

The methods used to incorporate viscous flow into the mathematical model have been unsuccessful in removing completely the discrepancy between the experimental and predicted residual stresses and strains. The stress and strain relationships in the case of the oil quench (figure 57, 58 and 59), reveal, that only the method which gives the highest viscous flow rates (method 1) allows the possibility of a residual tensile stress at the surface. However if the same method is used at temperatures below about 230°C the tensile stress generated at low temperatures decay to virtually zero by the end of the quench. In the case of a water quench, it is the high viscous flow rates predicted by method 1 that reduces the overall level of the predicted residual stress distribution and gives a reduction in the level of agreement between the experimental and predicted results. These observations suggest that high viscous flow at temperatures above 230°C followed by the cessation of the viscous effect at lower temperatures (towards the end of the quench), would bring about a better level of agreement between the experimental and calculated residual stresses for both the water and oil quench conditions. Thus by stopping all viscous flow at 230°C, the agreement between the calculated and experimental residual stress

distributions at the end of the oil quench is excellent
(figure 103), and this is achieved without a marked
deterioration in the level of agreement in the case of
the water quench (figure 104).

The conditions applied in the above method might at
first appear mutually exclusive, but it is of interest
that the early stages of the formation of martensite are
associated with a very rapid increase in the compressive
stress at the surface. The sudden introduction of a
large thermal stress is similar to the situation at the
start of an isothermal stress relaxation test, when the
relaxation rate is high so method 1 would be appropriate
at this stage in the quench. However, towards the end
of the quench very little additional thermal stress
would be introduced and that produced at an earlier stage
would continue to relax. The rate of this stress reduction
would now be similar to that found at a late stage in an
isothermal stress relaxation test; under these circum-
stances method 1 would no longer be appropriate. Further-
more at this late stage in the quench the thermal history
of the specimen is likely to induce considerable work
hardening which would significantly reduce the rate of
stress relaxation over that present in an isothermal test.
Hence, the cessation of the stress relaxation process at
temperatures below 230°C would seem to be appropriate,
even though some viscous flow has been detected in isothermal
tests at these temperatures. These conclusions must be

155.

speculative at the present time so a programme of experimental work will be required to examine the inter-actions of the stress relaxation processes at different stages in the quench. Only then will it be possible to produce a further improvement in the viscous flow methods described in the present work.

6.3.4 Martempering with an oil quench from the salt bath.

(i) Relationships between the stress and strain at the surface and centre of the plate:

The influence of viscous flow on the stress generation process during the martempering operation is shown in figures 63, 64, 65 and 105 which include the results obtained by the use of the four methods described above. In all cases the relationships between stress and strain during the initial stages of the process are similar to those produced during a water quench, which is due to the very high initial values of the surface heat transfer coefficients associated with the use of a salt bath. However, during the later stages of such a treatment there is a considerable reduction in this coefficient, with a consequent drop in the rate of cooling of the component. This allows sufficient time for a significant amount of viscous flow to be produced. The degree to which the viscous flow influences the relation-ships between stress and strain at this stage depends on the method by which it is incorporated into the mathematical model of the stress generation process. Methods 1 and 4, which produce the highest viscous flow

effect reduces the surface stress to virtually zero by the end of the salt bath treatment (figures 63 and 105). In the cases where viscous flow is less pronounced (methods 2 and 3) a residual stress remained after a cooling period of 80 seconds in the salt bath, although the strain present is unaffected by the method used to introduce viscous flow (see figures 64 and 65).

The subsequent oil quench to room temperature introduces a significant tensile stress increment at the surface, on account of the magnitude of the cooling rate during the early stages of this treatment, which is similar to that observed during the initial stages of a conventional oil quench (figure 57). The cooling rate is maintained at a high level for a very short time and the subsequent reduction in the surface heat transfer coefficient causes the surface stress to become less tensile in the case of methods 1 and 4 and to become more compressive in the case of methods 2 and 3. This effect is intensified once the surface reaches the M_s temperature. The relationships between stress and strain during the subsequent martensitic transformation is virtually identical to that observed at the same stage during a conventional oil quench.

The holding time in the salt bath is critical. In order to eliminate completely the temperature gradient across the plate, a long salt bath treatment is required, which is undesirable on account of the possibility of the

initiation of the bainite transformation specially between 400°C and 300°C (see TTT diagram, figure 30). Therefore a time of 80 seconds in the salt bath, at a temperature of 400°C, is chosen, which produces a temperature of 466°C at the surface and 469°C at the centre at the end of the salt bath treatment. The selected time is desirable from the point of view of productivity since the complete elimination of the temperature gradient would significantly reduce the rate at which components could be treated. Although the temperature gradient at the end of the salt bath treatment has become greatly reduced, it is re-established at the start of a subsequent oil quench. Thus there is no possibility of simultaneous transformation to martensite at all points in the plate which would prevent any further build up of stress during the final stages of the process.

The predicted relationships between stress and strain generated at the surface and the centre during martempering give a better understanding of the stress generation process in this type of heat treatment. Martempering differs from the conventional oil quench in that it allows a significant time for creep to occur at intermediate temperatures (550°C to 450°C) during the salt bath treatment (compare figure 57 to figure 63). However the additional viscous flow is largely counteracted by the enhanced strain of opposite sign generated at higher temperatures under the influence the high surface heat

transfer coefficient associated with a salt bath.

Consequently the final strain differred little from that

predicted by the conventional oil quench. Furthermore

the maximum stress generated during the martensite

transformation is only a little smaller than that

produced at this stage by an oil quench from 850°C. Thus

the use of an oil quench after the use of a salt bath

treatment at 400°C would not seem to be advantageous.

(ii) Comparison of experimental and predicted
     residual stresses and strains:

The experimentally obtained stress distribution

within the martempered plate at the end of the quench

(figure 106) shows a tensile value at the surface and

compressive stresses towards the centre. The various

mathematical models, all of which incorporate viscous

flow predict a residual stress distribution also shown in

figure 106, that differs from the experimental results

by an amount that is very similar to the corresponding

discrepancy found in material that had been subjected to

a conventional oil quench (figure 99). The mathematical

model in which the viscous flow is represented by method

1 at temperatures above 230°C (maximum viscous flow rate

obtained at each temperature) combined with zero viscous

flow at lower temperatures (i.e. method 4), again give an

excellent agreement between the predicted and experimental

results (see figure 108). This provides further support

for the accuracy of this model, which also gives the best

agreement between the predicted and experimental residual

stress distribution obtained after both the oil and the

water quench.

6.3.5 Martempering with air cool from the salt bath:

It is believed that martempering of components generally reduces the level of distortion produced in them at the end of the quench[119]. However, in the present work, both the experimental and predicted residual stresses and strains show that there is an insignificant difference between the results obtained by a conventional oil quench and those obtained by martempering (compare figures 99, 100 to figures 106, 107).

A study of the relationships between stress and strain (figure 65), reveal, that the presence of residual stress is largely a consequence of the oil quench after the salt bath treatment. Thus, if the plate is allowed to cool slowly (i.e. in air) subsequent to the salt bath treatment, stress generation at this stage can be prevented. The use of a very low surface heat transfer coefficient ($50W\ m^{-2}\ ^{\circ}C^{-1}$) simulated an air cool from the salt bath temperature, which resulted in zero predicted residual stress at all points in the plate. This slow cool in air, subsequent to the salt bath treatment, prevents the generation of significant temperature gradients across the plate and allows the simultaneous formation of martensite at all points in the component. However, the level of residual distortions produced, which are a consequence of the plastic flow in the initial

stages of the salt bath treatment, remain unaltered by
the change from an oil quench to an air cool in the later
stages of the martempering process. Furthermore the
longer time required to air cool the plate after its
removed from the salt bath may allow the production of
bainite. Thus the use of an air cool from the salt bath,
which is the preferred commercial method, will certainly
prevent both cracking during the formation of martensite
and the generation of any residual stress, but it can
have no influence on the distortion produced and some loss
of strength could be involved, on account of the formation
of bainite.

6.3.6 Martempering at lower salt bath temperature (250°C) followed by an oil quench at 20°C

A salt bath temperature of $400^{\circ}C$ was chosen
originally because this is the temperature which is least
likely to involve decomposition of austenite to bainite.
However commercial martempering operations tend to occur
at rather lower temperatures. Therefore an attempt was
made to study the effect of a reduction in the salt bath
temperature to $250^{\circ}C$ on the final stress distribution
obtained after the oil quench. Although such a reduction
attenuated the general temperature level obtained across
the plate after the stipulated 80 seconds, the temperature
gradient present after this time is the same as that
produced when the salt bath temperature was $400^{\circ}C$, and
the stress and strain generation process was virtually

unaffected by this temperature change (compare figures 105 and 109). Furthermore the subsequent oil quench generated a temperature gradient similar to that produced by the earlier oil quench thus generating stress levels similar to those observed in the previous case (i.e. salt bath temperature 400°C followed by oil quench to 20°C), compare figures 105 and 109.

6.3.7 Overall view of Martempering

The results obtained suggest that the value of the martempering operation is limited. The build up of stress during the formation of martensite can only be prevented by a very slow cool from the M_s temperature, such as can be provided by cooling in air. Whereas such a procedure is possible in the deep hardening steel at present under consideration in many steels it will be accompanied by the formation of bainite and a possible loss of strength. There is also little advantage to be gained from the point of view of residual distortion, since the results obtained differred little from those obtained after conventional oil quench from 850°C. It is therefore difficult to see how the extra cost of the martempering operation can be justified; except in the specialised case where it is essential to prevent any build up of stress during the formation of martensite and where the formation of bainite is not unduly detrimental.

From a theoretical point of view the additional data on a process which allows a particularly large amount of

viscous flow is very valuable when an assessment of the mathematical model of the stress generation process is to be made.

6.4 Transformation Plasticity included in the Mathematical Model

6.4.1 Reduction in flow stress below the Ms temperature to simulate transformation plasticity

The plastic flow observed as enhanced dilation during the transformation of austenite to martensite in the presence of an applied stress, is modelled by a reduction in the flow stress of the material to a value considerably lower than that obtained from the experimental tensile tests. This reduced yield stress is taken as the minimum stress at which enhanced dilation occurred (see section 4.4.1). The effect of viscous processes on the predicted results have already been discussed (section 6.3) and it is evident that the use of a high rate of stress relaxation up until the initial stage of the martensite transformation, followed by a cessation of any viscous flow effect at 230°C and below gives the best agreement between the predicted and experimental residual stress and strains. Consequently it is this viscous flow model which has been used in conjunction with the reduction in flow stress to simulate the effect of transformation plasticity on the calculated results.

(i) Oil quench

Figure 110 shows the relationship between stress and strain at the surface and the centre of the plate

163.

predicted by the mathematical model which incorporates transformation plasticity by the reduction in flow stress at temperatures below M_s. At the onset of the martensitic transformation the surface, which is already in compression is subjected to compressive plastic flow as a consequence of the reduction in flow stress. The build up of compressive stress at the surface is controlled by the rate of work hardening associated with this plastic flow. The plastic flow at the surface is stopped when the transformation begins towards the interior of the plate, and further transformation causes an unloading and the subsequent reversal of the surface compressive stresses. At the centre, the martensite transformation begins when the centre is in tension, so that there is a small amount of tensile plastic flow as the centre temperature falls between $300^{\circ}C$ and $286^{\circ}C$, before the unloading of the tensile stresses is produced by the expanding martensitic structure. When the results from this model are compared with those from the one that did not include transformation plasticity (figure 111) it is seen that the additional compressive and tensile plastic flow at the surface and the centre respectively, counteracts the amount of plastic strain already introduced during the earlier stages of the quench. The reduction in flow stress below M_s, prevents the build up of a high compressive stress at the surface during the initial stages of the martensitic transformation (compare figure 110 to figure 111). Thus at the end of

the quench, a higher tensile stress is developed at the surface than is possible in the case where transformation plasticity is not considered (figure 111).

The residual stresses and strains distribution obtained from this model are presented in figures 112 and 113 along with the experimental stress and strain distributions. An excellent agreement with the predicted residual stress distribution is observed. The degree of agreement is much improved by the introduction of the transformation plasticity effect into the mathematical model (compare the predicted residual stress distribution obtained from the model without transformation plasticity figure 103. The predicted residual strains from the mathematical model are still higher at all points than the corresponding experimentally obtained distribution (figure 113), although they are slightly lower than those predicted by the model that ignored transformation plasticity (figure 114).

(ii) Water quench

Figure 115 shows the relationships between stress and strain at the surface and the centre of a water quenched plate, when a reduction in flow stress is assumed between 300°C and 265°C. At the onset of the martensitic transformation, the surface, which is in compression, is subjected to a compressive plastic flow, due to the low flow stress values assumed at this stage. The extent of plastic flow is much higher than that obtained in the case

165.

of an oil quench (compare figure 115 and figure 110).

This is due to the high compressive stresses at the

surface produced by the steeper temperature gradients

across the plate at this stage in the water quench. This

additional plastic flow at the surface between $300^{o}C$ and

$265^{o}C$ is of the same order as the transformation plasticity

strain obtained experimentally from the stress dilation

tests (figure 50); which indicate a contraction of 0.4%

between $300^{o}C$ and $265^{o}C$ when the applied stress is -125MPa.

The effect of a reduction in flow stress at this stage,

is to reduce the level of the maximum compressive stress

produced at the surface (compare figure 115 and figure 116).

However the unloading of compressive stresses at the

surface due to the initiation of the martensitic trans-

formation in the interior of the plate occurs at a later

temperature ($220^{o}C$ compared to $244^{o}C$ in the case where

transformation plasticity is not considered, figure 116).

This is due to the softening of the interior of the plate

associated with the reduction in flow stress during the

initial stages of the martensitic transformation. As a

consequence of the low level of compressive stresses

produced at the surface, at this stage, a higher tensile

stress is produced at the surface towards the end of the

quench, than that obtained when transformation plasticity

is not considered (figure 116). This fact is evident

from the predicted residual stress distribution presented

in figure 117. A reduction in flow stress to simulate

transformation plasticity in the case of a water quench

increases the level of the predicted residual stress at all points (compare figure 117 and figure 104). This produces a deterioration in the good agreement between the experimental and predicted residual stress distribution obtained from the mathematical model which excluded transformation plasticity. The inclusion of transformation plasticity also reduced considerably the level of agreement between experimental and predicted residual strains (figure 118). The reduction in the level of residual strain at the surface is attributed to the additional plastic flow which occurs below the M_s temperature and counteracts the plastic strain introduced during the earlier stages of the quench (figure 115). The reduction in the level of compressive stresses generated at the surface during the martensitic transformation reduces the level of tensile plastic flow at the centre (figure 115) which brings about a reduction in the level of residual strain generated in this part of the plate. Thus it would appear that although the viscous processes represented by method 4 (high viscous flow rates above 230°C with no viscous processes below this temperature) in conjunction with transformation plasticity improve the level of agreement between experiment and prediction in the case of an oil quench, the use of the same model in the case of a water quench produces a reduction in the corresponding level of agreement.

It is of interest that some of the other methods by which viscous flow may be introduced into the model

(i.e. methods 2 and 3), when taken in conjunction with transformation plasticity give an excellent agreement between the predicted and experimental residual stress obatined after a water quench. Thus, although these were regarded unfavourably when transformation plasticity was not included the introduction of this effect allows these methods to be seen in a more favourable light (compare figure 70 to figure 96). However the level of agreement between the predicted and experimental residual strains still remained poor (compare figure 71 to figure 97). In the case of an oil quenched plate the use of these methods give a better level of agreement with the experimentally determined residual stresses, although the magnitude of the predicted tensile stress is still significantly lower than the corresponding experimental value at the same point in the plate (compare figure 74 to figure 93).

6.4.2 Transformation plasticity as an additional strain

The reduction of flow stress below the M_s temperature, is an indirect method of simulating the effect of transformation plasticity during the thermal stress generation process. It assumes that the enhanced dilation obtained during transformation in the presence of a stress is due to plastic flow associated with a reduction in yield stress and the transformation strain is always obtained from the dilatometry curve produced under stress free conditions. An alternative and possibly more realistic approach would involve the inclusion of this

effect in the mathematical model by giving due consideration to the dilatometry characteristics of the material when martensite forms under the influence of stress. This was achieved by the abstraction of the value of the additional strain, due, to the transformation plasticity direct from the experimental stress dilatometer tests and employing these strain values into the mathematical model (see section 4.4.2). The viscous effects in the model are represented by method 4 (high viscous flow rates above $230^{\circ}C$ followed by a cessation of viscous flow), which in the absence of transformation plasticity gave the best level of agreement between the predicted and experimental results.

(i) Oil quench

Figure 119 shows the relationship between stress and strain in the case of an oil quenched plate with transformation plasticity included as an additional strain. This method of including transformation plasticity has retarded the build up of compressive stresses at the surface, during the early stages of the martensitic transformation. This is due to the nature of the transformation plasticity strain under compressive stresses (i.e. a contraction) which opposes the expansion associated with the martensitic transformation under zero stress conditions. The maximum level of compressive stress generated at the surface at this stage is much smaller than that predicted by the mathematical model in the

169.

absence of transformation plasticity (compare figure 119 with figure 111). The unloading and the subsequent reversal of the compressive stresses at the surface, which occurs as the transformation front travels into the interior of the plate, finally produces a residual tensile stress at the surface. The martensitic transformation occurs at the centre while this part of the plate is in tension, so this state of stress produces an enhanced expansion due to transformation plasticity, which in turn causes the unloading of the tensile stresses. Thus shortly after the onset of the martensitic transformation a compressive stress is produced towards the centre. The residual stress distribution predicted by this model (figure 120) shows a tensile stress at the surface and compressive stress towards the centre, which is in excellent agreement with the experimentally obtained residual stress distribution (also shown in figure 120). However the predicted residual strains, still show a relatively poor level of agreement with the experimental results (figure 121).

(ii) Water quench

Figure 122 shows the relationship between stress and strain in the case of a water quenched plate predicted by the mathematical model that incorporates transformation plasticity as an additional strain component. At the onset of the martensitic transformation on the surface the generation of compressive stresses is

greatly reduced, which is a similar effect to that
observed in the case of an oil quenched plate. Never-
theless the steeper temperature gradient in a water
quenched plate produces substantially higher compressive
stresses than occurs at an equivalent point in the oil
quench (compare figure 119 to figure 122). The centre
at this stage is at a higher temperature and is subjected
to plastic flow. However transformation plasticity
reduces the amount of plastic flow because of the lower
level of compressive stresses produced at this time near
the surface.

The inclusion of transformation plasticity leads at
the end of the quench to a residual tensile stress at the
surface and a compressive stress at the centre (figure
123). This predicted stress distribution shows an
increase in the level of stress at all points compared
to that predicted when transformation plasticity is
excluded (figure 104) although the shape of the relevant
curve remains similar to that obtained experimentally
(figure 123). The predicted residual strain distribution
compares less well with the experimental results (figure
124), when the transformation plasticity is included:
this deterioration involves a change in the shape of the
curve showing the strain distribution across the plate.

6.4.3 <u>Transformation plasticity and its incorporation
into the mathematical model of thermal stress
generation</u>

The work of Desalos et al[111] suggests that

171.

the phenomenon of transformation plasticity arises from heterogeneous deformation consequent upon the martensite transformation. Attempts to incorporate this complex effect into a mathematical model that assumes homogeneous deformation, have failed to take this heterogeneity into account. Although the simulation of transformation plasticity by the reduction in flow stress below the M_s temperature shows plastic flow, it does not necessarily accurately model the situation that arises in a material subjected to internal stresses during a quench. Furthermore the lack of experimental evidence of a reduction in yield stress during the formation of martensite casts doubt upon the theoretical basis of the concept.

An alternative attempt has been made to simulate the effect of the heterogeneous nature of the strain by considering the transformation plasticity effect as an additional strain that depends on the transformation characteristics of the material while under the influence of stress. Nevertheless the additional transformation strain so considered is still elastic in nature, which means that there would be no permanent set in the material as a consequence of the transformation.

Thus neither of the proposed methods by which transformation plasticity has been considered is completely satisfactory, since both are at variance with some aspect of the experimental data viz: the lack of evidence of a significant reduction in yield stress below M_s in the one

hand and an absence of a permanent set on the other.
However, both of the models used improve the degree
of agreement with experimental residual stress, and so
appear to give a reasonable simulation of the heterogeneous
origins of transformation plasticity pointed out by
Desalos et al[111]. Nevertheless the lack of improvement
obtained in the case of residual strain is a matter of
concern, and further work is required.

6.5 General Discussion

The objective of this work has been to
incorporate the viscous flow effects into the mathematical
model that has been developed to predict the thermal stress
and strain produced in quenched plates of low-alloy steel.
It was apparent from the review of previous work that the
mathematical models developed to date have not made a
realistic attempt to include the effect of stress
relaxation and creep on the stress generation process.
Some of the models which attempted to include the viscous
effect, did so in an arbitary fashion, without due
consideration of the type of steel used and the structural
changes which occur during the quenching of steel. The
mathematical model used in the present work, which was
initially developed by Fletcher and Price[99] did not
take viscous processes into consideration. The calculated
results from this model showed a high level of agreement
with the experimentally obtained results in a water
quench situation, but the level of agreement was poor in

the case of an oil quench. This situation emphasised
the need for modification to the mathematical model, and
it was considered that the exclusion of viscous processes
was a major defect in the model, and was responsible for
the lack of agreement with the experimental results in
the case of an oil quench.

The approach taken in the present work has been to
obtain experimental data of the stress relaxation process
at temperatures between $850^{\circ}C$ and $100^{\circ}C$ and to represent
them quantitatively by the use of mechanical models. It
was found that the standard linear solid gave the best
representation of the experimental behaviour of the type
of steel used. The use of this model was further validated
by a comparison of the experimental creep rates, obtained
at high temperatures, with the creep rates predicted by
this model. Isothermal viscous flow data may be criticised
when it is applied to a continuous cooling situation.
This is because there may be a complex interaction
between deformation processes at high temperatures and
those that occur later in the quench, when the temperature
is much lower. This aspect of the problem has not been
considered experimentally during the present work, but
the examination of several different models of the viscous
process in the calculation have given an indication of
the extent to which such effects might influence the
thermal stress generation process. The method that gave
the best agreement between the experimental and predicted

residual stresses and strains suggests that the prior ·
deformation of the material during the earlier stages
of the quench had little effect on subsequent viscous
flow until a relatively low temperature ($230^{\circ}C$) was
reached. Below this temperature no viscous processes
were present i.e. the small amounts of stress relaxation
suggested by the isothermal experiments were completely
inhibited by the deformation that occurred earlier in the
quench.

The various methods by which viscous processes had
been introduced into the mathematical model were tested
by an investigation of the martempering process, where
a particularly long time is available for the viscous
processes to influence the generation of thermal stress and
strain at intermediate temperatures. Again method 4,
which represents viscous flow as a time independent
process at temperatures above $230^{\circ}C$, gives the best
agreement with the experimentally determined stress and
strain distributions. Although this agreement is very
good in the case of stress, the level of discrepancy in
the case of strain is about identical to that produced in
a direct oil quench. Hence substantially different
thermal histories, with markedly different amounts of
viscous flow led to virtually the same level of agreement
with experiment. This would appear to indicate that the
remaining descrepancy in the case of residual strains in
slowly cooled material is not due to inaccuracies in the
modelling of the viscous flow processes, but to some

other cause.

Experimental investigation of 835M30 steel have shown that the changes in length associated with the martensitic transformation are significantly affected by the magnitude and nature of the stress applied during the transformation process. The attempts to include this effect (transformation plasticity) into the mathematical model results in a further improvement in the level of agreement between the predicted and experimental residual stresses in an oil quenched plate (see figures 112 and 120), but reduces the level of agreement in the case of water quenched material (figures 117 and 123). Furthermore surprisingly good agreement is found when transformation plasticity is taken in conjunction with certain models of the viscous flow process which have not been very successful when transformation plasticity has been ignored. However in all the cases considered a poorer level of agreement is obtained between the predicted and experimental residual strain distributions. This is possibly due to the method by which transformation plasticity, which is a heterogeneous effect, is introduced into the mathematical model, which has been developed to consider only homogeneous deformation. A better understanding of the heterogeneous nature of the transformation plasticity is required, along with modification of the mathematical model, in order for it to be capable of handling this complex deformation phenomenon. The application of transformation plasticity to thermal stress generation

during quenching is a very recent development although at the present time it is the subject of intensive study[110,111]. It is to be expected that significant progress will be made in the near future.

7. CONCLUSIONS

1. The visco-elastic effect may be represented by means
   of mechanical models that consist of various
   combinations of springs and dashpots; of these models
   the standard linear solid produces the best agreement
   with experimentally determined stress relaxation data.

2. A good level of agreement may be obtained between the
   calculated and experimentally determined residual
   stress after an oil quench when viscous flow is
   included in the thermal stress mathematical model.
   This improvement over the results previously obtained
   in the absence of any consideration of viscous flow
   has been obtained at the expense of a small reduction
   in the corresponding level of agreement in the case
   of a water quench.

3. The introduction of viscous flow does not significantly
   improve the level of agreement between the experiment-
   ally determined and calculated residual strains. A
   high level of agreement may be obtained with
   consideration of viscous processes when a water quench
   is involved, but the significant discrepancy previously
   obtained in the case of an oil quench is not appreciably
   reduced by the inclusion of stress relaxation and
   creep in the mathematical model.

4. It is improbable that the use of martempering operation
   can reduce the amount of distortion involved in a

quenching operation, although an intermediate salt
bath treatment above the M_s temperature followed
by an air cool does prevent a stress build up during
the formation of martensite.

5. The use of an oil quench following the salt bath
    treatment, in order to prevent the formation of
    bainite, is of no value, since the stresses generated
    are similar to those produced by a conventional oil
    quench.

6. The inclusion of the effect of an applied stress on
    the dilation characteristics of the austenite $\longrightarrow$
    martensite transformation in the thermal stress
    mathematical model produced excellent agreement
    between the experimental and calculated residual
    stresses obtained after either an oil or a water
    quench. This was however, accompanied by a marked
    deterioration in the agreement obtained in the case
    of residual strains.

7. The major remaining omission from the mathematical
    model of the stress generation process during
    quenching, is the effect of continuous cooling on
    viscous flow. All the relevant data has been
    obtained isothermally and, although attempts have
    been made to use this data to represent the continuous
    cooling condition a further experimental programme is
    required to put this work on a sound basis.

8. Although there is as yet no clear evidence that it has a significant effect on the results obtained certain parts of the model are obviously susceptible to thermomechanical coupling, particularly transformation plasticity and viscous flow. This aspect of the subject also requires further investigation.

9. Notwithstanding conclusions 7 and 8 the mathematical model developed during the present programme would appear to have reached a point where it should be able to predict the generation of thermal stress with a reasonable degree of accuracy. Therefore it would be desirable to check the model in a wider range of experimental situations than has been possible during the present work, which has been primarily concerned with the development of the model.

8. RECOMMENDATIONS FOR FURTHER WORK

1. An investigation should be made on the effect of plastic flow generated at high temperatures on the stress relaxation rates obtained at lower temperatures. The influence of the initial stress level on the stress relaxation rates should also be investigated.

2. The latent heat associated with the phase transformation should be taken into consideration in the calculation of temperature distributions in the cooling plate.

3. The strain rates obtained during the formation of martensite are frequently very high, especially when transformation plasticity is involved. At such strain rates the heat generated by mechanical work may be significant, hence the assumption that thermo-mechanical coupling may be ignored may become invalid. An investigation of this effect is required.

4. The transformation plasticity effect should be studied in more detail so as to ascertain the nature of such deformation on a macroscopic scale. At the present time the mechanism by which the plastic flow is generated is not clear so that the inclusion of transformation plasticity effect in the calculations involving the stress generation must remain tentative.

5. In the longer term, when the points noted above have been clarified; the mathematical model may be extended to include steels of lower hardenability, where phases other than martensite are present.

REFERENCES

1. Orowan, E., Symposium on internal stresses in metals, London Institute of Metals, 1948.

2. J.K. Rai et al, Int. J. Prod. Res., 1978, 16, 6, (463).

3. Benham, P.P. and Hoyle, R.H., "Thermal Stress", London, Pitman, 1964.

4. Gatewood, B.E., "Thermal Stresses", McGraw Hill, New York, 1957.

5. Orowan, E., Proceedings of Symposium on Internal Stresses and Fatigue in Metals, Michigan, 1958.

6. Barrett, S.C., Metals and Alloys, 1934, June, 5, (131).

7. Andrews, K.W., "Physical Metallurgy Techniques and Applications", Vol. II, George Allen and Unwin, Ltd., 1973, (271).

8. Denton, A.A., Met. Rev., 1966, 11, 1, (101).

9. Dolan, T.J. Proceeding of Symposium on Internal Stress and Fatigue in Metals, Michigan, 1958.

10. Inoue, T. et al., J. Mech. Phys. Solids, 1978, 26, (187).

11. Finnie, I. and Heller, W.R., "Creep of Engineering Materials", McGraw Hill, New York, 1959.

12. Graffalo, F., "Fundamentals of Creep and Creep Rupture in Metals", MacMillan, Co., New York, 1966.

13. Odding, I.A., "Creep and Stress Relaxation in Metals", Oliver and Boyd Ltd., London, 1965.

14. Tapsell, H.J., "Creep of Metals", Oxford University Press, London, 1931.

15. Greenfield, P., "Creep of Metals at High Temperature", Mills and Boon Ltd., London, 1972.

16. Pomeroy, C.D., "Creep of Engineering Materials" Journal of Strain Analysis Monograph, Mech. Engg: Publ: Ltd., London, 1978.

17. Andrade, E.N. Dac., Proceedings of the Royal Society, London, 1911, Feb., LXXXIV, Series A.

18. Andrade, E.N. Dac and Jolliffe, K.H., Proceedings of the Royal Society, London, 1952, 213, Series A.

19. Kennedy, A.J., Proceedings of the Royal Society, London, 1952, 213, Series A.

20. Graffalo, F. Trans. AIME, 1963, 227, (351).

21. Johnson, A.E., Proc. Inst. Mech. Engrs., 1941, 145, (210).

22. Kennedy, A.J., "Processes of Creep and Fatigue in Metals", Oliver and Boyd, 1962.

23. Conrad, J., "Mechanical Behaviour of Materials at Elevated Temperature", McGraw Hill, 1961.

24. Dorn, J.E. et al, ASTM, STP, 1954, 165.

25. C.M. Sellars et al, Mem. Sci-Rev.Met. 1966, 63, (71).

26. Sherby, O.D. and Dorn, J.E., Symp. Strength Elevated Temp: Soc. Exper. Stress. Analy., 1953, XII, 1.

27. Dorn, J.E., "Mechanical Behaviour of Materials at Elevated Temperature", McGraw Hill, 1961.

28. Honeycombe, R.W.K., "The Plastic Deformation of Metals", Unwin Bros. Ltd., 1977.

29. Sherby, O.D., Act. Metall. 1962, 10, Feb.

30. Cahn, R.W., "Physical Metallurgy", John Wiley and Sons Inc., New York, 1965.

31. Nabarro, F.R.N., Report on Conference on Strength of Solids, Physical Society, London, 1948, (75).

32. Herring, C., J. Appl. Phys., 1950, 21, (437).

33. Ashby, M.F., Act. Metall., 1972, 20, July.

34. Rachinger, W.A., J. Inst. Met., 1952-53, 33, (81).

35. Martin, J.A. et al., Trans. AIME, 1957, 78, (209)

36. Rosenhain, W. et al., J. Inst. Metals, 1913, 10, (119).

37. Hanson and Wheeler., J. Inst. Metals, 1931, 45, (229).

38. McLean, D., J. Inst. Metals, 1951-52, 80, (507).

39. McLean, D., J. Inst. Metals, 1952-53, 81, (293).

40. McLean. D., J. Inst. Metals., 1952, 82, (507).

41. McLean, D. et al, J. Inst. Metals, 1956-57, 83, (1).

42. McLean, D., "Grain Boundaries in Metals", Oxford Univ. Press., 1957.

43. McLean, D. etal, J. Inst. Metals, 1956-57, 85, (41).

44. McLean, D., J. Inst. Metals, 1957, 85, (468).

45. Conrad, H., "Mechanical Behaviour of Materials at elevated temperature", McGraw Hill, 1961.

46. Siegfried, W., J. Appl. Mech., 1943, December, (A-202).

47. Chang, H.C. et al, Trans. AIME, 1952, 194, (619).

48. Chang, H.C. et al, Trans. AIME, 1953, 197, (1175).

49. Couling, S.L. et al, Trans. AIME, 1957, 209, (1253).

50. Harper, J.G. et al, Act. Metall., 1958, 6, (509).

51. Bruner, H. et al, J. Inst. Metals, 1956-57, 85, (77).

52. Gifkins, R.C., N.S.F. Swampscott conf. on fracture, 1959, April, (579).

53. Rachinger, W.A., Act. Metall., 1959, 7, (374).

54. Ke, T.S., Phys. Rev., 1947, 71, (533).

55. Ke, T.S., Phys. Rev., 1947, 72, (41).

56. Ke, T.S., Phys. Rev., 1948, 73, (267).

57. Ke, T.S., Metals Tech., 1948, TPNO 2370.

58. Brophy, G.R. et al, Trans. ASM, 1942, 30, (115).

59. Lubahn et al, Trans. AIMME, 1949, 180, (139).

60. Guarneiri, G.J., ASTM Spec. Tech. Publ., 165, 1954, June

61. Shepard, L.A. et al, WADC Tech. Rep. 53-236, ASTIA Document AD 23715, May-June 1954.

62. Daniels, N.H.G. et al, WADC Tech. Rep. 530336, ASTIA Document AD 102400, 1956, May.

63. Sherby, O.D. et al, Proc. Amer. Soc. Test. Mater. 1957, (56).

64. Popov, E.P., Journal of Appl. Mech., 1947, June (A-135)

65. Davenport, C.C., Journal of Appl. Mech., 1938, June.

66. Roberts, I., Proc. ASTM, 1951, 51, (811).

67. Woodford, D.A., Trans. of the ASME, 1976, Jan., (2).

68. Carslaw, H.S. and Jaegar, J.C., "Conduction of heat in solids", 2nd Ed., Oxford Univ. Press, 1959.

69. Aparci, V.S., "Conduction Heat Transfer", Addison-Wesley, Reading, Mass., 1966.

70. Croft, D.R. and Lilley, D.G., "Heat Transfer Calculations using Finite Difference Equations", Applied Science Publ., London, 1977,

71. Dusinberre, G.H., "Heat Transfer Calculations by Finite Differences", International, Scranton, Pa. 1961.

72. Adams, J.A. and Rogers, D.F., "Computer Aided Heat Transfer Analysis", McGraw Hill, New York, 1973.

73. Milne, W.E., "Numerical Solution of Differential Equations", John Wiley and Sons, New York, 1953.

74. McAdams, W.H., "Heat Transmission", 2nd Edition, McGraw Hill, New York, 1954.

75. Fletcher A.J. and Price, R.F., Metals Society, 1980, May, (203).

76. Atkins, M. et al., B.S.C. Internal Report, PGM/6757/-/73/A, 1973.

77. Johns, D.J., "Thermal Stress Analysis", Pergamon Press, London, 1965.

78. Boley, B.A. and Weiner, J., "Theory of Thermal Stresses", John Wiley and Sons Ltd., New York, 1960.

79. Manson, S.S., "Thermal Stress and Low Cycle Fatigue", McGraw Hill, New York, 1966.

80. Timoshenko, S.P. and Goodier, J.N.,,"Theory of Elasticity", 3rd Edition, McGraw Hill, New York, 1970.

81. Boley, B.A. J. Aeronautical Science, 1956, Jan, (67).

82. Landau, H.G. et al, J. Appl. Mech., 1960, 27.

83. Atkins, M. et al, B.S.C. Report, PTM/6622/-/72/A, 1972.

84. Toshioka, Y. et al, Trans. I.S.I. Japan, 1972, 12, (6).

85. Fletcher, A.J., Metals Technology, 1977, 6, (307).

86. Rockey, K.C., Evan, H.R., Griffiths, D.W., Nethercot, D.A., "The Finite Element Method", Crosby, Lockwood Staples, London, 1975.

87. Zeinkiewiez, O.C., The Finite Element Method in Engineering Science", McGraw Hill, New York, 1971.

88. Desai, C.S. and Abel, J.F., "Introduction to the Finite Element Method", Van Nostrand, Princeton N.J.

89. Martin, H.C. and Carey, G.F., "Introduction to Finite Element Analysis", McGraw Hill, New York, 1973.

90. Norrie, D.H. and DeVries, G., "An Introduction to Finite Element Analysis", Academic Press, New York, 1978.

91. Toshioka, Y., J.I.S.I. Japan, 1976, 11, 13, (1756).

92. Inoue, T. and Tanaka, K., Int. J. Mech. Sci., 1975, 17, (361).

93. Inoue, T. et al, Trans. ISIJ, 1978, 18, (11).

94. Fujio, H. et al, Bull. JSME, 1977, 20, 146, (1050).

95. Fujio, H. et al, Bull. JSME, 1977, 20, 150, (1655).

96. Archambault, P. et al, Mat. Sci. Engg., 1980, 43, (1).

97. Denis et al, Trans. I.S.I.J., 1982, 22, 7, (504).

98. Greenwood, G.W., Johnson, R.M., Proc. Roy. Soc., 1965, 283A, (403).

99. Fletcher, A.J. and Price, R.F., Metals Technology, 1981, Nov. (427).

100. Price, R.F., Ph.D. Thesis, Sheffield City Polytechnic, 1980.

101. Mendelson, A. et al, Journal of Basic Engg., 1959, Dec. (585).

102. Cuicas, H., M.Sc. Dissertation, Sheffield City Polytechnic, 1979.

103. Bush, R.H. et al, Acta Metall., 1964, 12, (102).

104. Sauveur, A., Iron Age, 1924, 113, (581).

105. Porter, L.F. and Rosenthal, P.G., Acta Metall., 1959, 7.

106. Wasserman, G. and Sattler, H.P., J. Less Com. Met., 1972, 28, (119).

107. Bolling, G.F. and Richman, R.H., Acta Metall., 1970, 18, June, (673).

108. Tamura, I., Metal Science, 1982, 16, May, (245).

109. Beck, G. et al., Res. Mechanica Letters, 1981, 1, (207).

110. Beck, G. et al, Internal Stress Conference, Deutsche Gesellschaft für Metallkunde, 14th-16th April, 1983, Karlsruhe, Federal Republic Germany.

111. Desalos et al, I.R.S.I.D., Report no. RE 902, 1982, May.

112. Fletcher, A.J. Private communication.

113. British Standards 3500.

114. Atkins, M., Andrews, K.W., Russell, J.E., British Steel Corporation, Internal report, 1973.

115. Sharp, K.W.B., "Practical Engineering Metrology", Pitman Press, 1970.

116. Wakabayashi, M. et al, Bull. Jap. Soc. Prec. Engg., 1979, 13, (2).

117. Peters, J. et al, Proc. Agard. Conf. Ad. Fabr. Processes, Sept. 78/March 79, Florence, Italy.

118. Nowikcwski, L.J. et al, Automotive Engineer, 1961, Aug.

119. American Soc. for Metals, Metals Handbook, 9th edition, Vol. 4, 1981, (85).

120. Woolman, J. and Mottram, R.A., "The Mechanical and Physical Properties of B.S. En Steels", London, Pergamon Press, 1966.

Table 1: Thermal Property Data Used by Toshioka[91].

Heat Transfer coefficient, h (W/m^2C)	Water	°C	0		100	110	300	500	1000
		h	628		837	8793	8793	6280	209
	Oil	°C	0		200	750	1000		
		h	209		209	1884	1884		
Thermal Conductivity, ($W/m^2°C$)	Ferrite Bainite) Martensite)	°C	0		200	400	800	1000	
			52.3		50.2	41.87	(27.2)	(14.7)	
	Austenite	°C	0	1000					
			14.65	27.2					
Specific Heat, Cp ($J/kg°C$)	Ferrite Bainite) Martensite)	°C	0		420	700	800	1000	
		Cp	460		628	837	1005	1885	
	Austenite	°C	0		500	1000			
		Cp	502		628	649			

Latent heat of Trans-formation (J/kg)		
Austenite + Ferrite:	75,366
Austenite + Bainite:	75,366
Austenite + Martensite:	83,740

188.

Table 2: Physical Data used by Toshioka[91] for Displacement and Stress Calculation.

Young's modulus, E $(N/mm^2) \times 10^5$	$^{\circ}C$	0	400	550	700	1000
	E	2.107	1.842	1.646	1.372	0.588

Yield Strength (N/mm^2)	$^{\circ}C$	0	550	800	1000
	Austenite	196	98	49	29.4
	Ferrite	294	98	29.4	
	Bainite	392	343		
	Martensite	490	392		

Strain hardening coefficient $(d\sigma/d\varepsilon)$	Austenite	0.02 x E
	Ferrite	0.08 x E
	Bainite	0.5 x E
	Martensite	0.6 x E

Linear Thermal Expansion Coeff. $\alpha_{ex}(^{\circ}C^{-1})$	Austenite, $\alpha_{ex}=11.9 \times 10^{-6}+8.14 \times 10^{-9}\theta$ Ferrite, $\alpha_{ex}=16.5 \times 10^{-6}+7.06 \times 10^{-9}\theta$

Linear Transformation Expansion, $\Delta\varepsilon$ (mm/mm)	$\Delta\varepsilon = 7.15 \times 10^{-3} - 0.460 \times 10^{-5}\theta_f + 0.540 \times 10^{-4}\theta_f^2$ (θ_f=Temperature of transformation finish

Poisson's ratio	0.3

Table 3: Comparison of creep rates from creep equation (X) with those calculated from amount of stress relaxation (Y).

$\theta \, (^{\circ}C)$	$X \quad s^{-1}$	$Y \quad s^{-1}$
850	2.3×10^{-4}	2.25×10^{-4}
750	1.68×10^{-4}	1.66×10^{-4}
650	1.18×10^{-4}	1.17×10^{-4}
550	7.87×10^{-5}	7.81×10^{-5}
450	4.95×10^{-5}	4.92×10^{-5}
350	2.82×10^{-5}	2.81×10^{-5}
250	1.41×10^{-5}	1.41×10^{-5}
150	4.67×10^{-5}	4.67×10^{-6}

N.B. The following values of stress and time were used in the equations:

$$\sigma^{0} \; = \; 100 MPa$$
$$t \; = \; 0.1 \; s$$

Table 4: Mechanical Property data used in the thermal
stress calculations.

	Property	Symbol	(°C)	Relationship used
(a)	Austenite flow stress(100)	(σ_f)	> 850 850 → 400 < 400	40 MPa 257.2-0.2556 θ MPa 155 MPa
(b)	Martensite flow stress	$(\sigma_f)_\gamma$	90	1600 MPa
(c)	Flow stress below M_S(85)	σ_f	300 → 90	$V(\sigma_f)_\alpha + V(\sigma_f)_\gamma$ (V_α and V_γ as per figure 43)
(d)	Austenite strain(100) hardening coefficient	W_1	> 600	8950-7.75 θ MPa
		W_1	< 600	4300 MPa
		W_2	> 600	10600-11.5 θ MPa
		W_2	< 600	3700 MPa
(e)	$\dfrac{E}{1-\nu}$(99)		850 → 90	$2.935 \times 10^5 - 141.77$ θ MPa
(f)	Dilatometer data		850 → 90	see equations 4.3.2
(g)	Reduction in flow stress below M_S to simulate transformation plasticity	σ_f	300 → 265 265 → 90	0.625θ -136.67 MPa as per (c)
(h)	Strain hardening during transformation plasticity	W	300 → 265	46,860 MPa
(i)	Transformation plasticity as additional strain			see equations 4.4.2

Table 5: Variation of surface heat transfer coefficient with surface temperature.

Quenchant	θ (^{o}C)	h ($W/m^{2o}C$)
a) Oil (RDN175)[75]	> 800 800 → 542 542 → 470 470 → 434.4 434.4 → 308.3 < 308.3	842 $1.191\theta -111$ $11422-20.08\theta$ 1990 $11.34\theta -2937$ $221+1.097\theta$
b) Water[75]	> 826.8 826.8 → 381 381 → 275 275 → 93.75 < 93.75	1470 $23800-27.008\theta$ $3504+26.236\theta$ $51.584\theta -3466$ 1370
c) Salt bath at 400°C (Nitrate-Nitrite of eutectic composition) followed by Oil quench at 20°C[102]	850 → 530 530 → 430 430 → 330 330 → 90	$14.463\theta -6660.043$ $8.05\theta -3261.5$ $1242.75-2.425\theta$ $0.125\theta +401.25$

192.

Table 6: Comparison of percentage rate of stress relaxation as calculated by method 1 and method 2 (figure 42).

θ ($^{\circ}$C)	Method 1*, %	Method 2[+], %
850	40	40
650	24	3.59
450	11.3	1.6
350	6.8	1.2
250	3.6	0.7
150	1.3	0.4
100	0.5	0.2

* Δt = 0.1 s equation 4.2.6

+ t^{n+1} = 0.1 s, 13.6s, 20s at temperatures of 850°C, 650°C and 450°C, equation 4.2.8

Table 7: Variation of thermal diffusivity and thermal conductivity with temperature[100,114].

Material	$\theta(^{\circ}C)$	Thermal diffusivity α_{td} (mm^2/s)
835M30	> 355	$\alpha_{td}=4.0698+1.7802 \times 10^{-3}\theta$
	$355 \to 286$	$\alpha_{td}=0.03762\theta - 8.668$
	$286 \to 265$	$\alpha_{td}=2.1$
	$265 \to 154$	$\alpha_{td}=11.769-0.03644\theta$
	$154 \to 20$	$\alpha_{td}=7.357-0.00722\theta$

Material	$\theta(^{\circ}C)$	Thermal conductivity $(W/m^{\circ}C)$
835M30	> 328	$\lambda = 20.1+0.00829\theta$
	$328 \to 223$	$\lambda = 33.152-0.03143\theta$
	$223 \to 20$	$\lambda = 25.521+0.002726\theta$

N.B. From the above data, the average values between 850°C and 100°C were used in the calculations.

viz: $\alpha_{td} = 0.5279 \times 10^{-3} mm^2/s$

$\lambda = 25.2 \ W/m^{\circ}C$

Table 8: Key to individual calculations of thermal stress and strain.

Calculation number	Description	Relevant figure numbers
CD1	Water quench without viscous flow	51,54,55
CD2	Oil quench without viscous flow	56,60,61
CD3	Martemper without viscous flow	62.66,67
CD4	Water quench with viscous flow by method 1	52,54,55
CD5	Water quench with viscous flow by method 2	53,54,55
CD6	Oil quench with viscous flow by method 1	57,60,61
CD7	Oil quench with viscous flow by method 2	58,60,61
CD8	Oil quench with viscous flow by method 3	59,60,61
CD9	Martemper with viscous flow by method 1	63,66,67
CD10	Martemper with viscous flow by method 2	64,66,67
CD11	Martemper with viscous flow by method 3	65,66,67
CD12	Water quench, flow stress reduced below M_s, with viscous flow by method 2	68,70,71
CD13	Water quench, flow stress reduced below M_s, with viscous flow by method 1	69,70,71
CD14	Oil quench, flow stress reduced below M_s, with viscous flow by method 2	72,74,75
CD15	Oil quench, flow stress reduced below M_s, with viscous flow by method 1	73,74,75
CD16	Water quench, transformation plasticity as additional strain, with viscous flow by method 2	76,78,79
CD17	Water quench, transformation plasticity as additional strain, with viscous flow by method 1	77,78,79

Calculation number	Description	Relevant figure numbers
CD18	Oil quench, transformation plasticity as additional strain, with viscous flow by method 2	80,82,83
CD19	Oil quench, transformation plasticity as additional strain, with viscous flow by method 1	81,82,83

Method 1   The viscous flow rate obtained from the initial slope of the stress relaxation/creep curve. Represents high viscous flow (see section 4.2.1)

Method 2   The viscous flow rate reduces with time and temperature and a steady stage condition maintained after 20 seconds (see section 4.2.1)

Method 3   The viscous flow rate reduces with time and temperature throughout the quench (see section 4.2.1)

Further abbreviations used in figure caption.

W = water, O = oil, M = Martempering, NVF = No Viscous Flow

VF1 = Viscous flow by method 1, VF2 = Viscous flow by method 2,

VF3 = Viscous flow by method 3, FSR = Flow stress reduced

below M_s, TPAS = Transformation plasticity as additional

strain.

Table 9:   Experimental results of distortion of 15mm plate
of 835M30 after oil quench.

Measurement location	Change in length produced by quench (Δ Y)%	Measurement location	Change in length produced by quench (Δ Y)%
1A	0.0683	1F	0.0410
2A	0.0816	2F	0.0333
3A	0.0993	3F	0.0515
4A	0.0989	4F	0.0573
5A	0.1236	5F	0.0934
1B	0.0771	1G	0.0363
2B	0.0657	2G	0.0404
3B	0.0824	3G	0.0644
4B	0.0787	4G	0.0807
5B	0.1053	5G	0.0898
1C	0.0686	1H	0.0140
2C	0.1520	2H	0.0496
3C	-	3H	0.0478
4C	0.1109	4H	0.0663
5C	0.0857	5H	0.1000
1D	0.0747	1J	-0.0103
2D	0.0719	2J	0.0204
3D	0.0839	3J	0.0345
4D	0.0751	4J	0.0485
5D	0.0762	5J	0.0724
1E	0.0754	1K	-0.0307
2E	0.0733	2K	-0.0002
3E	0.0869	3K	0.0130
4E	0.0857	4K	0.0393
5E	0.0980	5K	0.1230
Mean value at position 1	0.041		
Mean value at position 2	0.0588		

Table 9 (continued)

Measurement location	Change in length produced by quench (ΔY)%	Measurement location	Change in length produced by quench (ΔY)%
Mean value at position 3	0.626	Average change in plate width calculated from change in thickness of plate (free from edge effect).	0.071 (calculated from 0.239% change in thickness.
Mean value at position 4	0.0740		
Mean value at position 5	0.0967		

198.

Table 10: Experimental results of distortion of 15mm plate of 835M30 after martempering treatment

Measurement location	Change in length produced by quench (Δ Y)%	Measurement location	Change in length produced by quench (Δ Y)%
1A	0.0346	1F	0.0302
2A	0.0613	2F	0.0359
3A	0.0748	3F	0.0445
4A	0.0737	4F	0.0542
5A	0.0787	5F	0.0538
1B	0.0372	1G	0.0262
2B	0.0493	2G	0.0384
3B	0.0738	3G	0.0460
4B	0.0706	4G	0.0537
5B	0.0737	5G	0.0486
1C	0.0421	1H	0.0191
2C	-	2H	0.0350
3C	-	3H	0.0537
4C	-	4H	0.0471
5C	0.069	5H	0.0495
1D	0.0556	1J	0.0247
2D	0.0648	2J	0.0349
3D	0.0732	3J	0.0494
4D	0.0711	4J	0.0532
5D	0.0721	5J	0.0494
1E	0.0605	1K	0.0234
2E	0.0588	2K	0.0341
3E	0.0739	3K	0.0493
4E	0.0710	4K	0.0520
5E	0.0745	5K	0.0456
Mean value at position 1	0.0354	Average change in plate width calculated from change in thickness of plate (free from edge effect)	0.053 (calculated from 0.275% change in thickness
Mean value at position 2	0.0458		
Mean value at position 3	0.0598		
Mean value at position 4	0.0607		
Mean value at position 5	0.0615		

TABLE 11: Properties of RDN 175 Quenching Oil[100].

Specific Gravity	0.861
Open Flash Point	192°C
Closed Flash Point	186°C
Pour Point	-12°C
Redwood Viscosity at 21°C	184 s
" " " 60°C	53 s
" " " 93°C	38 s
Kinematic Viscosity at 38°C	21.5 s
" " " 99°C	4.10 s
V.I.	99

TABLE 12: Properties of Cassel T.S.150 Nitrate-Nitrite salt.

Specific Gravity at 400°C	1.81
" " " 20°C (fused)	2.12
Solidification Temperature	145°C
Working Temperature Range	160-550°C

TABLE 13: Chemical Composition (wt%) of 835M30 steel.

C	Mn	Si	Ni	Cr	Mo	Fe
0.30	0.72	0.42	4.83	1.25	0.28	Balance

Table 14. Correction for edge effect[99].

Width of plate Y mm	Thickness of plate TH mm	Correction factor $\dfrac{Y}{Y-TH}$
120	20	1.2
120	15	1.14

$$\sigma_{actual} = \sigma_{measured} \times \frac{Y}{Y-TH}$$

FIGURE 1:   Schematic production of stresses in a
            quenched bar both with and without
            transformation during quenching.

    (a) Cooling curves at surface and centre.

    (b) Stresses generated with no plastic
         flow (broken line), and relaxation
         of stress due to plastic flow
         (solid line).

    (c) Stresses generated with plastic
         flow and phase transformation
         during the quench

         (After Andrews[7])

(a)

(b)

(c)

202.
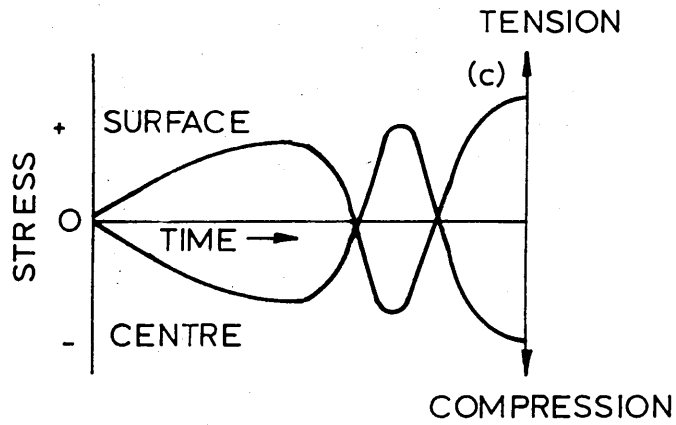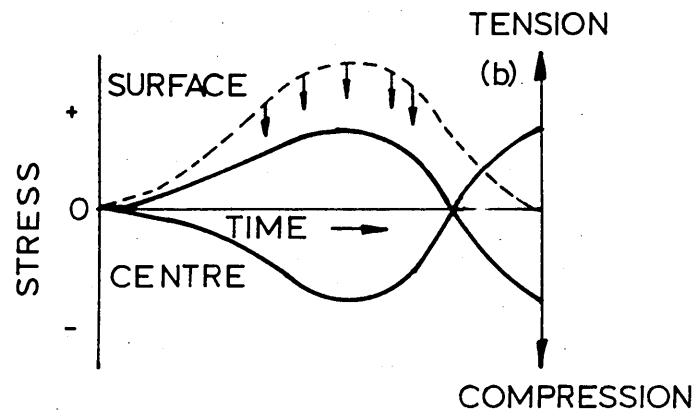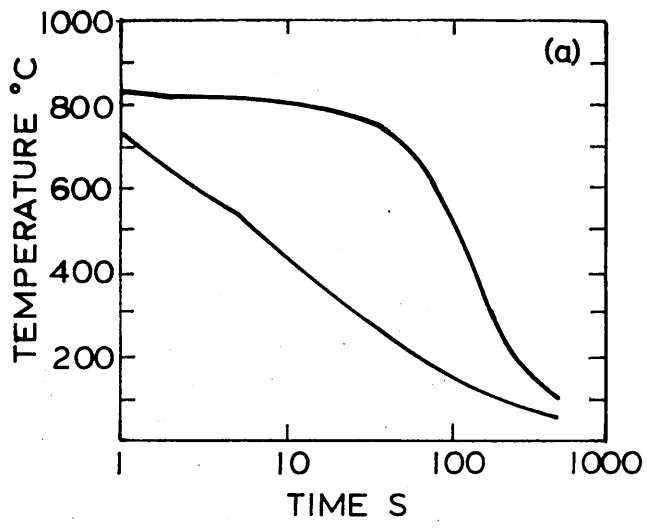
FIGURE 2:   Dilatometer curve for the
                 austenite ⟶ martensite
                 transformation in 835M30 steel.

                 (After Price[100])
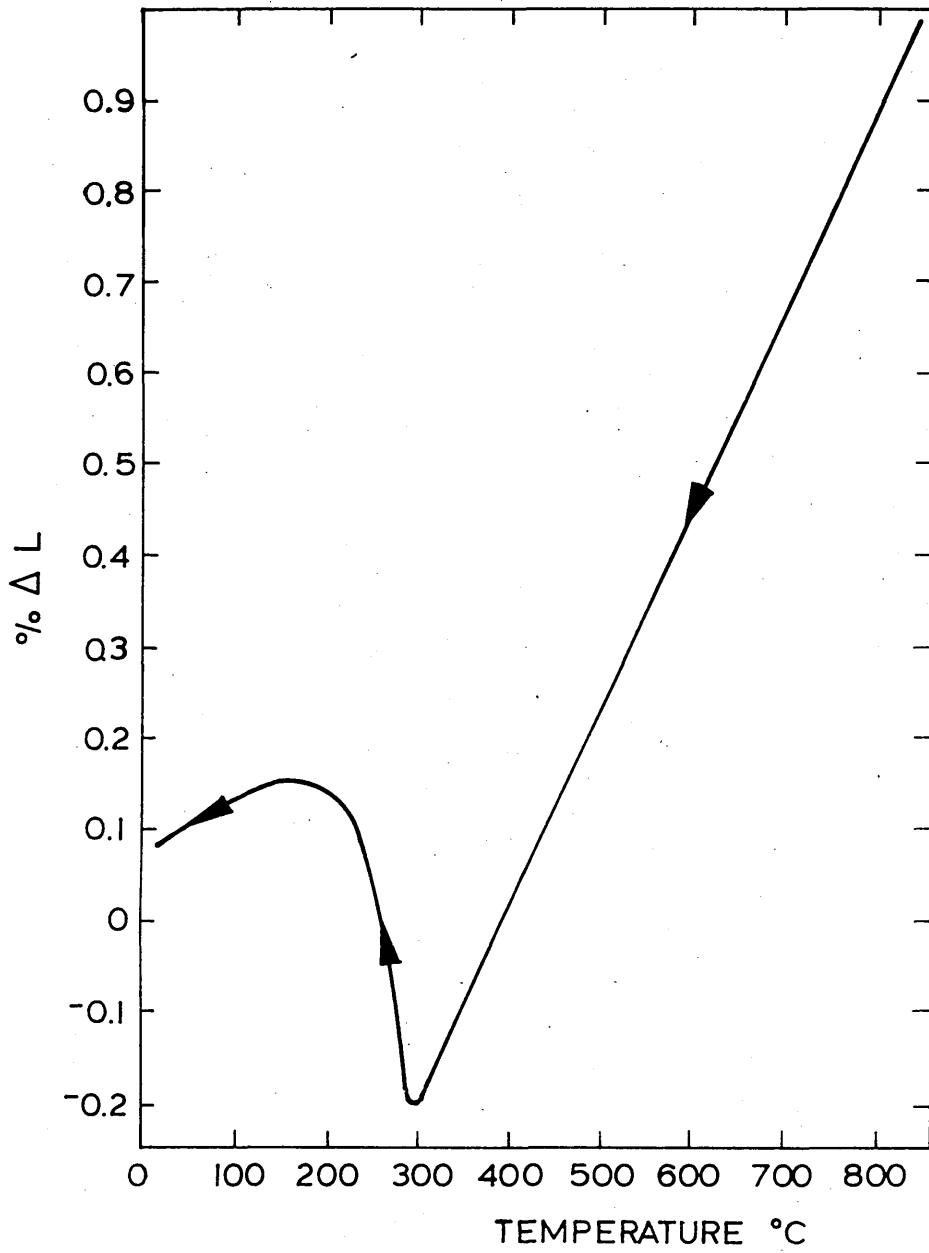
FIGURE 3:   A typical creep curve showing the
              different stages observed during
              a creep test.

FIGURE 4:   A typical stress relaxation curve
              showing a reduction in stress
              with time.

STRAIN

PRIMARY
SECONDARY
TERTIARY
FRACTURE

I

II

III

TRANSIENT

INITIAL INELASTIC STRAIN

STEADY STATE (MINIMUM RATE)

INITIAL ELASTIC STRAIN

TIME   hours

204.
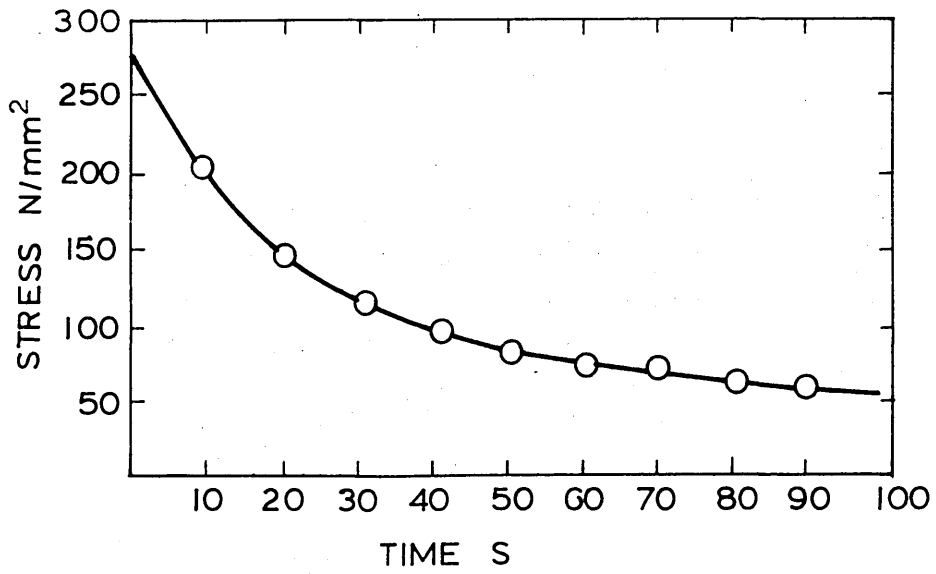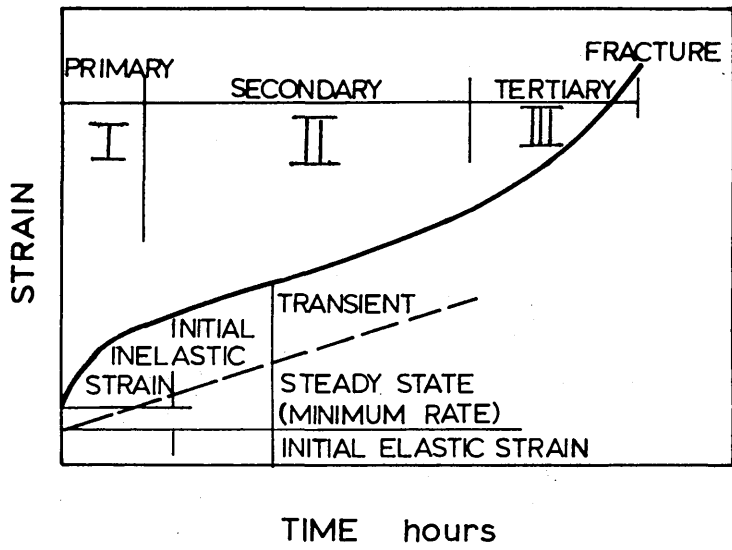
FIGURE 5:   Subgrain formation observed during
Creep.

(After Sherby[29])

FIGURE 6:   Ashby deformation map showing the
regions of temperature and stress
where different mechanisms of creep
are dominant.

(After Ashby[33])

theoretical shear stress

disl^n glide

disl^n creep

coble creep

naba rro creep

elastic regime

σ/G

T/Tm
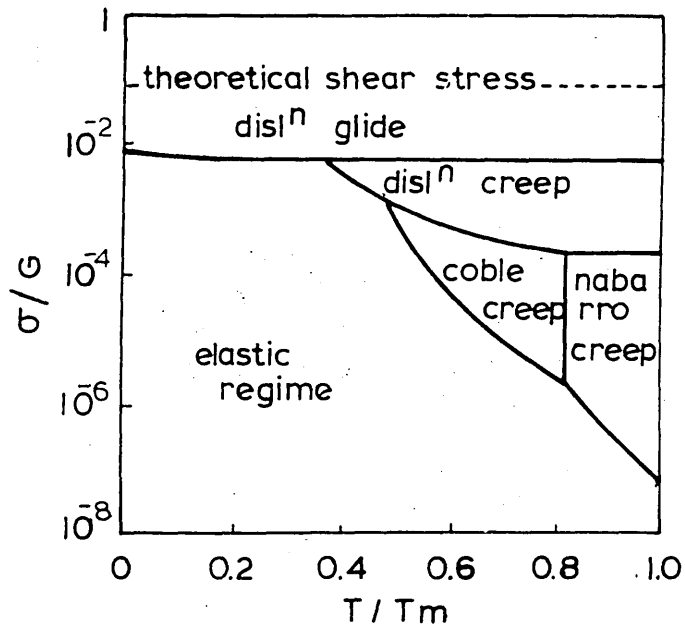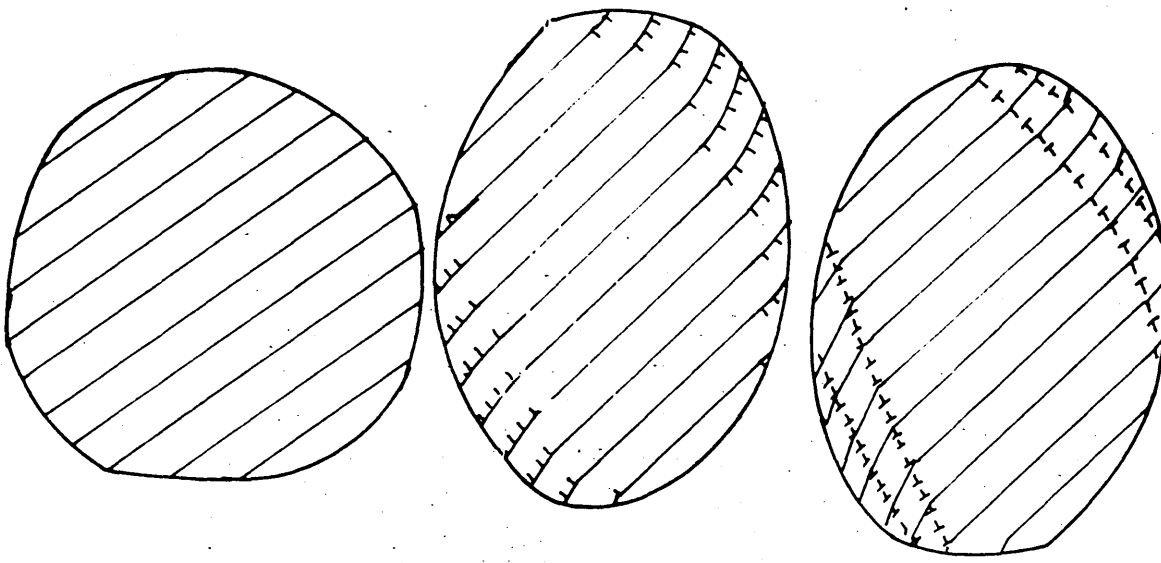
FIGURE 7:   Decrease in grain boundary strength
             with temperature.

             (After Siegfried[46])

FIGURE 8:   The ratio of grain boundary sliding
             to the total creep strain.

             (After McLean and Farmer[43])

FIGURE 9:   Total creep = visible slip + subgrain
             tilting + grain boundary shearing.

             (After McLean[38])
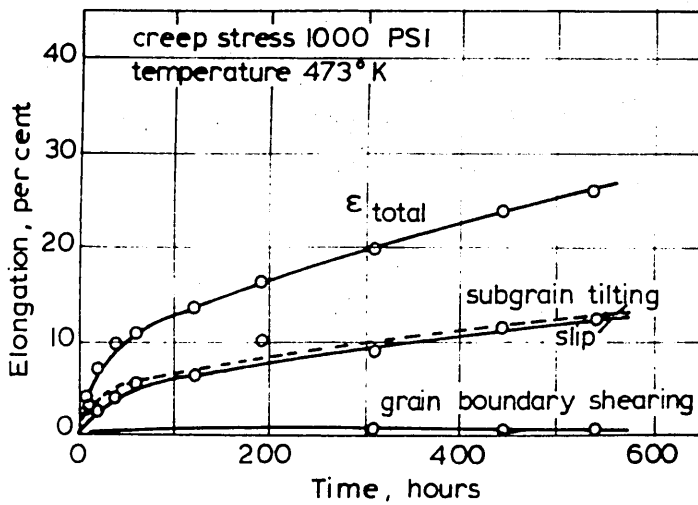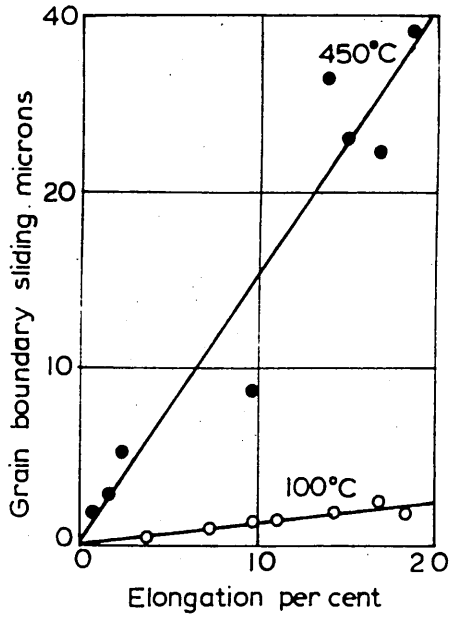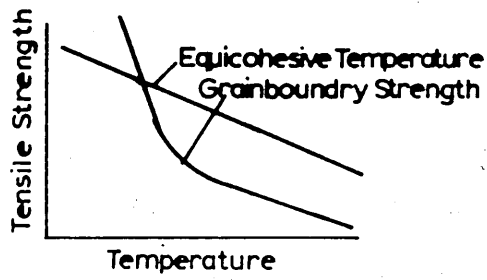
FIGURE 10:   The relationship between grain boundary
             displacement and time with various
             combinations of grain size and applied
             stress.

             A   4.5grains/mm: 1650psi,
             B   1.0grains/mm: 1650psi,
             C   9.2grains/mm: 1100psi,
             D   4.5grains/mm: 1100psi,
             E   4.5grains/mm: 750psi.

             (After McLean[39])

FIGURE 11:   Effect of time on grain boundary
             displacement (a) and total creep
             strain (b).

             (After McLean[41,44])
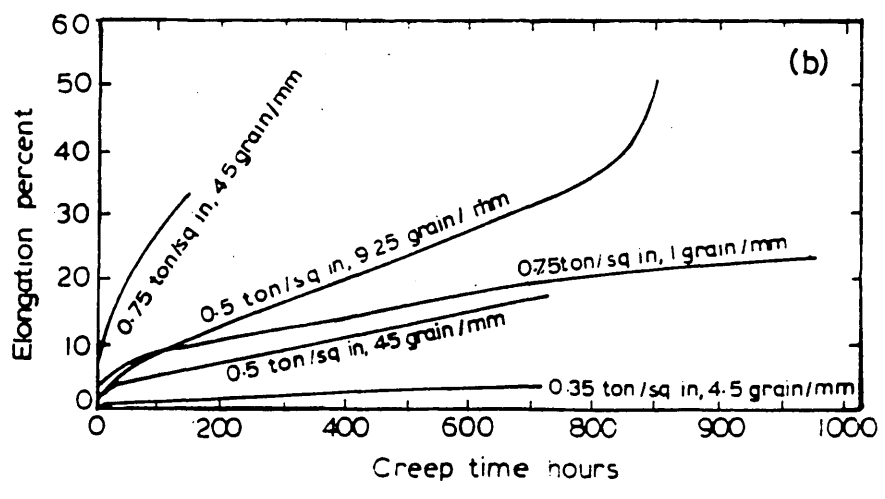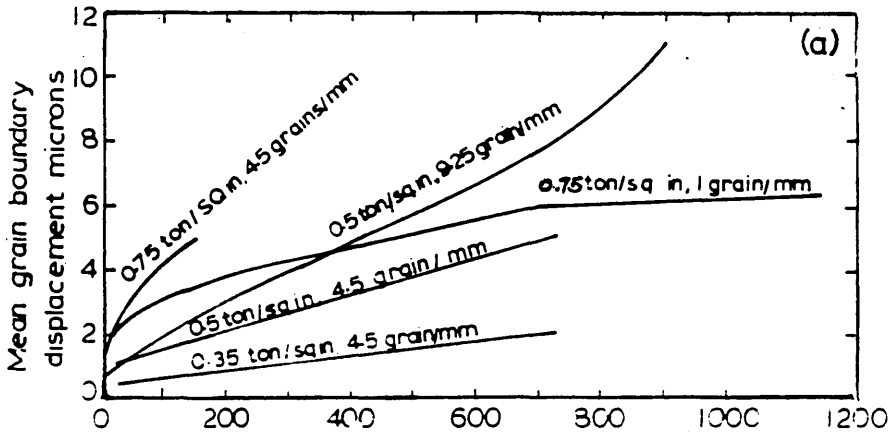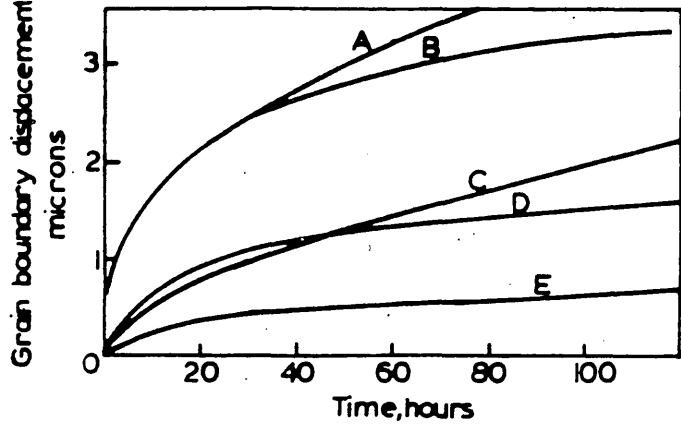
FIGURE 12:   Effect of varying load (a) and
temperature (b) on the creep rate
of high purity lead.

(After Lubahn et al[50])

208.

(a)

40,000psi 35,000psi

30,000 psi

25,000psi

20,000psi

Time, hour

Time-hardening rule

(b)

40,000psi 35,000psi

30,000 psi

25,000 psi

20,000 psi

Time, hour

Strain-hardening rule

209.
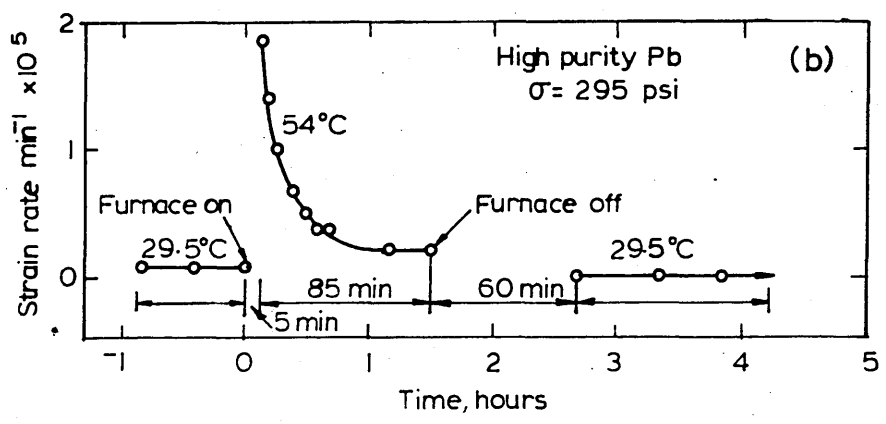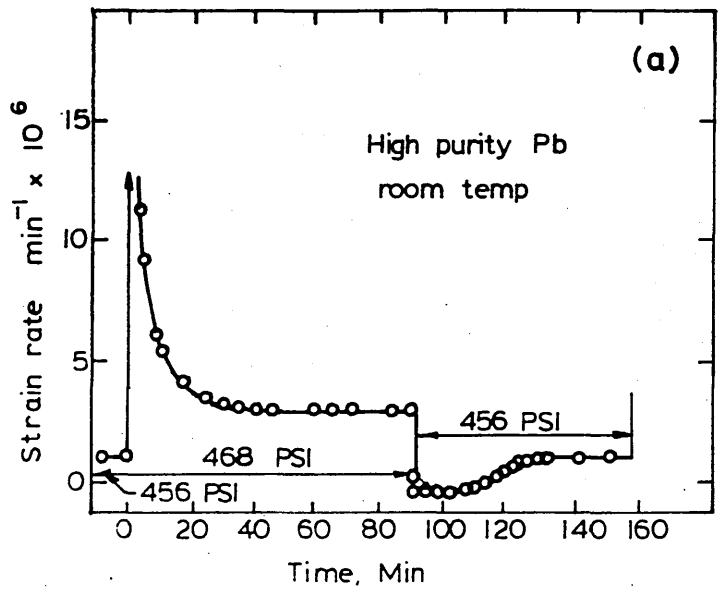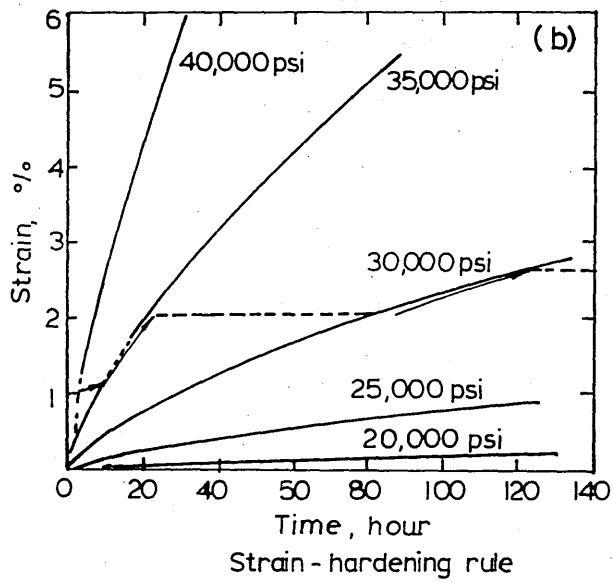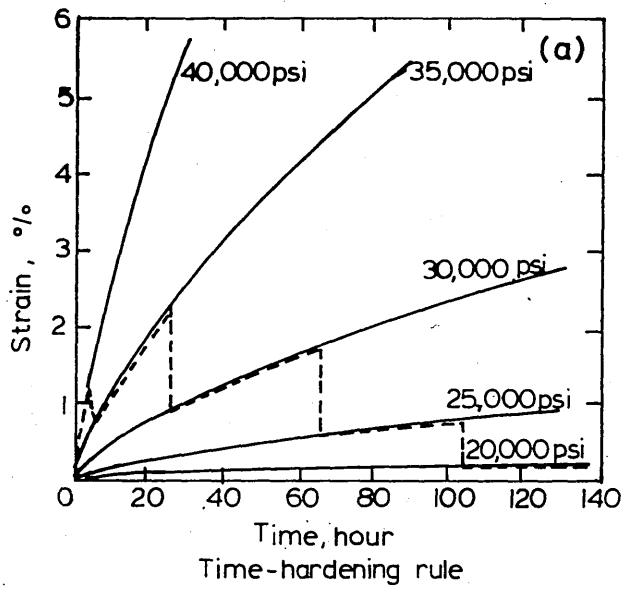
FIGURE 14:   The variation of the surface heat
transfer coefficient as a function
of temperature,

(a) Oil quench   (After Price[100])

(b) Water quench   (After Price[100])

(c) Martemper   (After Cuicas[102])

210.
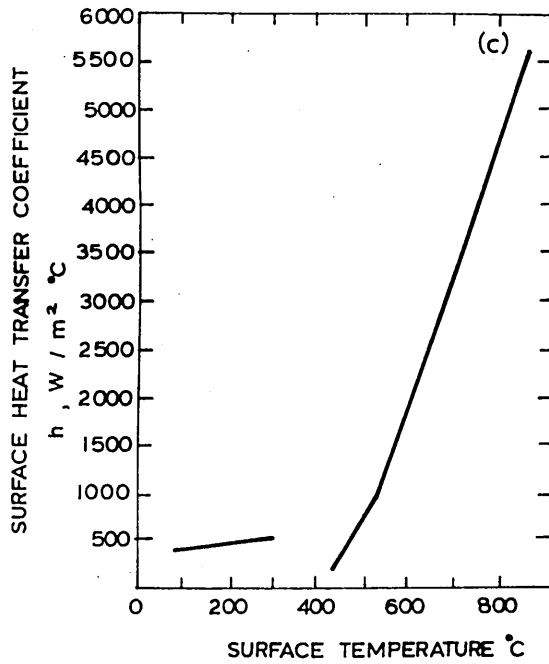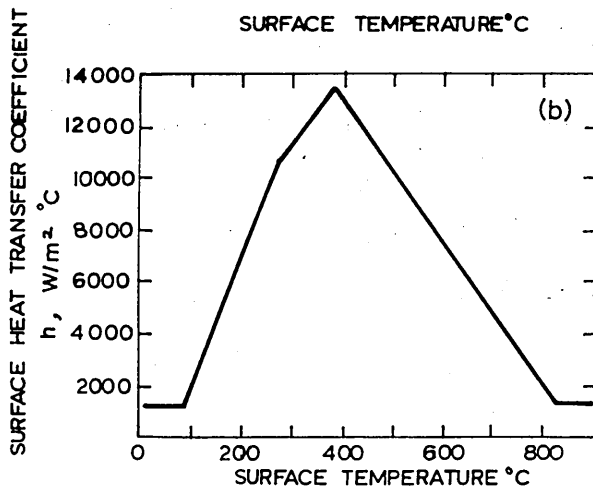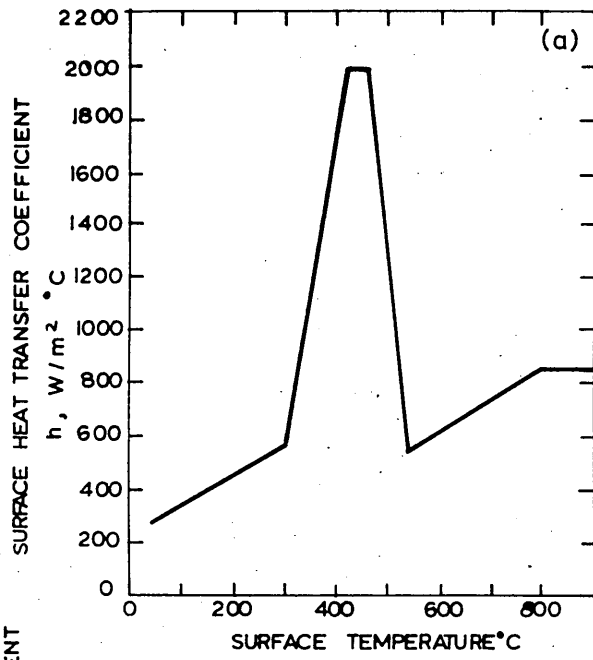
FIGURE 15:   The effect of temperature on the
               specific heat (a), thermal
               diffusivity (b) and thermal
               conductivity (c).

               (After Atkins et al[76])

FIGURE 16:   Comparison of calculated and
               experimentally determined distortions

               (After Toshioka[91])

211.
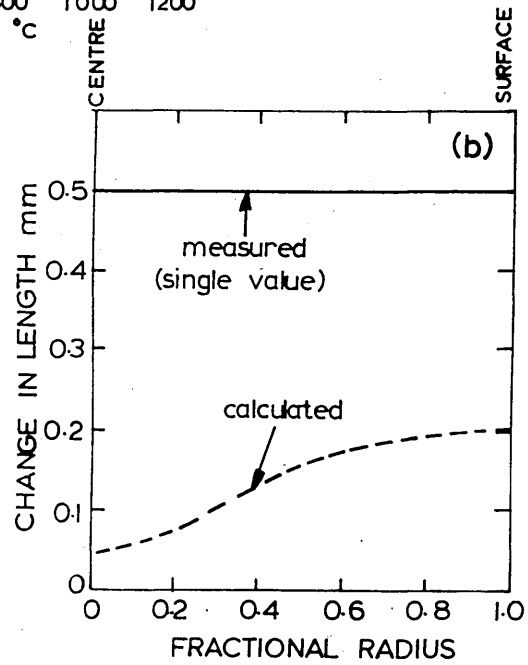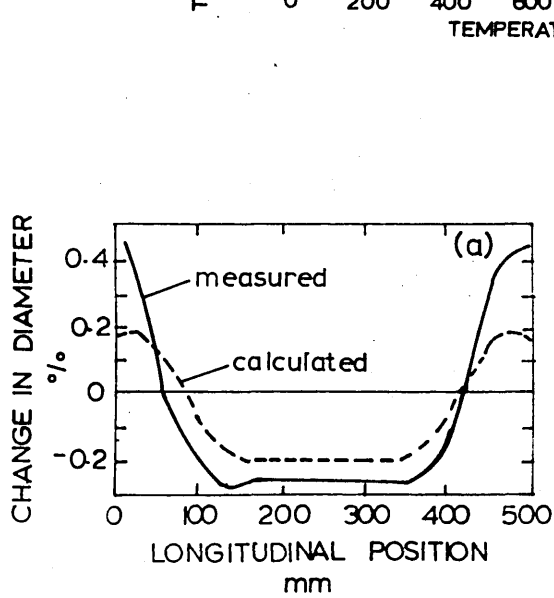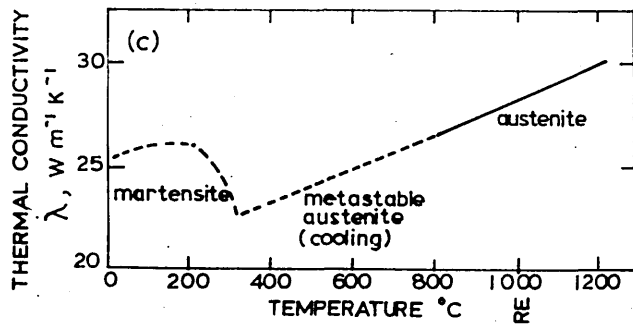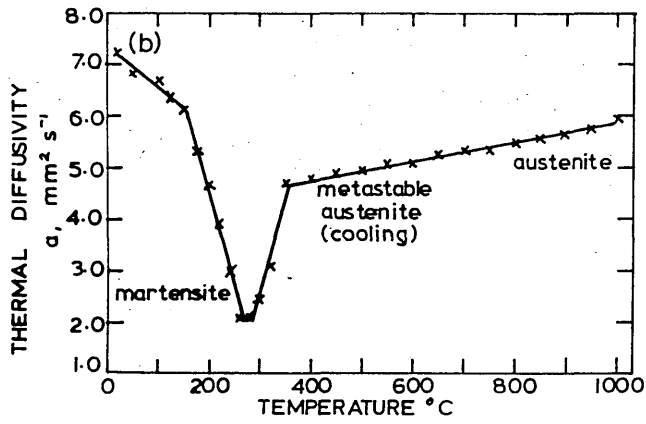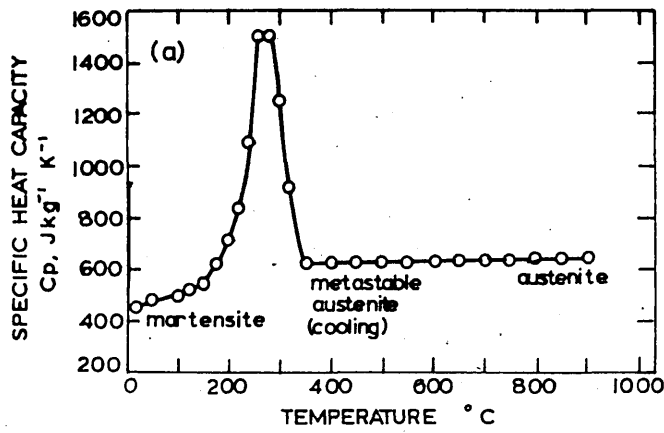
FIGURE 17:   Comparison of experimental and predicted
               residual stresses in 0.43%C steel
               cylinders quenched in water.

               (After Inoue and Tanaka[92])

FIGURE 18:   Reduction in residual stress levels
               after accounting for creep due to
               tempering of 12%Cr steel cylinders.

               (After Inoue et al[93])

212.
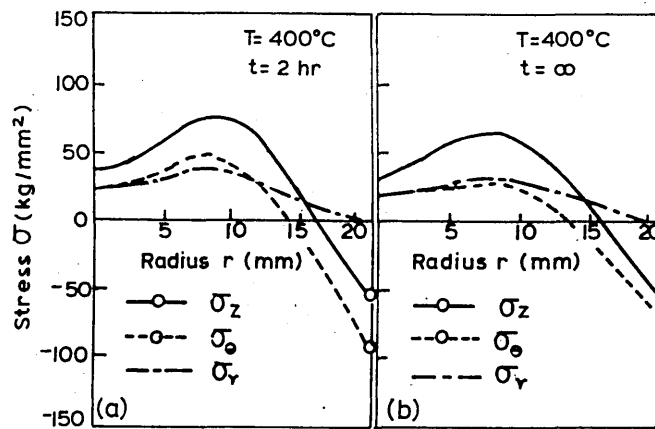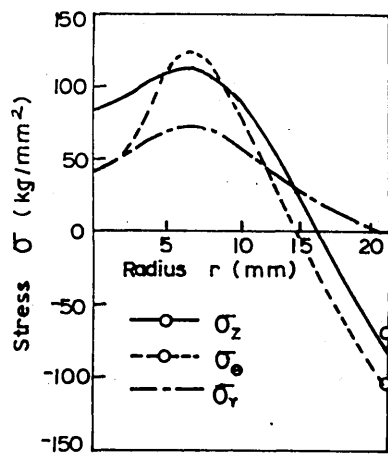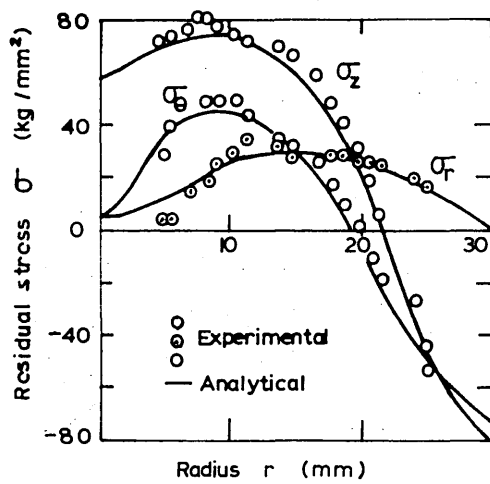
FIGURE 19:   Variation of length of dilatometer
               specimen with temperature.

               (a) Cooled to produce 0% martensite.
               (b) Cooled to produce 50% martensite.
               (c) Cooled to produce 100% martensite.

               (After Fujio et al[94])

FIGURE 20:   Variation of flow stress with temperature
               in specimens
               (a) Cooled to produce 0% martensite
               (b) Cooled to produce 50% martensite
               (c) Cooled to produce 100% martensite

               (After Fujio et al[94])

FIGURE 21:   Comparison of the calculated and
               experimental residual stress
               distribution in a 50mm diameter
               cylinder of a 0.45%C steel after quenching

               (After Fujio et al[94])

213.
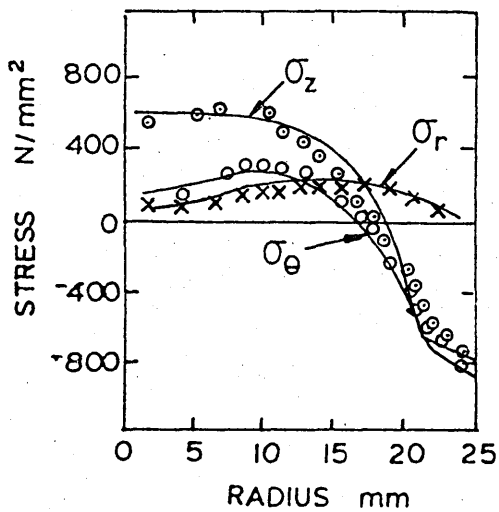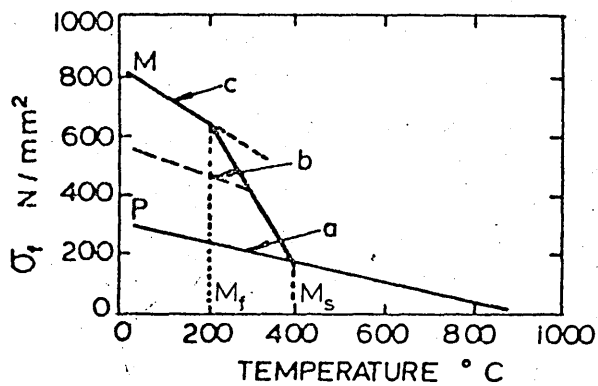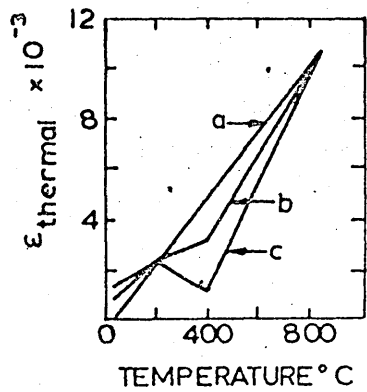
FIGURE 22:   The predicted and experimental distortion
               values of a gear tooth profile.

               (After Fujio et al[95])

FIGURE 23:   Diameter change of tip cylinder and
               change of gear tooth height before and
               after quenching.

               (After Fujio et al[95])

FIGURE 24:   Determination of optimum cooling rate
               in aluminium alloys

               (After Archambault et al[96])

214a.

Tooth profile
before quenching

Tooth profile after
quenching

● Measured values
by over pin method

○ Theoretical
values

before quenching-
after quenching-

Calculated

—— tooth height
---- diameter of tip cylinder

214.
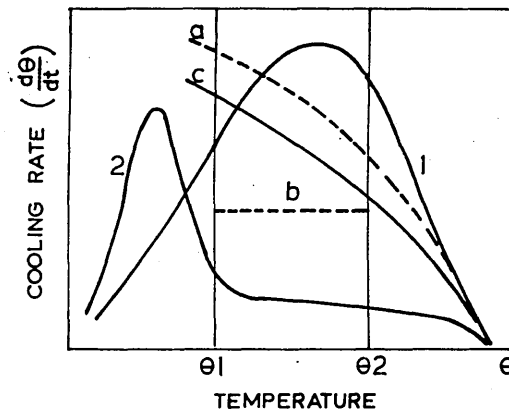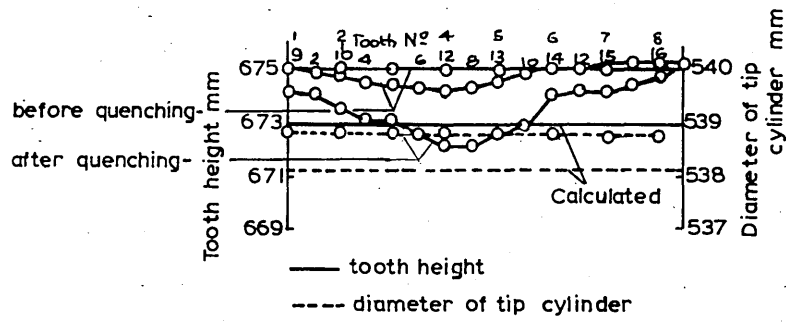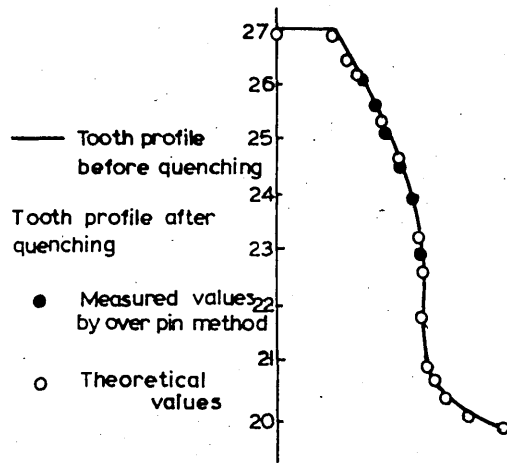
FIGURE 25:   Comparison between experimental and
              calculated residual stress distributions
              in a quenched plate of 835M30 steel.

      (a) Water quench

      (b) Oil quench

(After Fletcher and Price[99])

FIGURE 26:   Schematic illustration showing chemical
              free energy of austenite and martensite
              as a function of temperature.

(After Tamura[108])

(a)

(b)
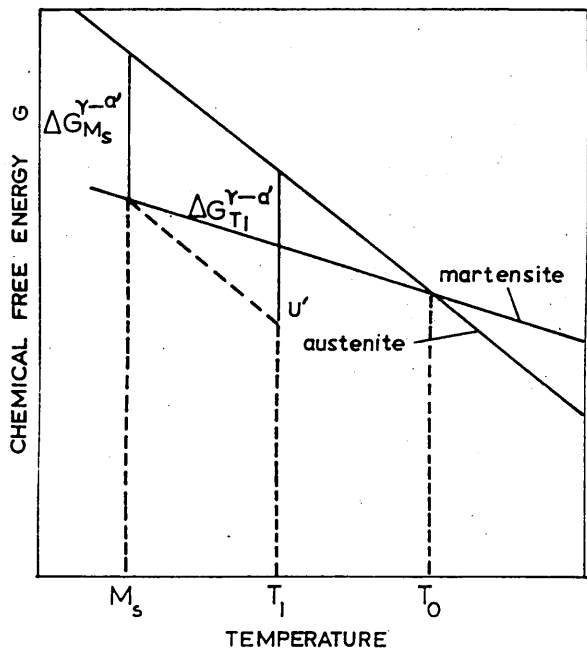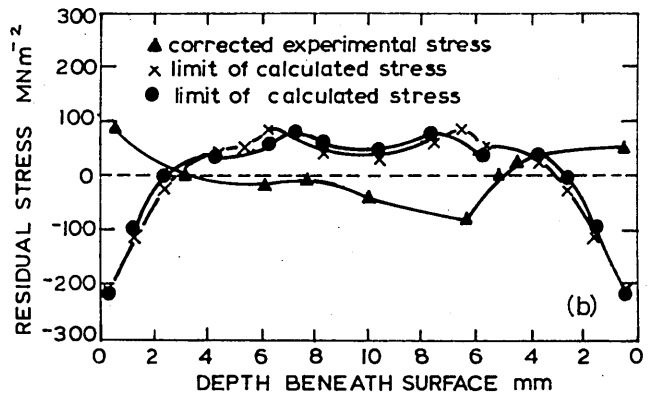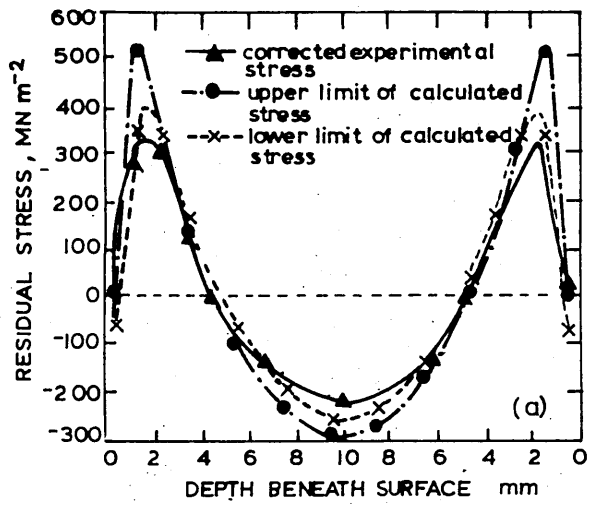
FIGURE 27:   Variation of strain rate with time
during water quenching of 40mm thick
plate.

(After Fletcher and Price[99])

FIGURE 28:   Furnace callibration showing relationship
between furnace temperature and control
position.

216a.

216.
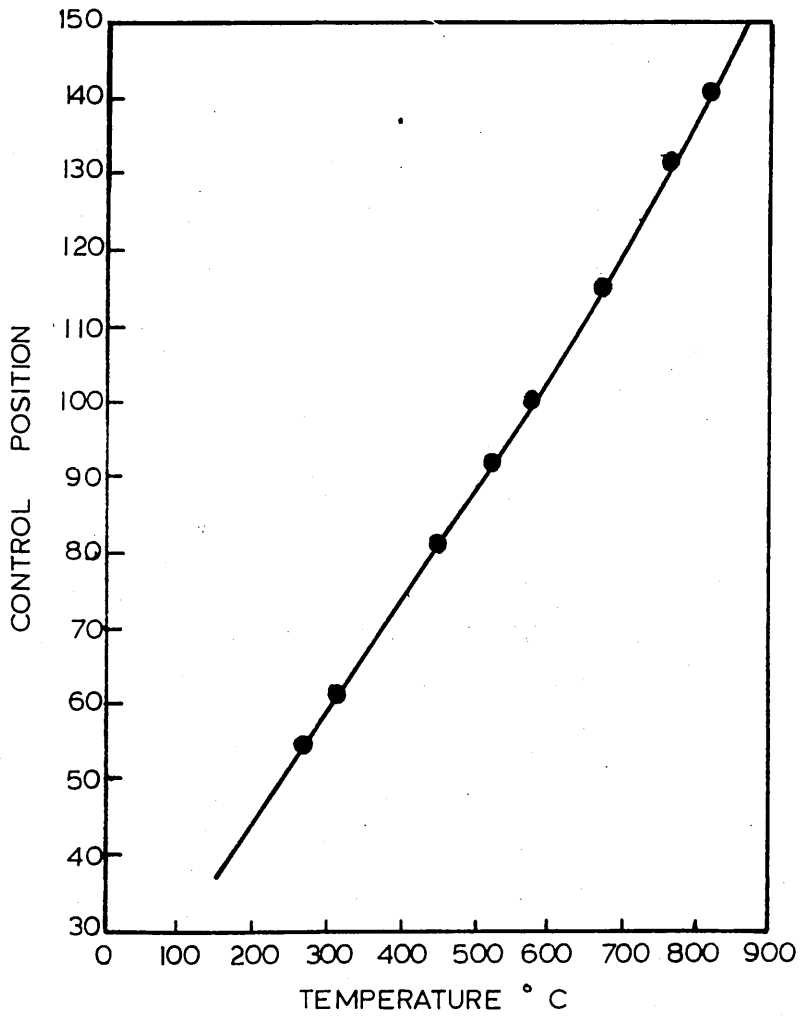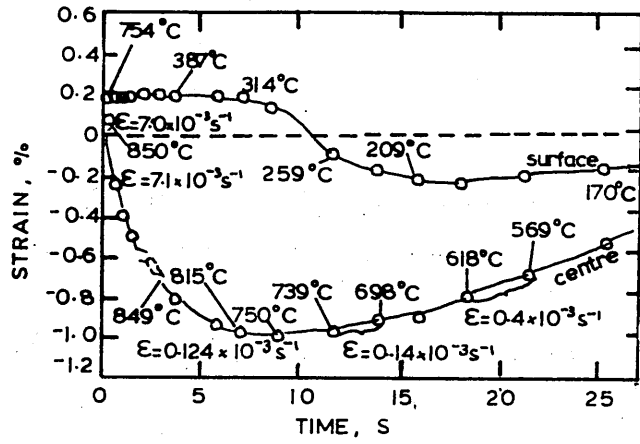
FIGURE 29:   Dimensions of the cylindrical test
              specimen used for the stress
              relaxation and creep experiments.

FIGURE 30:   Time-temperature transformation diagram
              for 835M30 steel.

              (After Woolman and Mottram[118])

217.

218.
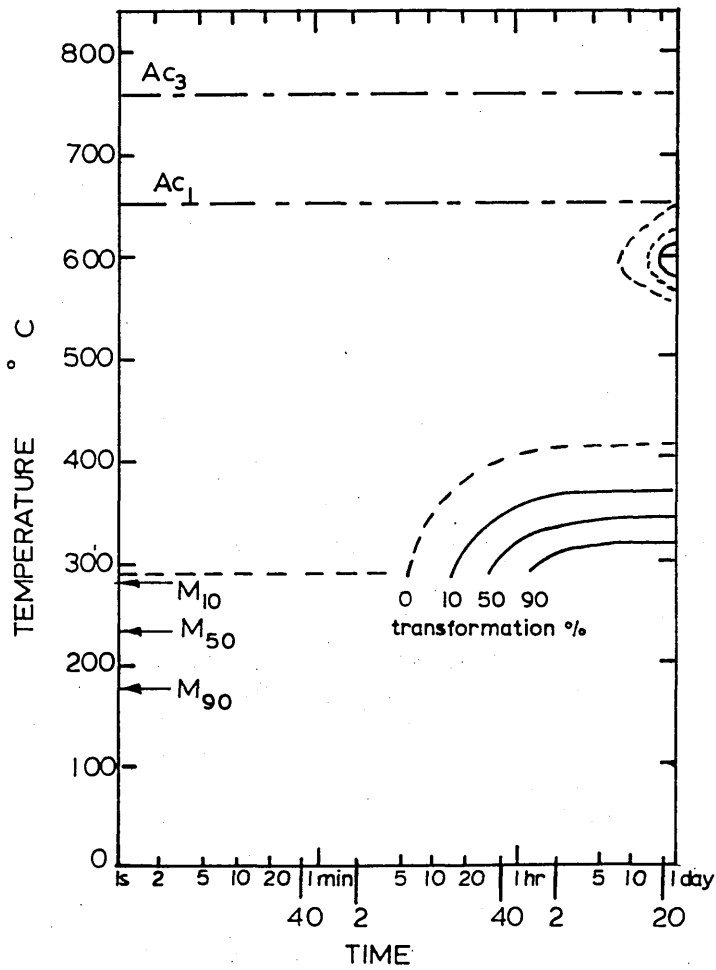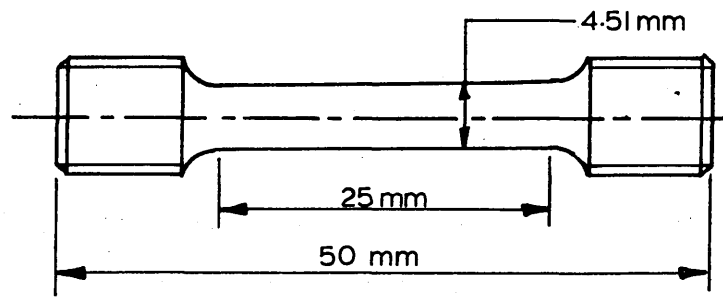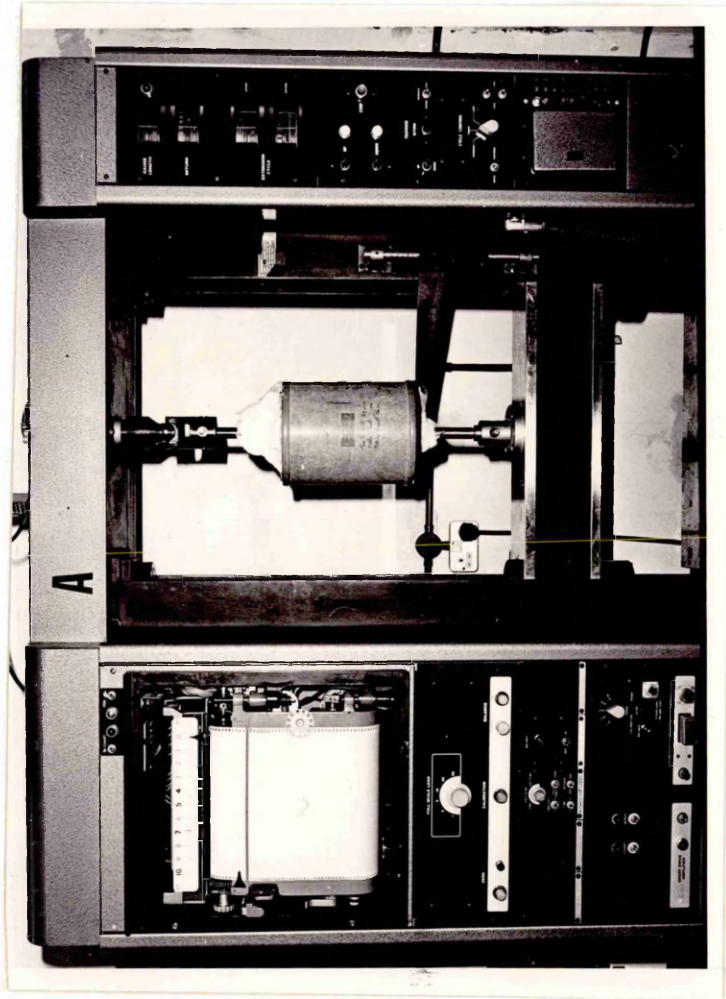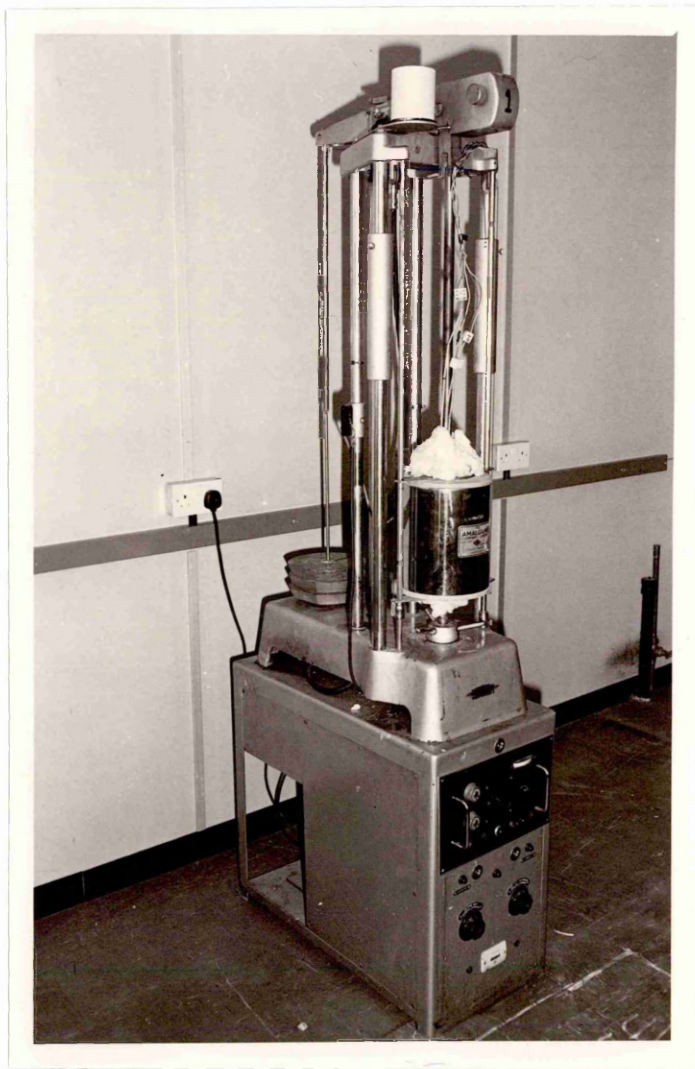
FIGURE 31:   Relationship between experimental
               stress relaxation and time for
               835M30 steel specimen that had
               been austenitised at 850°C and tested
               at the appropriate test temperature.

220.
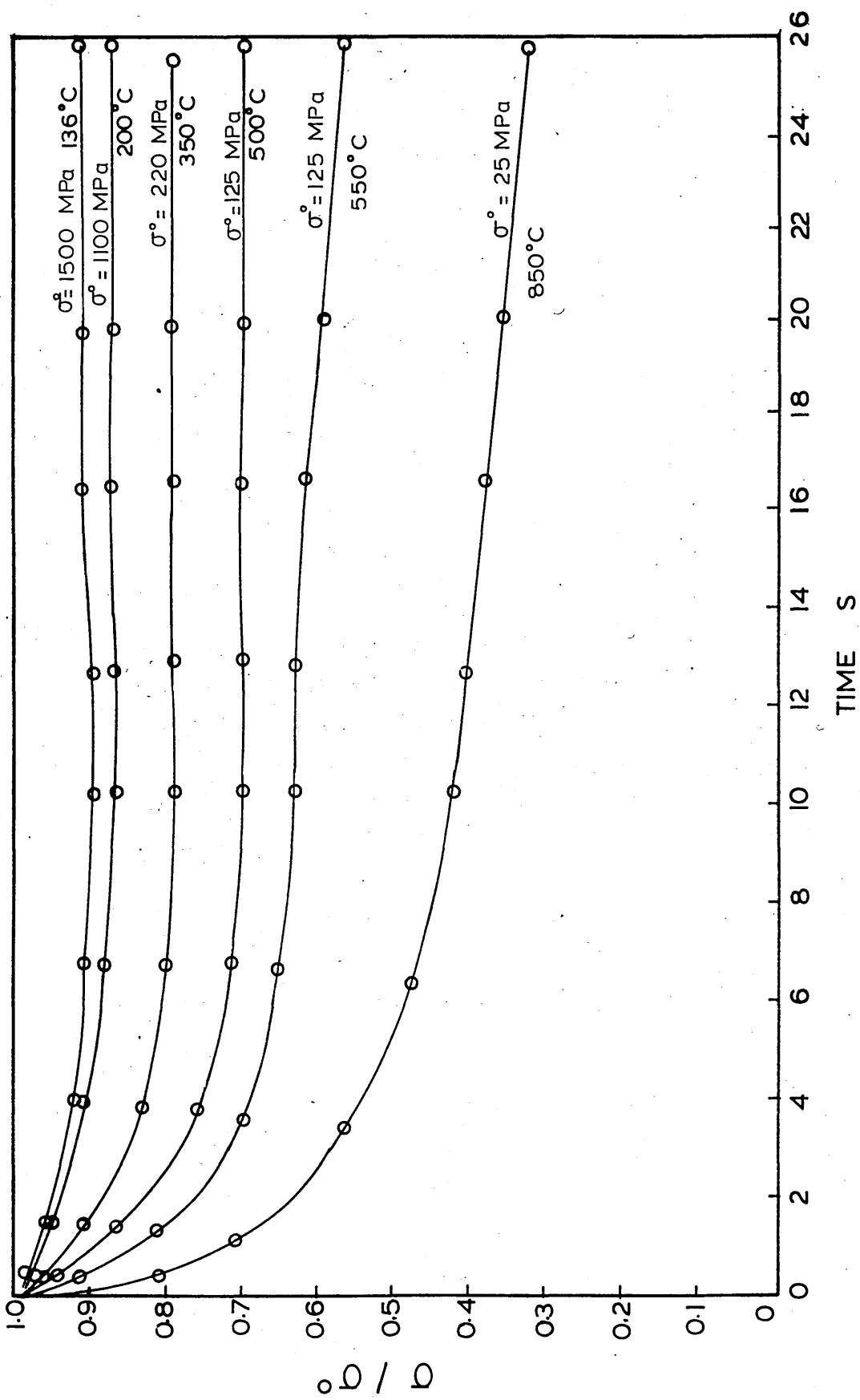
FIGURE 32:   Relationship between steady state creep
rate and temperature for 835M30 steel
specimen during a creep test at
temperatures of 850°C, 800°C and 750°C.

STEADY STATE STRAIN RATE $\dot{\varepsilon} \times 10^7 \text{ S}^{-1}$

TEMPERATURE °C

221.
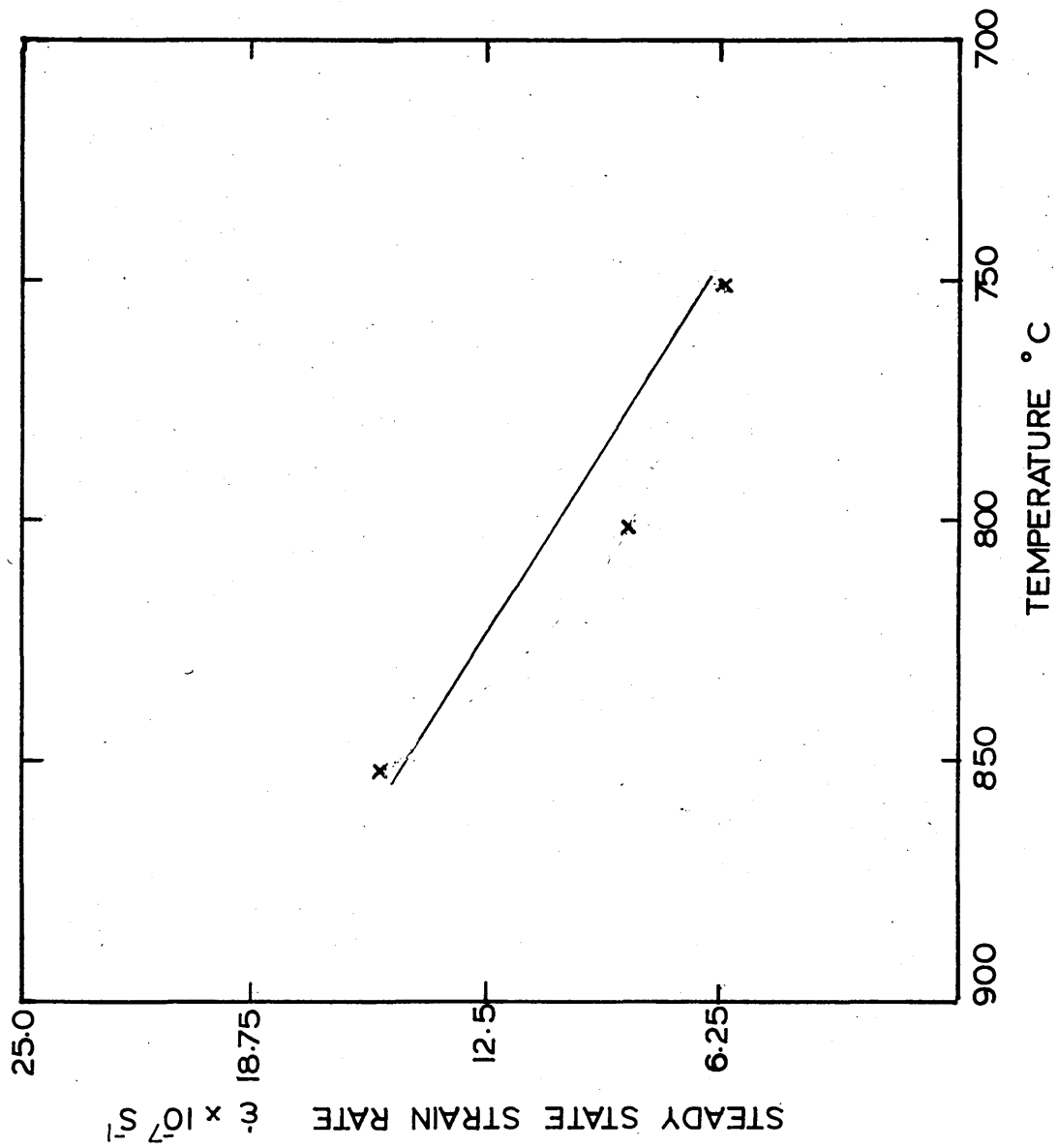
FIGURE 33:   Mechanical models representing the visco-elastic behaviour of material.
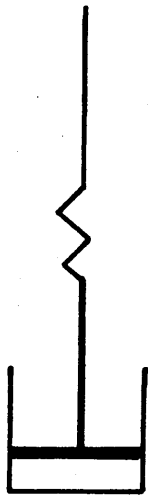
a) Maxwell body
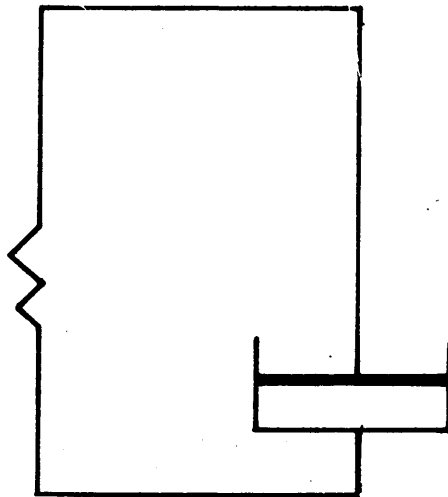
b) Kelvin body
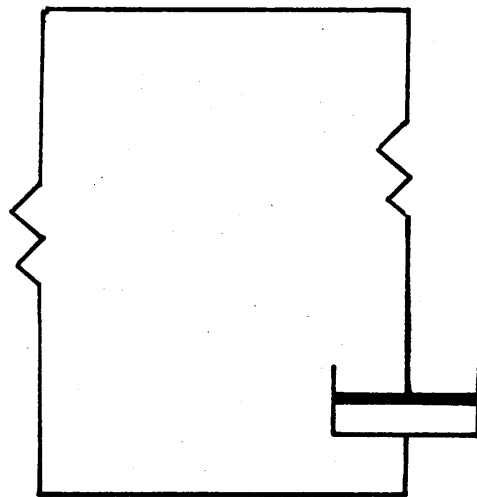
c) Standard linear solid

222.

FIGURE 34:   Comparison of predicted stress
              relaxation behaviour by the Maxwell
              body and Standard linear solid with
              the experimental stress relaxation
              behaviour of 835M30 steel specimen.

223.
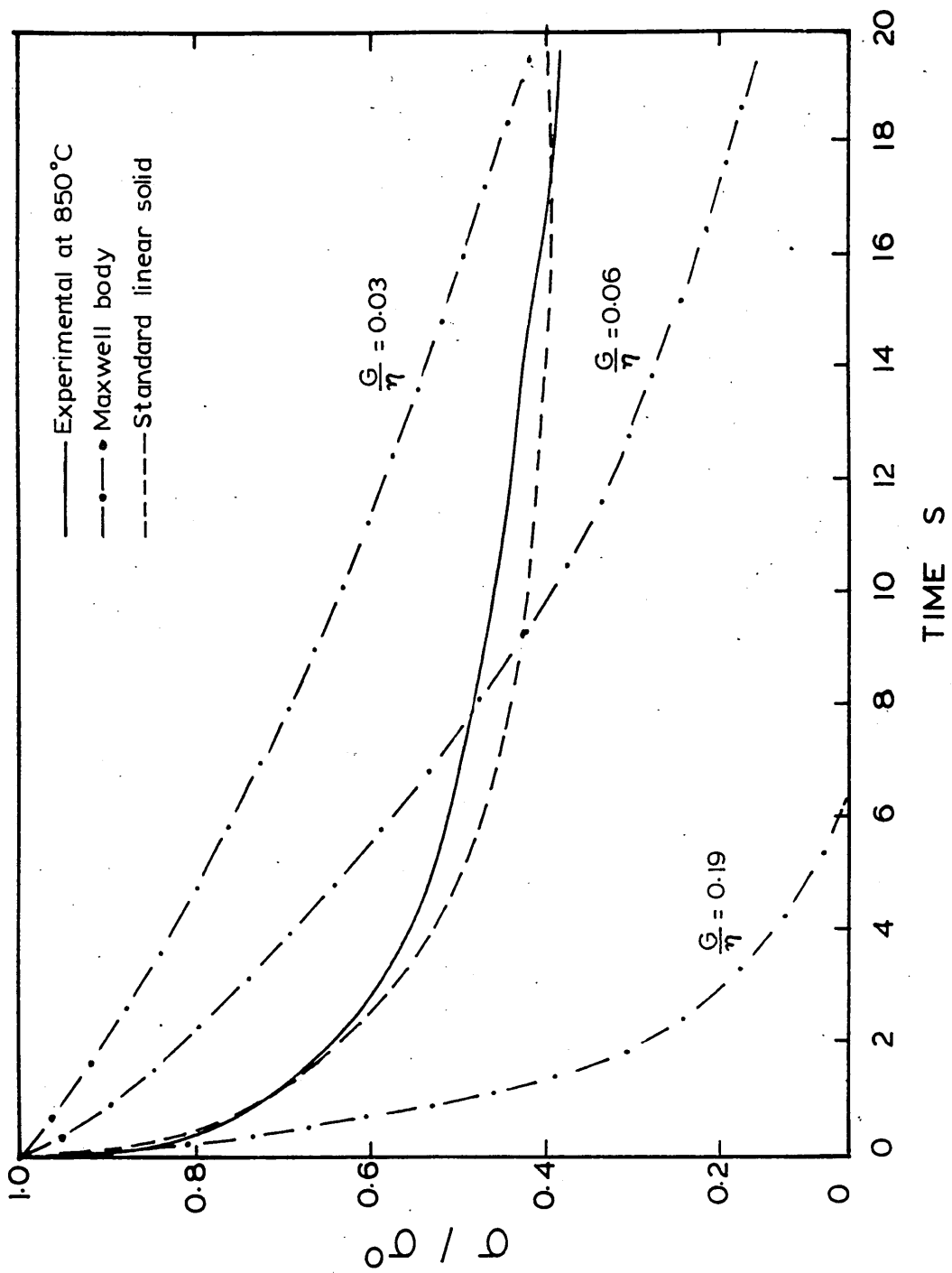
FIGURE 35:   The predicted stress relaxation
              behaviour by the Standard linear
              solid and the experimental stress
              relaxation data of 835M30 steel
              specimen.

136°C (A=0.93
        B=0.18)

200°C (A=0.88
        B=0.3)

350°C (A=0.82
        B=0.32)

500°C (A=0.72
        B=0.35)

550°C (A=0.65
        B=0.4)

850°C (A=0.39
        B=0.7)

TIME S

q/q_0

224.
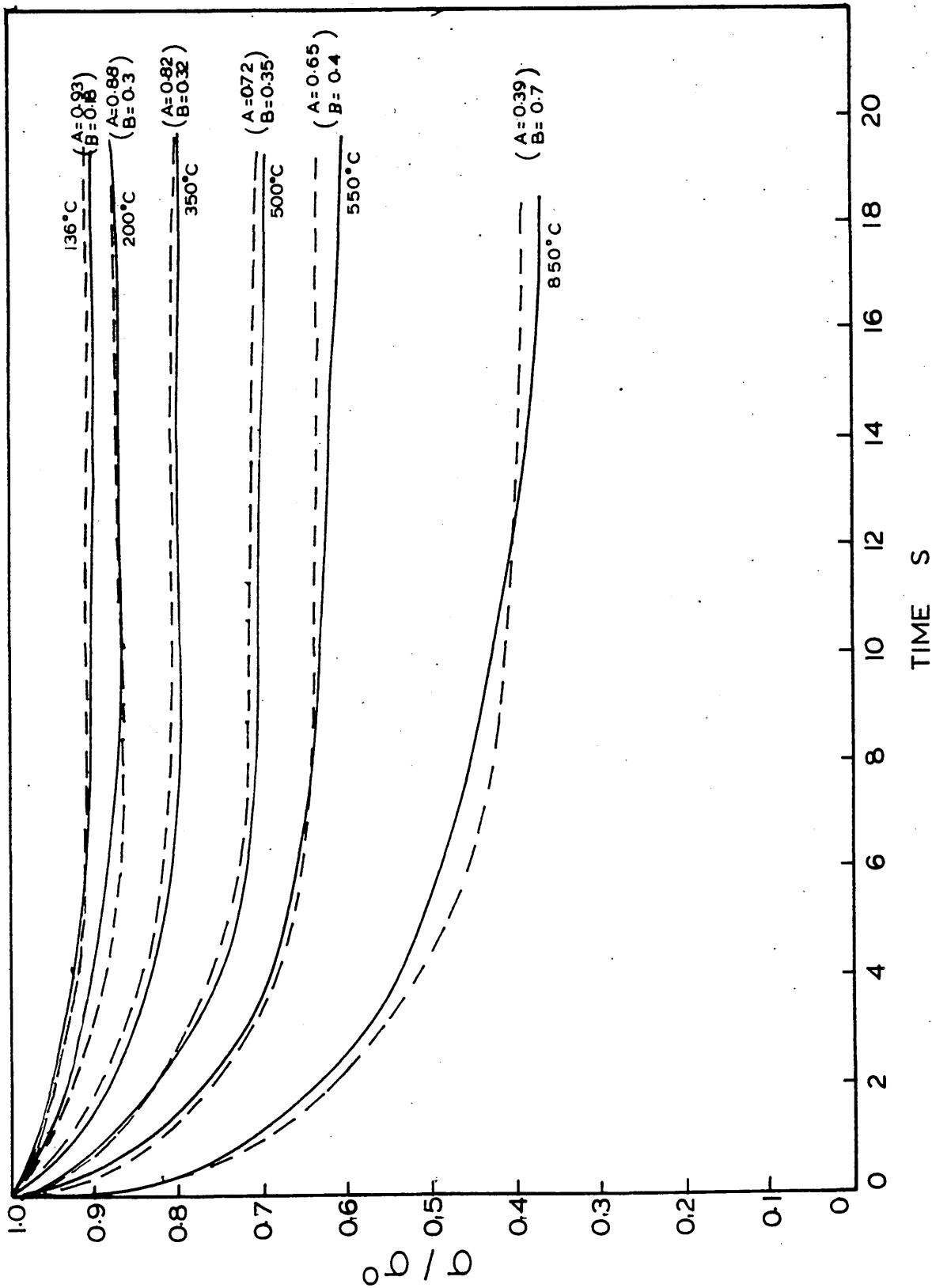
FIGURE 36:   Comparison of predicted and experimental
               creep behaviour of 835M30 steel specimen.

225.
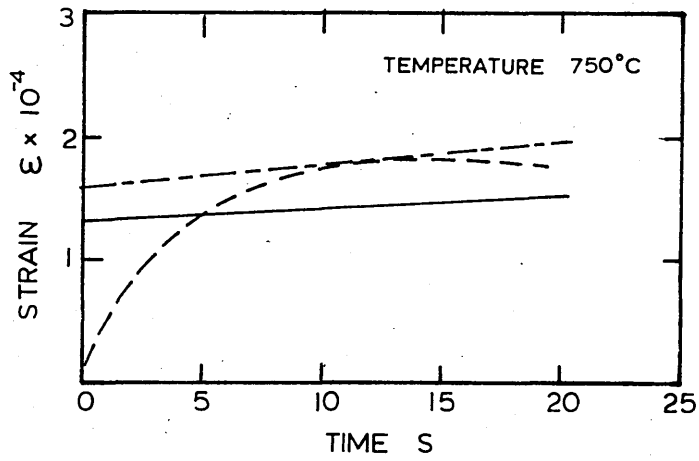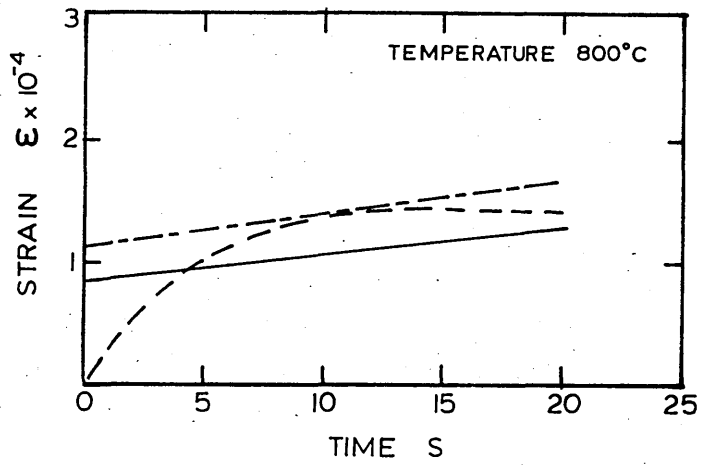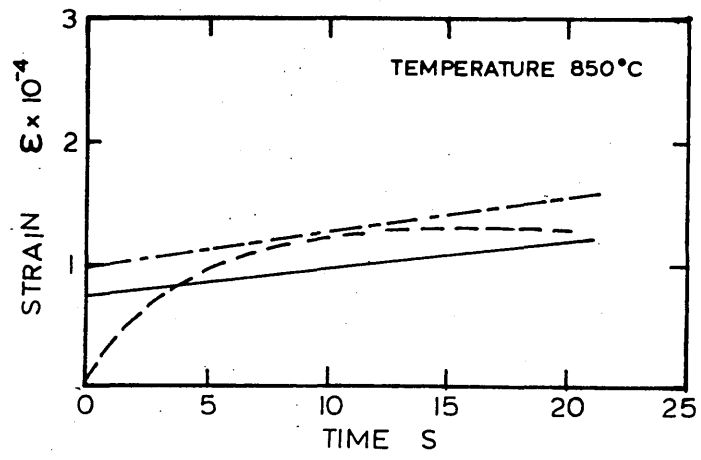
FIGURE 37:   Variation of the standard linear solid
              parameters A and B with temperature

$$A \;\; = \;\; \frac{2\phi\eta(1 \; + \; \nu)}{E}$$

$$B \;\; = \;\; \frac{G}{\eta}$$
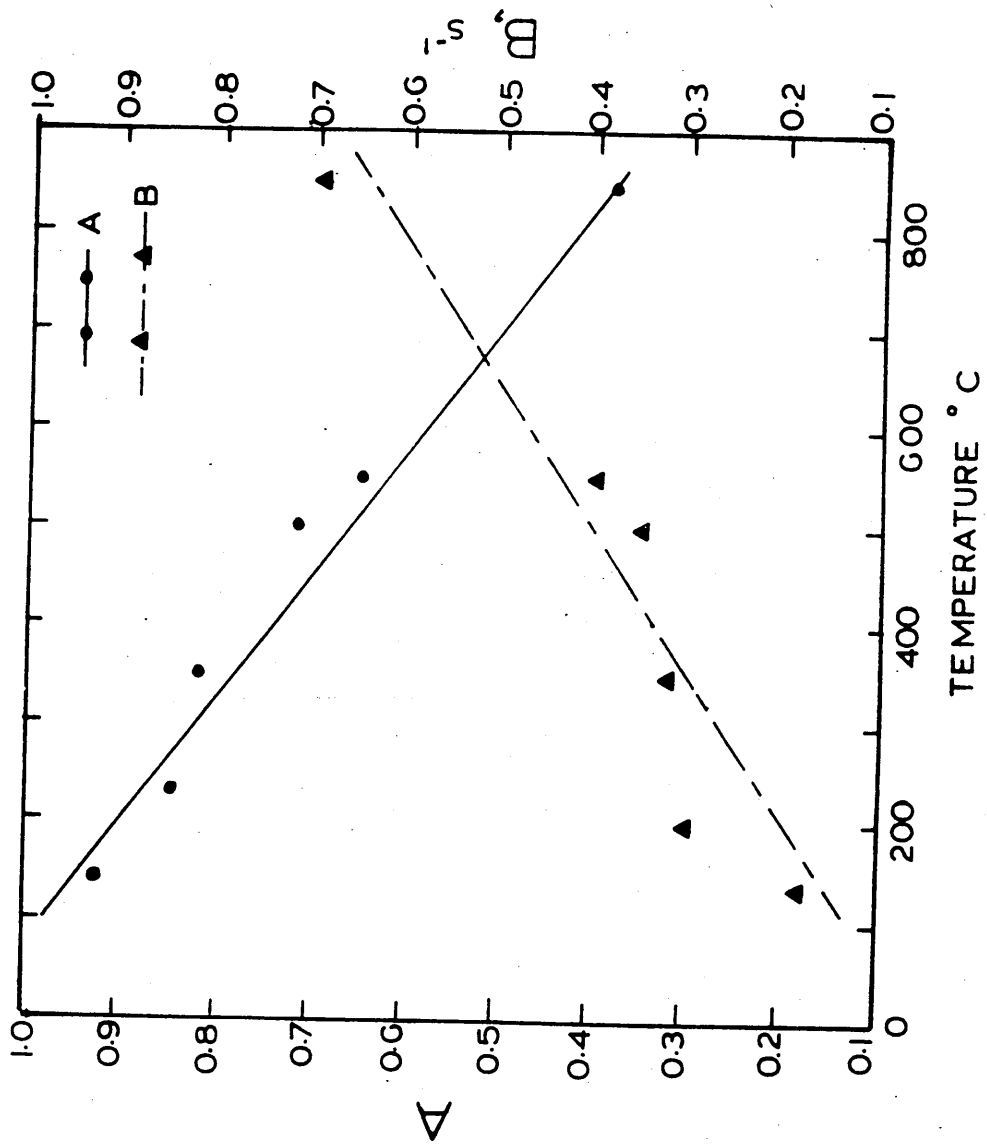
FIGURE 38:   Infinite plate with plane stress
               acting in directions parallel to the
               edge of the plate.

FIGURE 39:   Variation of strain hardening coefficient
               with temperature.

               (After Fletcher and Price[99])

$$\sigma = \sigma_x = \sigma_y$$
$$\sigma_{xy} = \sigma_{yz} = \sigma_{zx} = 0$$
$$\sigma_z = 0$$
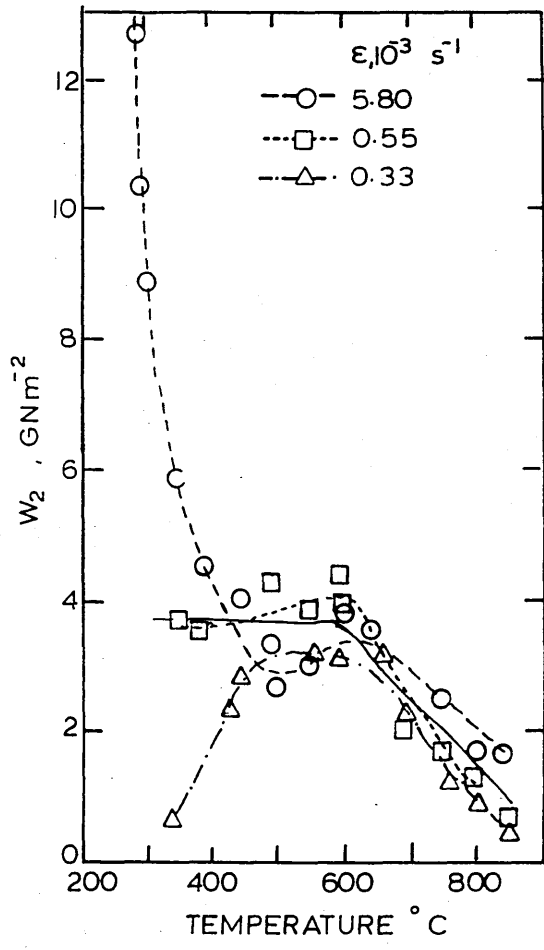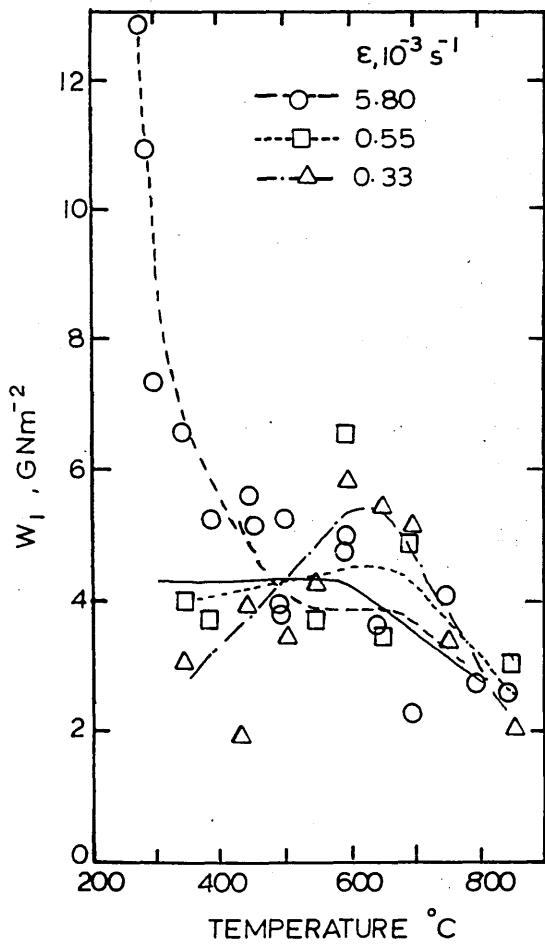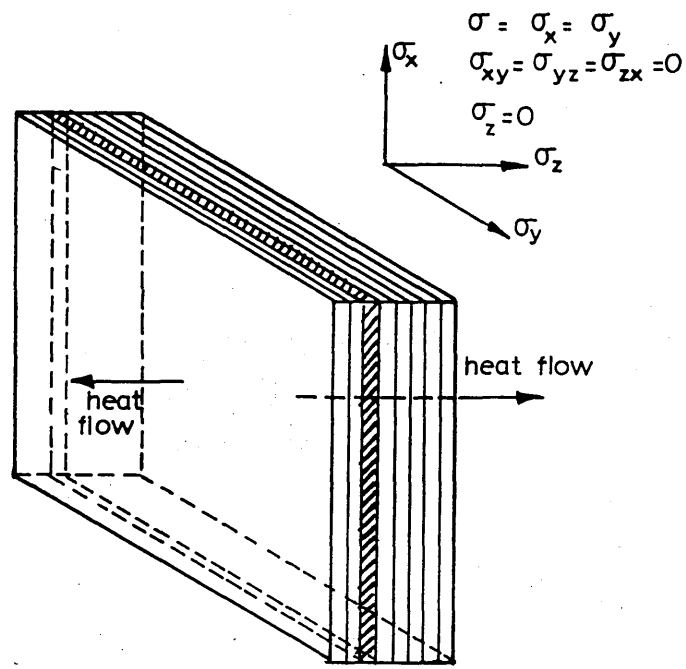
FIGURE 40: Flow chart of the calculation of thermal
stresses and strains, modified to
include viscous flow.

$$\boxed{\text{START}}$$

$$\Theta_i^{\,n}, \ \Theta_{stop}, \ a, \ b,$$
$$j, \ \sigma_f, \ W, \ \alpha_{ex}$$
$$\left.\begin{array}{l} A \\ B \end{array}\right\} \ f(\Theta)$$

$$\text{①}$$

$$n = n+1$$

$$\sigma_{sum} = 0$$

$$i = 0$$

$$i = i + 1$$

$$(\sigma_i^n)_r = \sigma_i^{n-1} + \alpha_{ex}\left[a\left\{\Theta_i^{n-1} - \Theta_i^n\right\} - \frac{b}{2}\left\{(\Theta_i^{n-1})^2 - (\Theta_i^n)^2\right\}\right]$$

$$\sigma_{sum} = \sigma_{sum} + (\sigma_i^n)_r$$

is $i < j$

YES

NO

$$(\overline{\sigma}^n)_r = \frac{\sigma_{sum}}{j}$$

$$\text{②}$$

continued.

228.

2

i = 0

i = i + 1

$$\sigma_i{}^n = (\sigma_i{}^n)_r - (\overline{\sigma}{}^n)_r$$

is i < j — YES

NO

i = 0

3

i = i + 1

is $\Theta_i{}^n < 100$ — YES

NO

$A = 1.038475 - 0.000816\,\Theta_i{}^n$
$B = 0.04959 + 0.000658\,\Theta_i{}^n$

$$(\sigma_i{}^n)_{av} = \frac{\sigma_i{}^n + \sigma_i{}^{n-1}}{2}$$

$$\sigma_i{}^n = \sigma_i{}^n$$

4

5

Fig. 40 continued

$$(\Delta\sigma_i{}^n)_{Rel} = \frac{(\sigma_i^n)_{av}\left[(1-A_i^n)\exp(-\Theta_i^n t^n)+A_i^n\right]\Delta t}{t^n}$$

$$\sigma_i{}^n = \sigma_i{}^n - (\Delta\sigma_i{}^n)_{Rel}$$

5

3 ← YES ← is i < j

NO

$$\sigma_{sum} = 0$$

$$i = 0$$

$$i = i + 1$$

$$\sigma_{sum} = \sigma_{sum} + \sigma_i{}^n$$

YES ← is i < j

NO

$$\overline{\sigma} = \frac{\sigma_{sum}}{j}$$

6

Fig. 40 continued

230.

⑥

is $|\bar{\sigma}| \geqslant 0.1$ — YES

NO

i = 0

i = i + 1

$\sigma_i^n = \sigma_i^n - \bar{\sigma}$

$\sigma_i^n = \sigma_i^n$

is i < j — YES / NO

m = 0

$(\sigma_i^n)_S = \sigma_i^n$

⑦

m = m+1

$\sigma_{sum} = 0$

i = 0

⑧

i = i+1

is $\sigma_i^n > \sigma_{fi}^n$ — NO ⑨ / YES ⑩

fig. 40 continued

231.

Fig. 40 continued

232.

(11)

i = 0

i = i+1

$(\sigma_i^n)_S = (\sigma_i^n)_S - \bar{\sigma}$

$\sigma_i^n = (\sigma_i^n)_S$

$\varepsilon_p = \dfrac{(\sigma_i^n)_S - \sigma_{fi}^n}{a - b\,\Theta_i^n}$

$\sigma_{fi}^n = \sigma_{fi}^n + W \times \varepsilon_p$

is i < j

YES

NO

(7)

(12)

i = i + 1

Θ_i^n is < 100

YES

NO

$(\Delta\varepsilon_i^n)_{cr} = 0$

$(\Delta\varepsilon_i^n)_{cr} = \dfrac{(\sigma_i^n)_{av}(1-A_i^n)\left\{1-\exp(-A_i^n \cdot B_i^n t^n)\right\}\Delta t}{(a - b\,\Theta_i^n)\,A_i^n\,t^n}$

$\varepsilon_i^n = \varepsilon_i^{n-1} + \left(\dfrac{(\sigma_i^n)_S}{a-b\Theta_i^n} - \dfrac{\sigma_i^{n-1}}{a-b\Theta_i^{n-1}}\right) + (\Delta\varepsilon_i^n)_{cr}$

is i < j

YES

NO

(1)

Θ_i^n is $< \Theta_{stop}$

NO

YES

E N D

233.

FIGURE 41:   The reduction in the average stress
relaxation and creep rates with time,
with a cut off at 20 seconds to
represent the steady state conditions.

(a) Average creep rate (—·—·—·—·)

(b) Average stress relaxation
                    rate (—·—·—·—·)
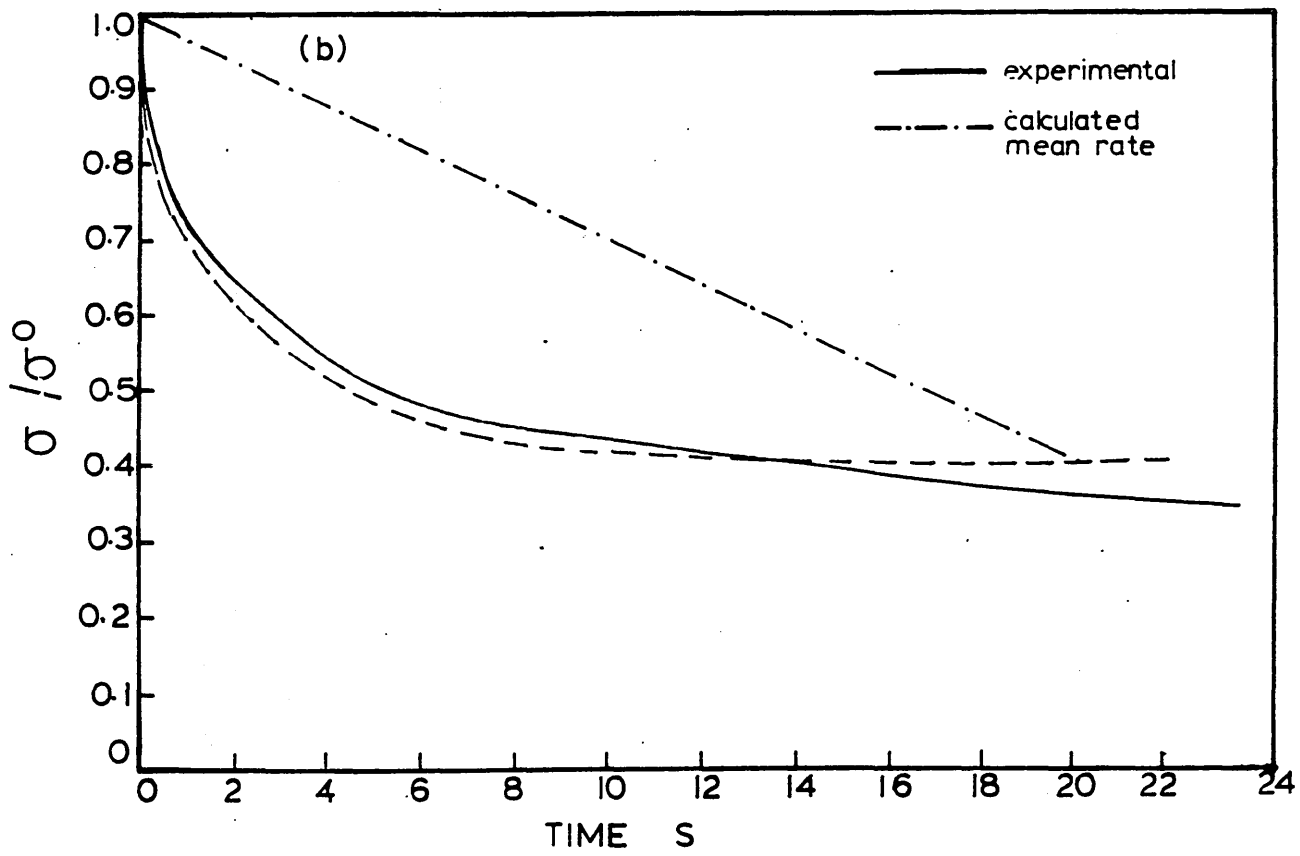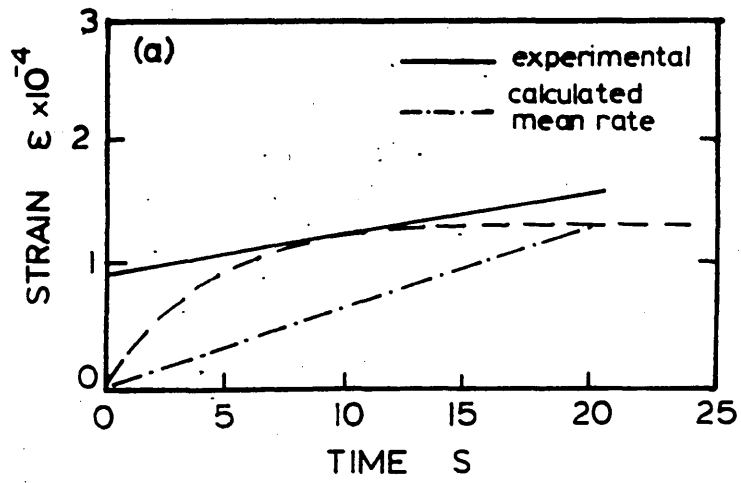
FIGURE 42:   The reduction in the stress relaxation
              rate with decreasing temperature as
              predicted by method 1 and method 2.

235.
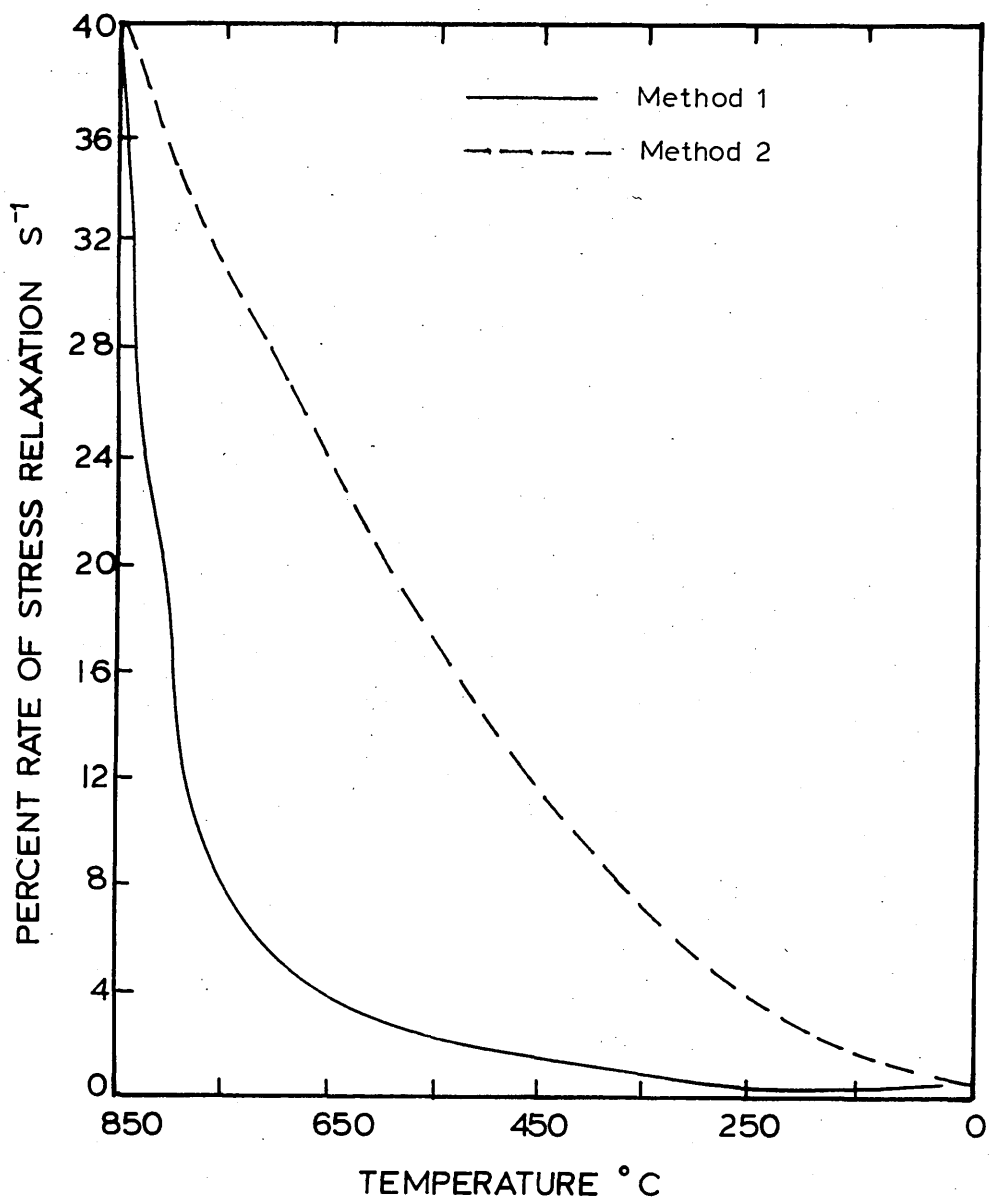
FIGURE 43:   Determination of the volume fraction
of austenite and martensite present
below the M_s temperature.

(After Fletcher and Price[99])

$$\text{at } \theta$$

$$V_\gamma = \frac{a}{a+b}$$

$$V_\alpha = \frac{b}{a+b}$$

236.
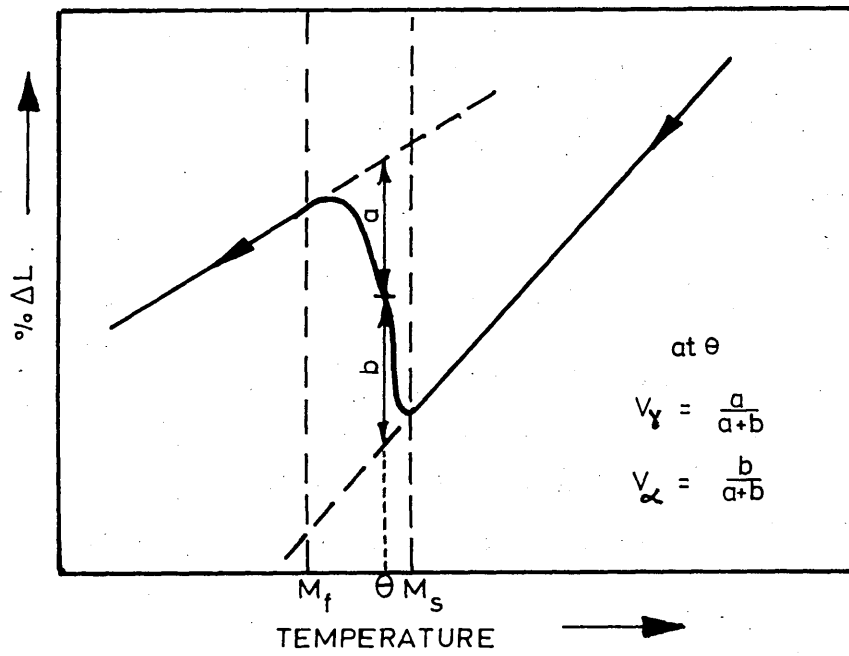
FIGURE 44:   Variation of uniaxial flow stress
with temperature in 835M30 specimens
that had been initially austenitized
at 850°C.

(After Fletcher and Price[99])

FIGURE 45:   Variation of $\left(\frac{E}{1-v}\right)$ with temperature of
835M30 steel.

(After Fletcher and Price[99])

237.
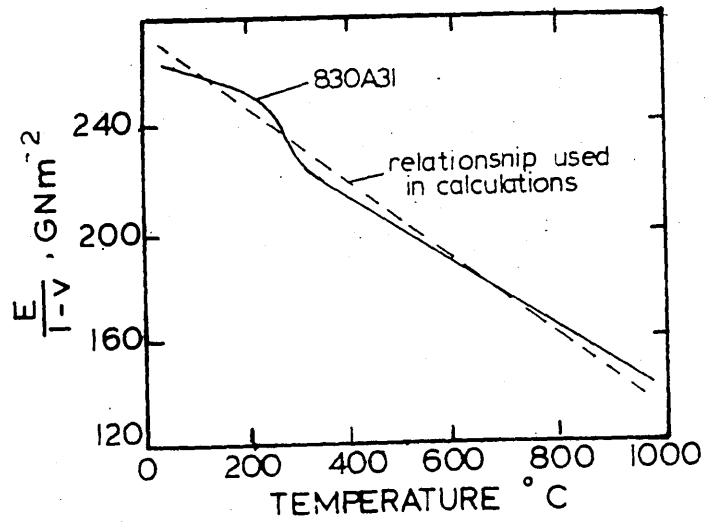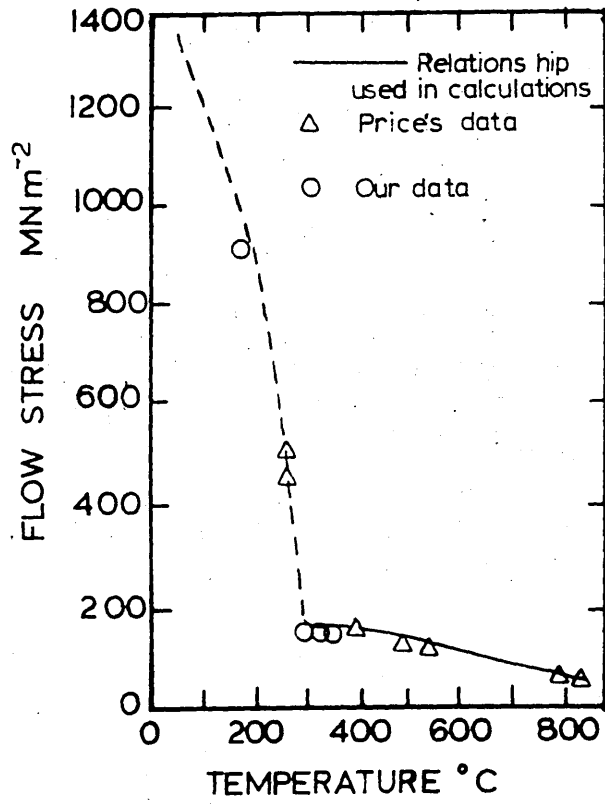
FIGURE 46:   The influence of compressive stress
              on the dilation characteristics of
              835M30 steel specimen during
              transformation.

238.
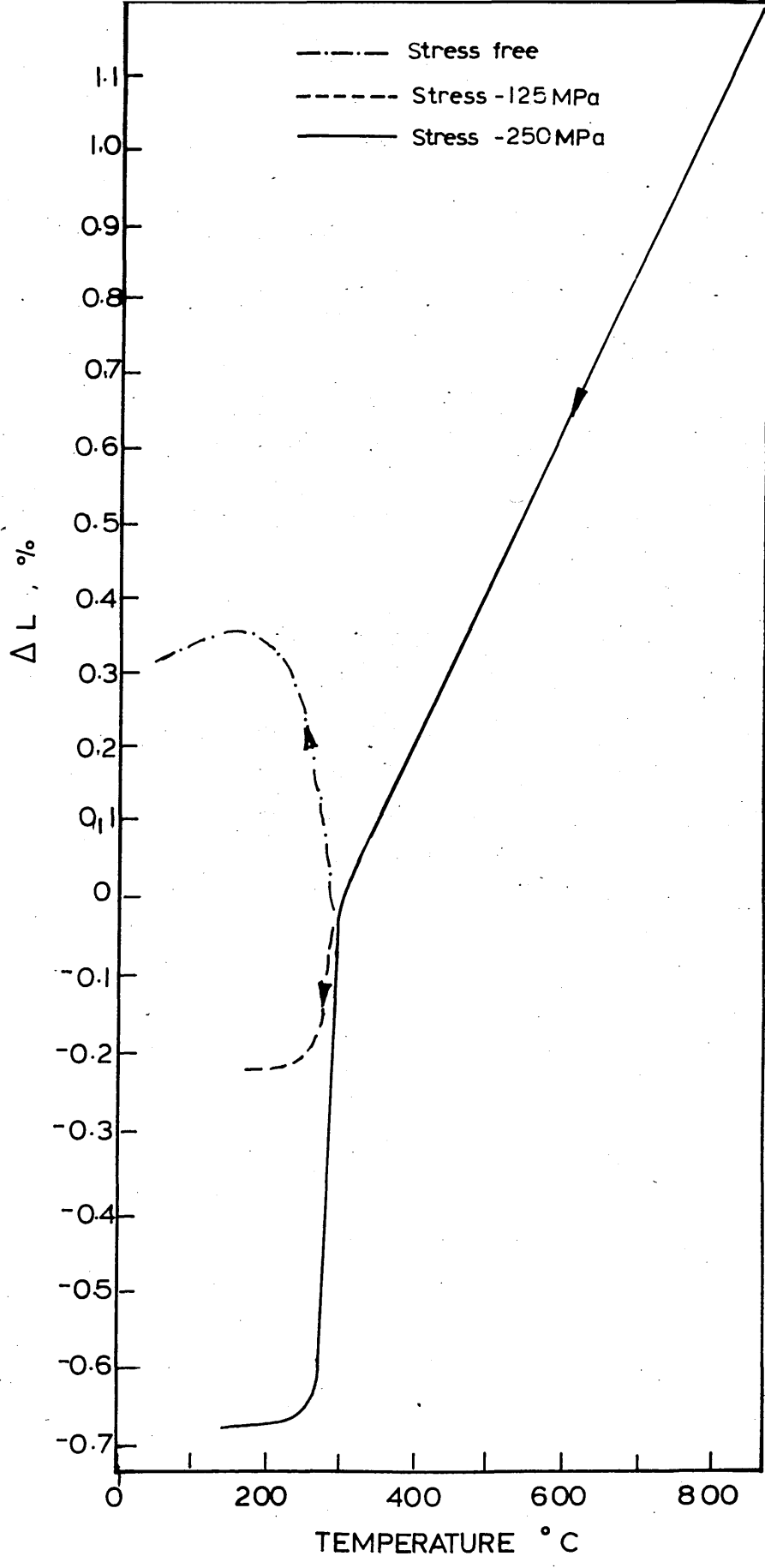
FIGURE 47:   The relationship between stress and
             strain obtained from stress-dilatometer
             data for 835M30 steel.

239.
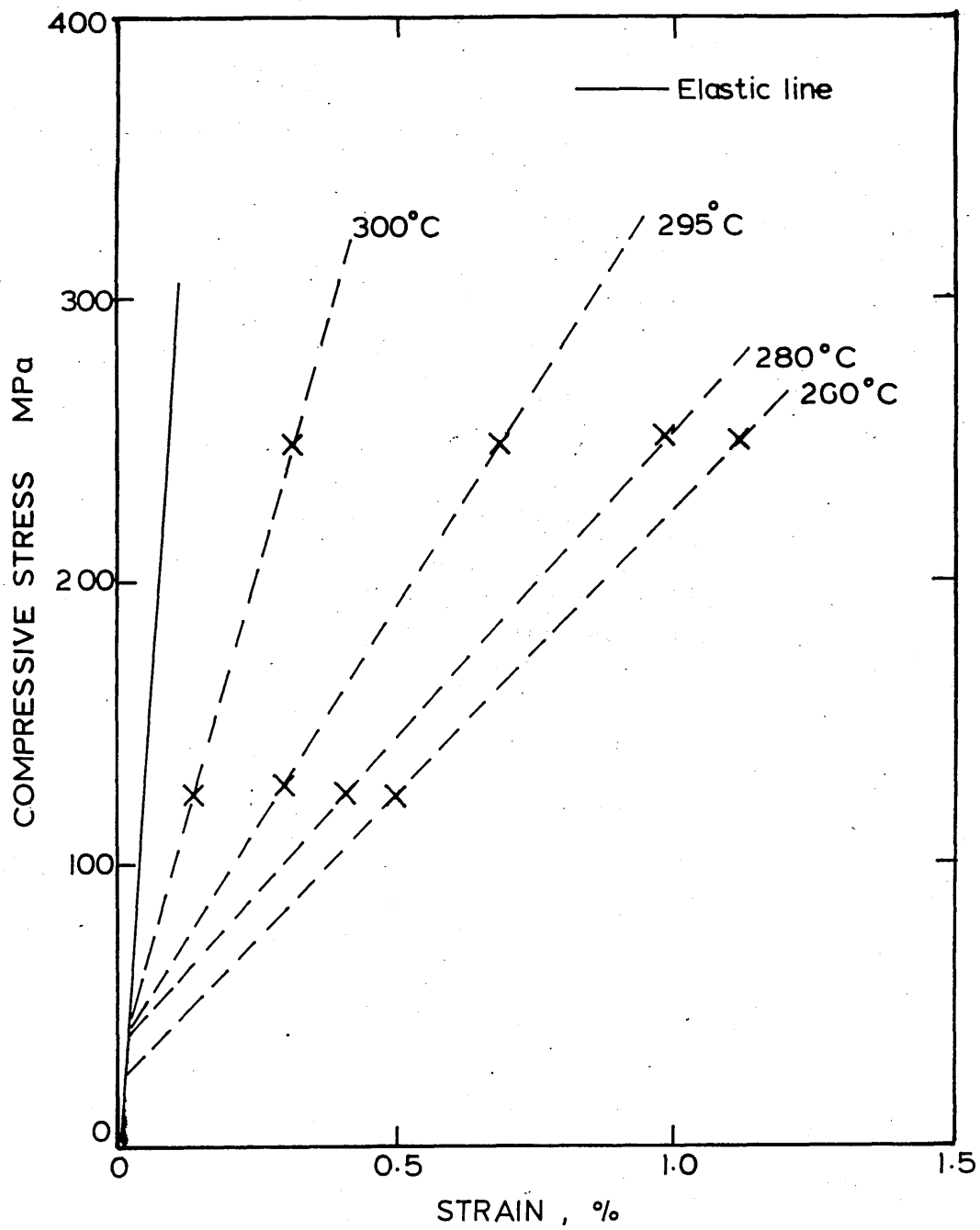
FIGURE 48:   The relationship between flow stress
               with temperature used in the mathematical
               model to simulate transformation plasticity.
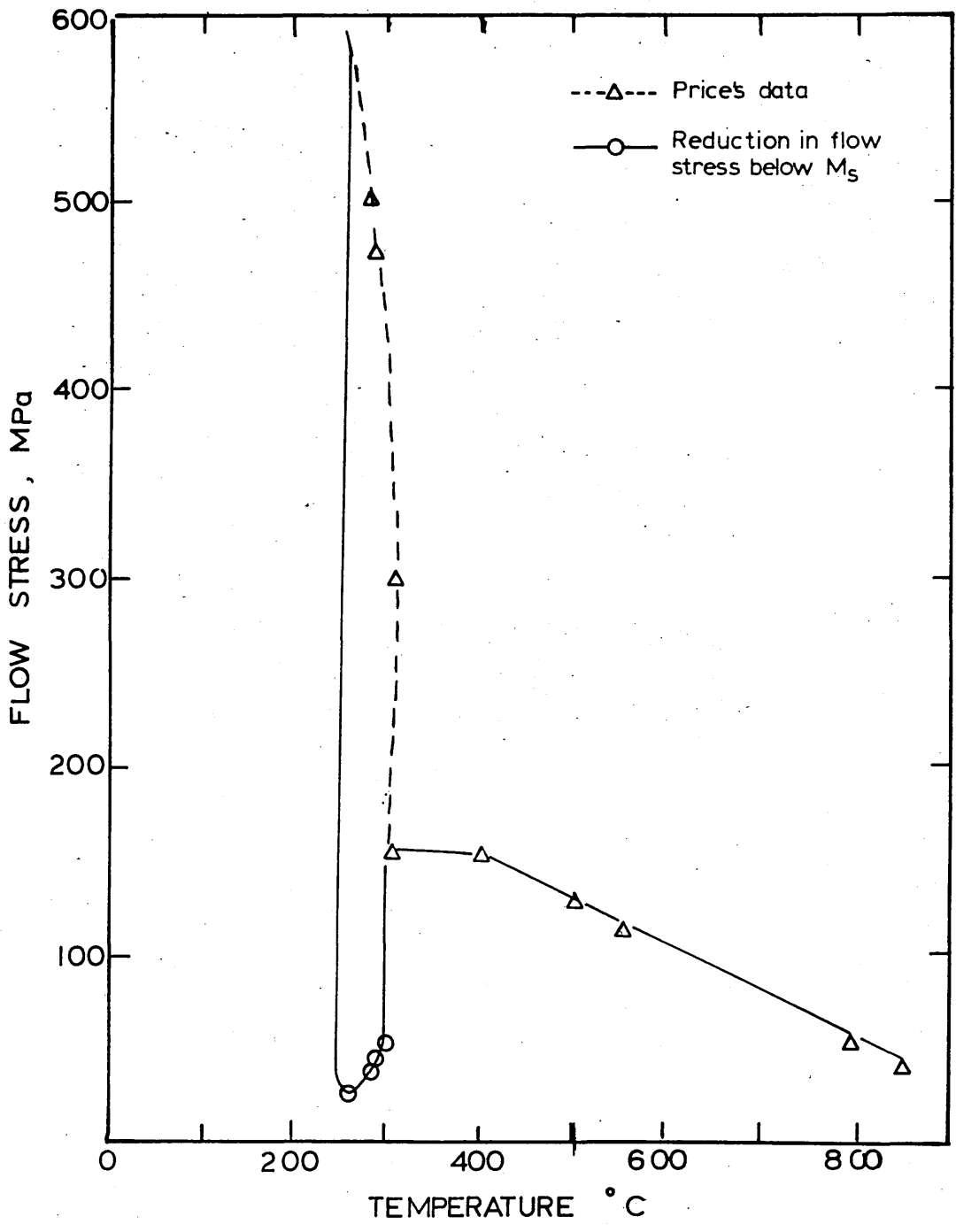
FIGURE 49:   Comparison of dilatometer curve
              obtained under no applied load with
              that obtained in the presence of a
              compressive stress.

Axis labels: ΔL, % (vertical axis); TEMPERATURE °C (horizontal axis)

Curve labels:
- stress free dilatometer curve
- transformation plasticity strain
- dilatometer curve obtained under applied stress of -250 MPa

241.
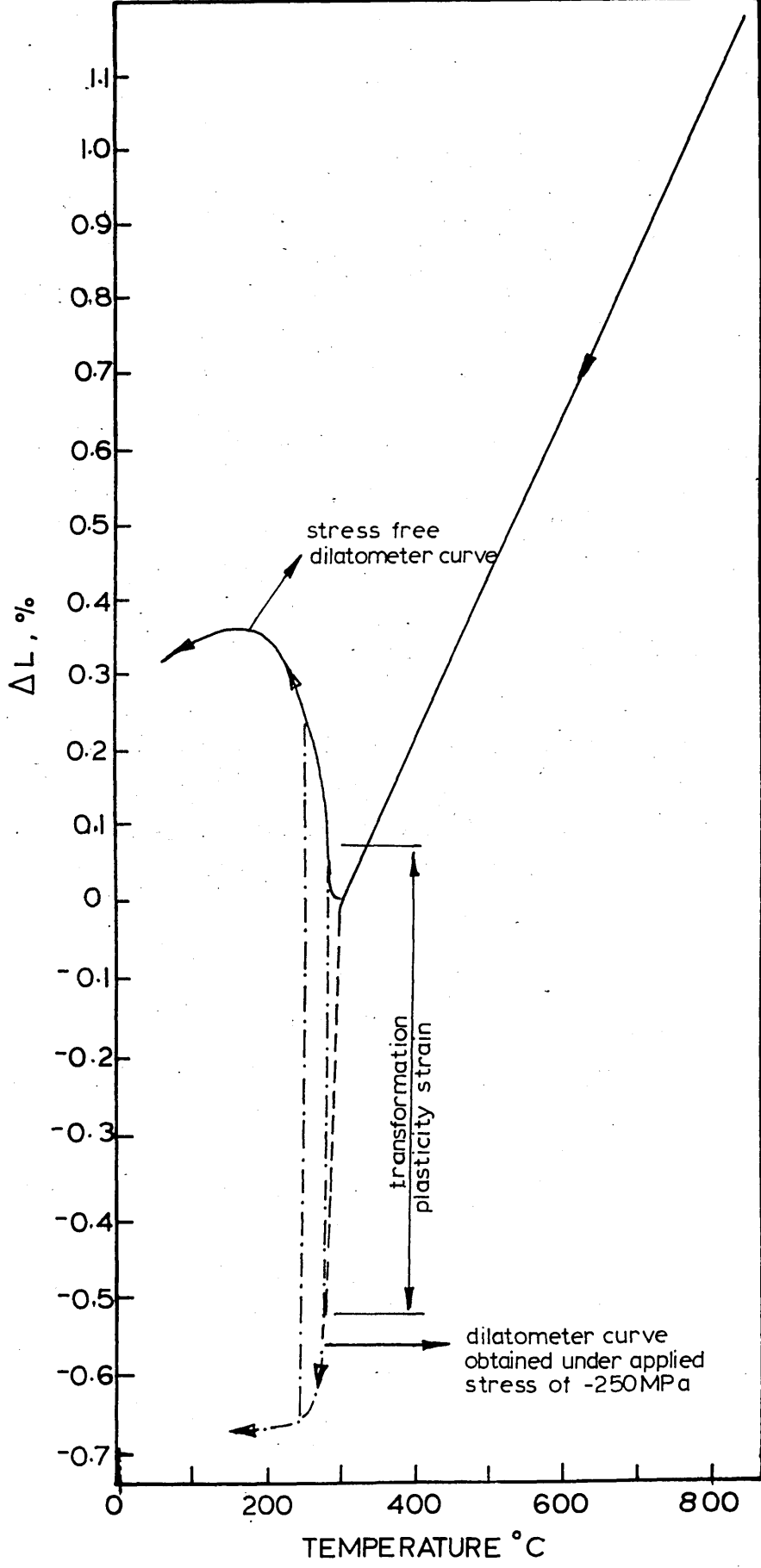
FIGURE 50:   Variation of transformation plasticity
              strain with temperature at different
              levels of applied stress.

242.
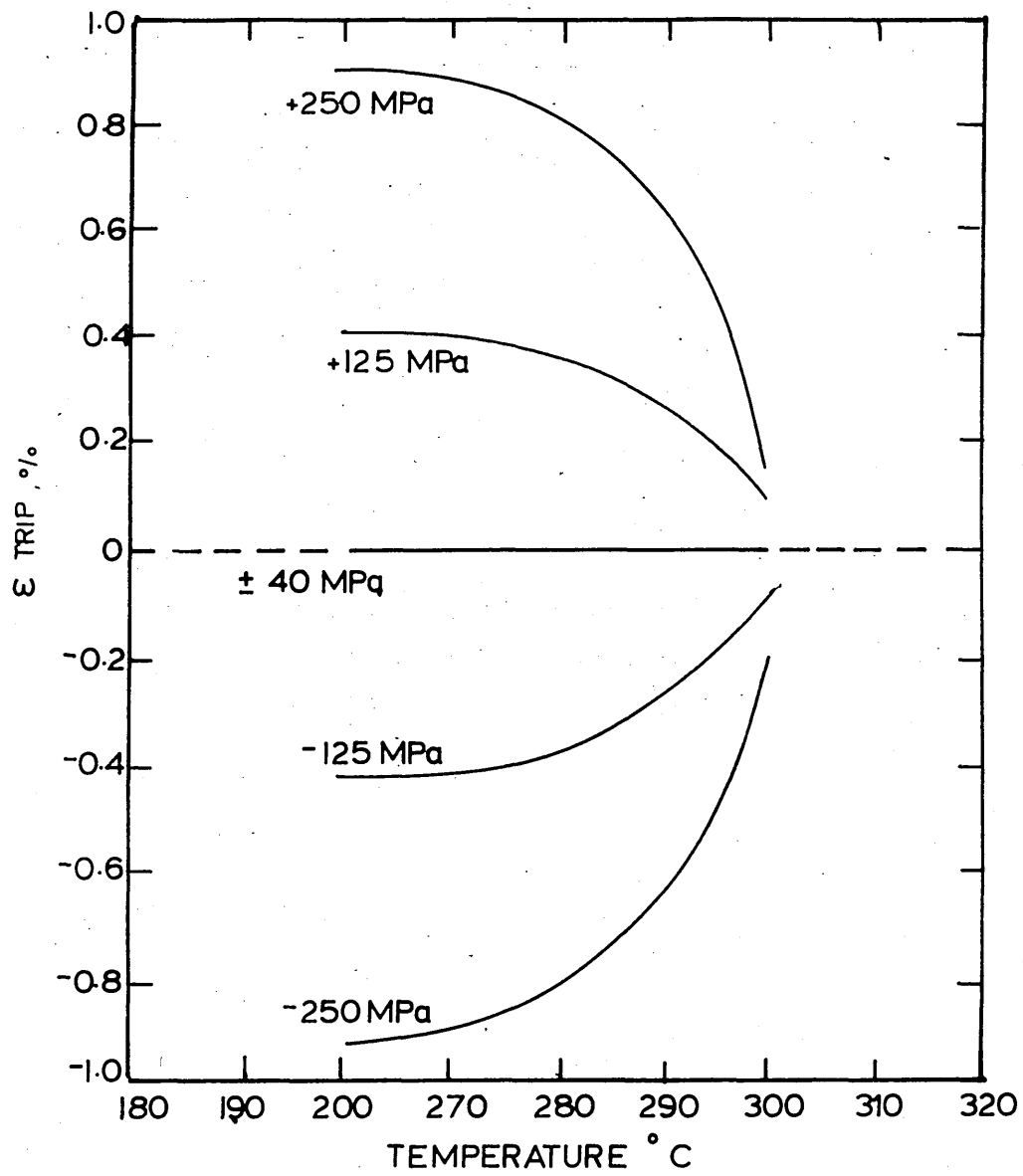
FIGURE 51:   Calculated stress and strain at the
              centre and surface of a 20mm plate
              during water quenching (no viscous
              flow).

              (Calculation CD1/W/NVF) see table 8.

243.
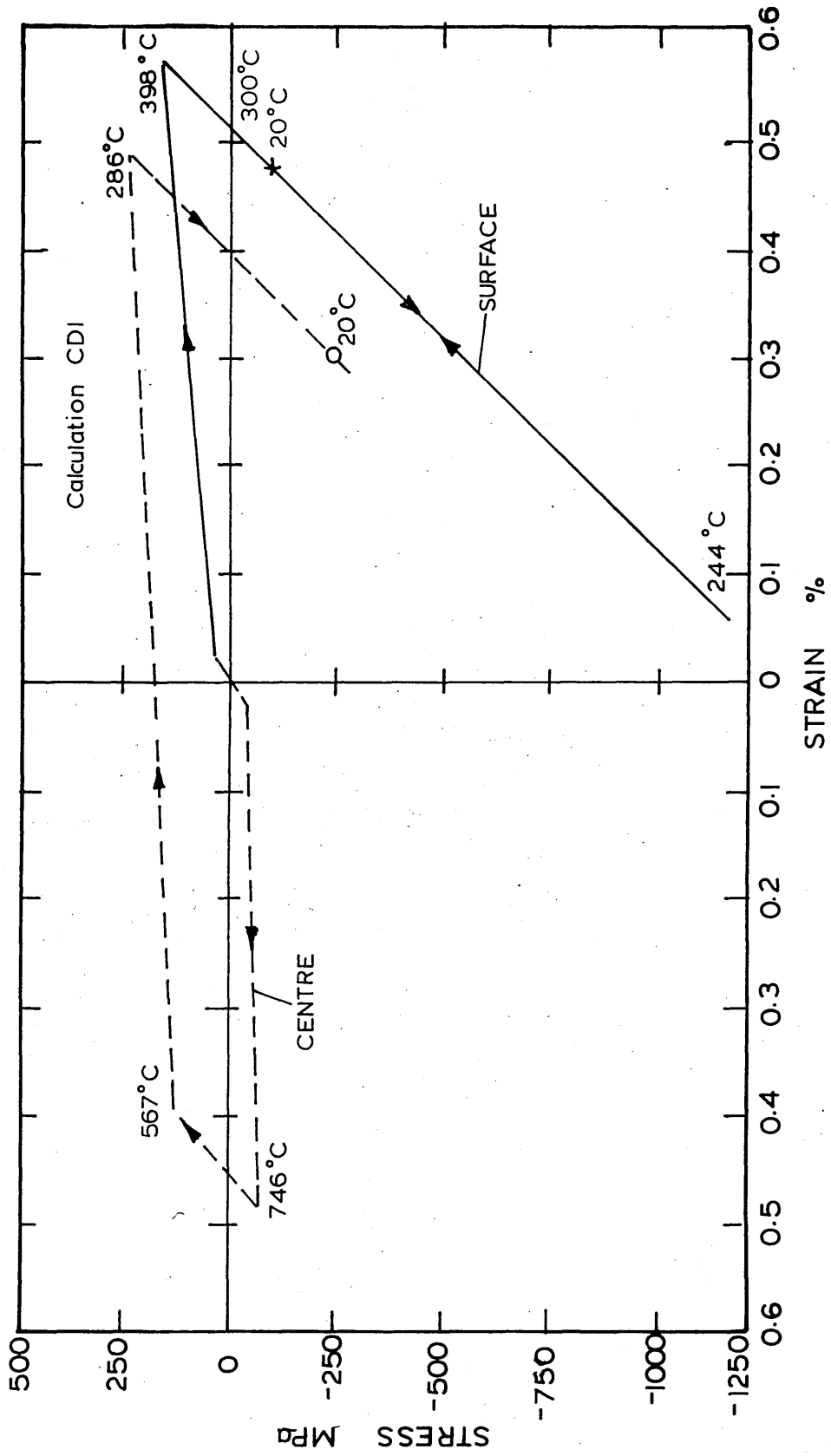
FIGURE 52:   Calculated stress and strain at the
              centre and surface of a 20mm plate
              during water quenching (viscous flow
              represented by method 1).

              (Calculation CD4/W/VF1) see table 8.

244.
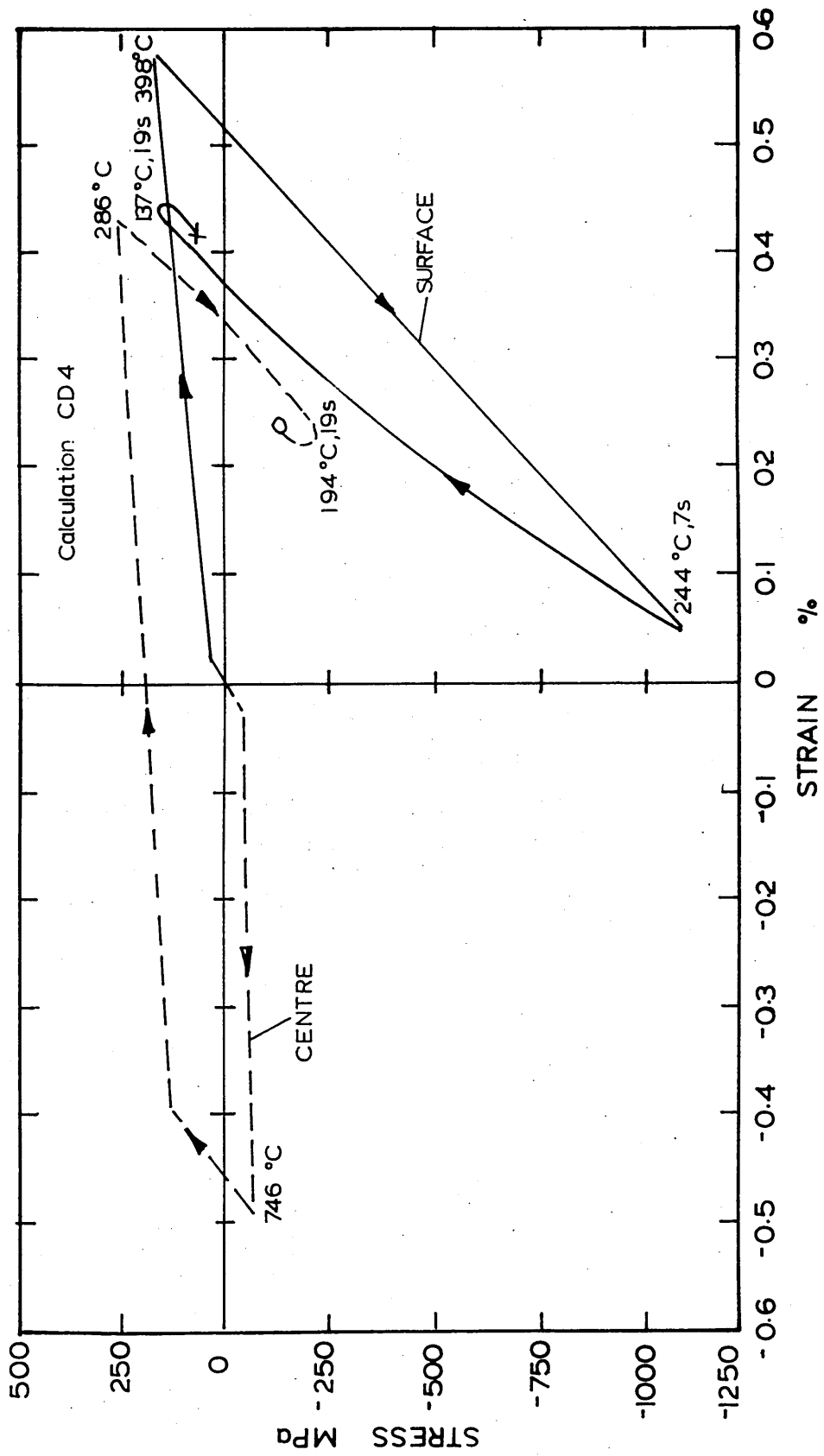
FIGURE 53:   Calculated stress and strain at the
              centre and surface of a 20mm plate
              during water quenching (viscous flow
              represented by methods 2 and 3).

              (Calculation CD5/W/VF2 and 3)
              see table 8.

Calculation CD 5

STRESS MPa

STRAIN %
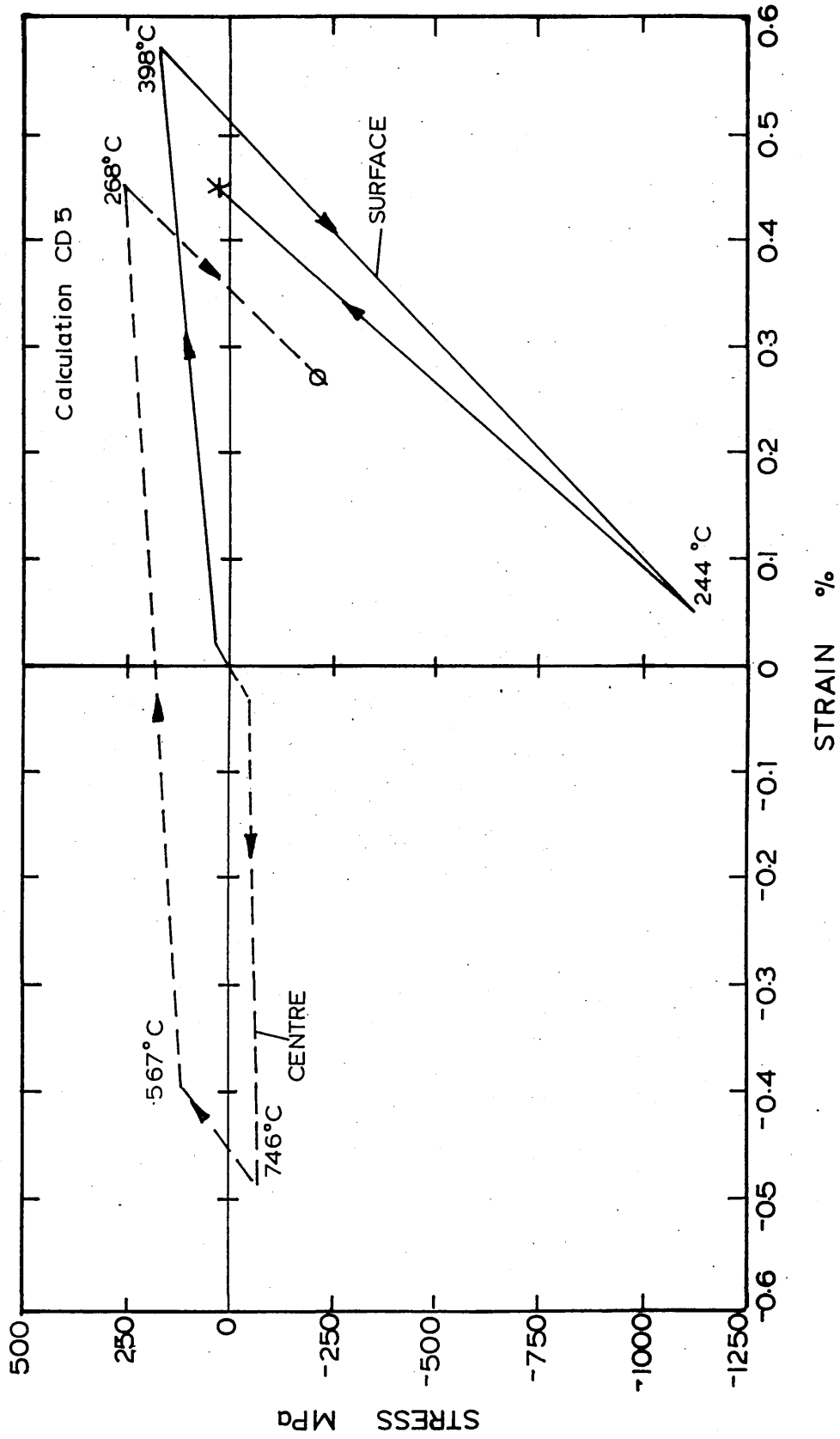
FIGURE 54:   Influence of viscous flow on the
               calculated residual stress
               distribution in a 20mm plate after
               water quenching.

               Calculation no:
               CD1/W/NVF   )
               CD4/W/VF1   )   see table 8
               CD5/W/VF2 and 3)
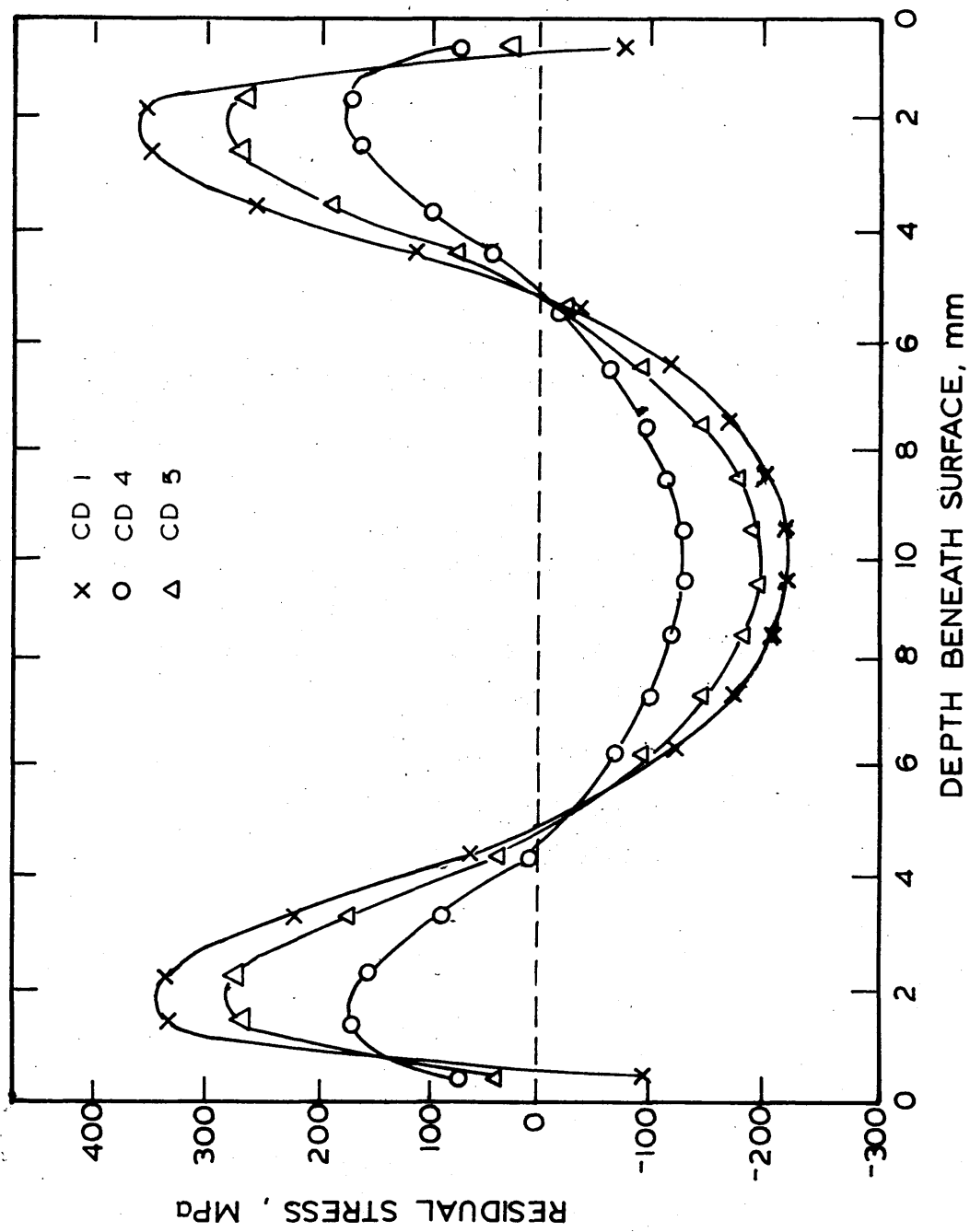
FIGURE 55:   Influence of the viscous flow on the
   calculated residual strain distribution
              in a 20mm plate after water quenching.

              Calculation no:

              CD1/W/NVF   )
              CD4/W/VF1   )   see table 8
              CD5/W/VF2 and 3   )

247.
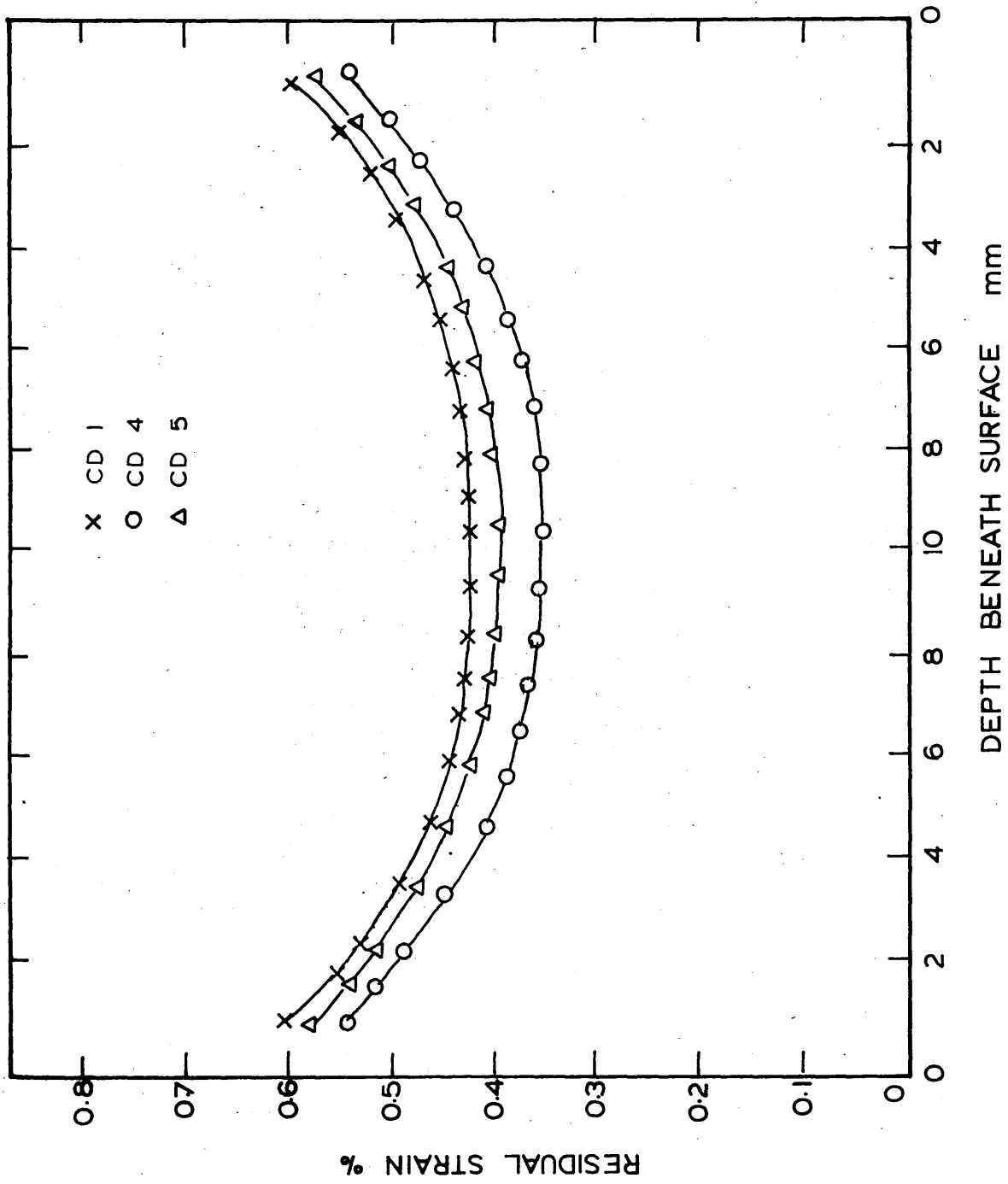
FIGURE 56:   Calculated stress and strain at the
              centre and surface of a 15mm plate
              during oil quenching (no viscous flow)

              (Calculation CD2/0/NVF) see table 8.

248.
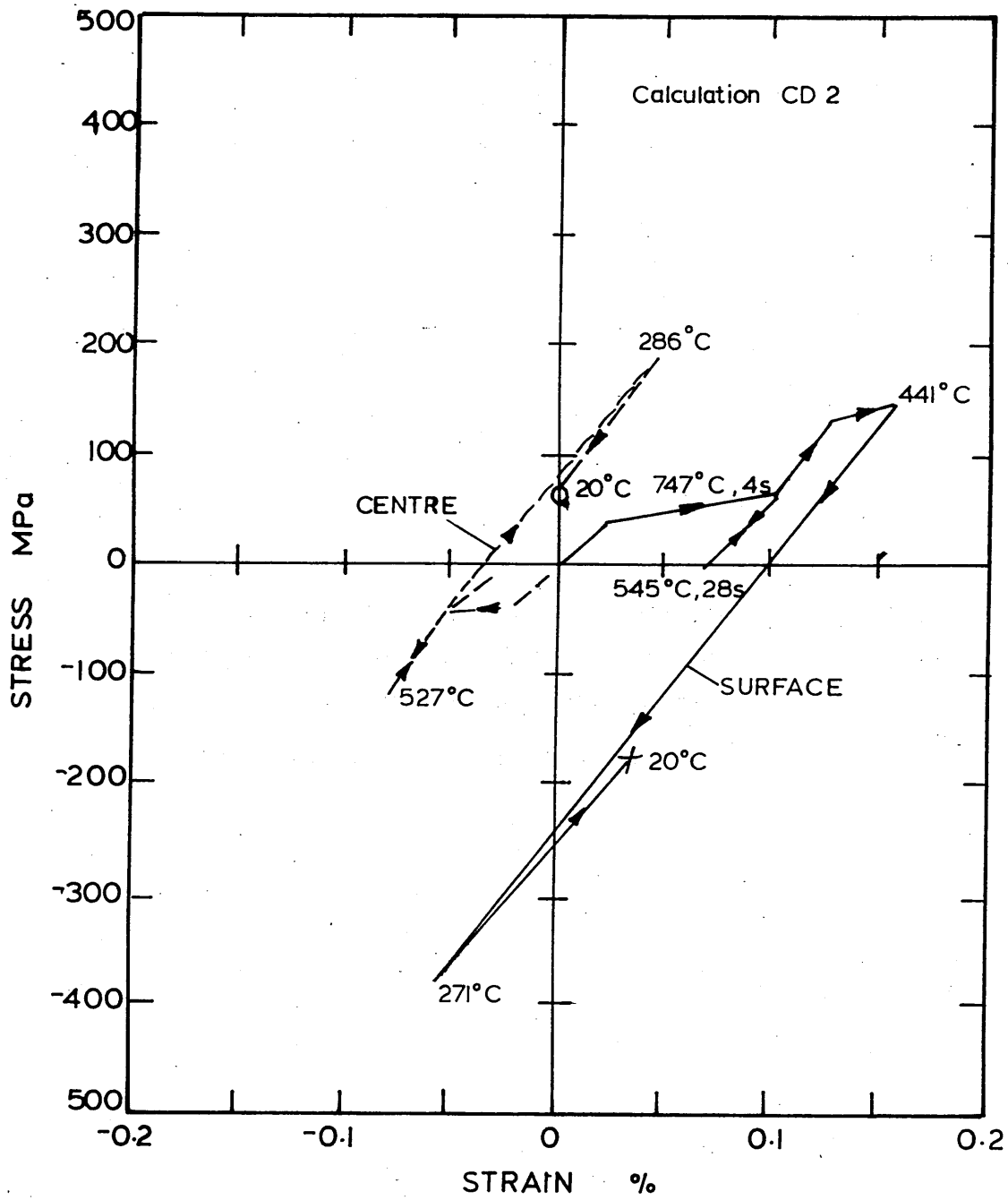
FIGURE 57:   Calculated stress and strain at the
centre and surface of a 15mm plate
during oil quenching (viscous flow as
represented by method 1).

(Calculation number CD6/O/VF1) see table 8

Calculation CD6

249.
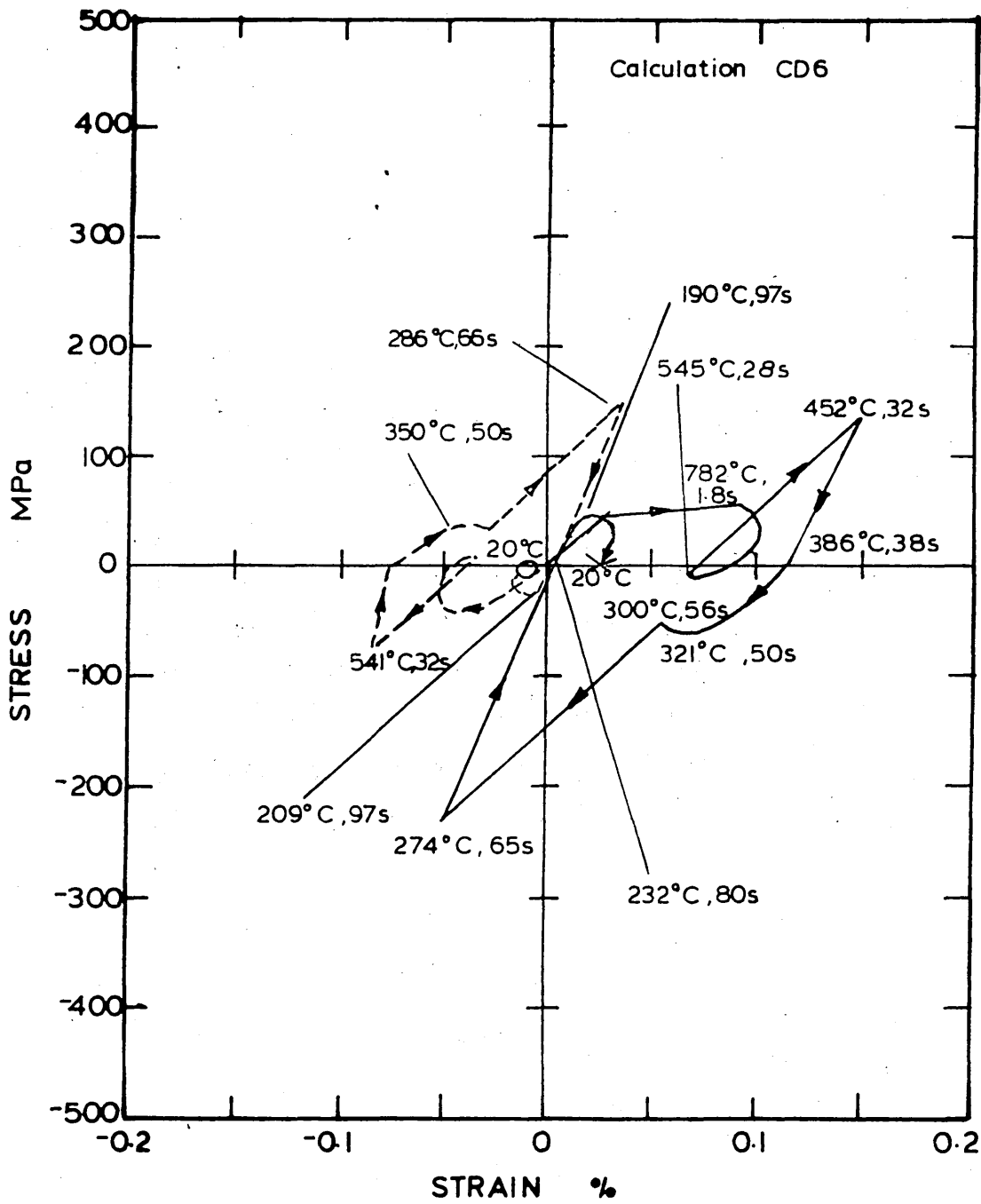
FIGURE 58:   Calculated stress and strain at the
centre and the surface of a 15mm plate
during oil quenching (viscous flow as
represented by method 2).

(Calculation CD7/0/VF2) see table 8

250.
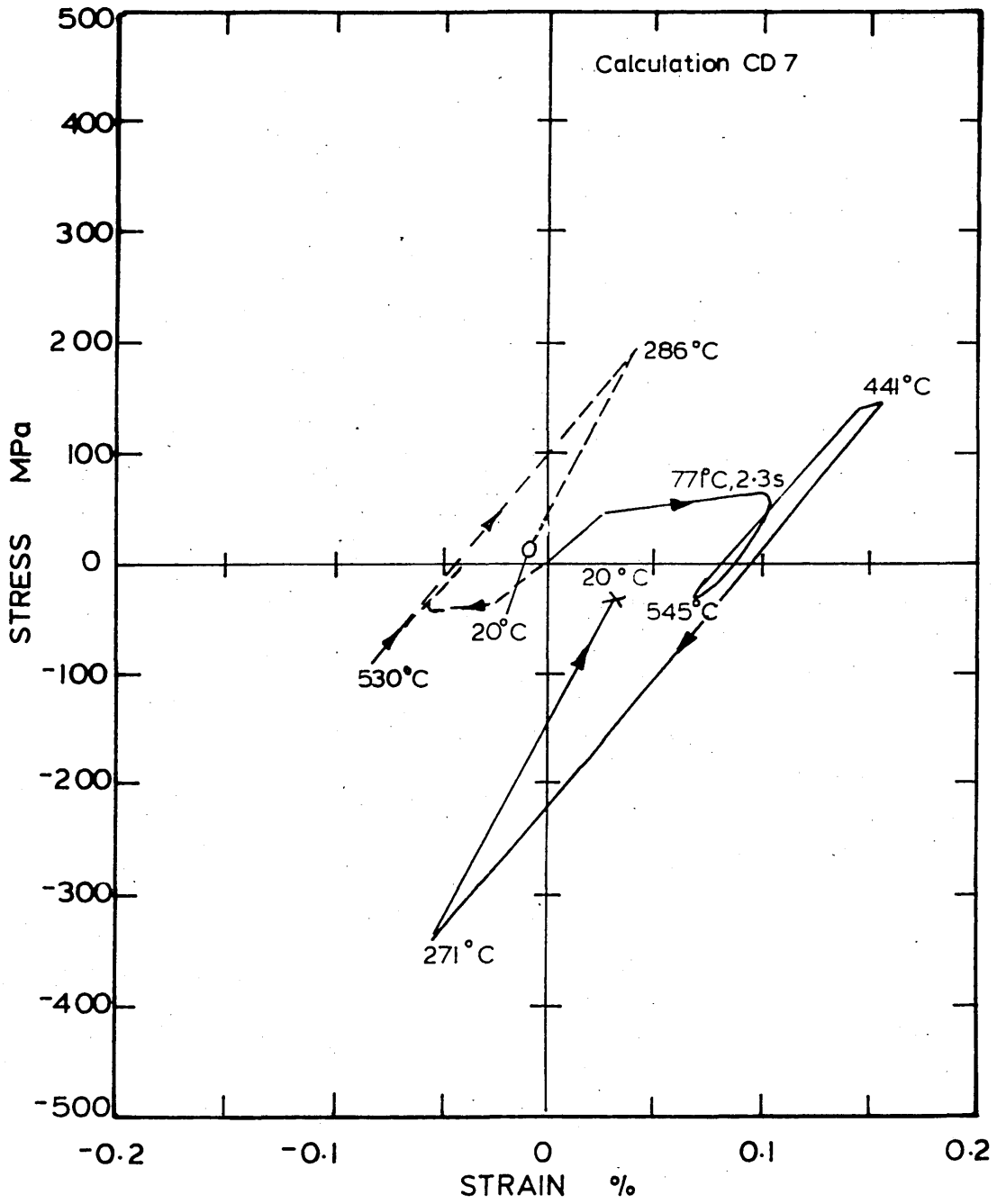
FIGURE 59:   Calculated stress and strain at the
centre and the surface of a 15mm plate
during oil quenching (viscous flow as
represented by method 3)

(Calculation CD8/O/VF3) see table 8

Calculation CD 8

251.
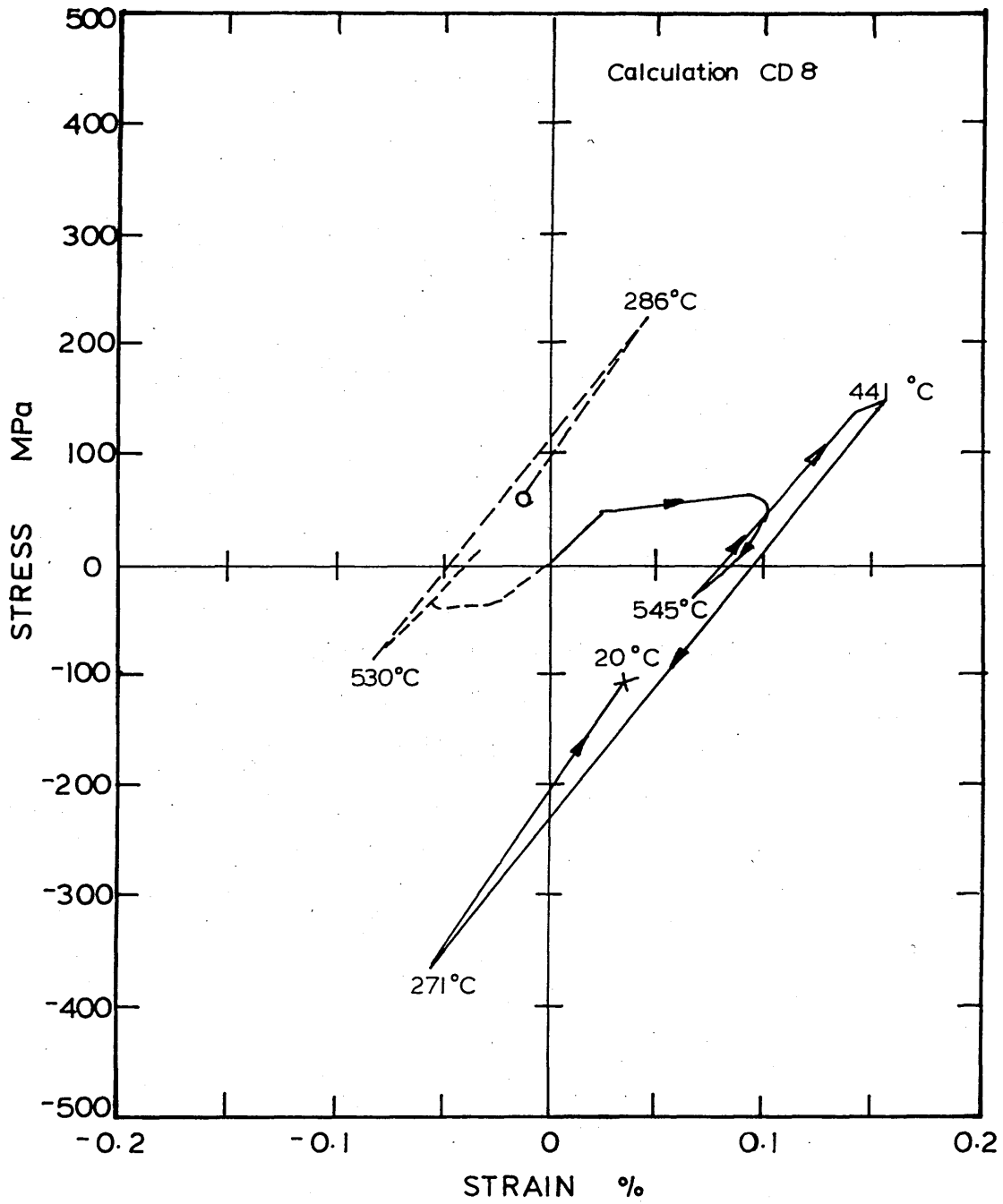
FIGURE 60:   Influence of viscous flow on the
               calculated residual stress distribution
               in a 15mm plate after oil quenching.

               Calculation no:

               CD2/O/NVF   )
               CD6/O/VF1   )
               CD7/O/VF2   )   see table 8
               CD8/O/VF3   )

252.
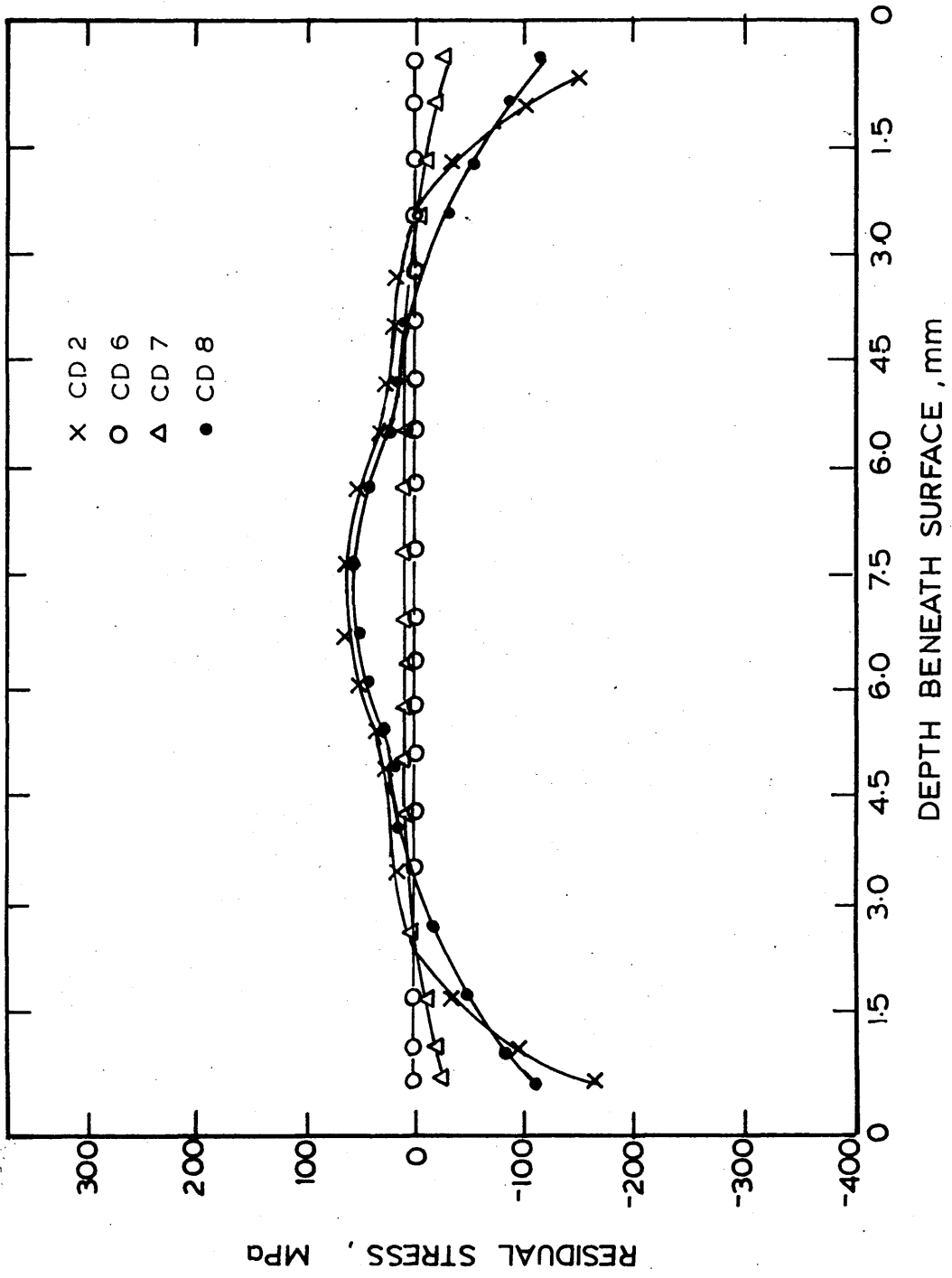
FIGURE 61:   Influence of viscous flow on the
calculated residual strain distribution
in a 15mm plate after oil quenching.

Calculation no:

CD2/O/NVF   )
CD6/O/VF1   )
CD7/O/VF2   )   see table 8
CD8/O/VF3   )

253.
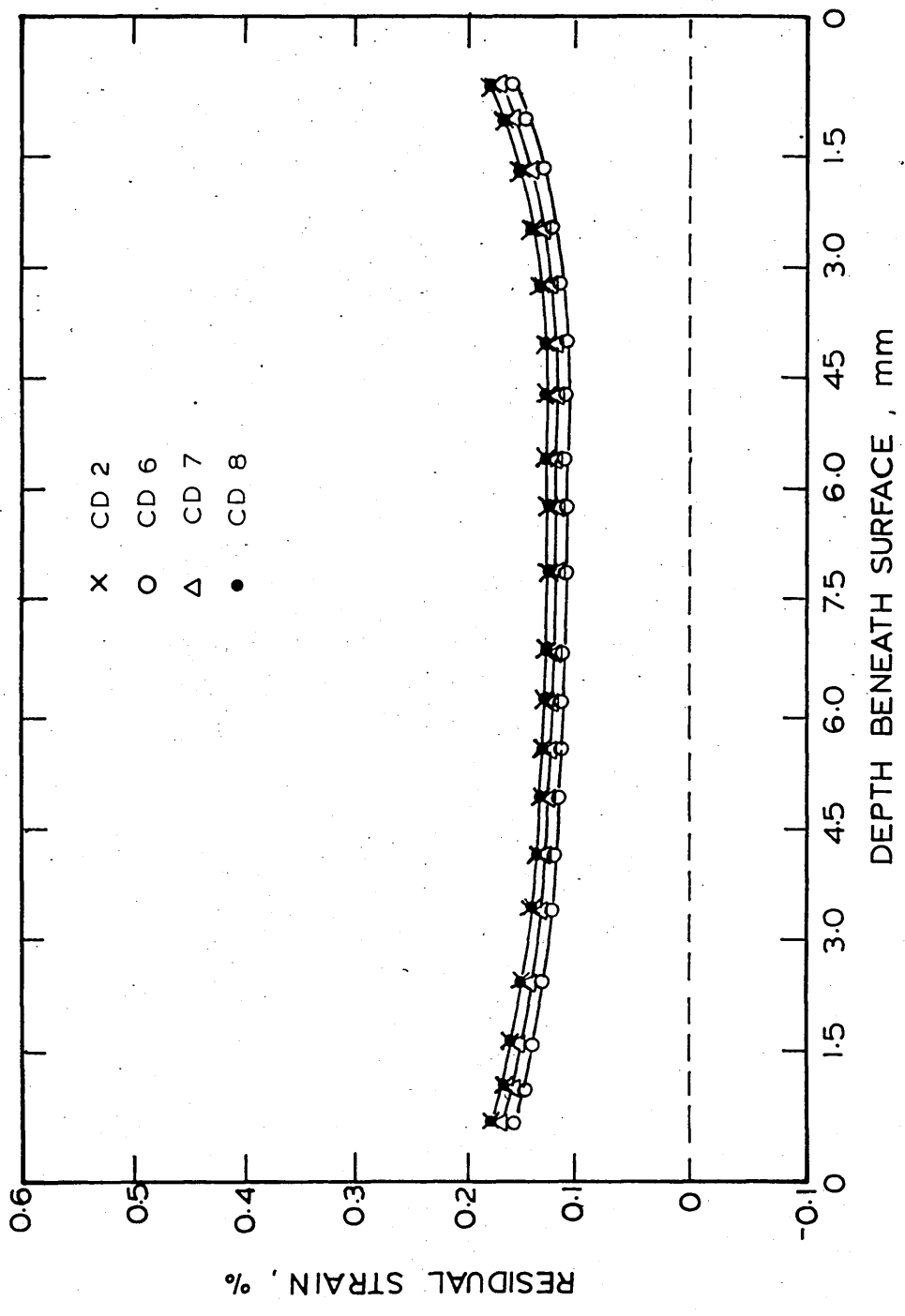
FIGURE 62:   Calculated stress and strain at the
              centre and the surface of a 15mm plate
              during martempering (no viscous flow).

              (Calculation CD3/M/NVF) see table 8

Calculation CD3

254.
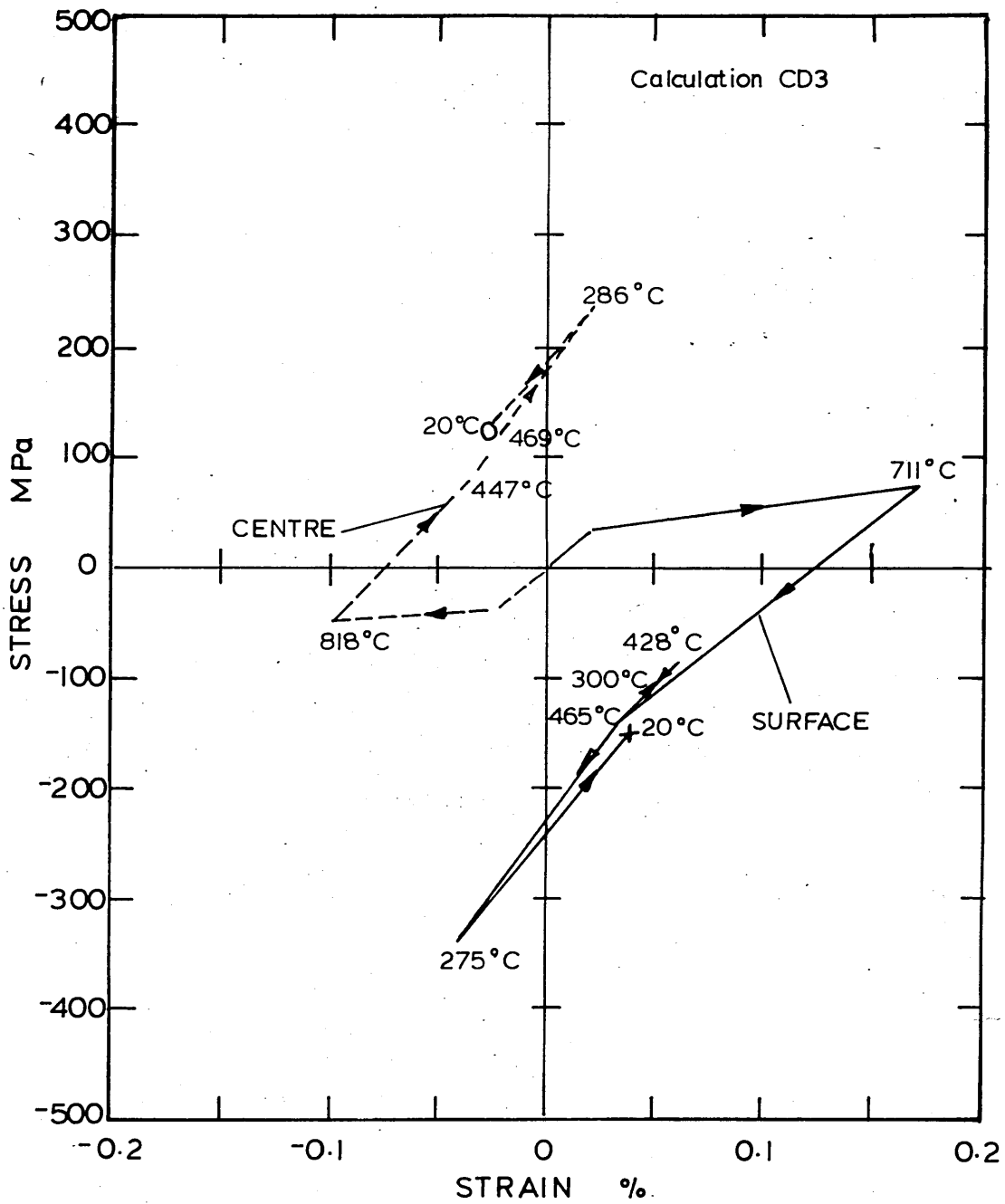
FIGURE 63:   Calculated stress and strain at the
              centre and the surface of a 15mm plate
              during martempering (viscous flow
              represented by method 1).

              (Calculation CD9/M/VF1) see table 8.

255.
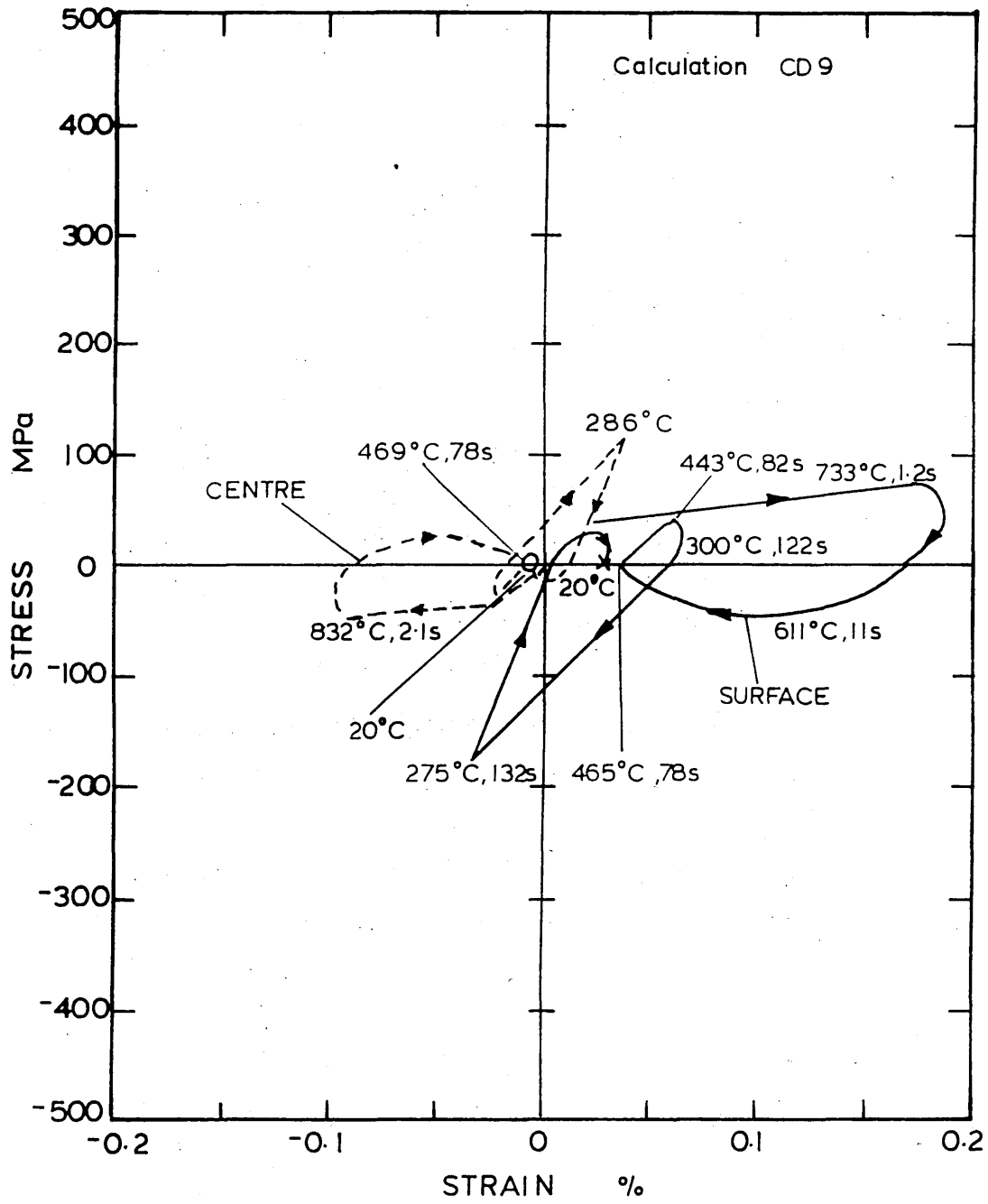
FIGURE 64:   Calculated stress and strain at the
centre and the surface of a 15mm plate
during martempering (viscous flow
represented by method 2).

(Calculation CD10/M/VF2) see table 8
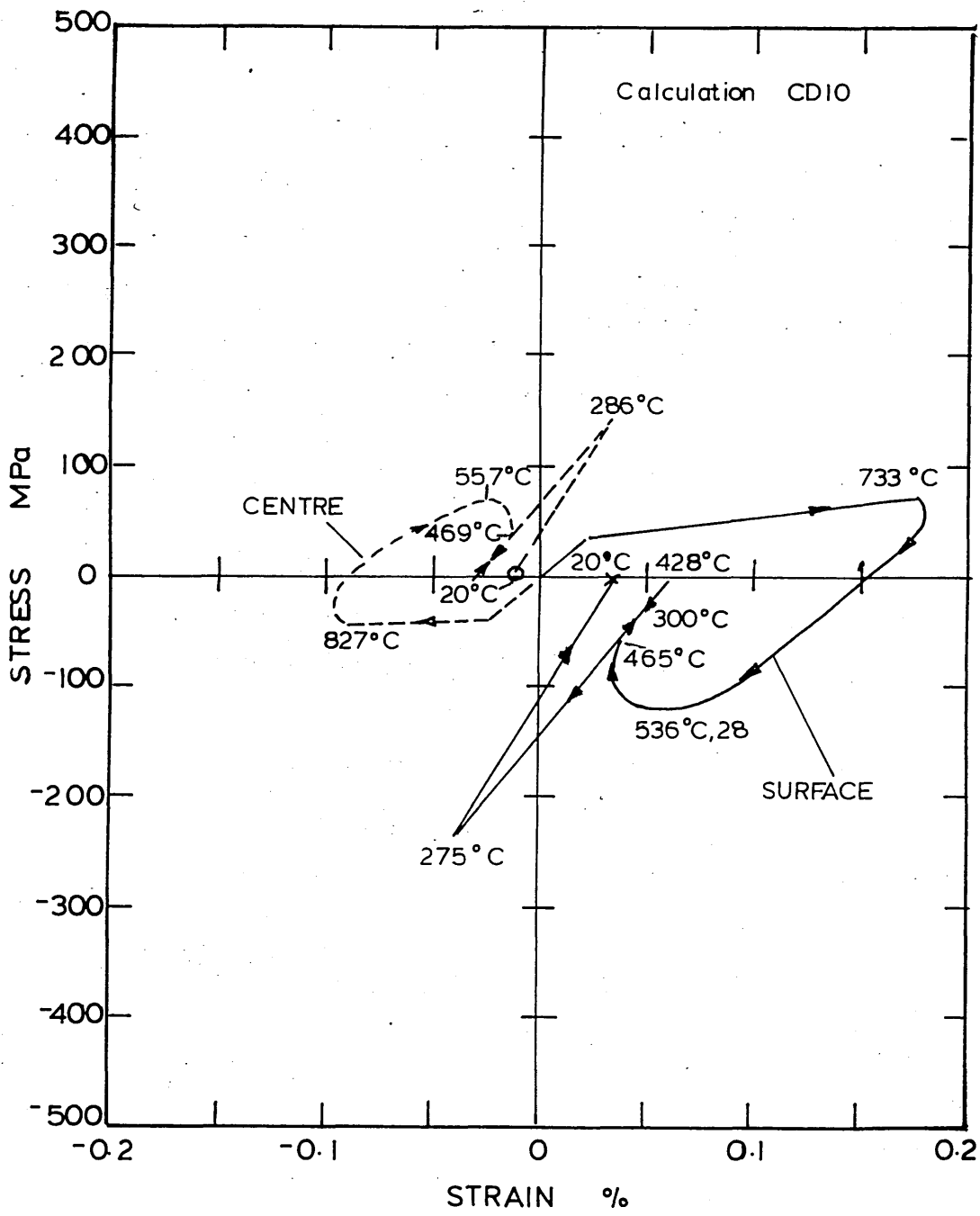
Calculation CD10

FIGURE 65:   Calculated stress and strain at the
              centre and the surface of a 15mm plate
              during martempering (viscous flow
              represented by method 3).

              (Calculation CD11/M/VF3) see table 8

Calculation CD11

257.
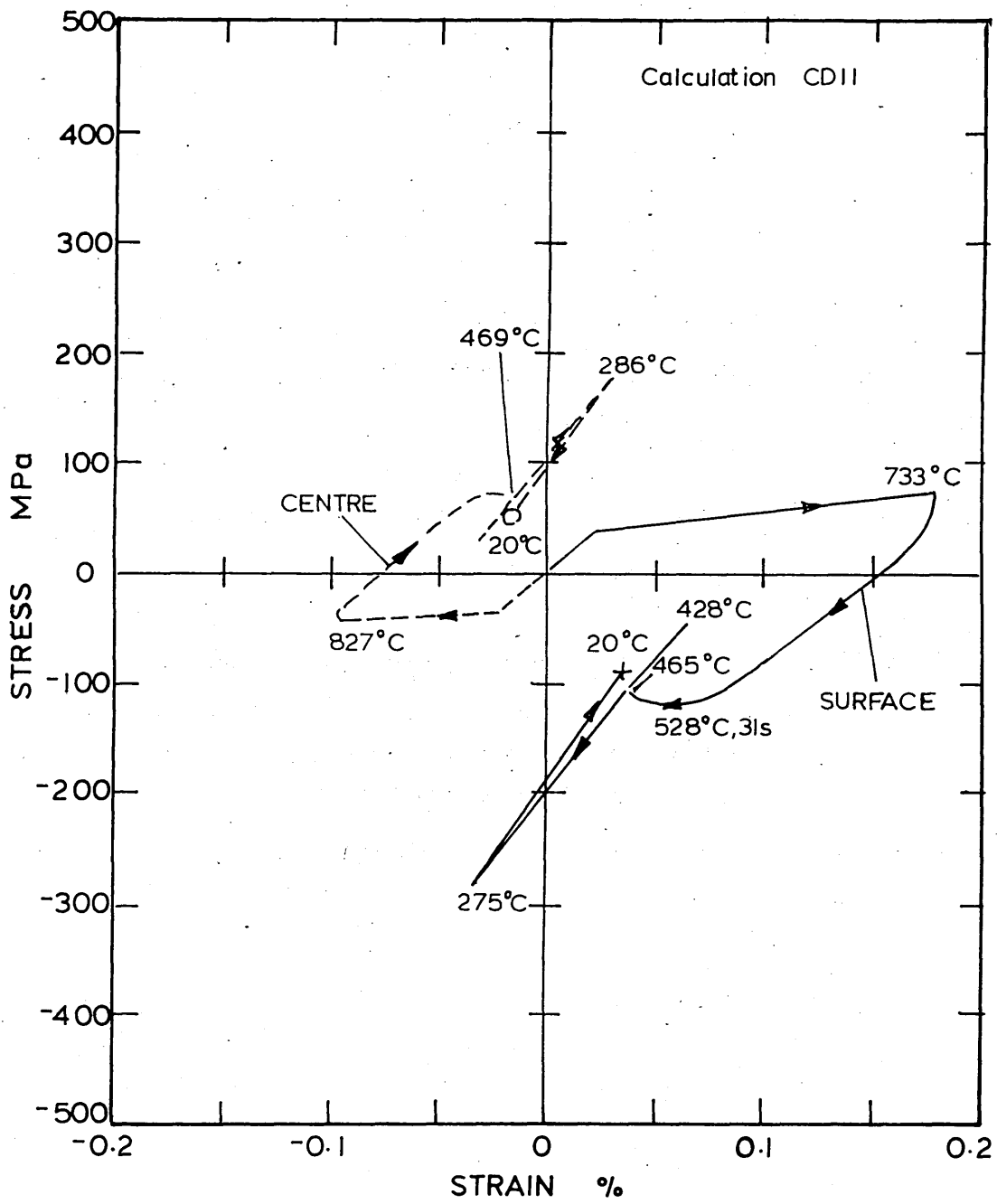
FIGURE 66:   Influence of viscous flow on the
             calculated residual stress distribution in
             a 15mm plate after martempering.

             Calculation no:

             CD3/M/NVF   )
             CD9/M/VF1   )
             CD10/M/VF2   )   see table 8
             CD11/M/VF3   )

258.
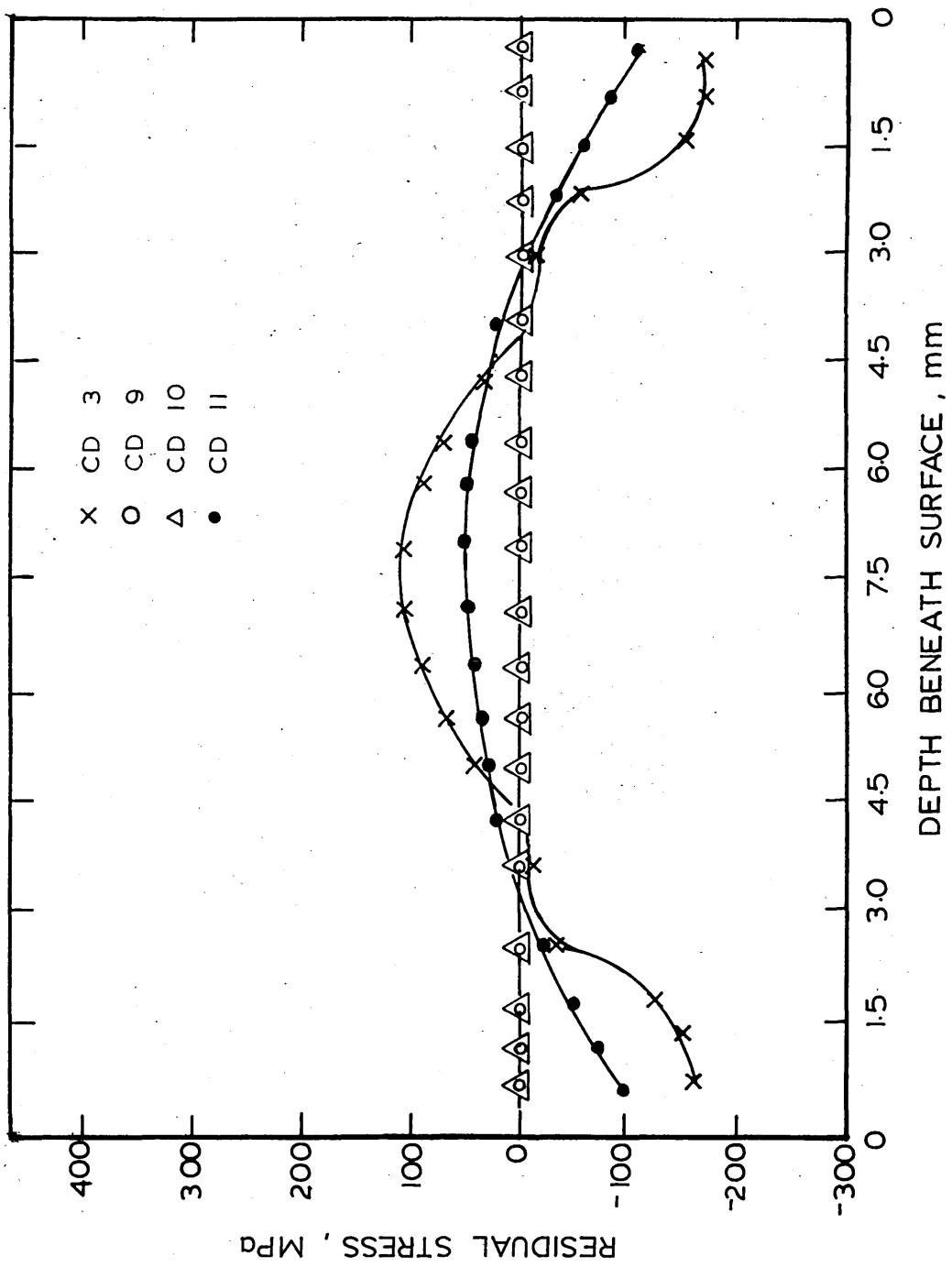
FIGURE 67:   Influence of viscous flow on the
calculated residual strain
distribution in a 15mm plate
after martempering.

Calculation no:

CD3/M/NVF   )
CD9/M/VF1   )
CD10/M/VF2   )   see table 8
CD11/M/VF3   )

259.
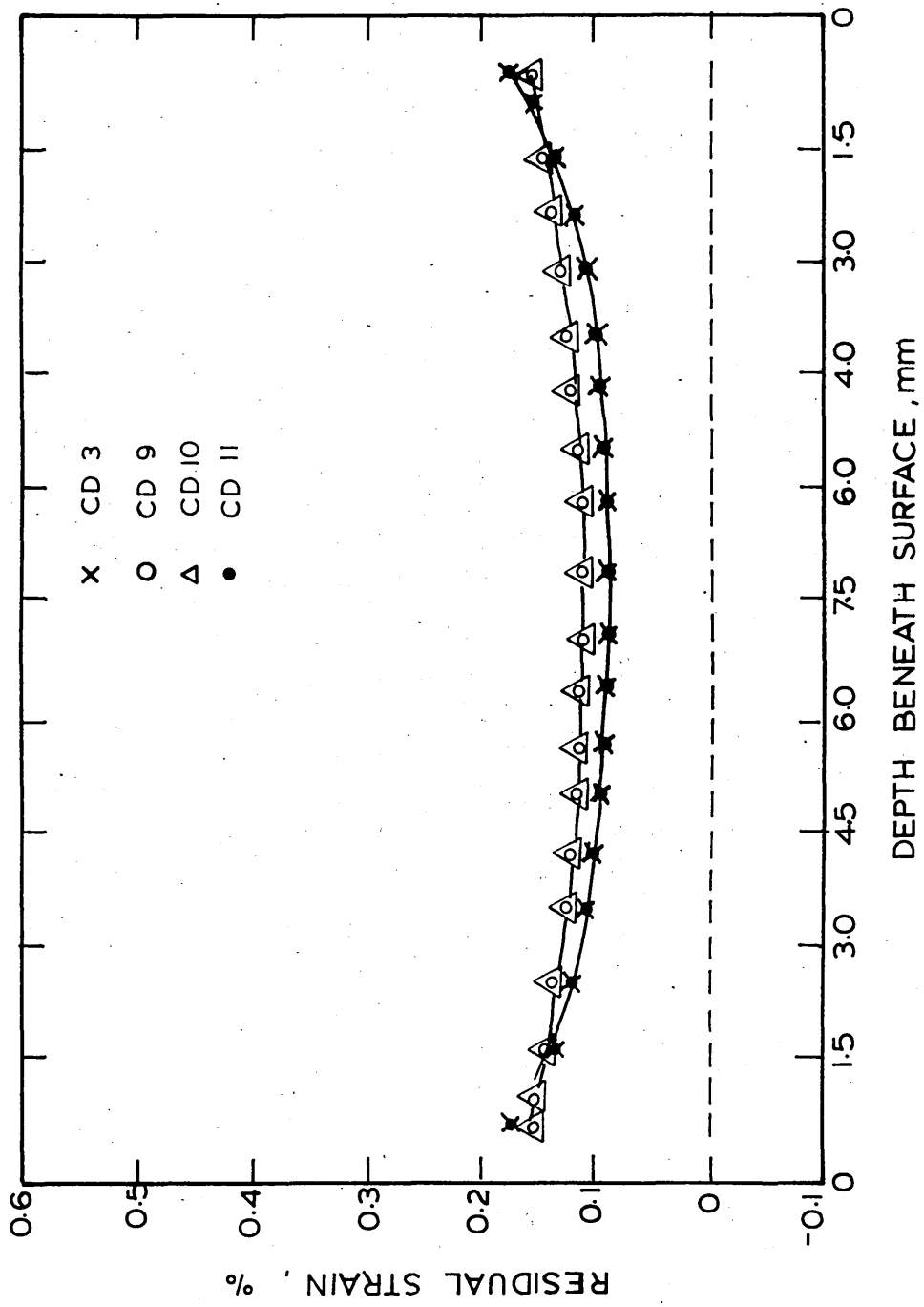
FIGURE 68:   Calculated stress and strain at the
              centre and the surface of a 20mm
              plate during water quenching (reduction
              in flow stress to simulate transformation
              plasticity and viscous flow represented
              by method 2).   ·

              (Calculation CD12/W/VF2/FSR) see table 8

Calculation CD12

SURFACE

CENTRE

300°C

20°C
286°C
273°C
265°C
265°C
20°CO

STRAIN   %

STRESS MPa

500 250 0 -250 -500 -750 -1000 -1250

-0.6 -0.4 -0.2 0 0.2 0.4 0.6

260.
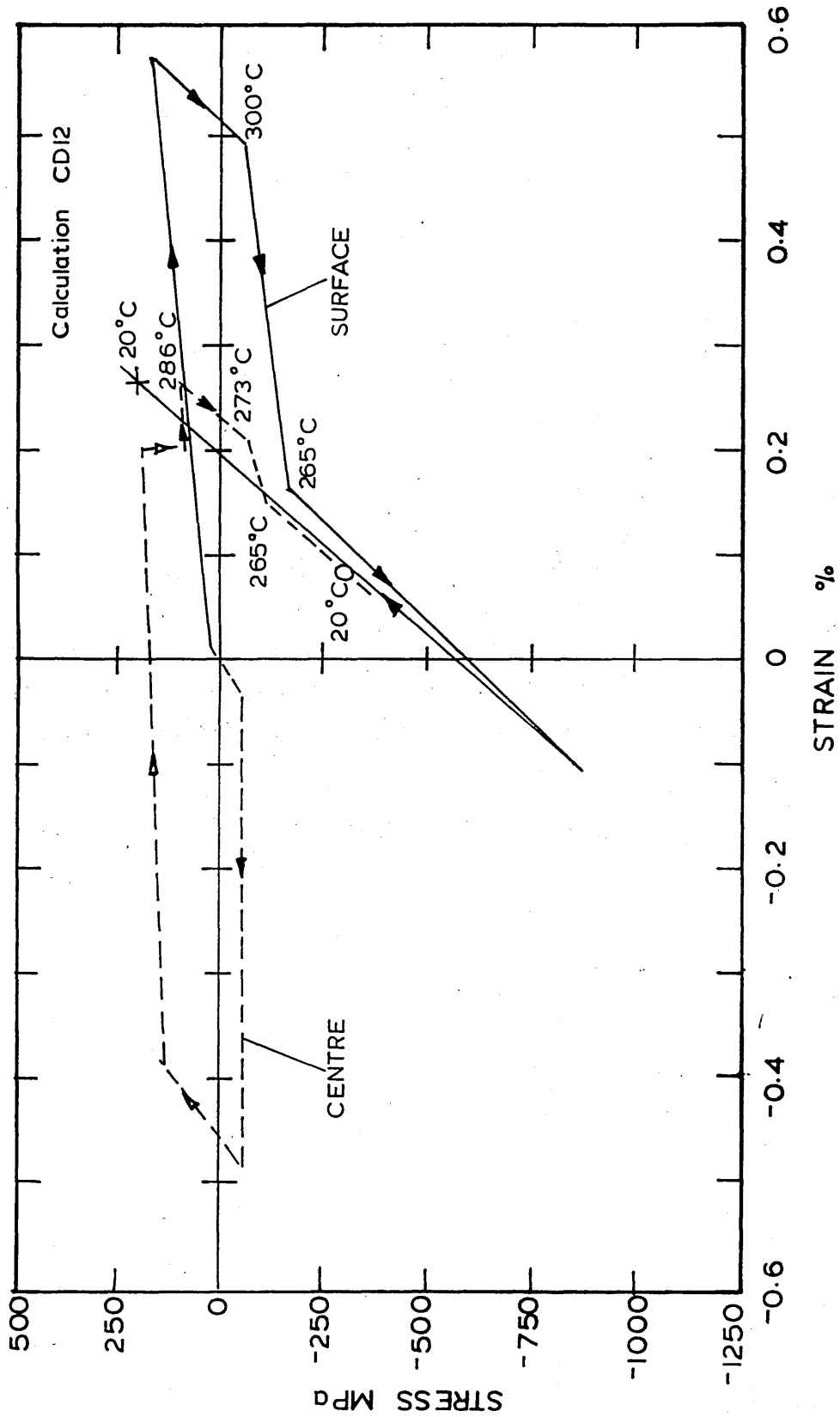
FIGURE 69:   Calculated stress and strain at the
             centre and the surface of a 20mm plate
             during water quenching (reduction in
             the flow stress to simulate transformation
             plasticity and viscous flow represented
             by method 1).

             (Calculation CD13/W/VF1/FSR) see table 8

Calculated CD13

STRAIN , %

STRESS , MPa

261.
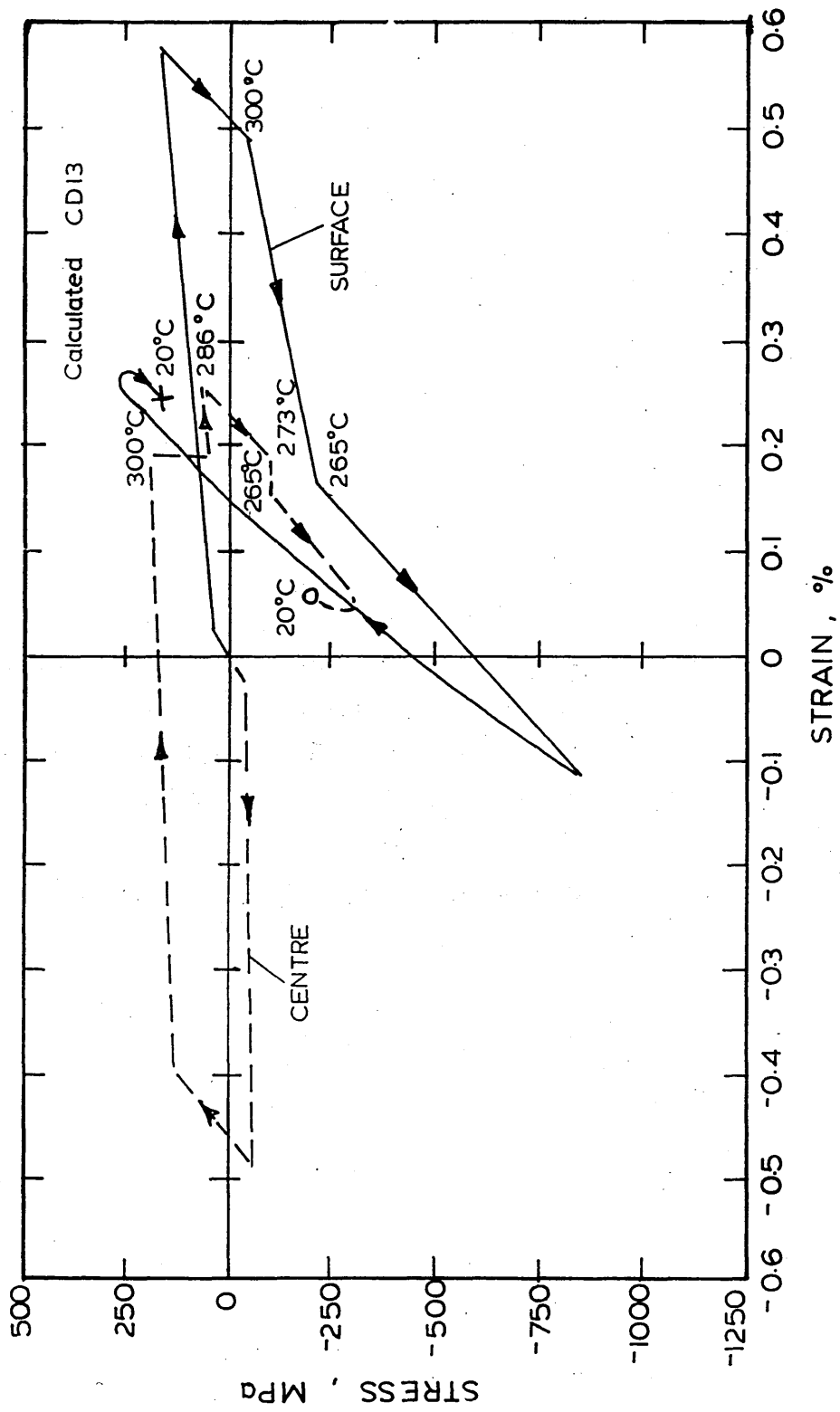
FIGURE 70:   Calculated residual stress distributions
in a 20mm plate after water quenching
(include viscous flow and a reduction in
flow stress to simulate transformation
plasticity).

Calculation no:

CD12/W/VF2/FSR   )
CD13/W/VF1/FSR   )   see table 8

262.
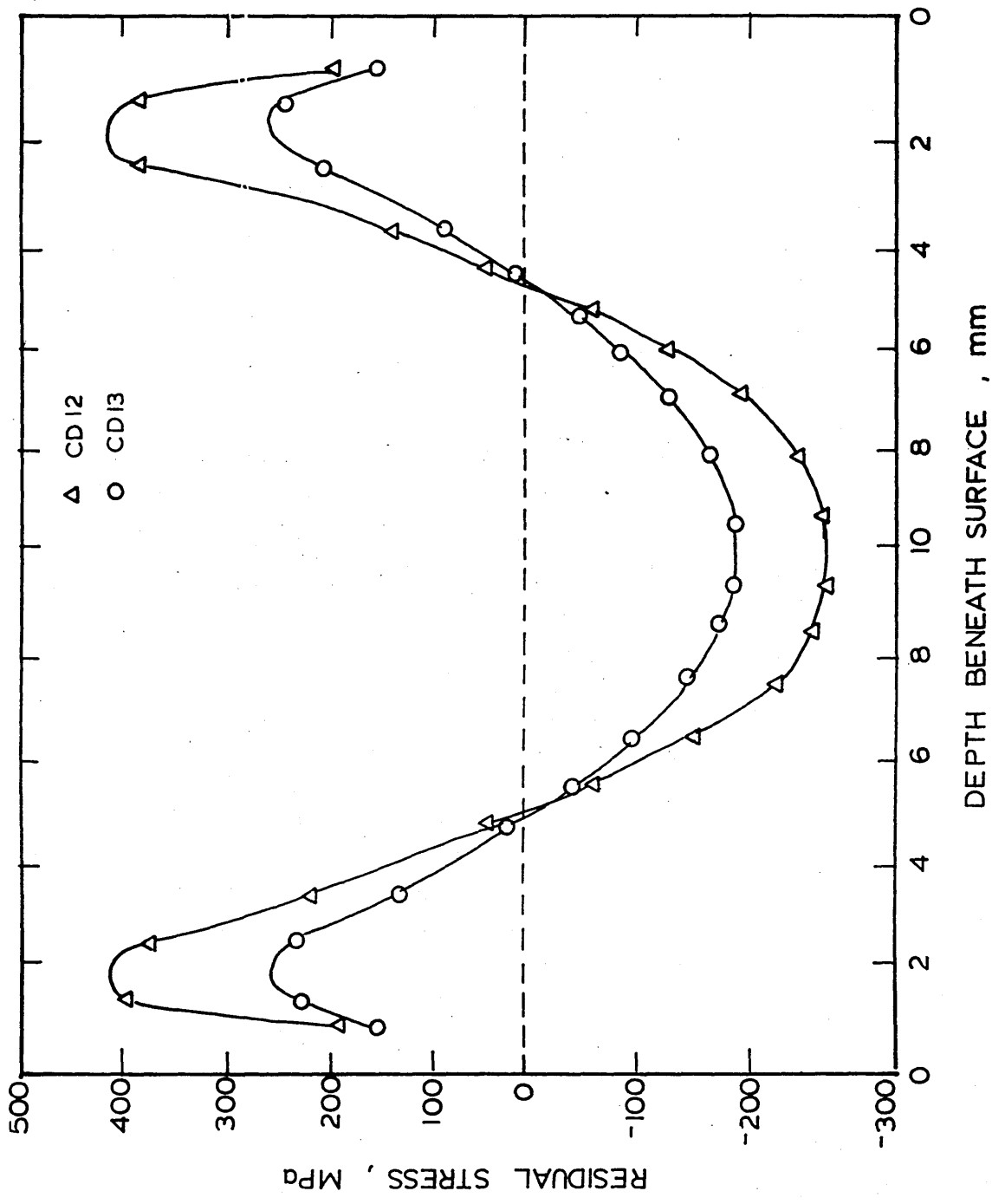
FIGURE 71:   Calculated residual strain distributions
              in a 20mm plate after water quenching
              (include viscous flow and a reduction in
              flow stress to simulate transformation
              plasticity).

              Calculation no:

              CD12/W/VF2/FSR   )   see table 8
              CD13/W/VF1/FSR   )

263.
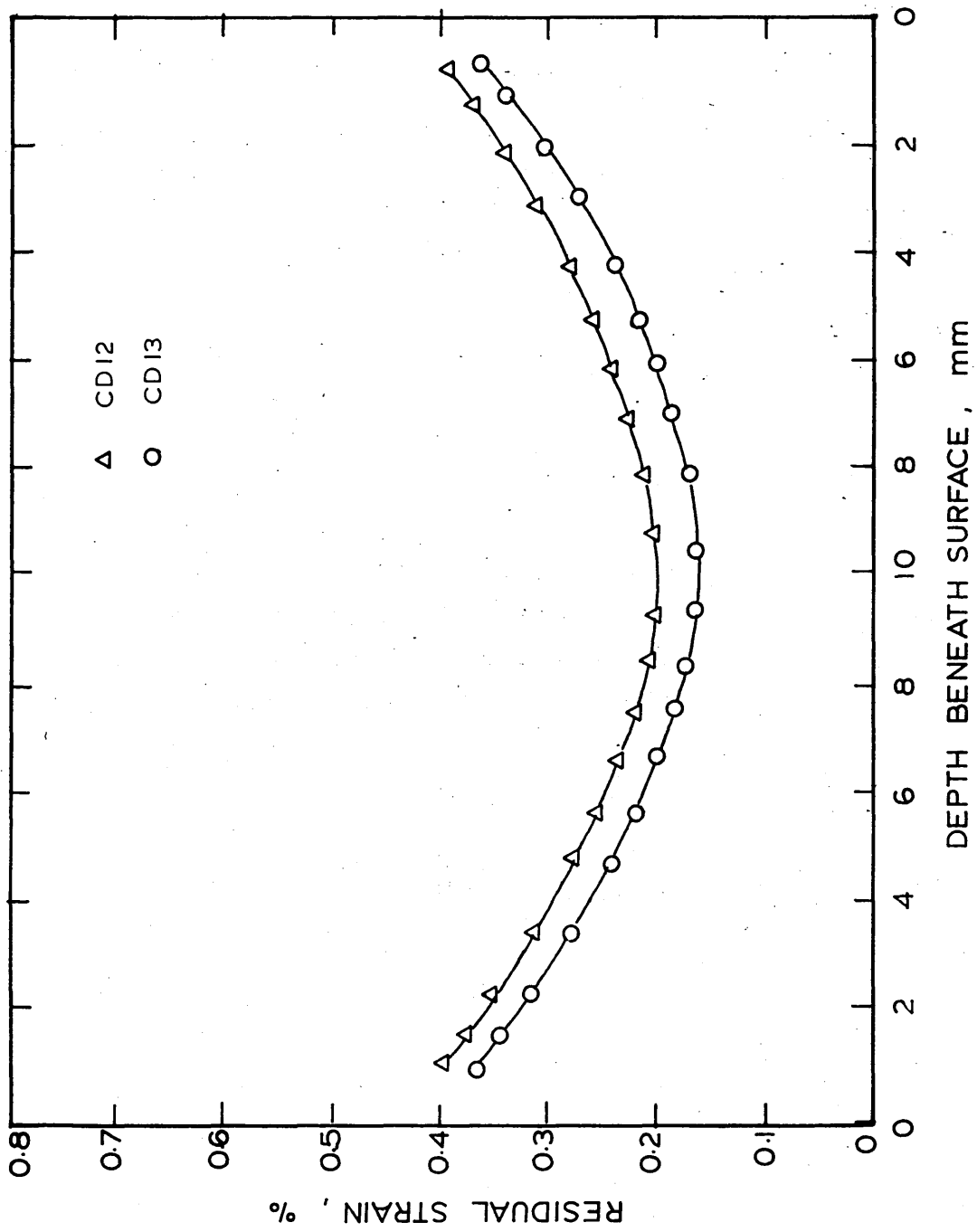
FIGURE 72:   Calculated stress and strain at the
               centre and the surface of a 15mm plate
               during oil quenching (reduction in the
               flow stress to simulate transformation
               plasticity and viscous flow represented
               by method 2).

               (Calculation CD14/O/VF2/FSR) see table 8

264.
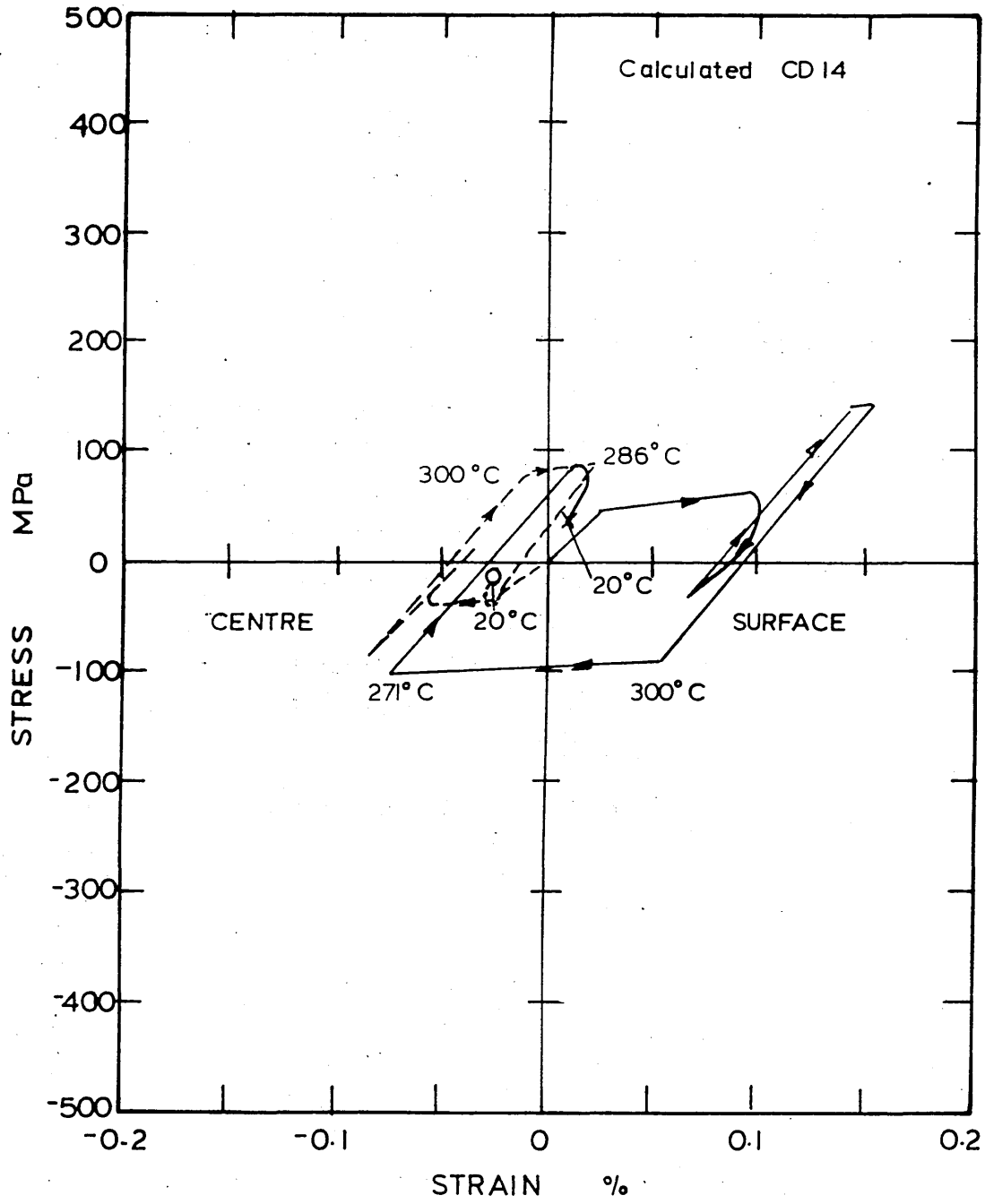
FIGURE 73:   Calculated stress and strain at the
              centre and the surface of a 15mm
              plate during oil quenching (reduction
              in the flow stress to simulate
              transformation plasticity and viscous
              flow represented by method 1).

              (Calculation CD15/0/VF1/FSR) see table 8
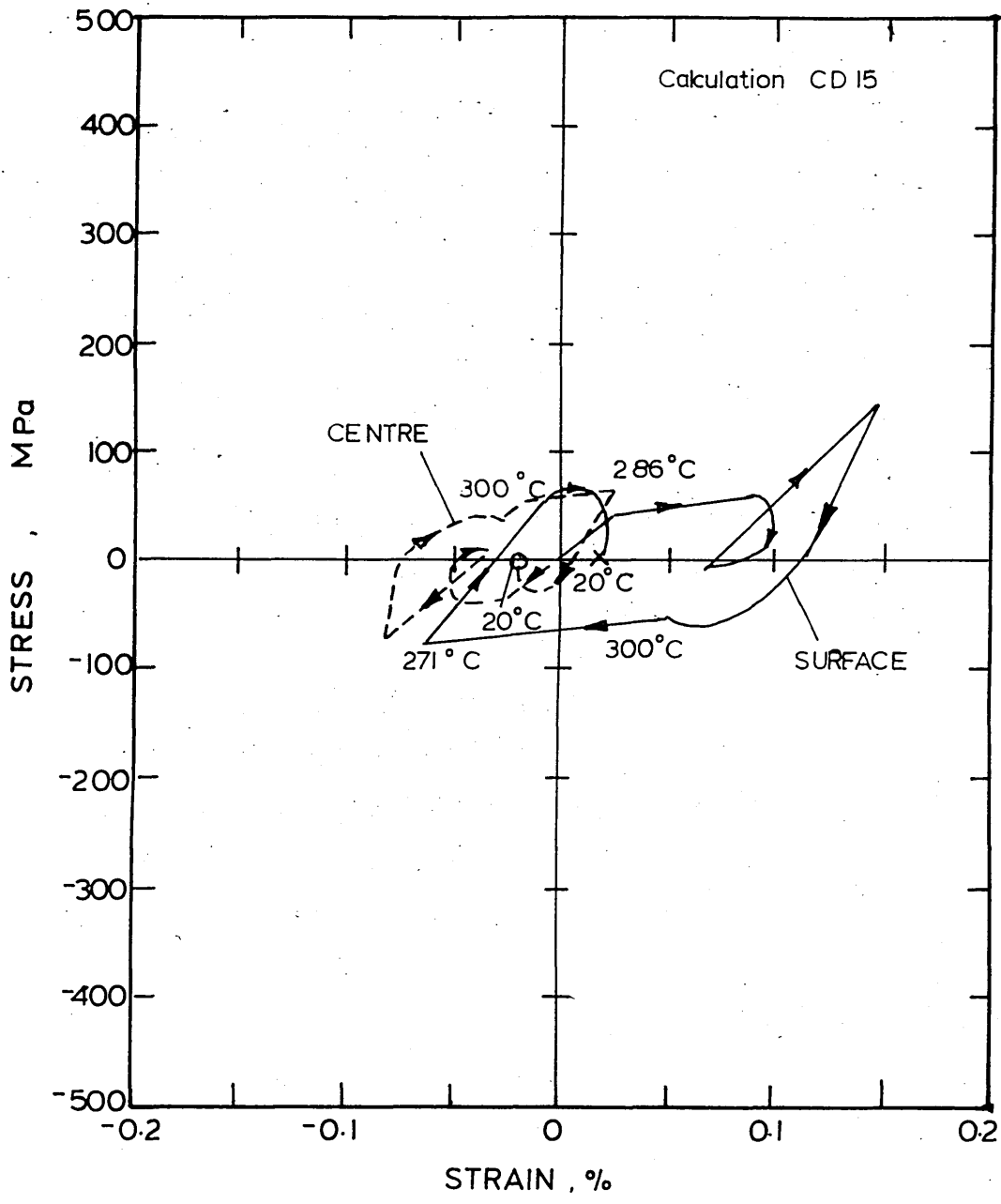
FIGURE 74:   Calculated residual stress distributions
in a 15mm plate after oil quenching
(include viscous flow and a reduction in
flow stress to simulate transformation
plasticity).

Calculation no:

CD14/O/VF2/FSR   )
CD15/O/VF1/FSR   )   see table 8
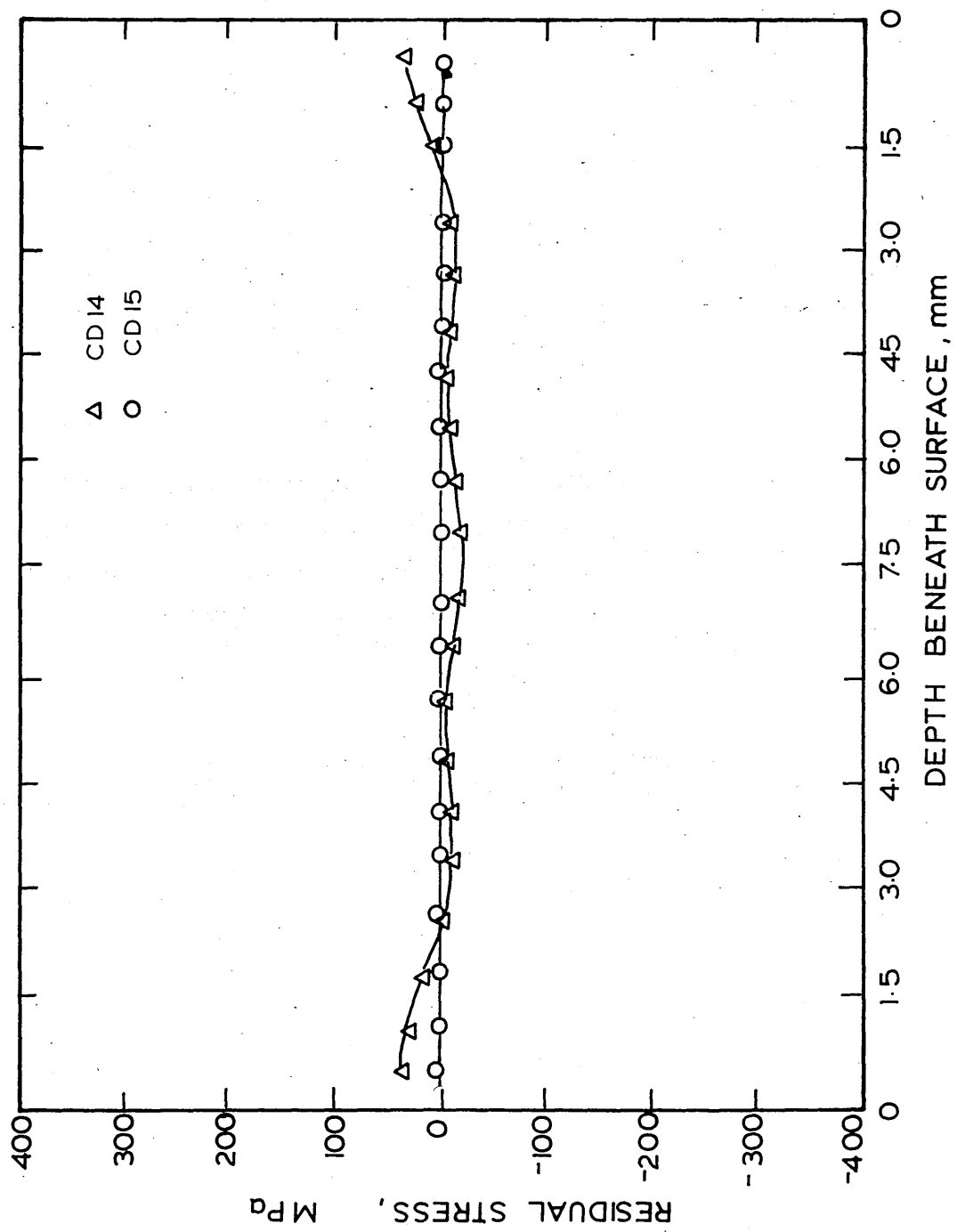
FIGURE 75:   Calculated residual strain distributions
in a 15mm plate after oil quenching
(include viscous flow and a reduction in
flow stress to simulate transformation
plasticity).

Calculation no:

CD14/O/VF2/FSR   )   see table 8
CD15/O/VF1/FSR   )

267.
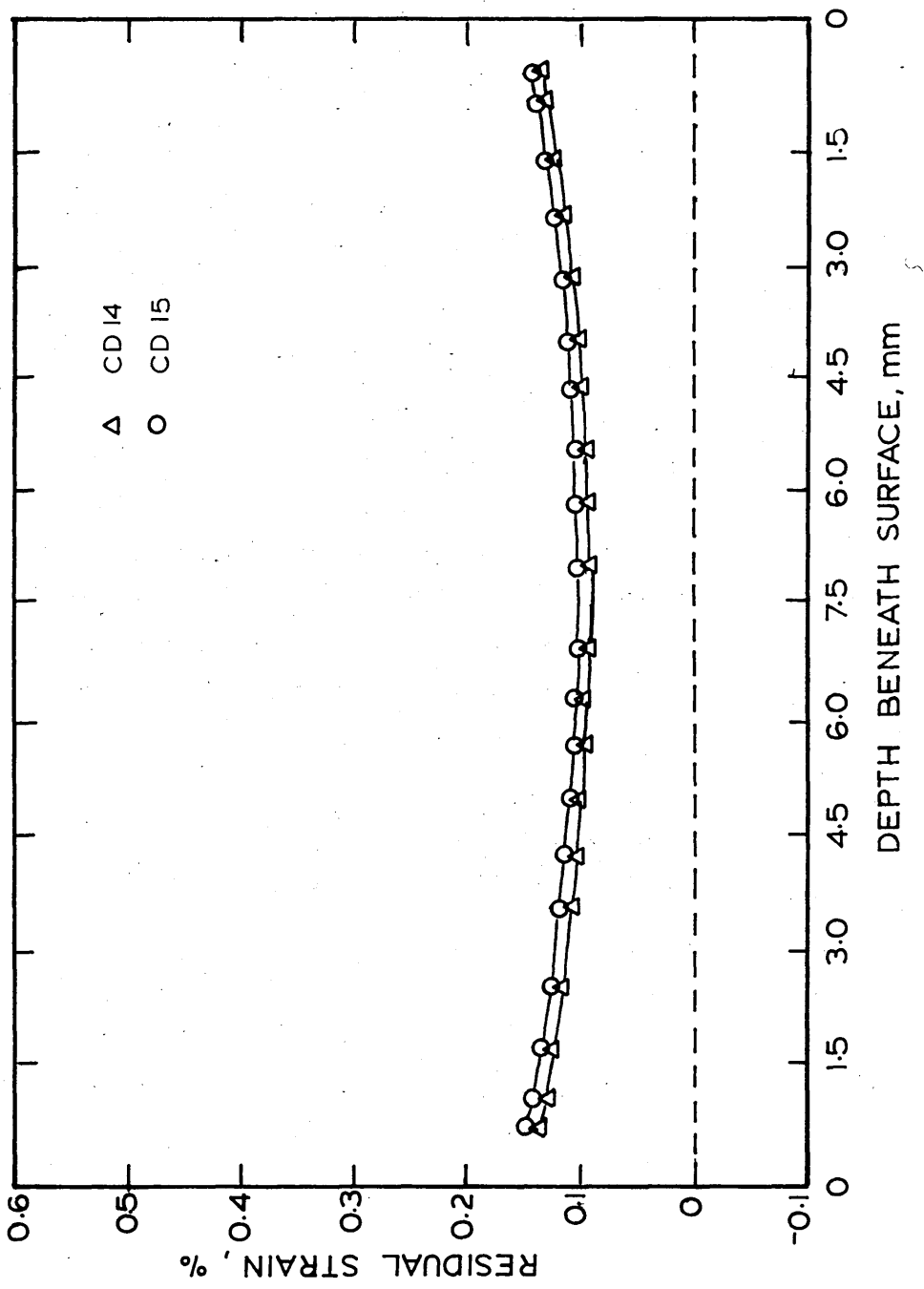
FIGURE 76:   Calculated stress and strain at the
               centre and the surface of a 20mm
               plate during water quenching
               (transformation plasticity simulated
               as additional strain and viscous flow
               represented by method 2).

               (Calculation CD16/0/VF2/TPAS) see table 8

Calculation CD 16

SURFACE

CENTRE

STRAIN %

STRESS MPa

268.
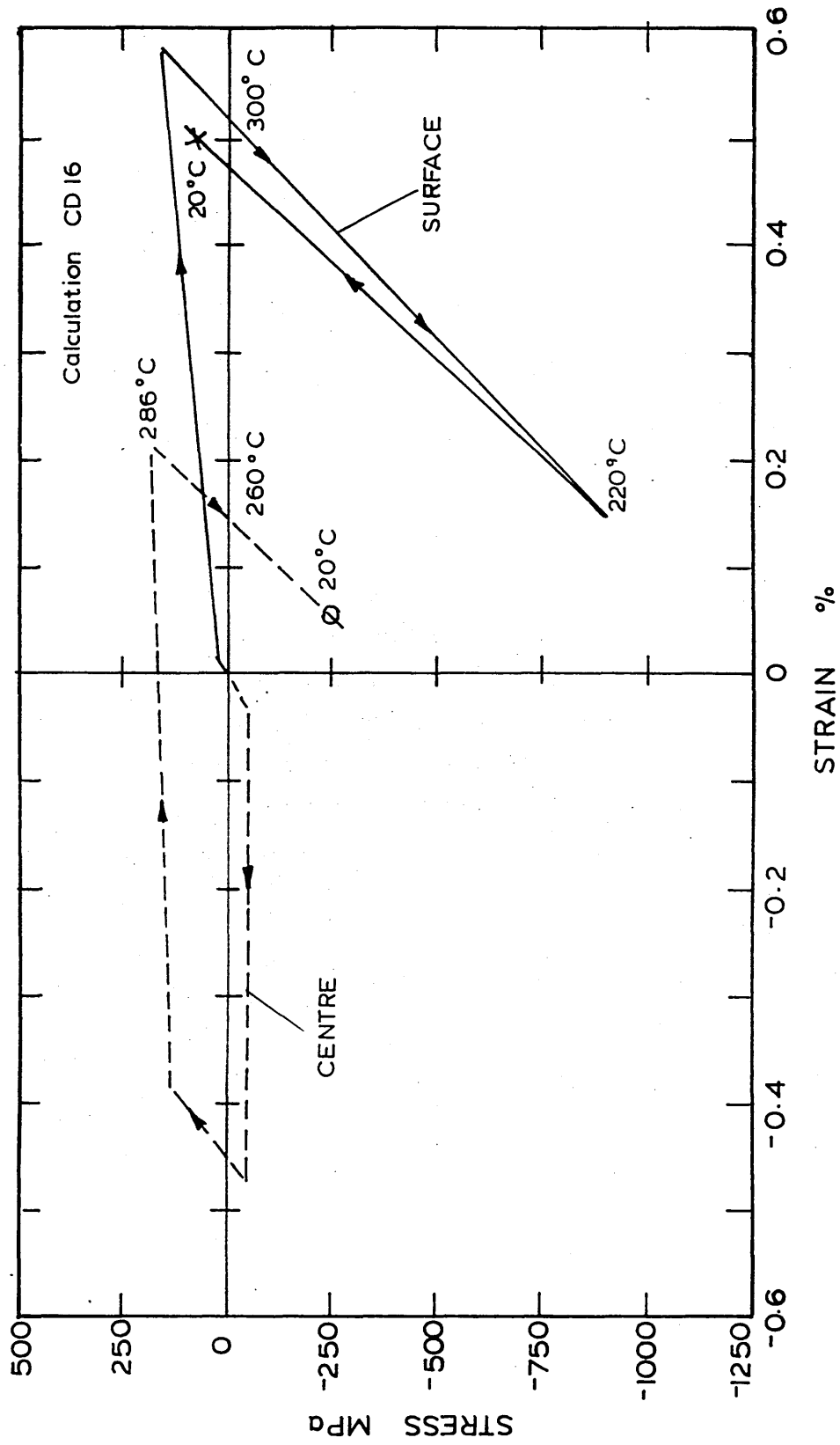
FIGURE 77:   Calculated stress and strain at the
              centre and surface of a 20mm plate
              during water quenching (transformation
              plasticity simulated as additional
              strain and viscous flow represented
              by method 1).

              (Calculation CD17/W/VF1/TPAS) see table 8

Calculation CD17

SURFACE

CENTRE

STRAIN %

STRESS MPa

Temperature labels on curves: 137°C, 20°C, 300°C, 260°C, 220°C, 286°C, 260°C, 20°C, 194°C

269.
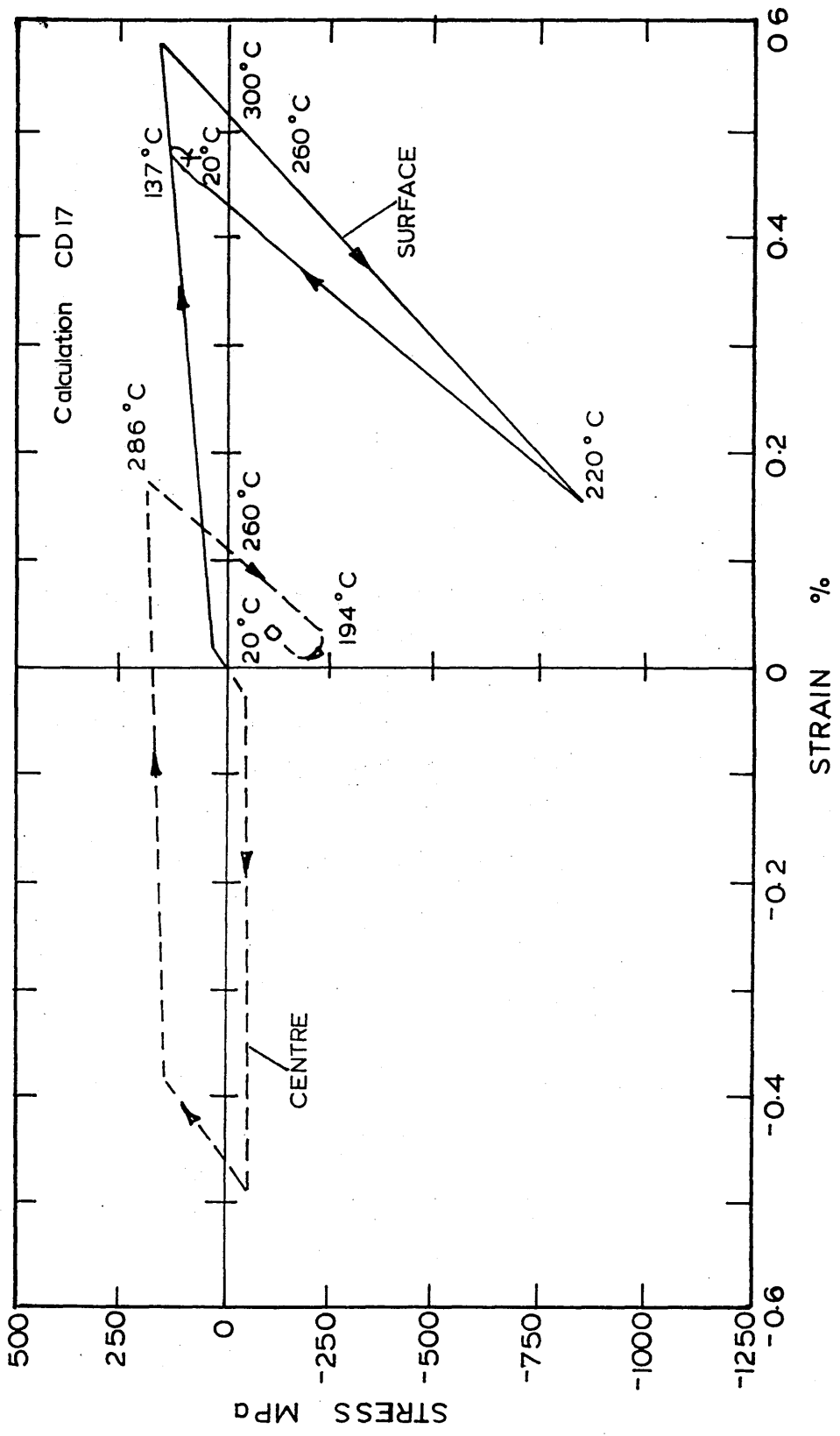
FIGURE 78:   Calculated residual stress distribution
               in a 20mm plate after water quenching
            (includes viscous flow and transformation
               plasticity simulated as additional
               strain).

   Calculation no:

               CD16/W/VF2/TPAS   )
               CD17/W/VF1/TPAS   )   see table 8
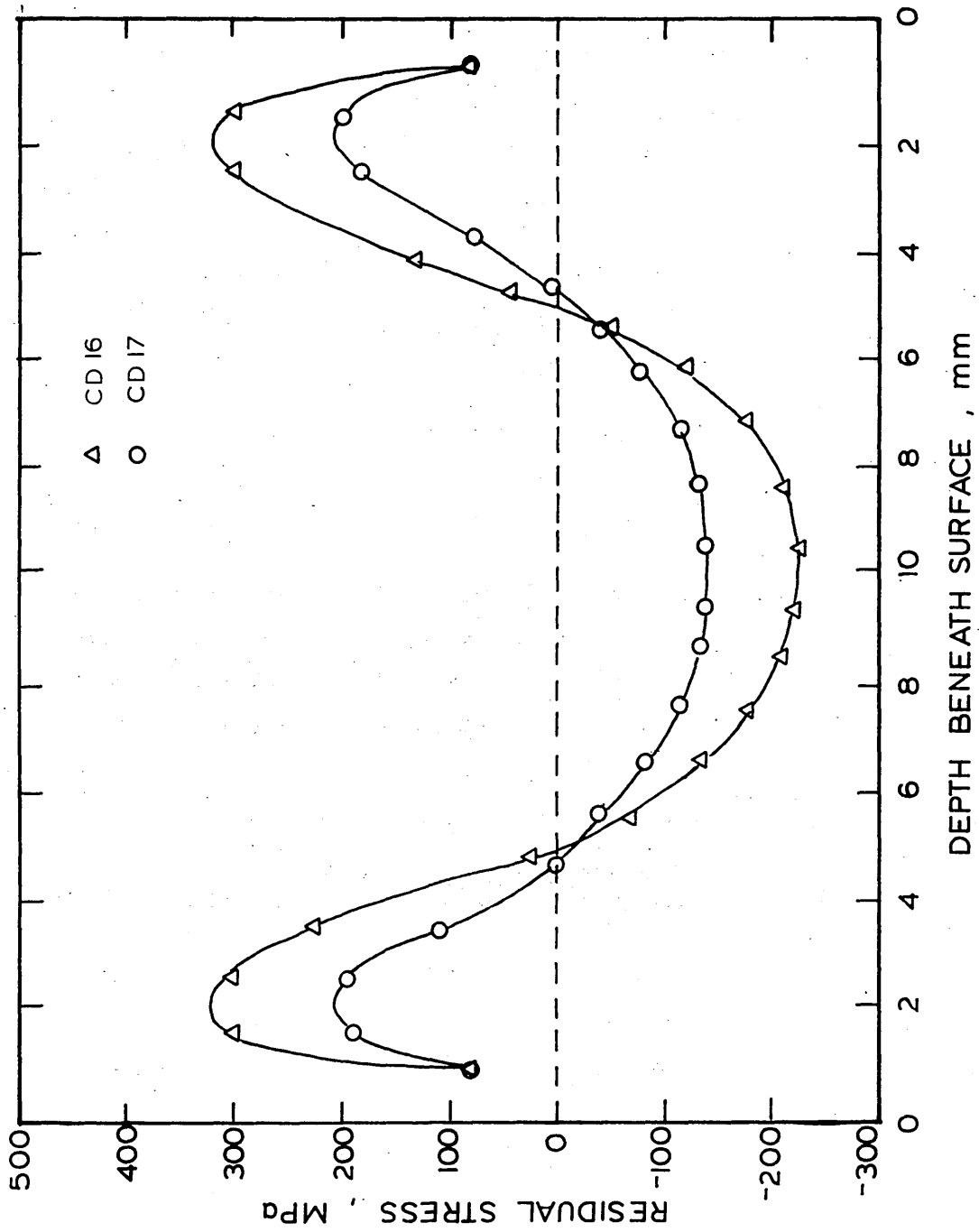
FIGURE 79:   Calculated residual strain distribution
              in a 20mm plate after water quenching
              (includes viscous flow and transformation
              plasticity simulated as additional strain).

              Calculation no:

   CD16/W/VF2/TPAS   )
              CD17/W/VF1/TPAS   ) see table 8

271.
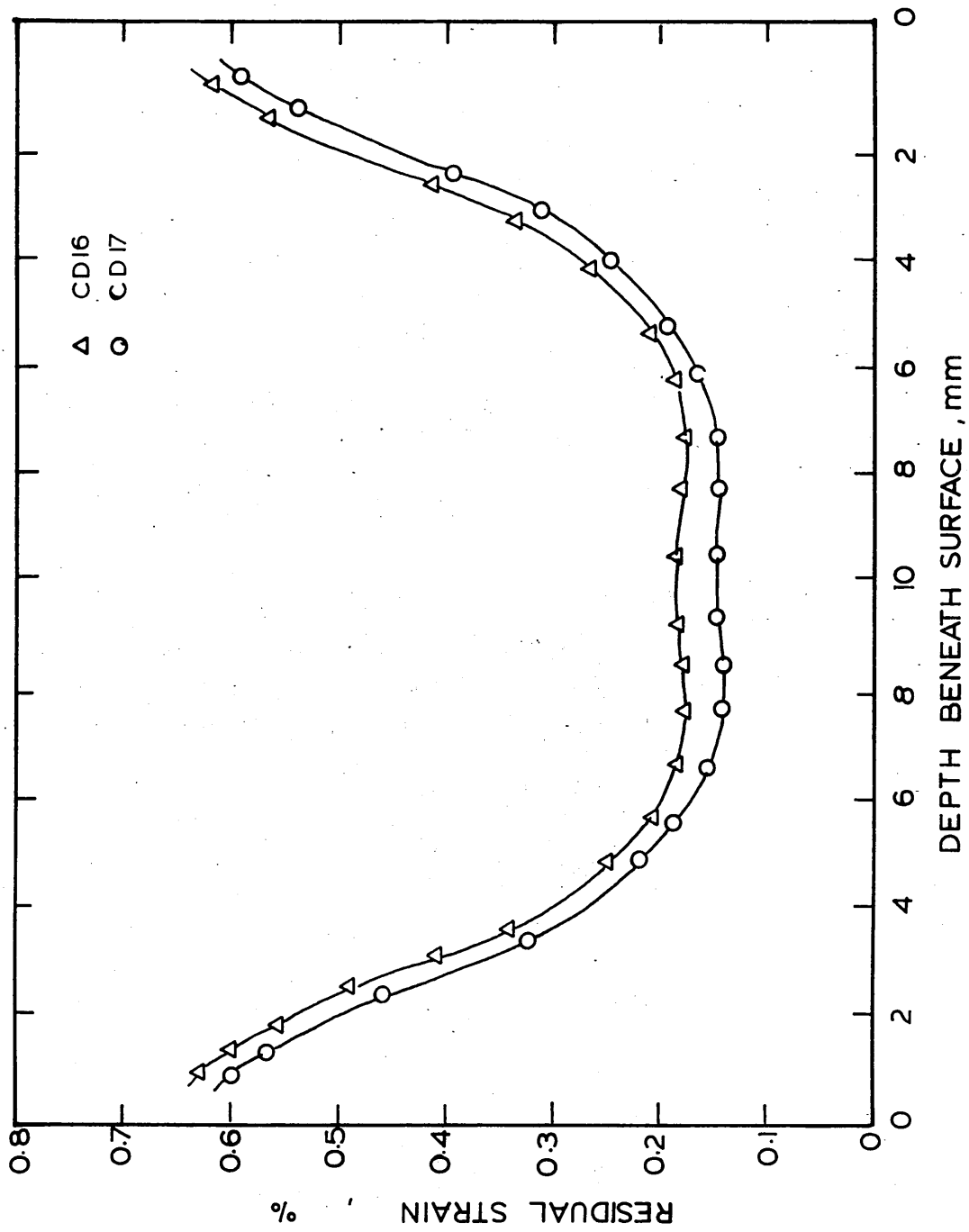
FIGURE 80:   Calculated stress and strain at the
              centre and the surface of a 15mm
              plate during oil quenching (transformation
              plasticity simulated as additional strain
              and viscous flow represented by method 2).

              (Calculation CD18/O/VF2/TPAS) see table 8

272.
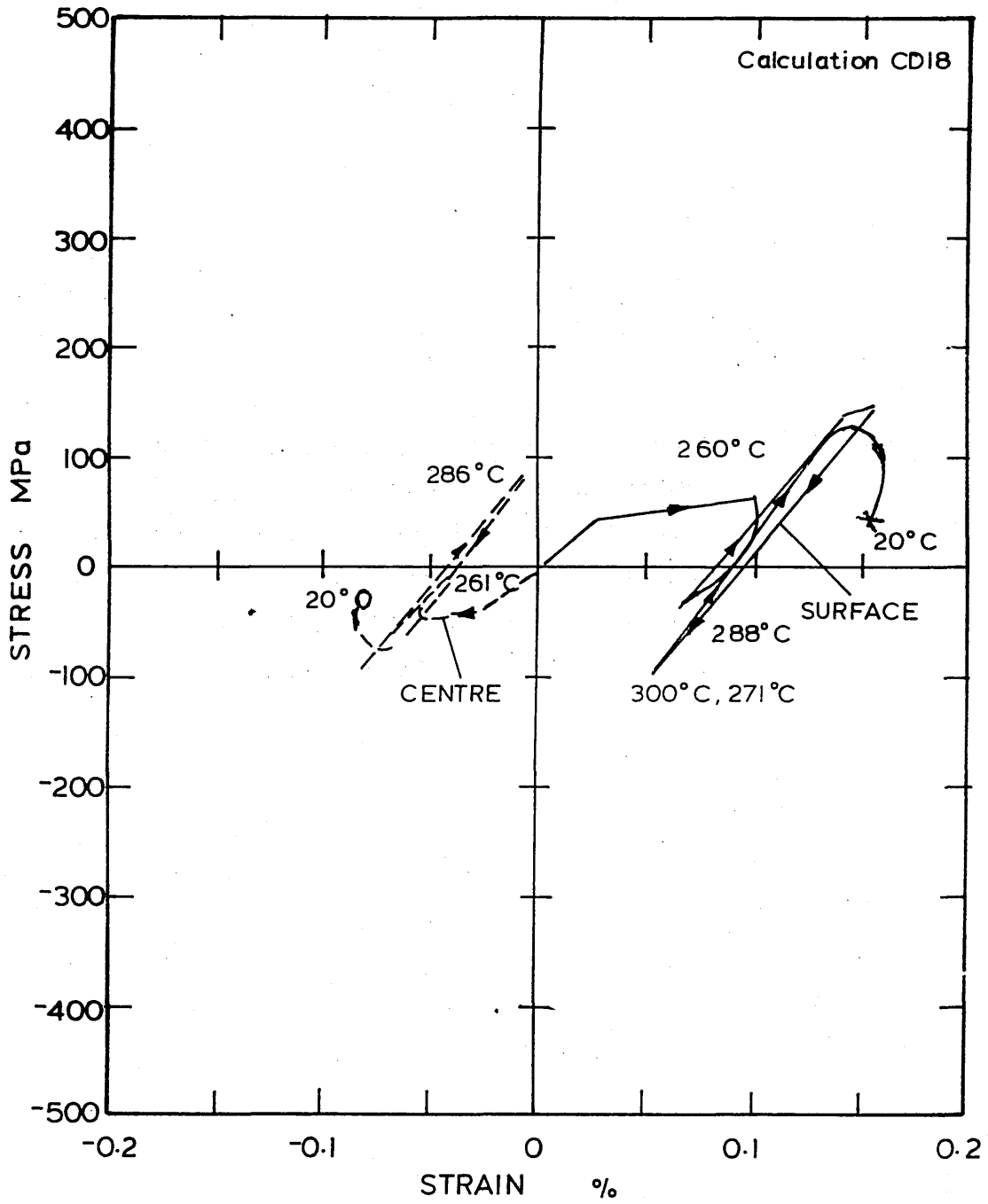
FIGURE 81:   Calculated stress and strain at the
centre and the surface of a 15mm plate
during oil quenching (transformation
plasticity simulated as additional
strain and viscous flow represented
by method 1).

(Calculation CD19/O/VF1/TPAS) see table 8

273a.

Calculation CD 19

STRESS MPa versus STRAIN %

286°C

20°C

261°C

20°C

300°C

CENTRE

261°C

SURFACE

273.
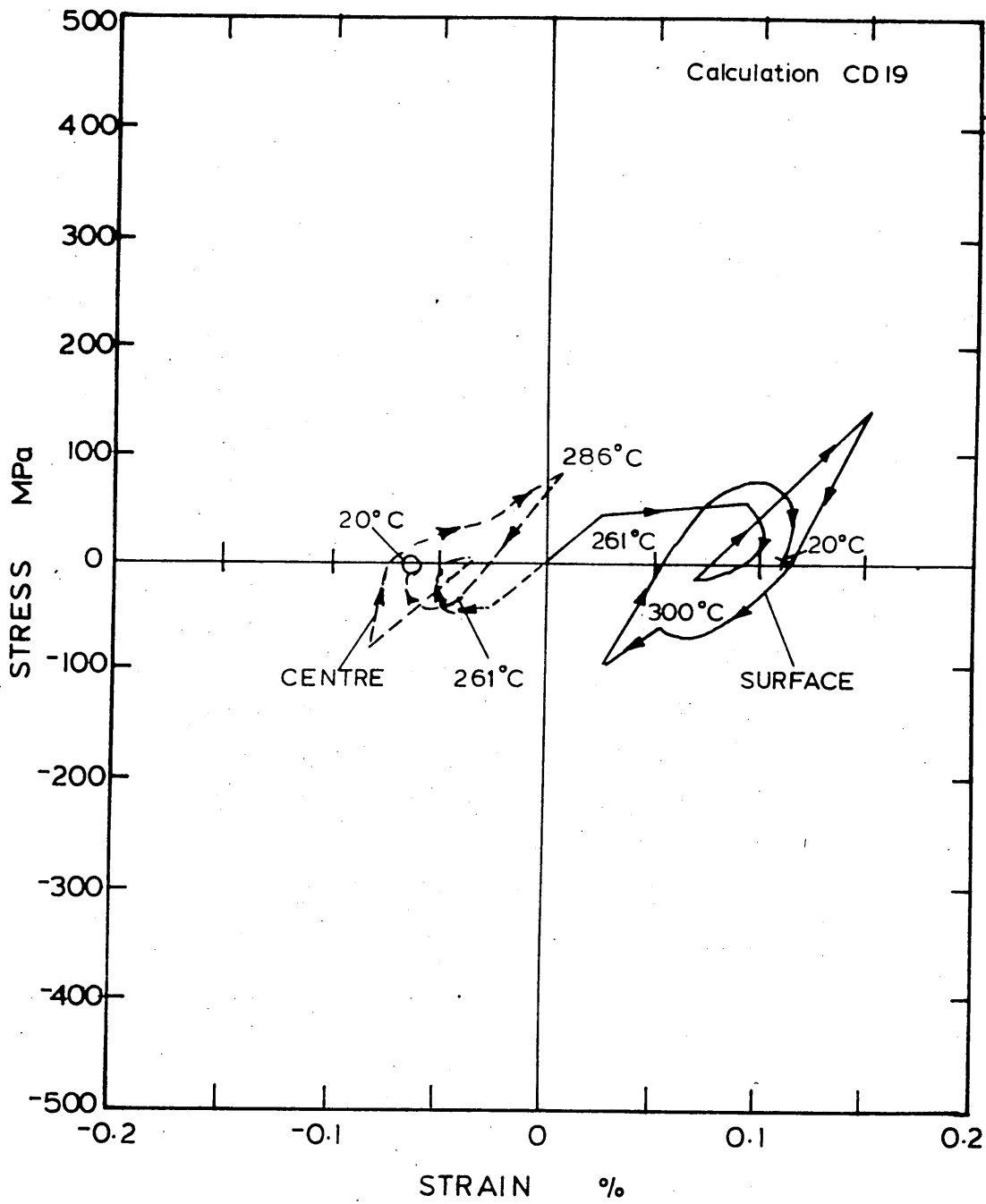
FIGURE 82:   Calculated residual stress distribution
in a 15mm plate after oil quenching
(includes viscous flow and transformation
plasticity simulated as additional strain).

Calculation no:

CD18/0/VF2/TPAS   ) see table 8
CD19/0/VF1/TPAS   )

274.
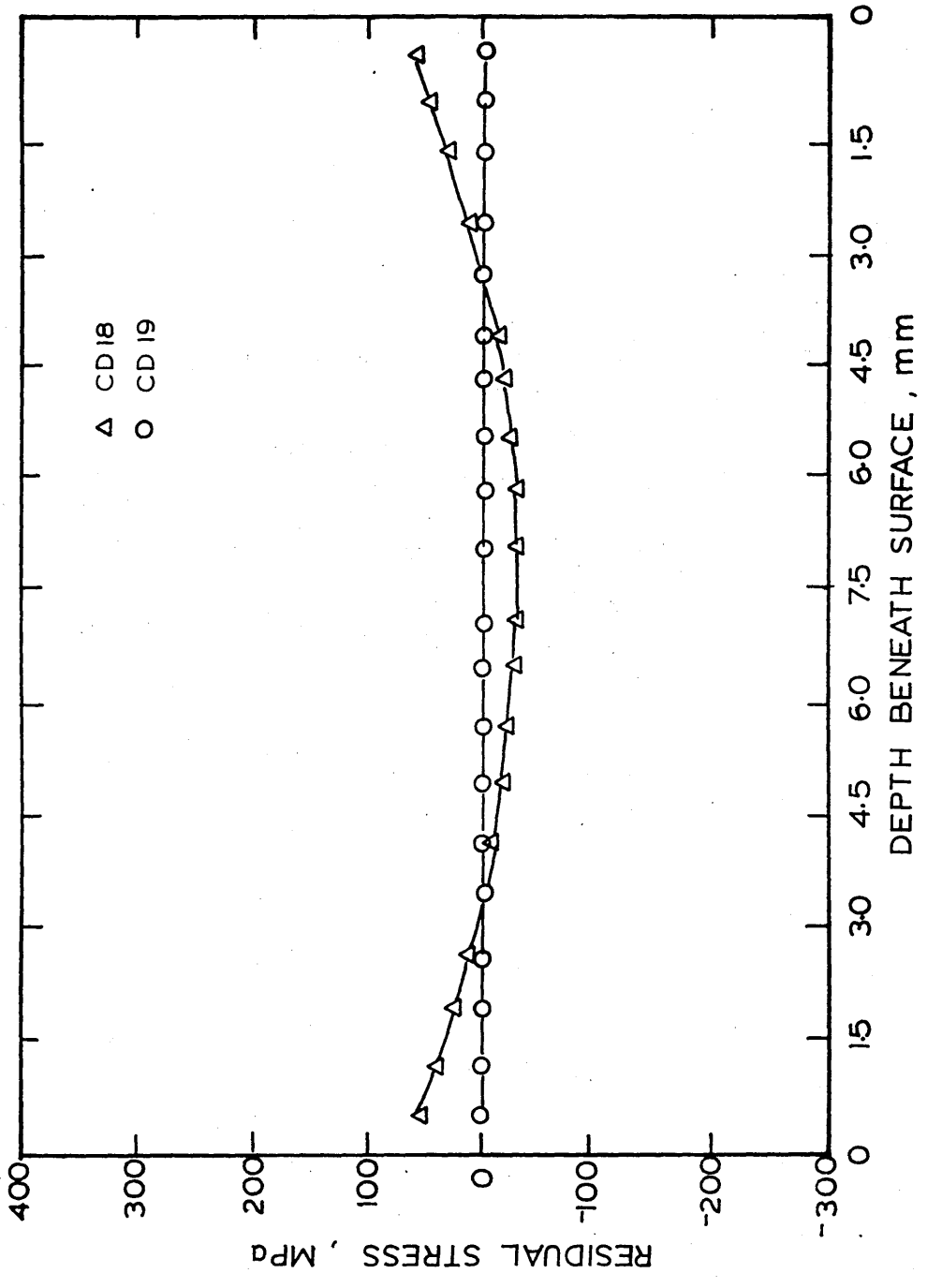
FIGURE 83:   Calculated residual strain distribution
              in a 15mm plate after oil quenching
              (includes viscous flow and transformation
              plasticity simulated as additional strain).

              Calculation no:

              CD18/0/VF2/TPAS   ) see table 8
              CD19/0/VF1/TPAS   )

275.
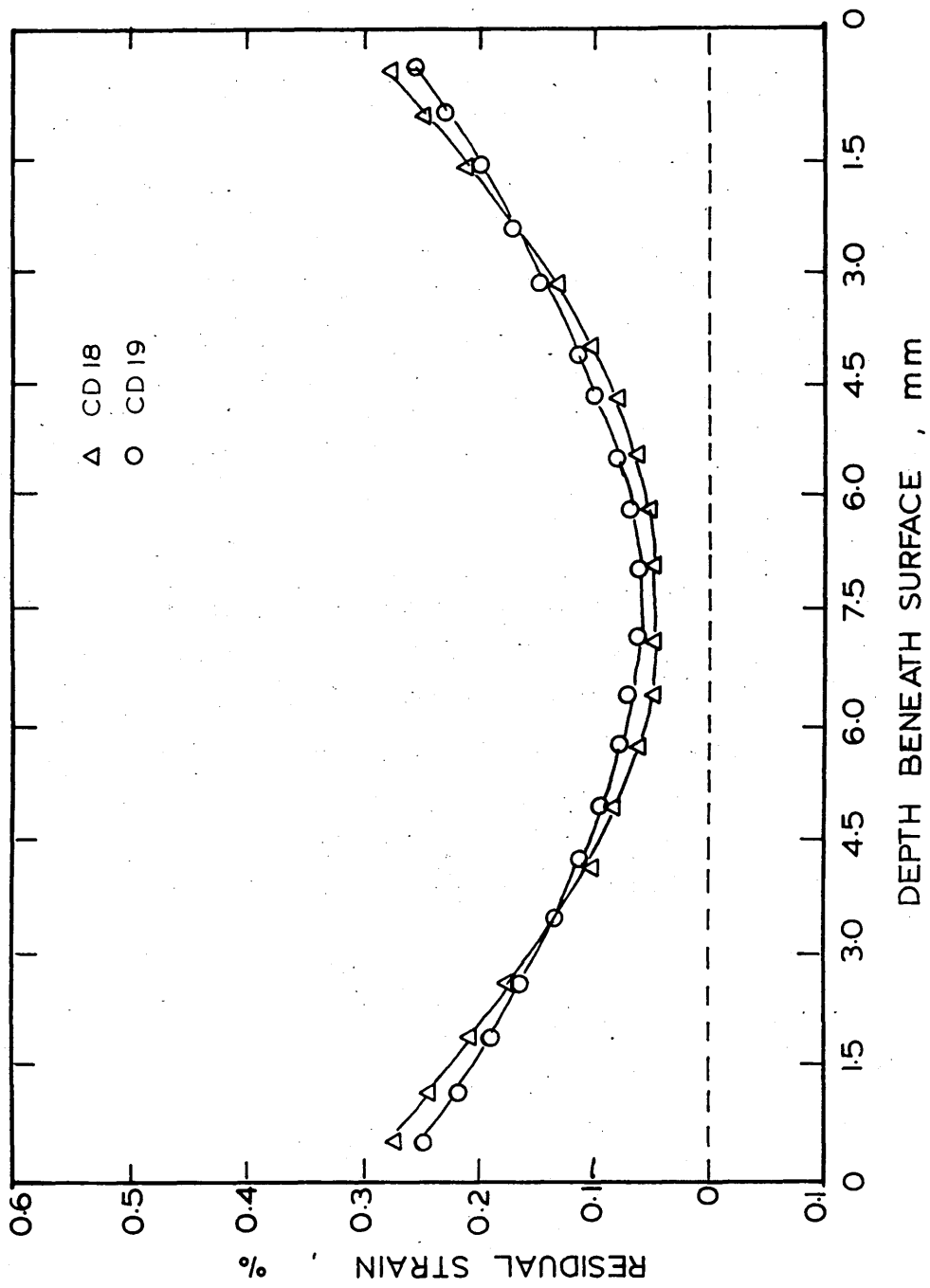
FIGURE 84:   835M30 steel specimen used for the
              experimental determination of
              residual stress and strain.

eye bolt to facilitate
handling of specimen

10 mm

6 mm of Kaol Wool
insulation held in
position by a nickel
frame

120 mm

120 mm
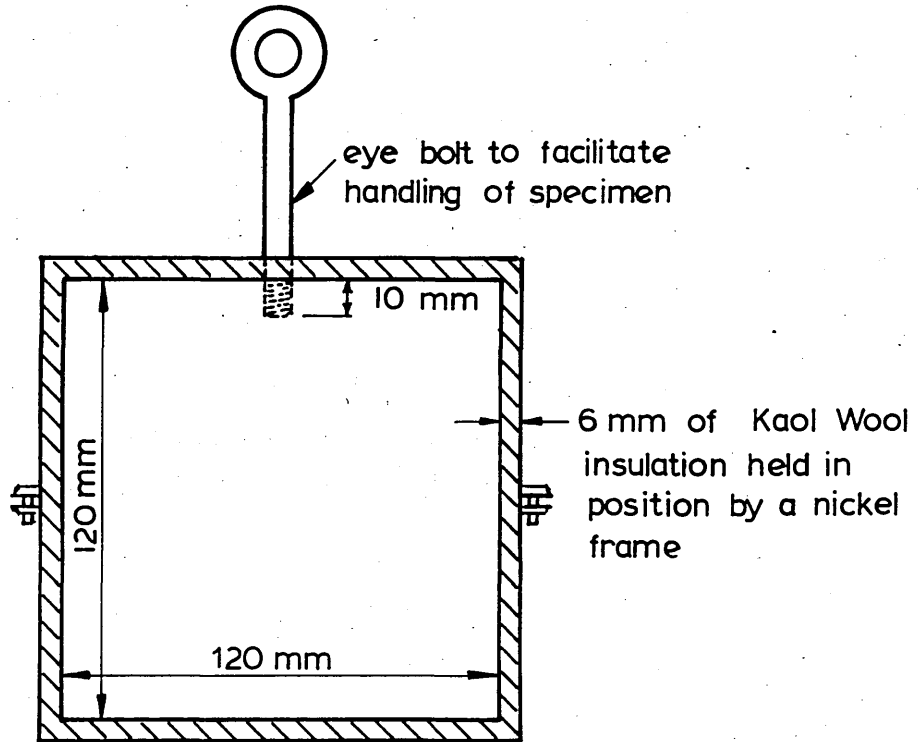
Material - 835M30 steel, all surfaces plated with
0.05 mm of nickel.

FIGURE 85:   Quenching tank, fixture and stirrers
              used during the experimental quenching.

variable speed stirrers

PLAN VIEW

520 mm

specimen guide channels

300 mm

250 mm

75 mm

SIDE VIEW

825 mm

specimen

277.
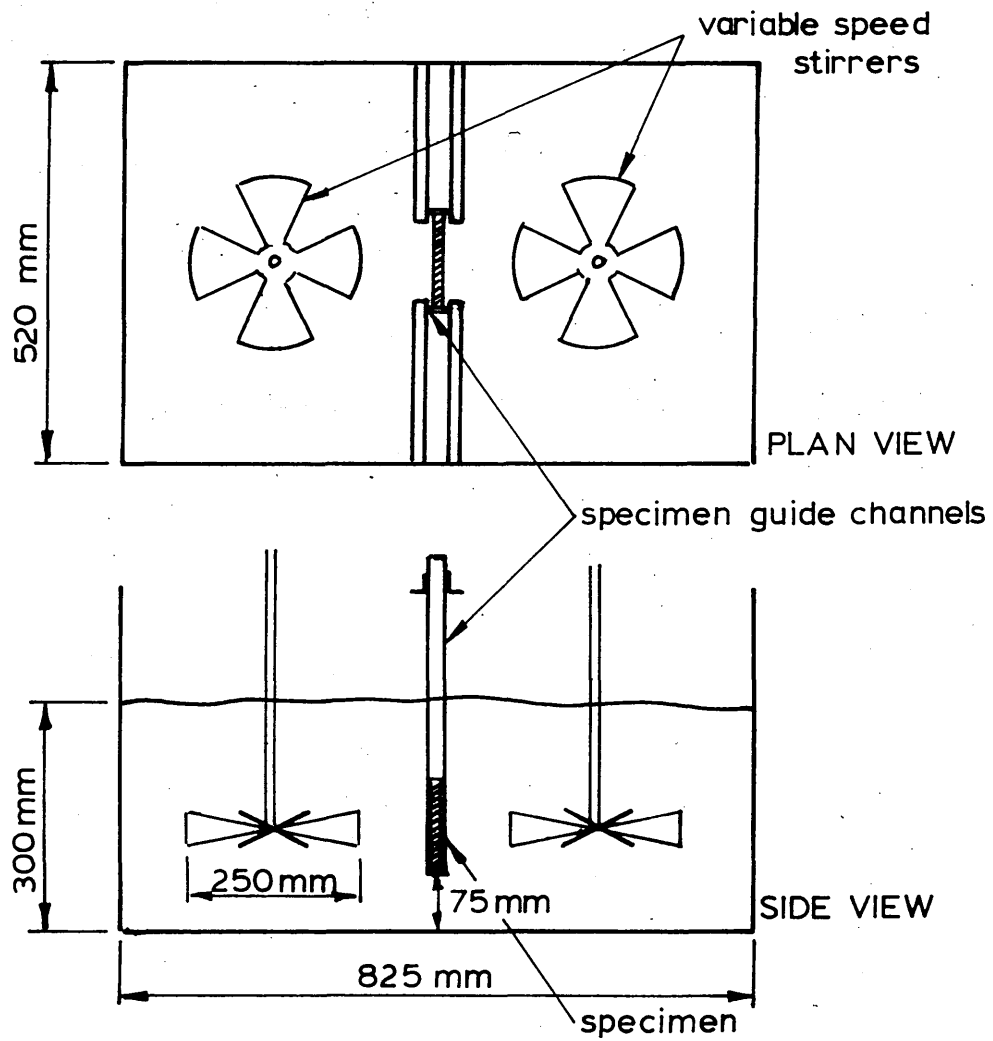
FIGURE 86:   The plate specimen showing the location
               of the measurements used to determine
               the distortion   between the edges of
               the plate.

Electronic comparator

Slip gauge combination

Plasticine

y

10 mm

11 10 9 8 7 6 5 4 3 2 1

x ———— x

A   B

10 mm

120 mm

120 mm

y

279.
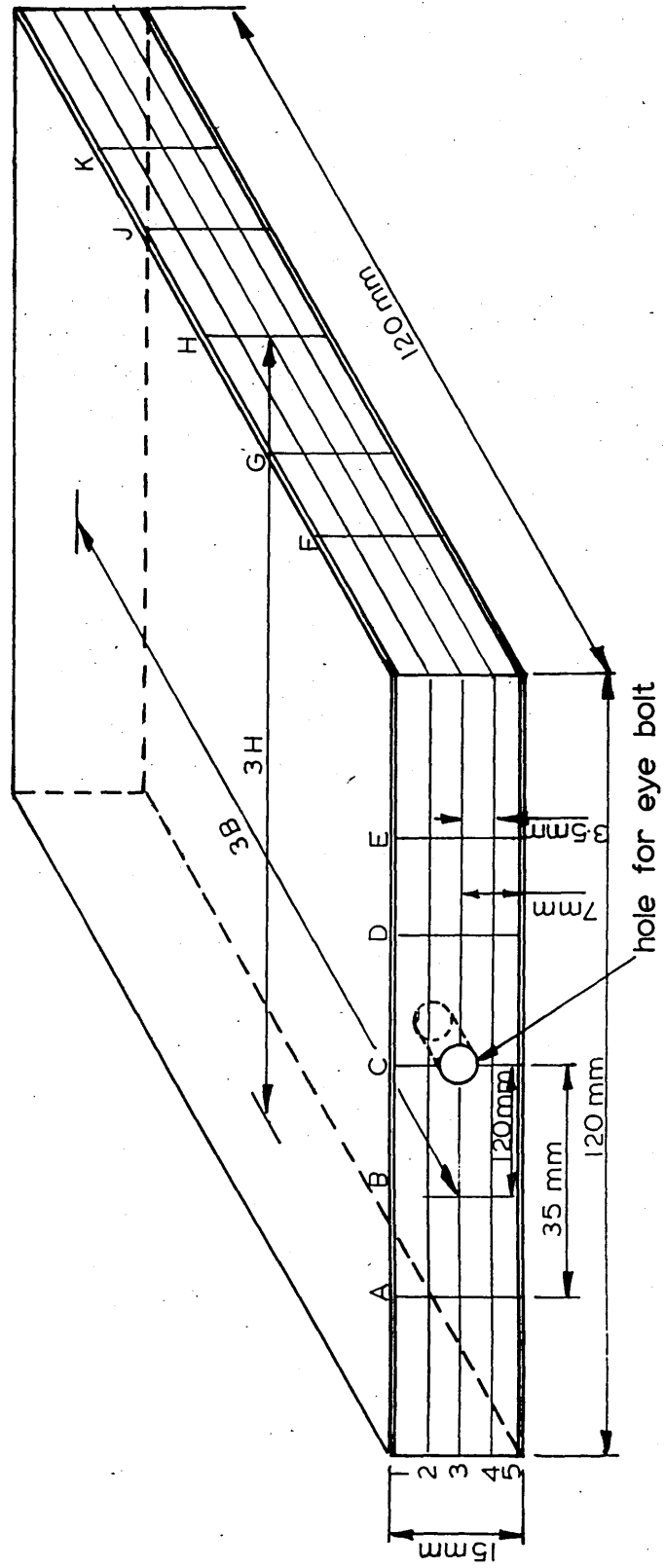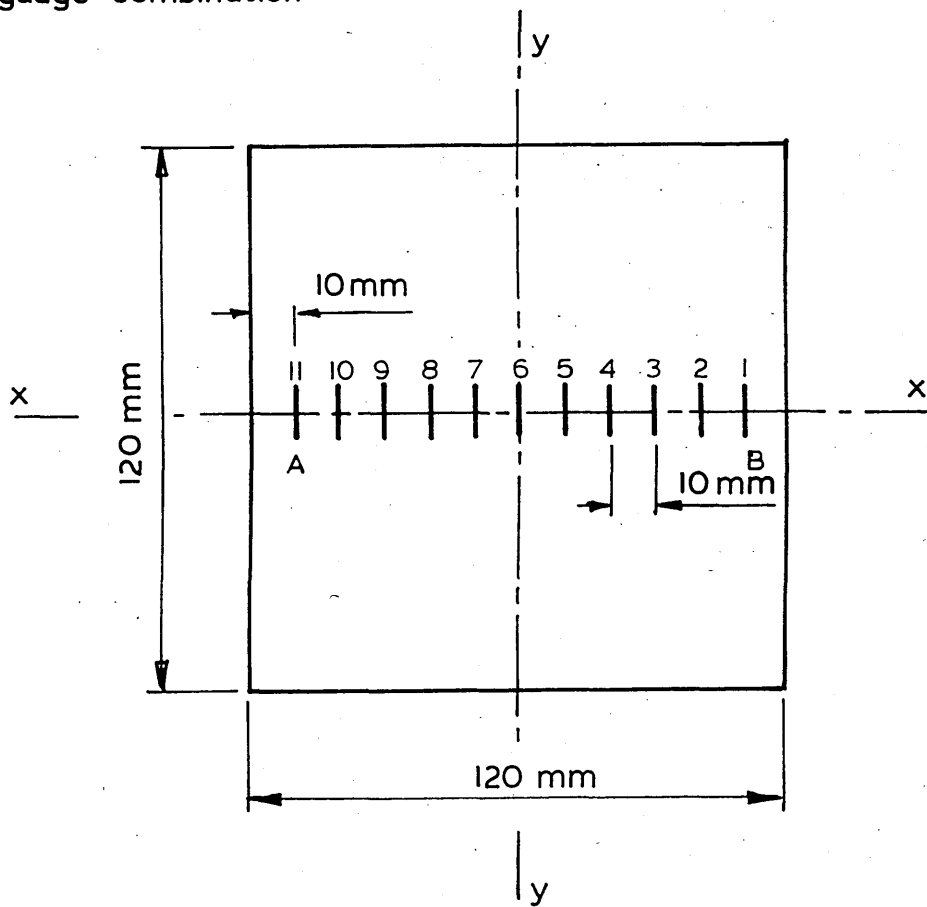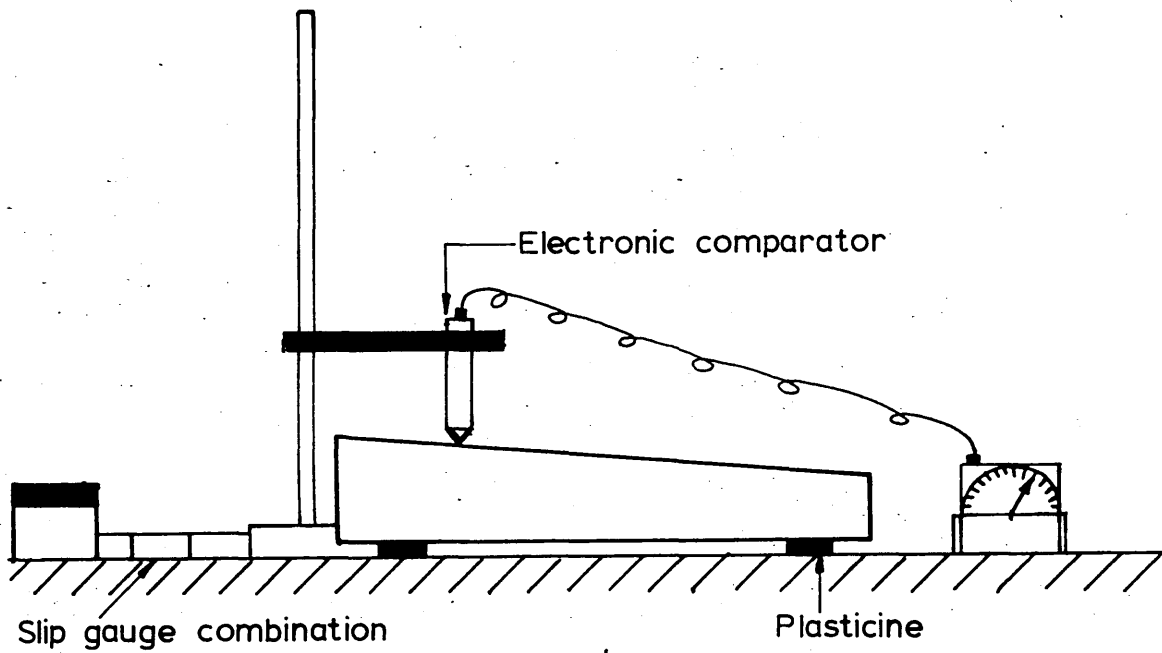
FIGURE 88:   Positions at which the comparator
               readings are taken to determine the
               through thickness of the plate.
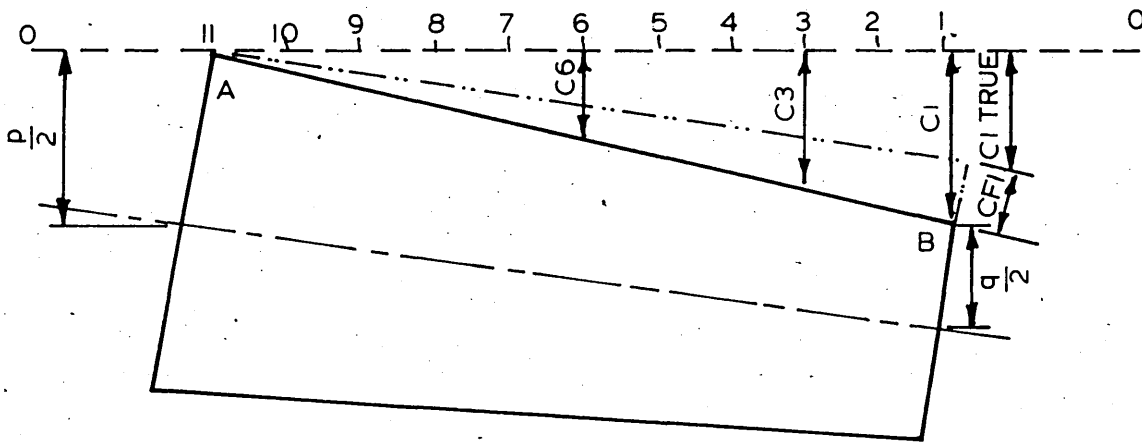
a) $C1\ TRUE = C1 - \dfrac{(p-q)}{2}$ $CF_1 = C1 - C1\ TRUE$

b) $CF_N = C_N - \dfrac{11-N}{10}\ C1\ TRUE$

$\dfrac{1}{2}\ TH_N = \dfrac{p}{2} - CF_N$

280.
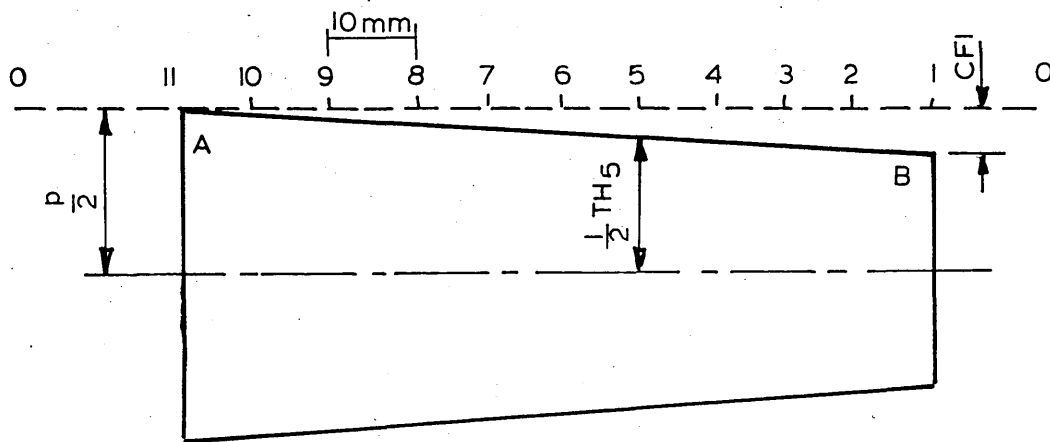
FIGURE 89:   Plan view of the underside of the plate
              showing strain gauge installation used
              to measure residual stresses.

Standard strain
gauge rossette
(on support plate)

Terminal
Strips

Recess machined in
support plate

Underside of
plate specimen

To bridge supply
and output

Active strain
gauge rossette

Support
plate

Strain gauge installations
coated with polyurethane
lacquer and whole of recess
filled with paraffin wax.

281.
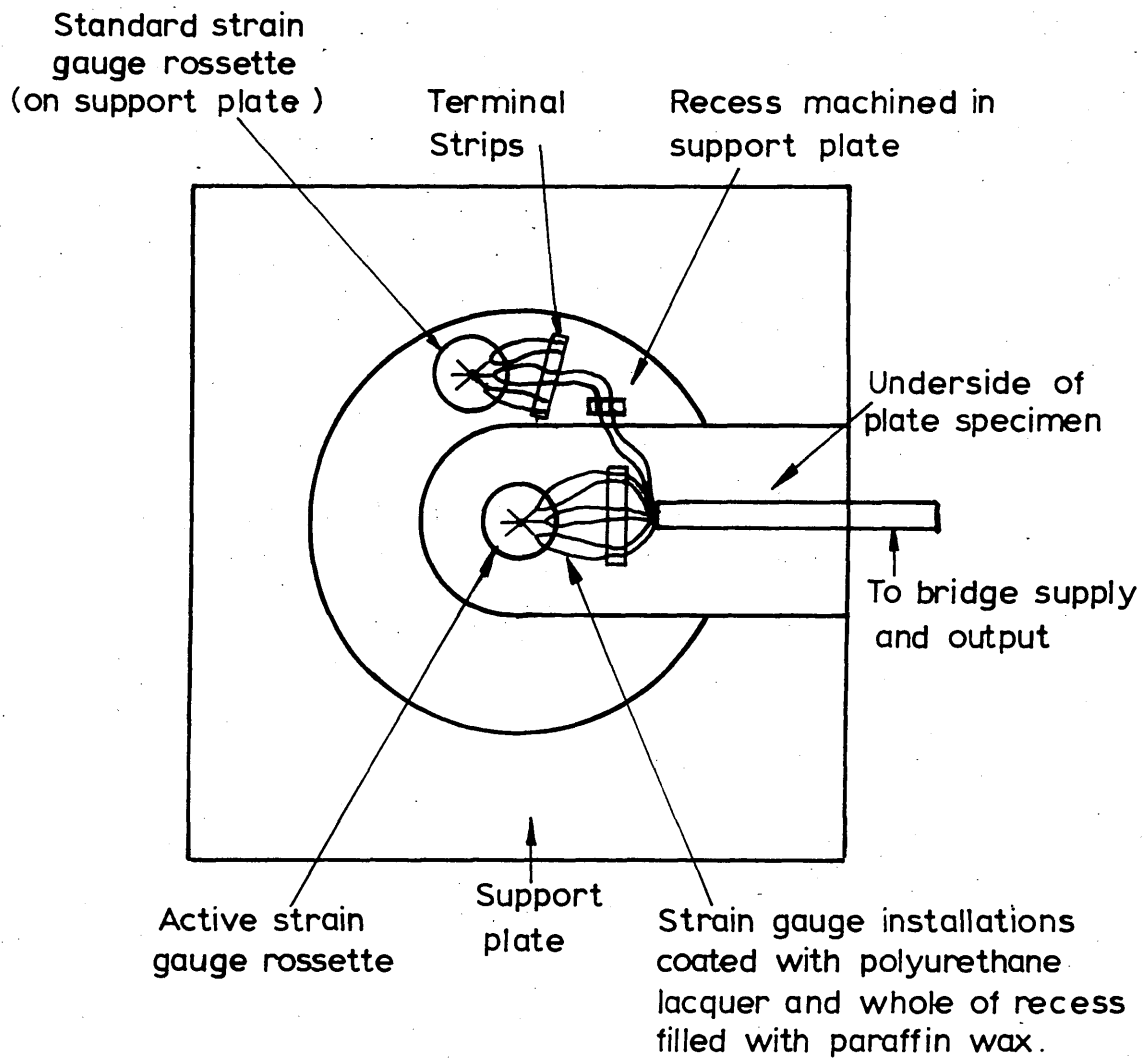
FIGURE 90:   The circuit diagram for wheat-stone bridge.

VOLT
METER

AMPLIFIER AND
BALANCE UNIT

Wheatstone
bridge

o/p
o/p
+
–

POWER
SUPPLY

240 V.AC

C V.DC

Strain rosette on
the specimen plate

Strain rosette on
the support plate

1
2
3
4
5
6
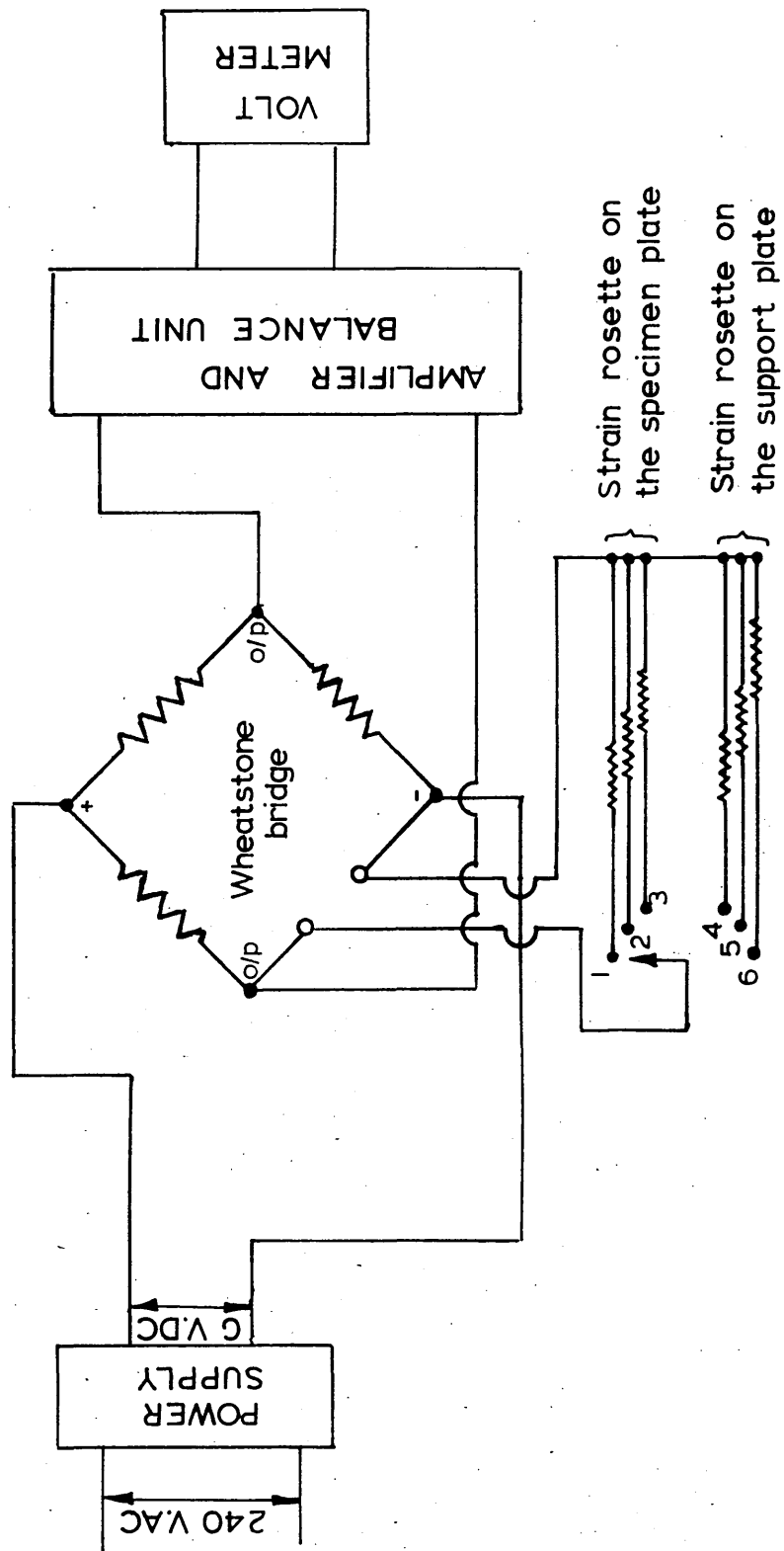
FIGURE 91:   Experimentally determined residual strain
              distribution in a 15mm plate after oil
              quenching.

DEPTH BENEATH SURFACE , mm
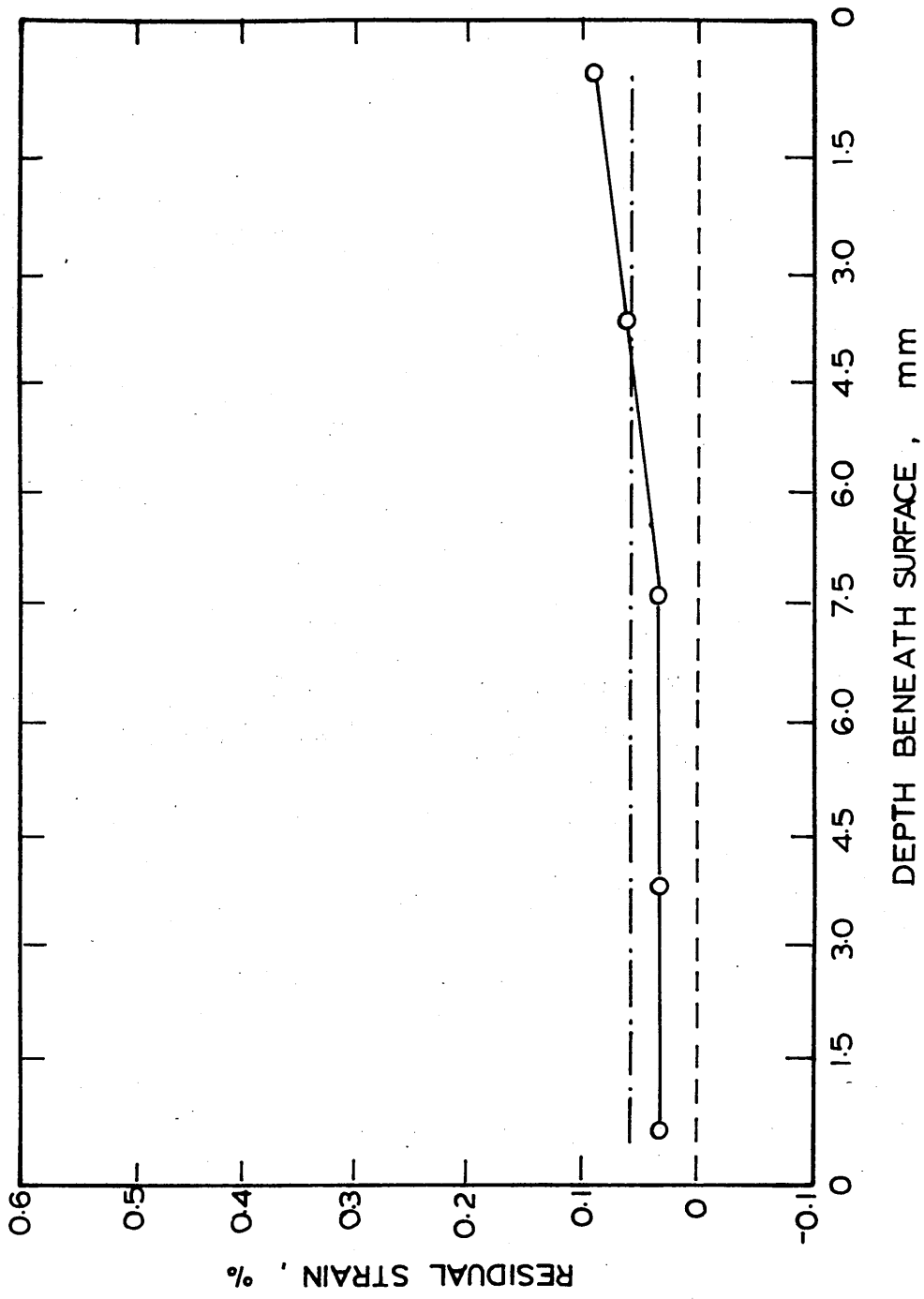
RESIDUAL STRAIN , %

FIGURE 92:   Change in thickness at different positions
in a 15x120x120mm plate after oil quenching.

CHANGE IN PLATE THICKNESS, %

DISTANCE FROM CENTRE OF PLATE, mm

x-x

y-y

Mean change in thickness $\varepsilon_z = 0.239$
Free of edge effects

120 mm

120 mm

x

y
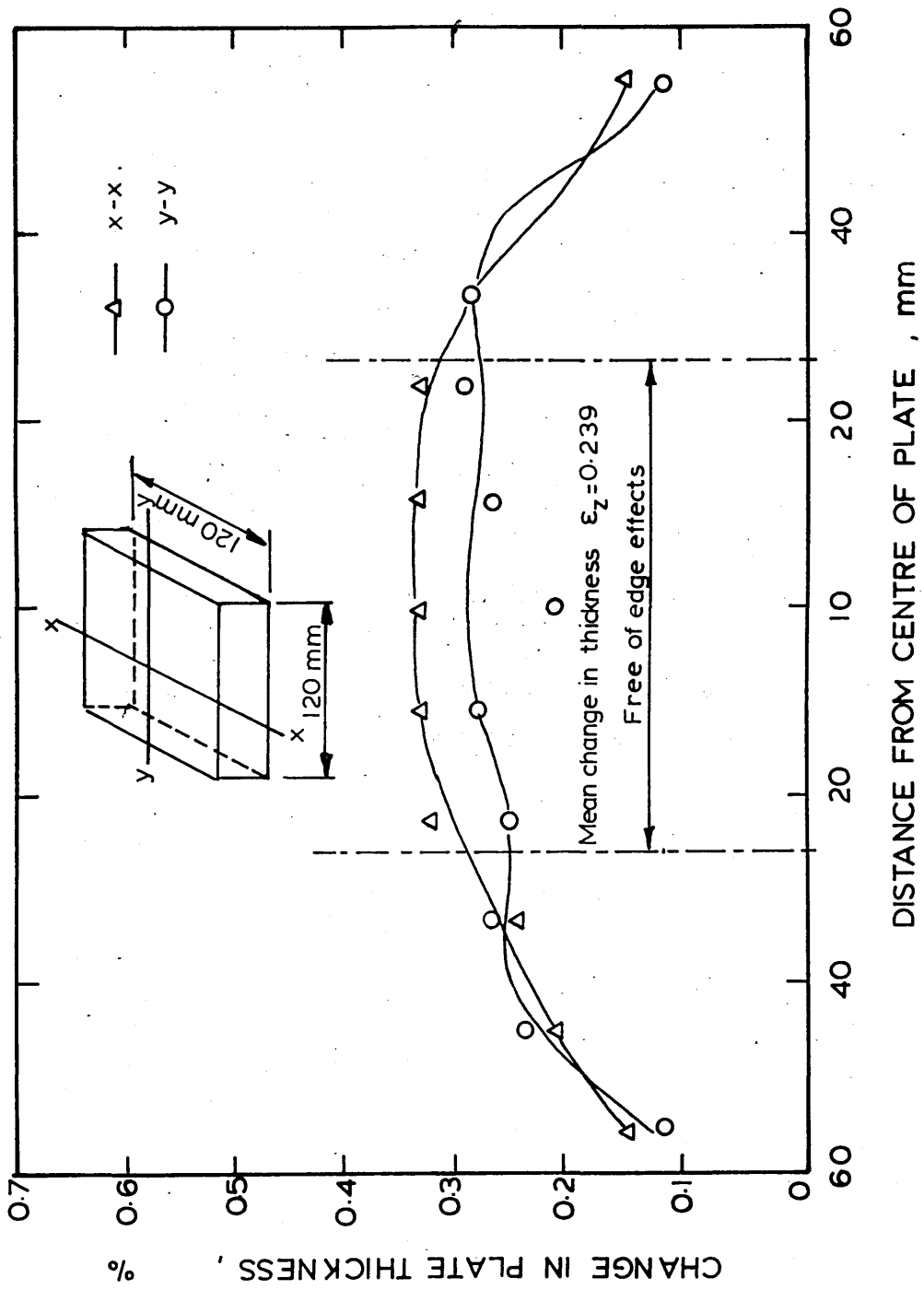
FIGURE 93:   Experimentally determined residual stress
             distribution in a 15mm plate after oil
             quenching.

DEPTH BENEATH SURFACE , mm

RESIDUAL STRESS , MPa

285.
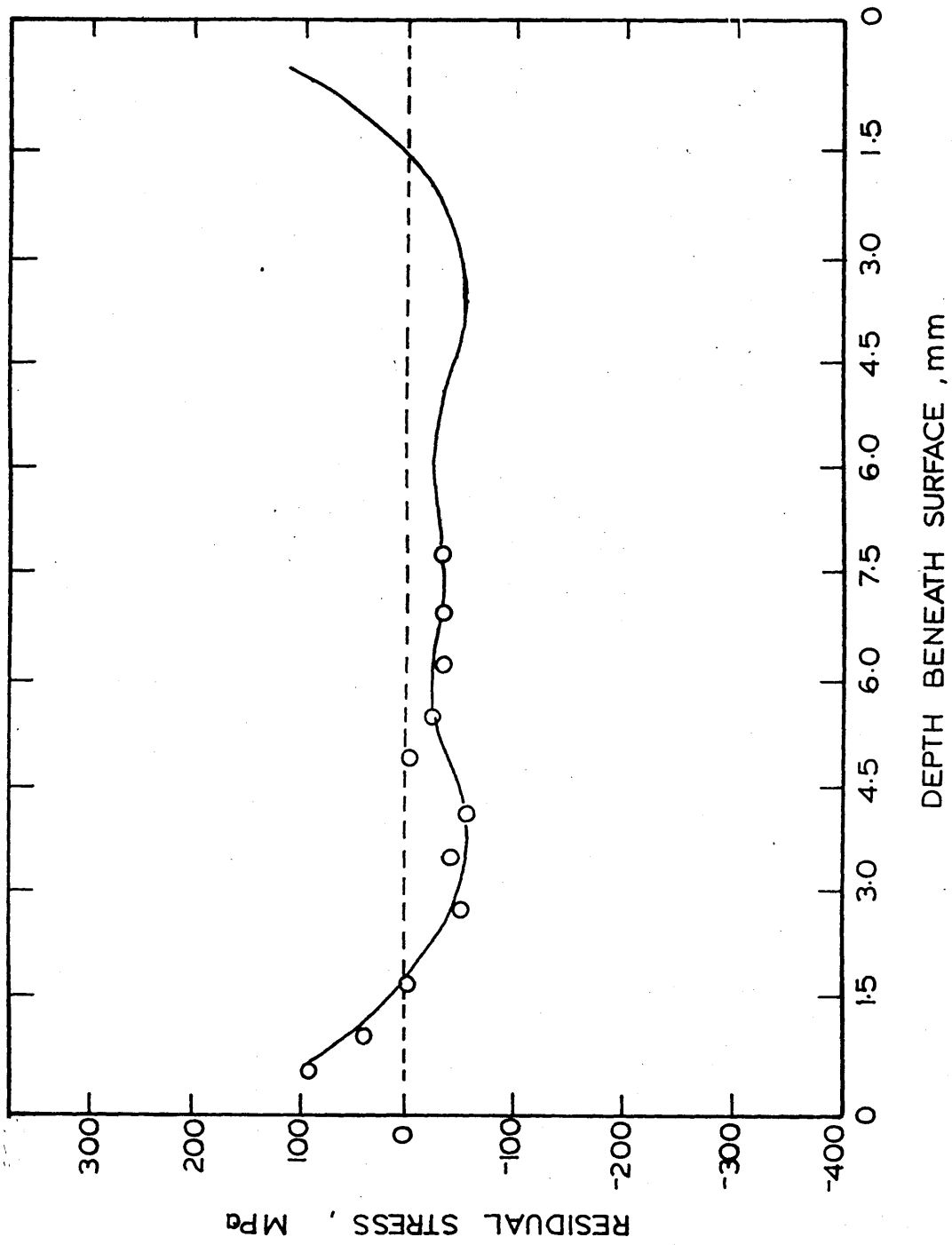
FIGURE 94:   Experimentally determined residual
              strain distribution in a 15mm plate
              after martempering.

286.
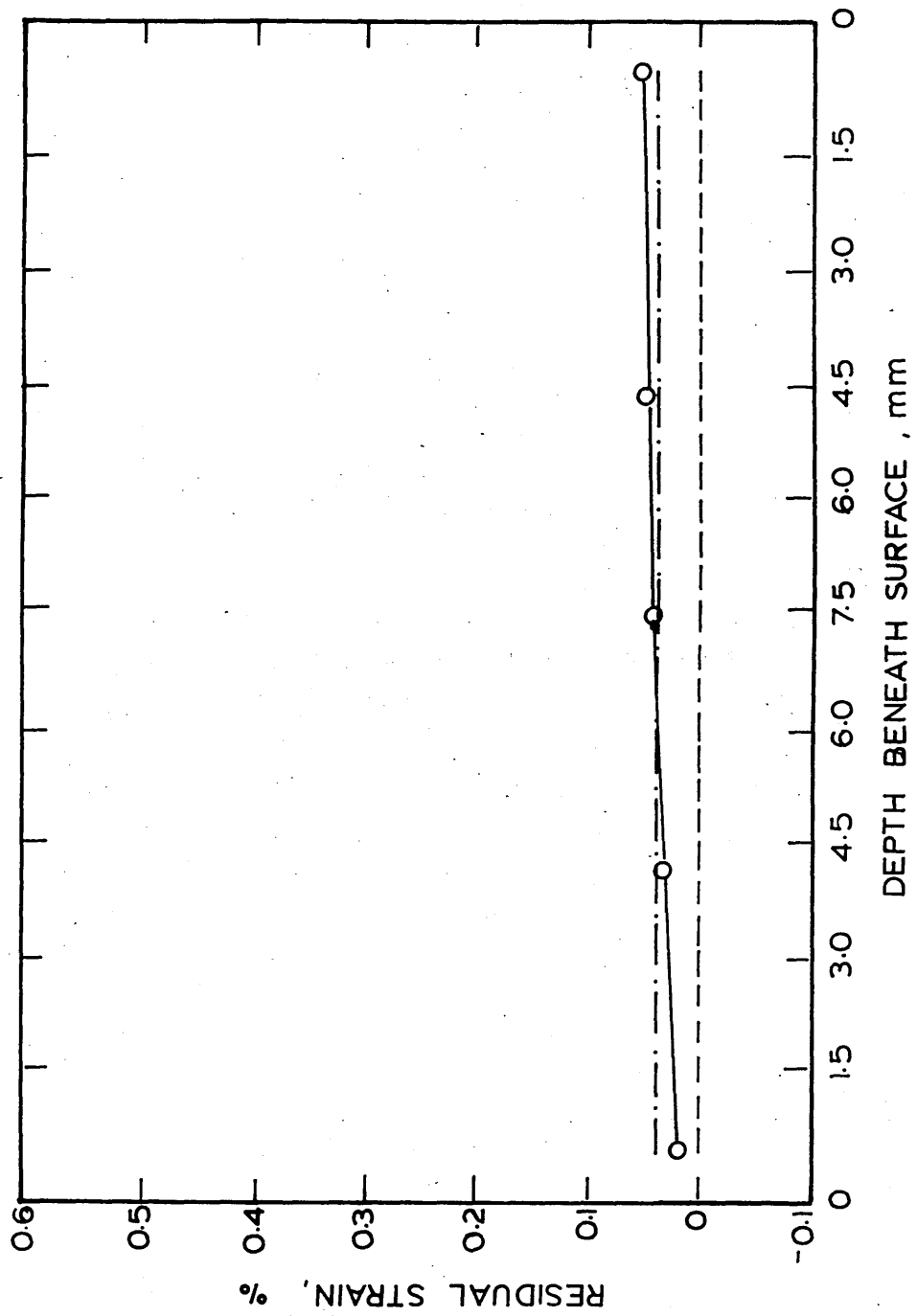
FIGURE 95:   Experimentally determined residual
             stress distribution in a 15mm plate
             after martempering.

DEPTH BENEATH SURFACE, mm
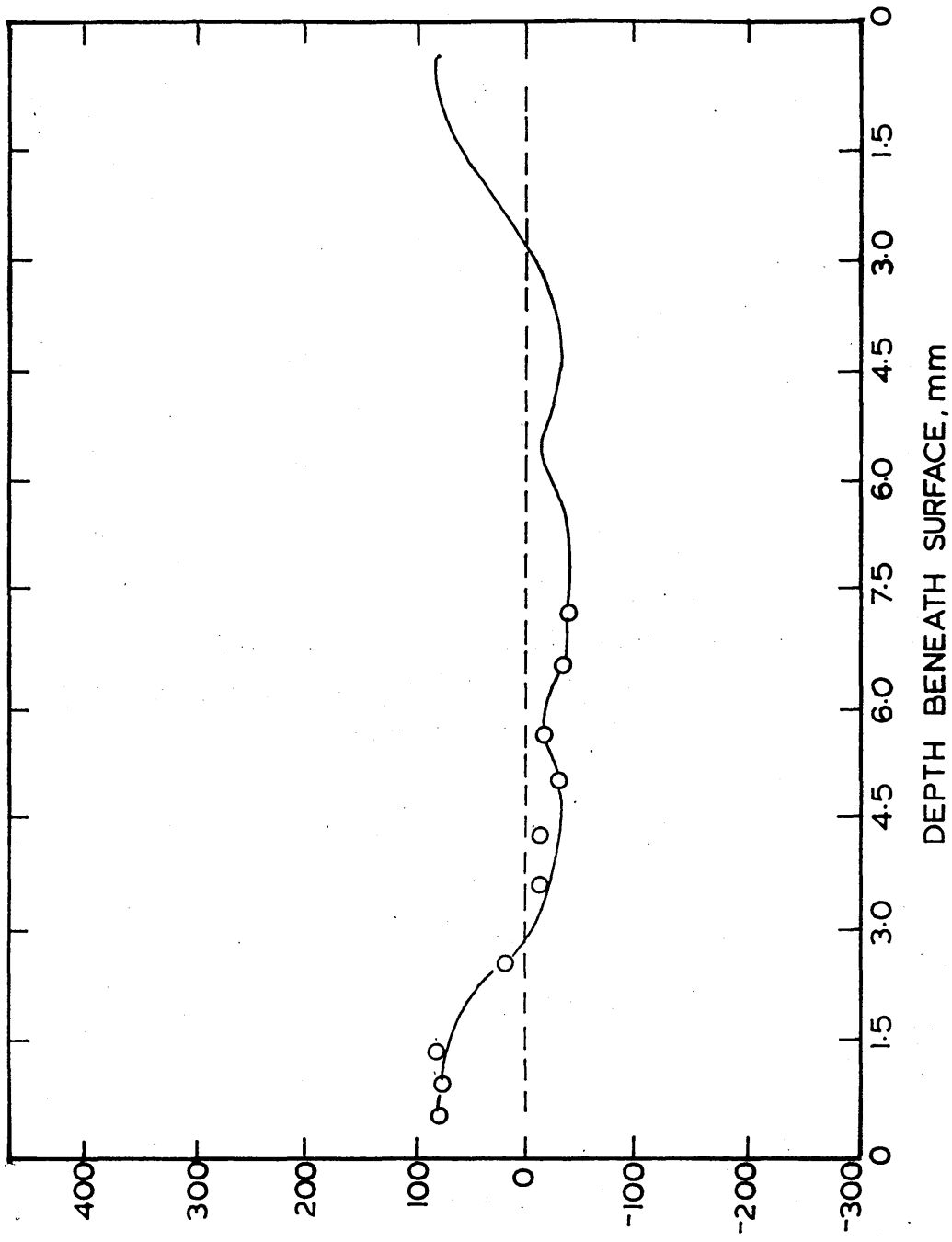
FIGURE 96:   Experimentally determined residual
              stress distribution in a 20mm plate
              after water quenching.
              (After Price[100])

288.
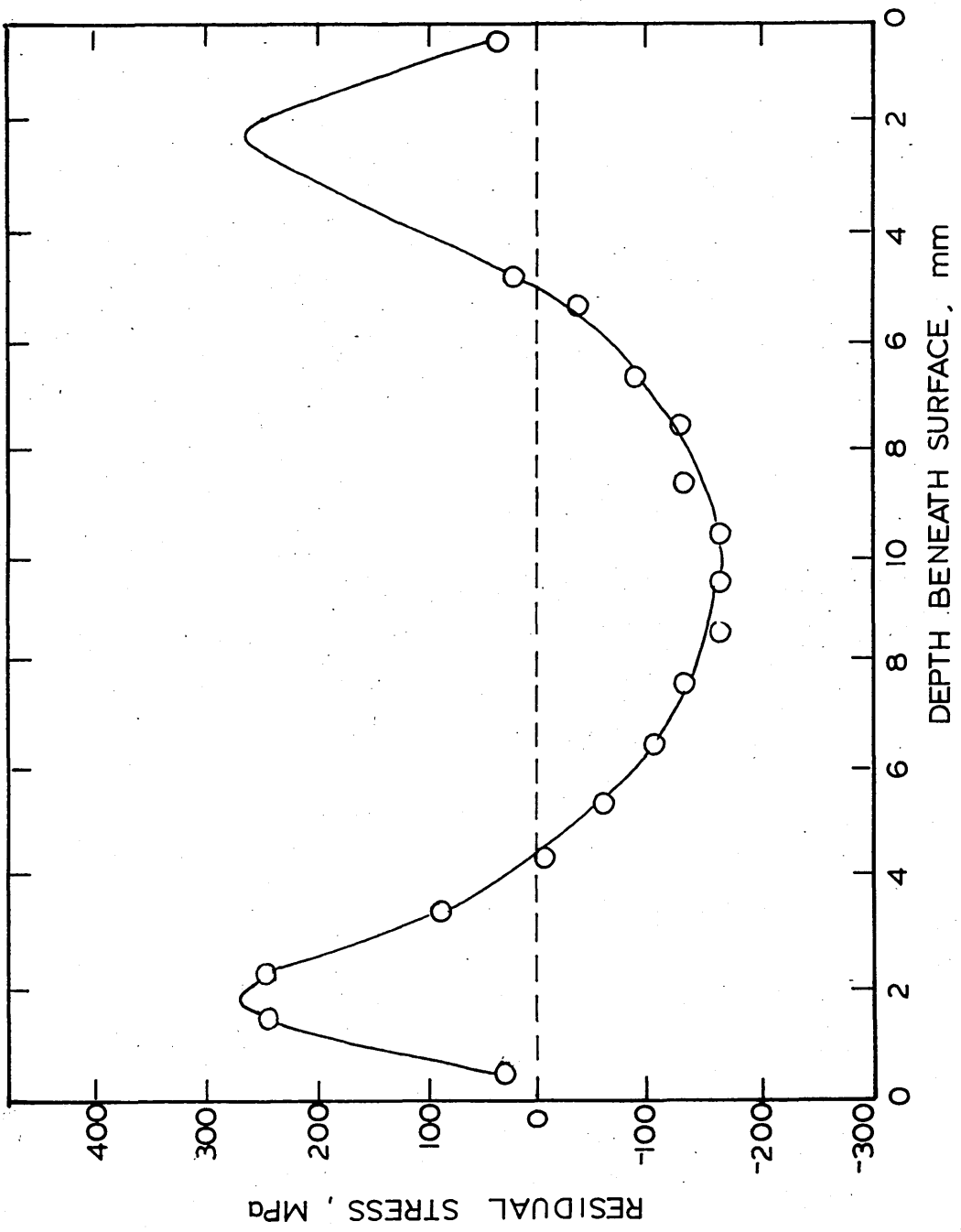
FIGURE 97:   Experimentally determined residual
              strain distribution in a 20mm plate
              after water quenching.
              (After Price[100])

289.
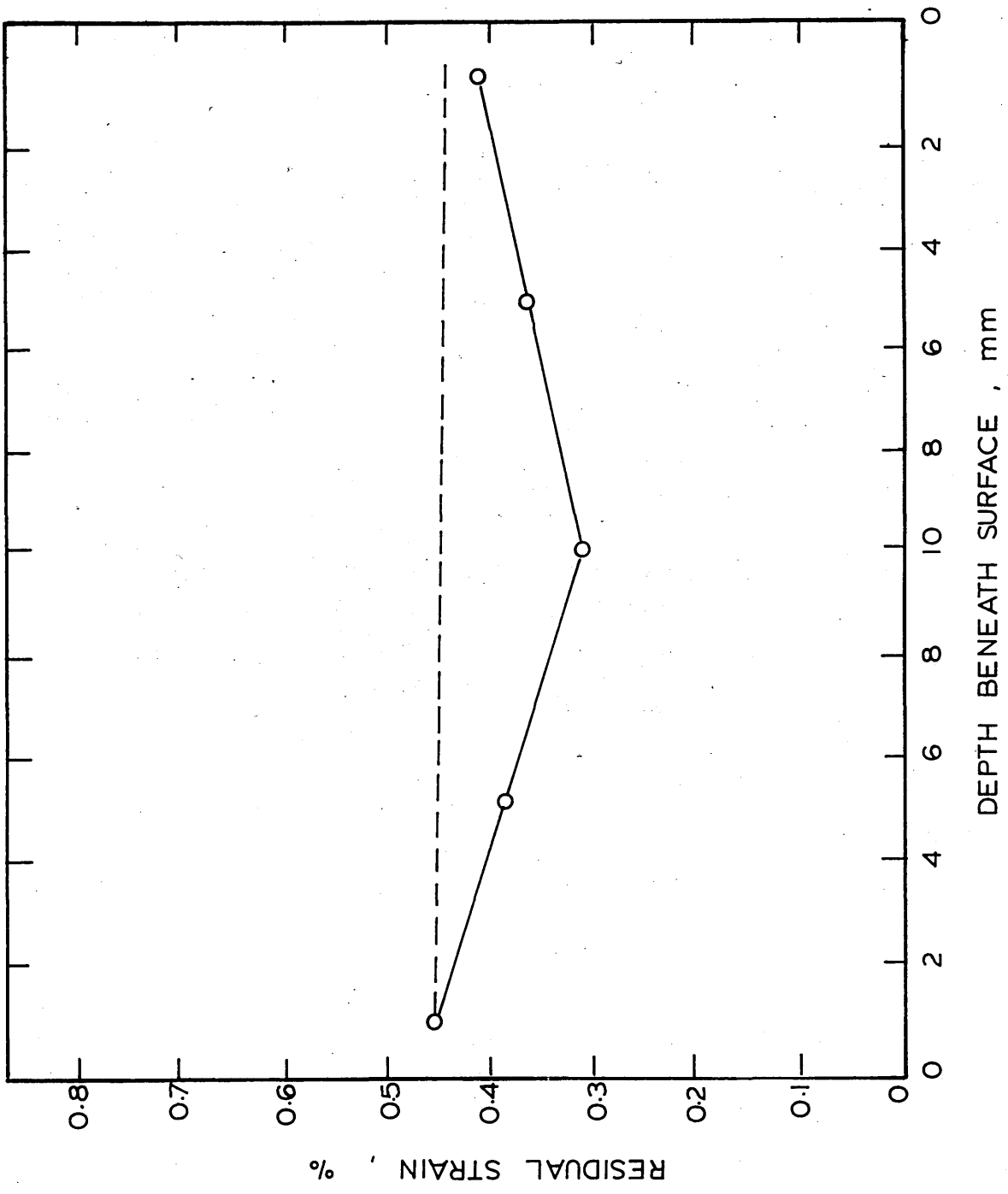
FIGURE 98:   Schematic representation of characteristic
               stages in the relationship between stress
               and strain at the surface and centre of a
               plate during quenching without consideration
               of viscous flow.
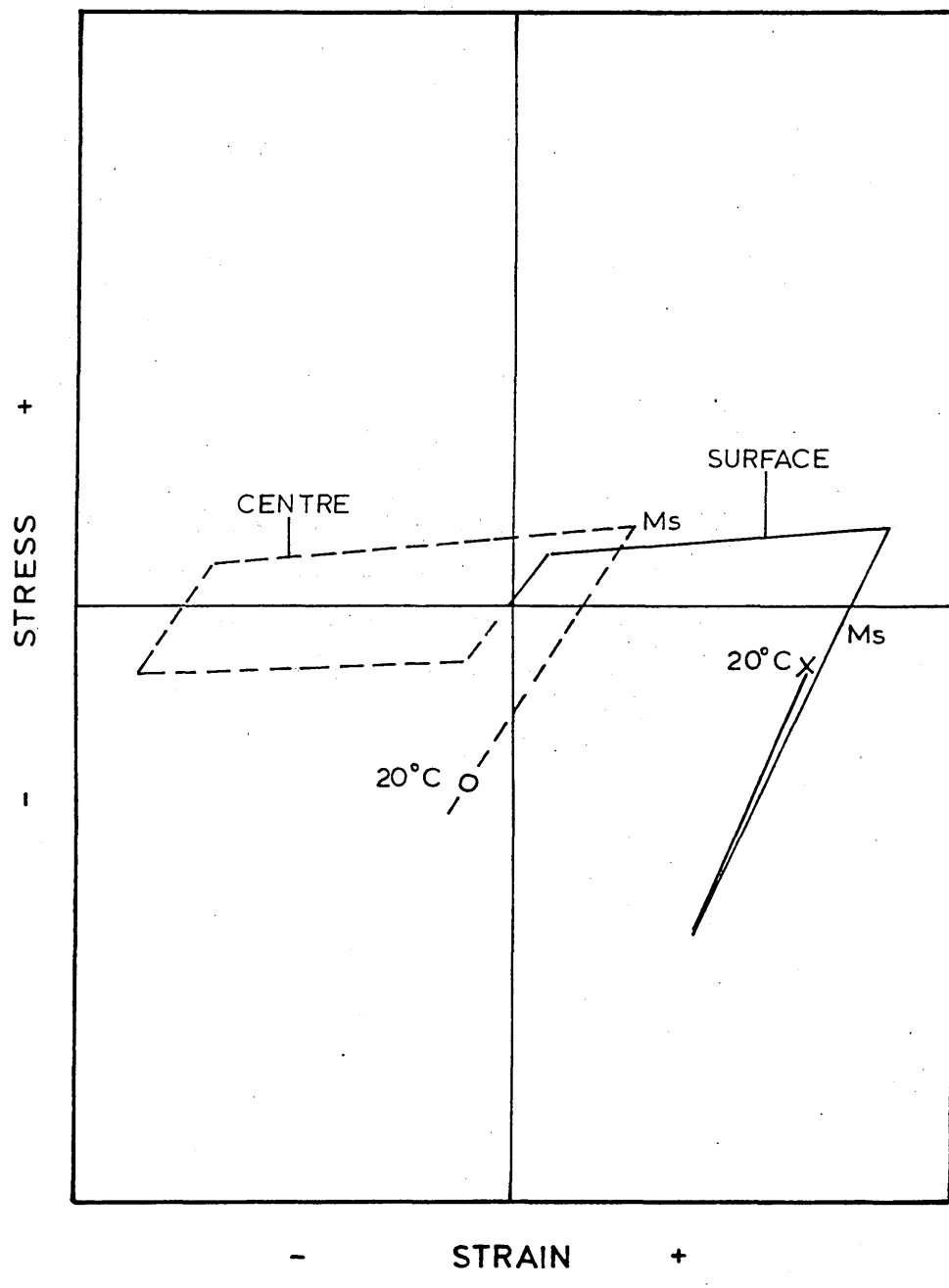
FIGURE 99:   Comparison of experimental and calculated
              residual stress distribution in a 15mm
              plate after oil quenching.

              Calculation no:

              CD2/O/NVF   )
              CD6/O/VF1   )
   CD7/O/VF2   ) see table 8
              CD8/O/VF3   )
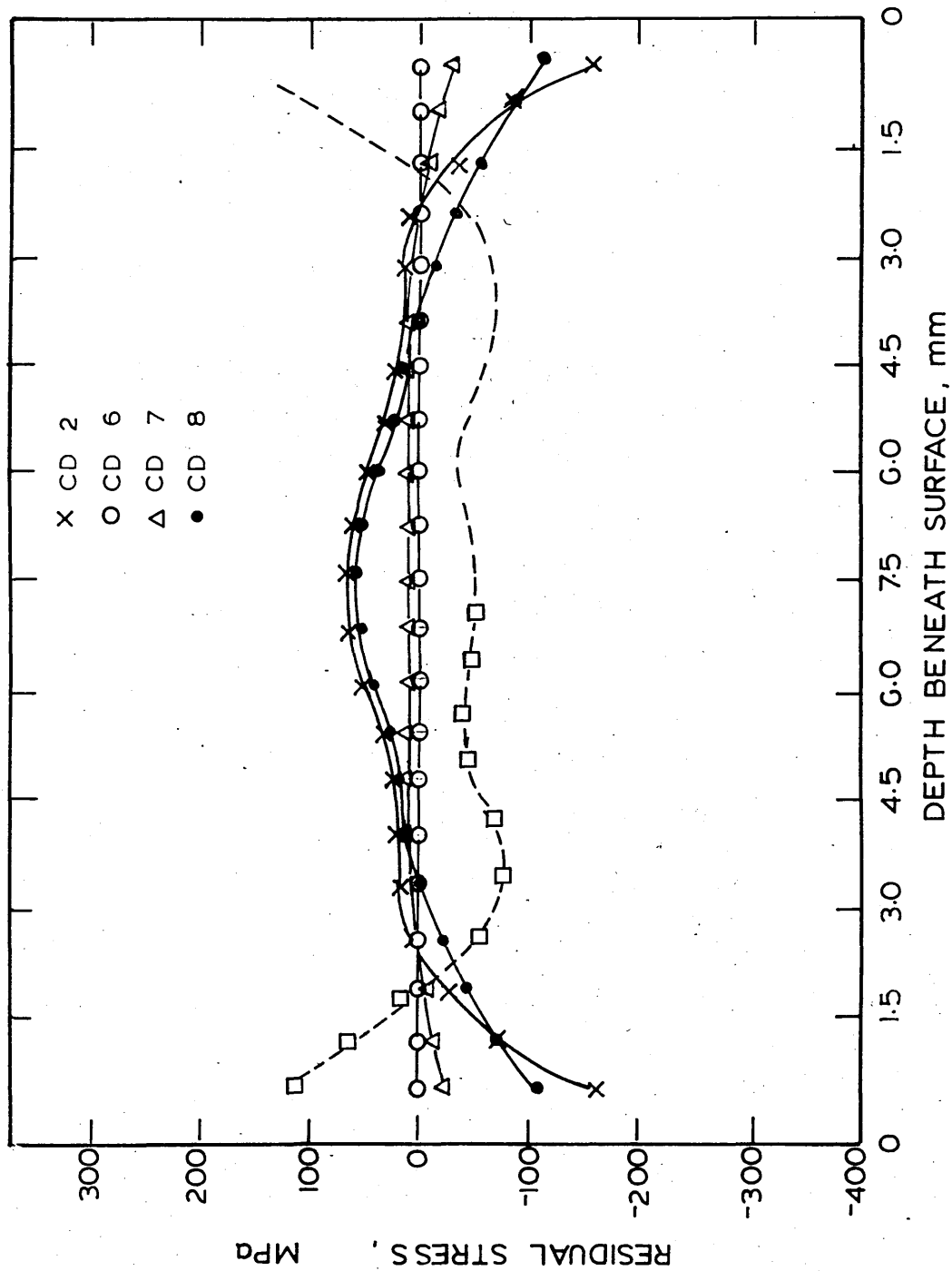
FIGURE 100:   Comparison of experimental and
               calculated residual strain distribution
               in a 15mm plate after oil quenching.

               Calculation no:

               CD2/O/NVF   )
               CD6/O/VF1   )
               CD7/O/VF2   )   see table 8
               CD8/O/VF3   )
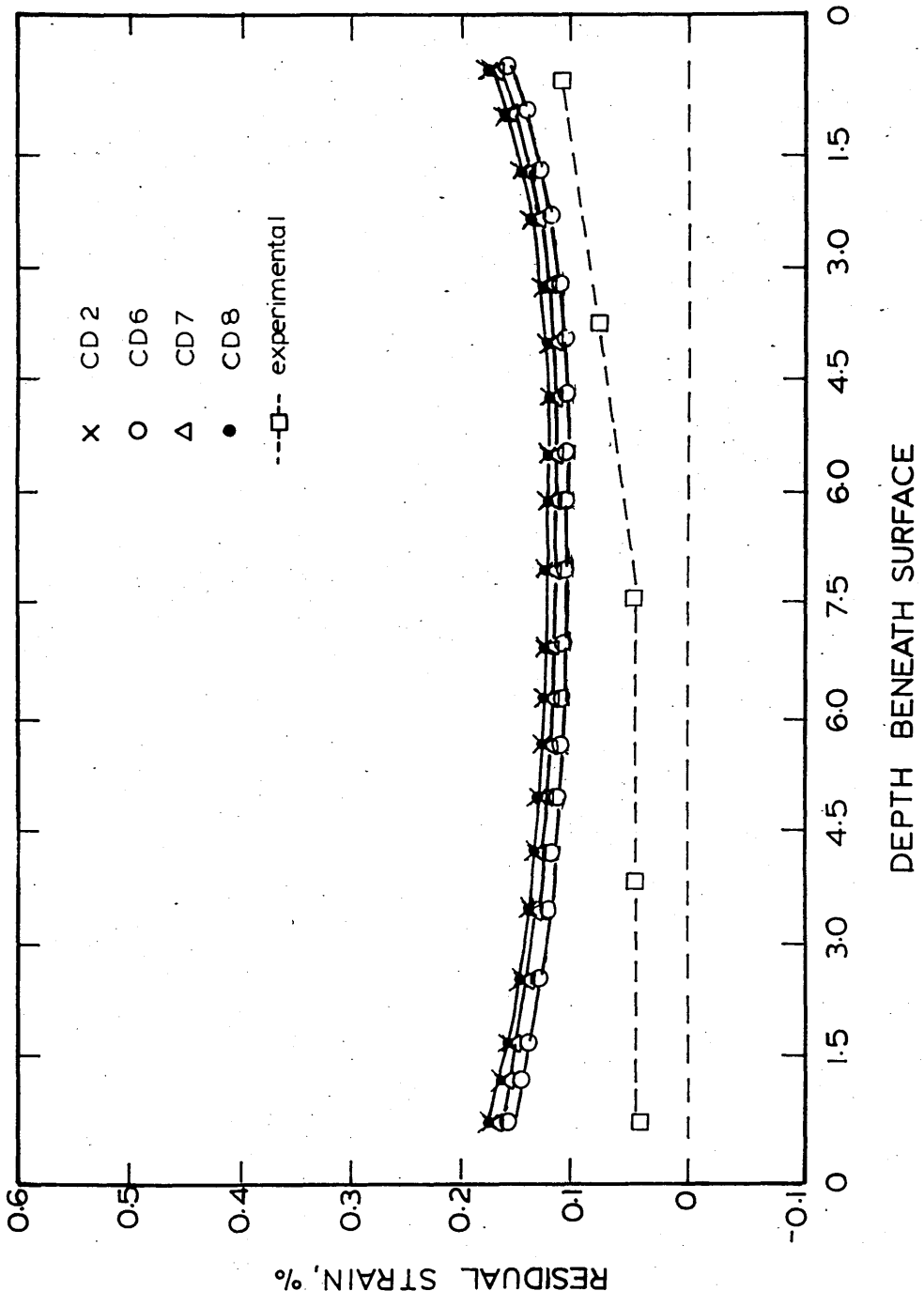
FIGURE 101:   Comparison of experimental and
calculated residual stress
distribution in a 20mm plate
after water quenching.

Calculation no:

CD1/W/NVF   )
CD4/W/VF1   ) see table 8
CD5/W/VF2 and 3)

293.
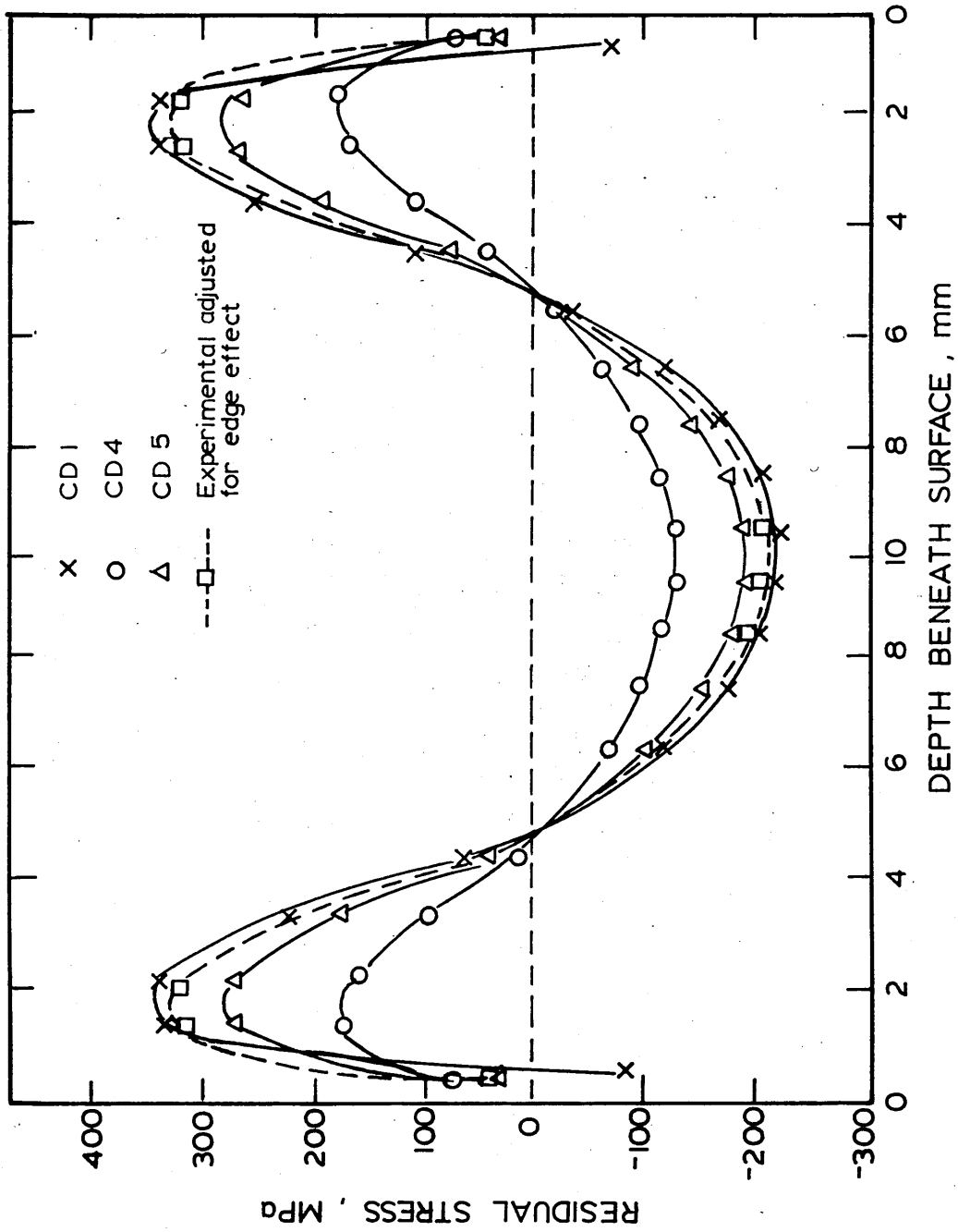
FIGURE 102:   Comparison of experimental and
               calculated residual strain
               distribution in a 20mm plate
               after water quenching.

               Calculation no:

               CD1/W/NVF   )
               CD4/W/VF1   )   see table 8
               CD5/W/VF2 and 3   )

294.
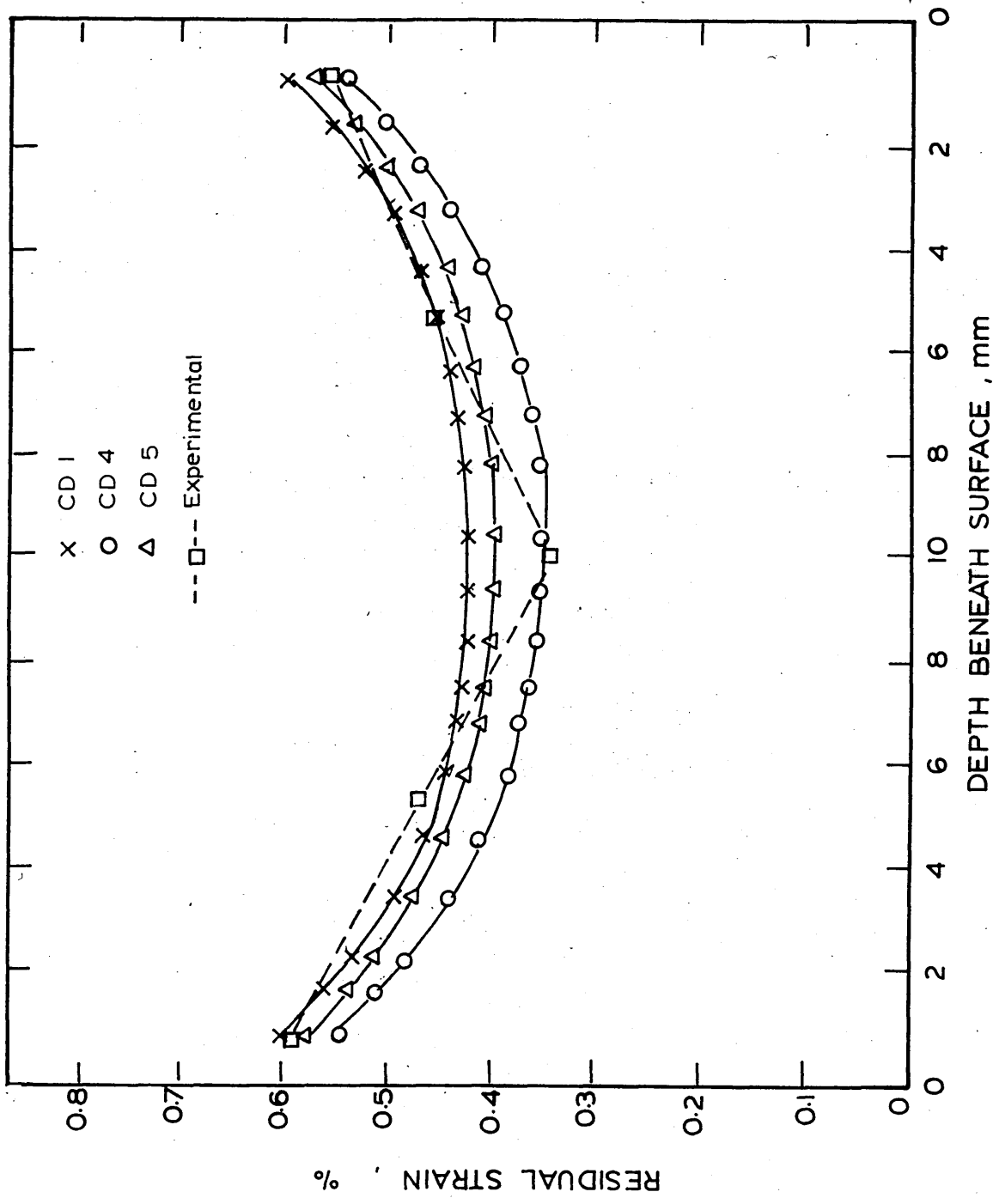
FIGURE 103:   Calculated residual stress distribution
in a 15mm plate after oil quenching with
viscous flow represented by method 4.

295.
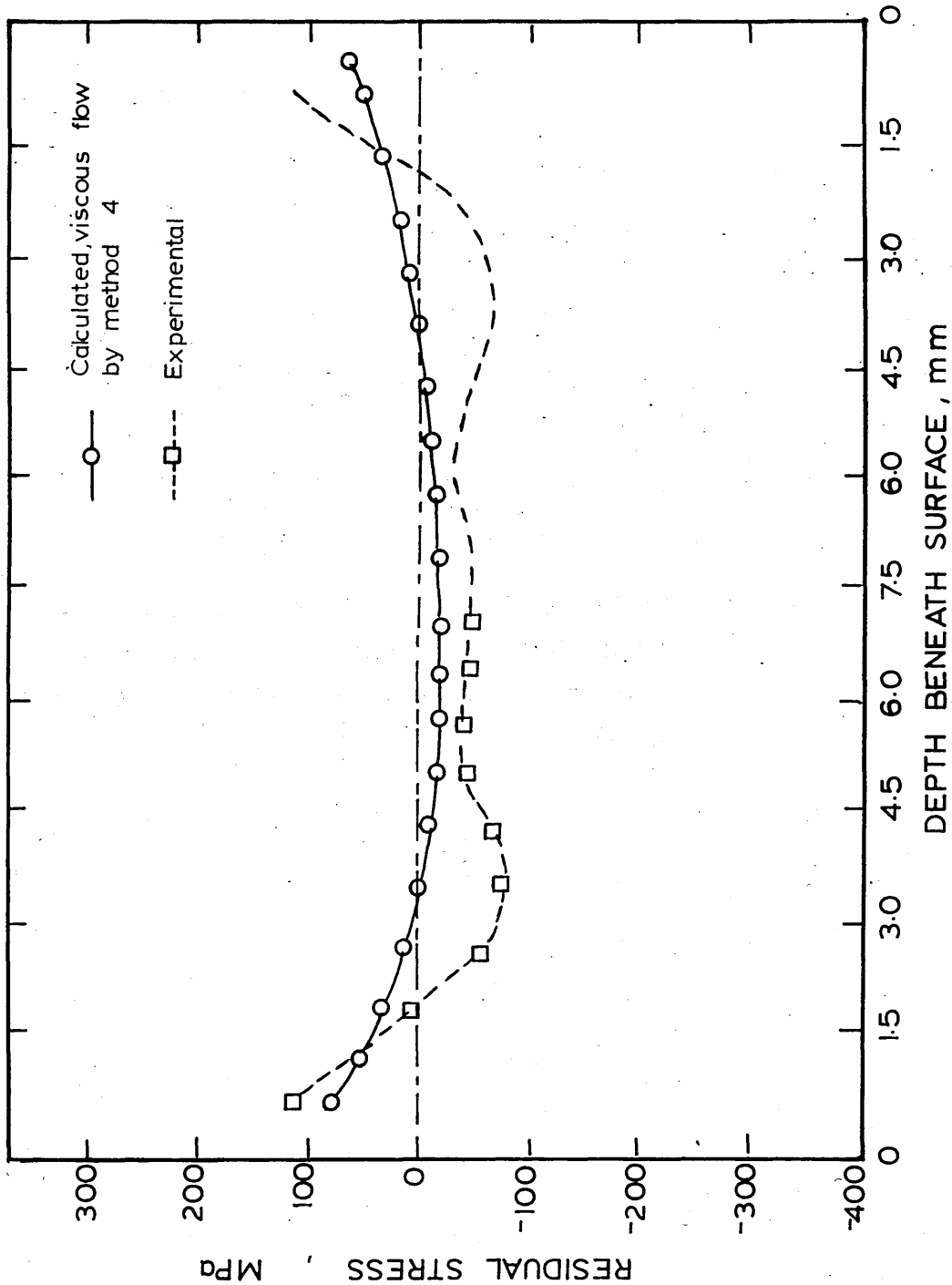
FIGURE 104:   Calculated residual stress distribution
               in a 20mm plate after water quenching
   with viscous flow represented by method 4.
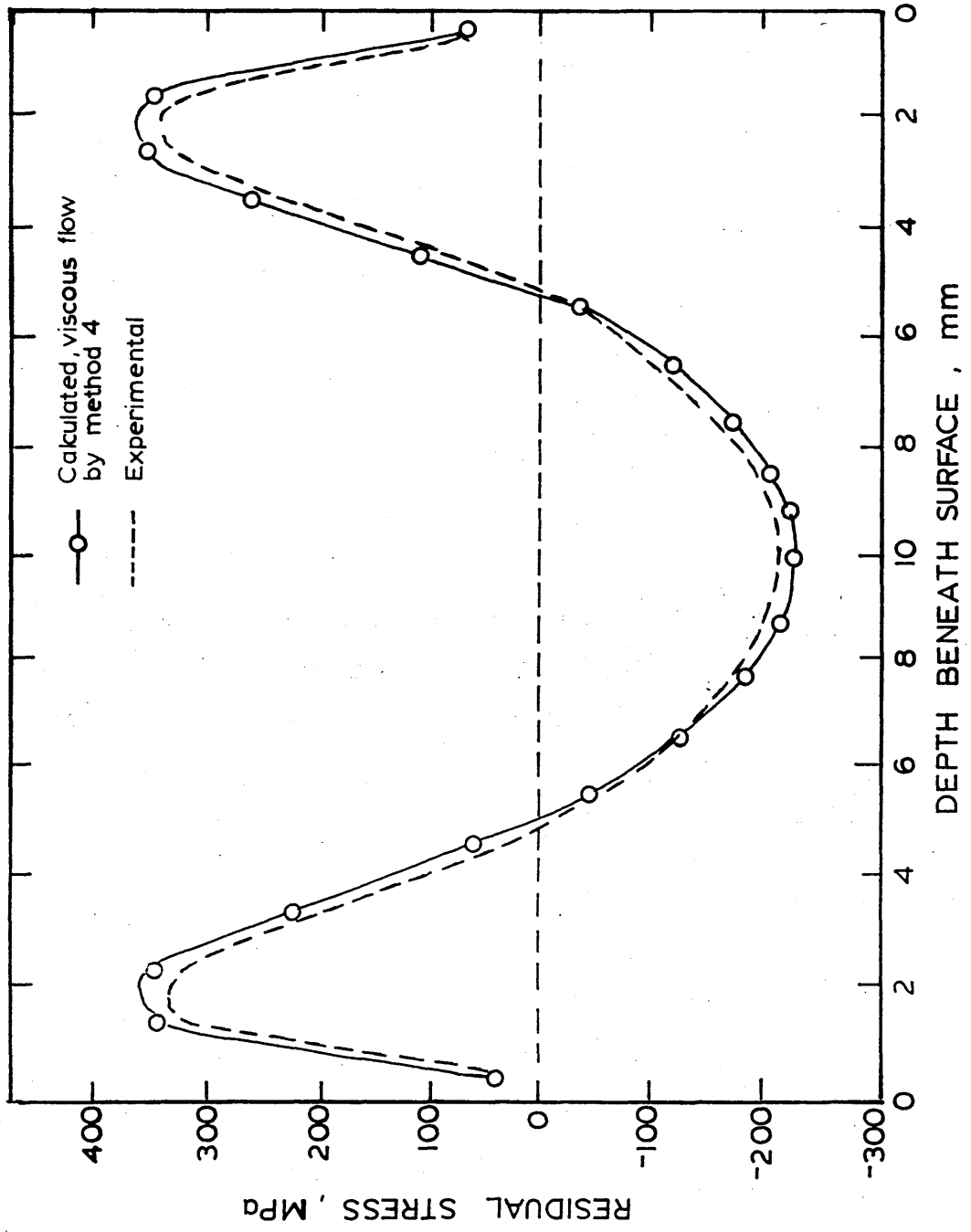
FIGURE 105:   Calculated stress and strain at the
centre and the surface of a 15mm plate
during martempering with viscous flow
represented by method 4.

STRESS, MPa (y-axis), STRAIN, % (x-axis)

Viscous flow by method 4

469°C, 78s
286°C
443°C, 82s
20°C
733°C, 1·2s
CENTRE
300°C, 122s
832°C, 2·1s
20°C
611°C, 11s
SURFACE
465°C, 78s
275°C, 132s

297.
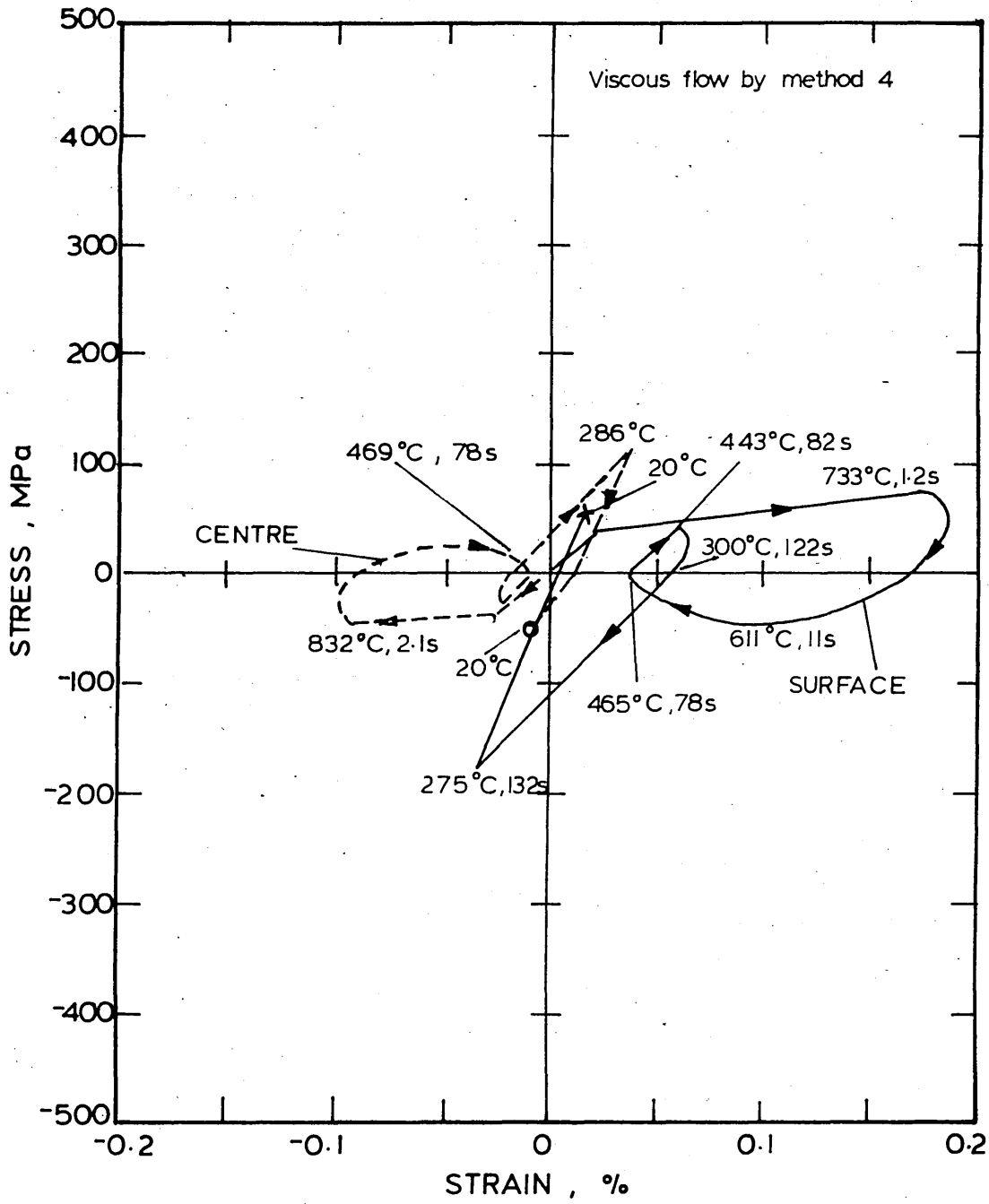
FIGURE 106:   Comparison of experimental and
              calculated residual stress
              distribution in a 15mm plate
              after martempering.

              Calculation no:

   CD3/M/NVF   )
              CD9/M/VF1   )
              CD10/M/VF2   )   see table 8
              CD11/M/VF3   )

298.
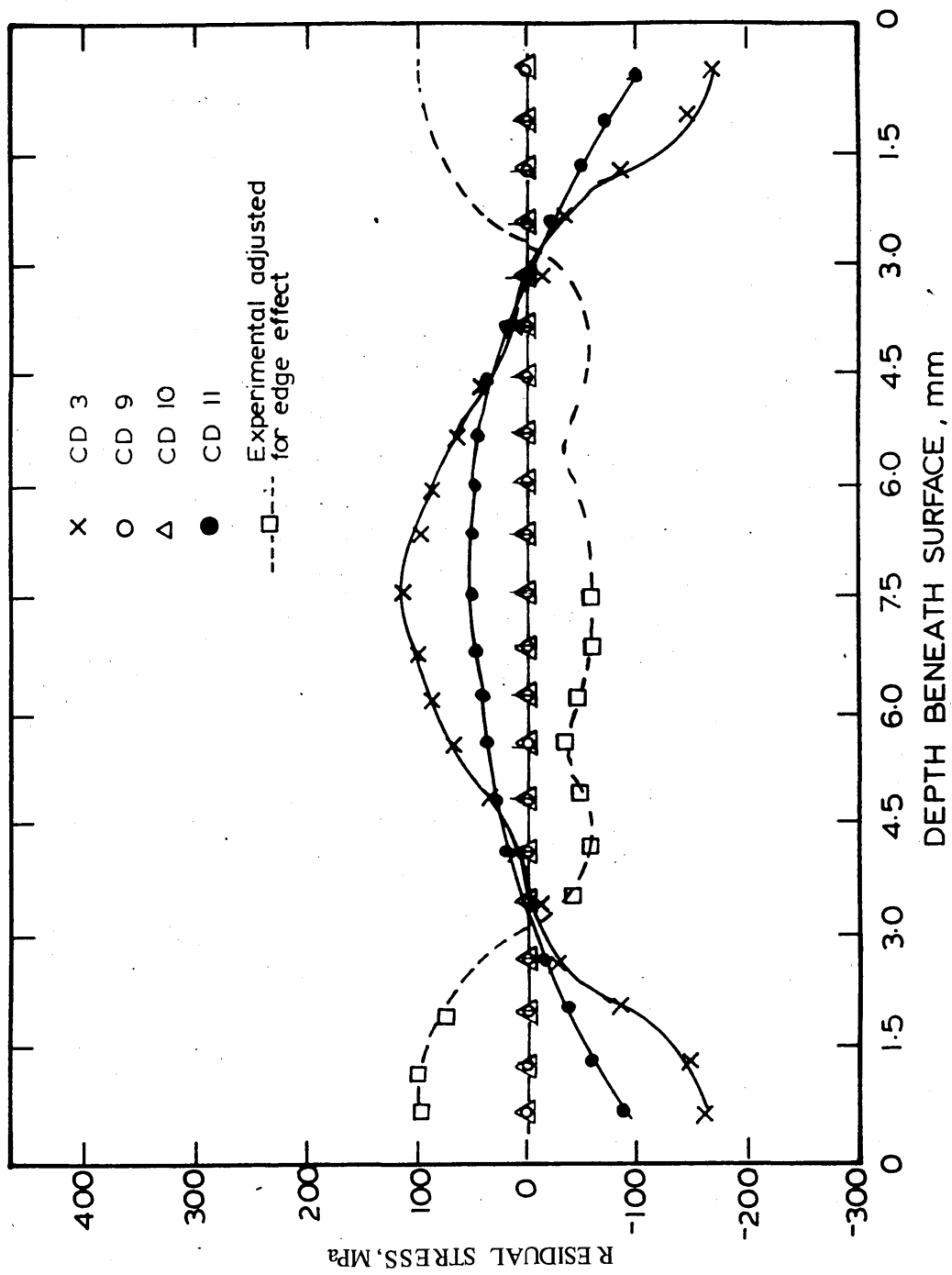
FIGURE 107:   Comparison of experimental and
                calculated residual strain
                distribution in a 15mm plate
                after martempering.

                Calculation no:

   CD3/M/NVF   )
                CD9/M/VF1   )
                CD10/M/VF2   )   see table 8
                CD11/M/VF3   )

DEPTH BENEATH SURFACE, mm

RESIDUAL STRAIN, %

x CD 3
o CD 9
△ CD 10
● CD 11
--□-- Experimental
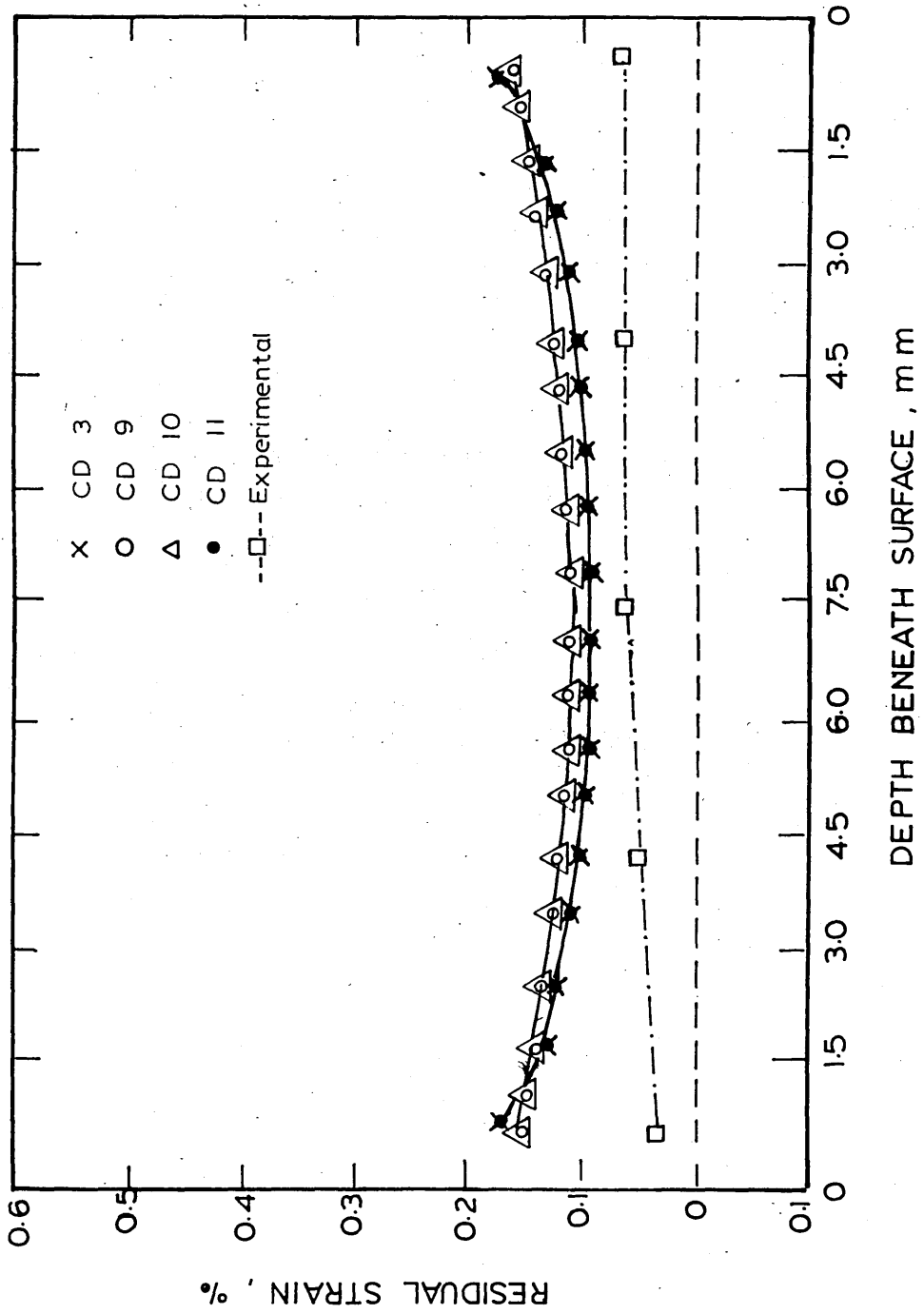
FIGURE 108:   Calculated residual stress distribution
in a 15mm plate after martempering with
viscous flow represented by method 4.

Calculated, viscous flow
by method 4
Experimental

DEPTH BENEATH SURFACE, mm

RESIDUAL STRESS, MPa
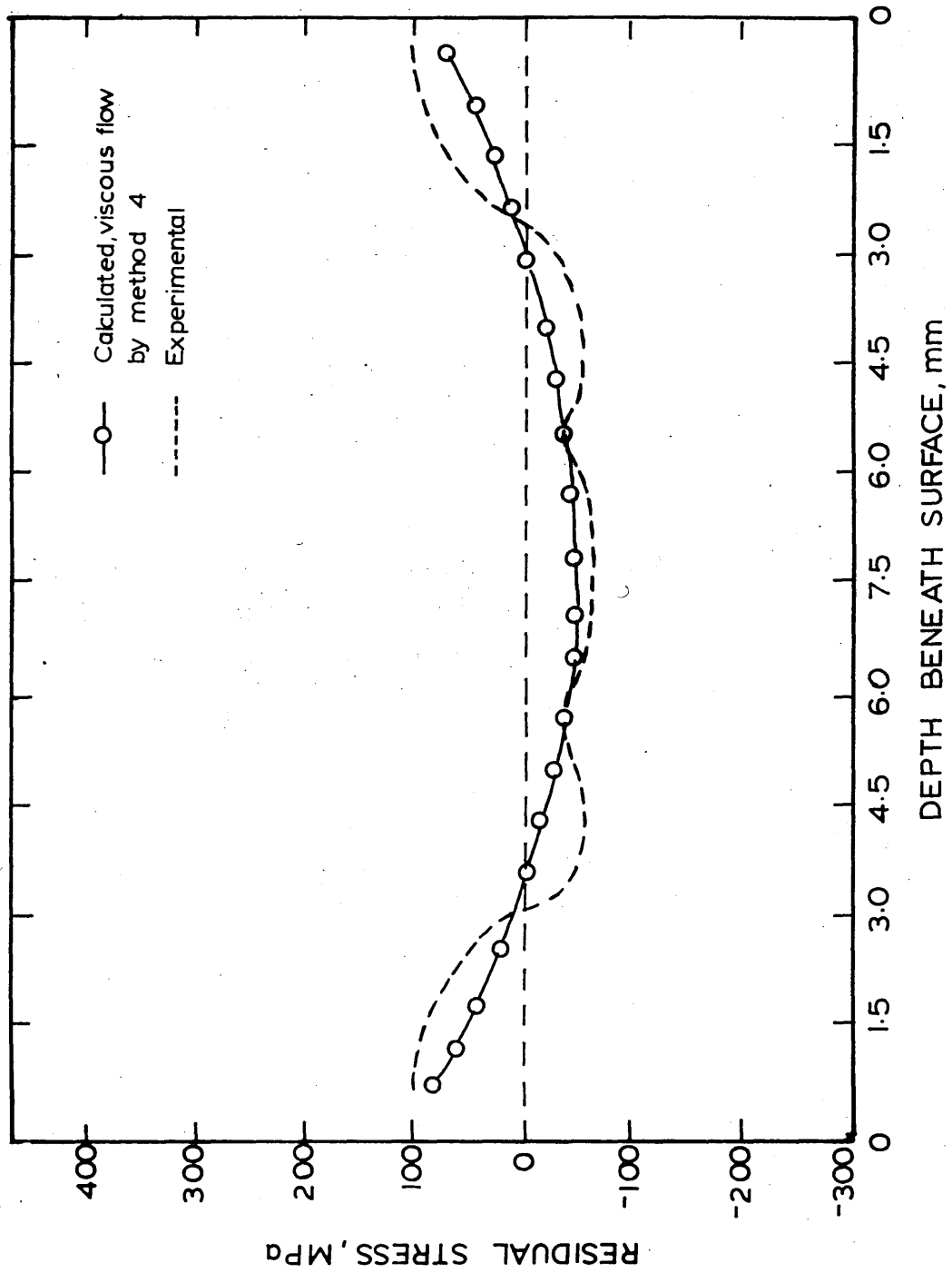
FIGURE 109: Calculated stress and strain at the
centre and the surface of a 15mm
plate during martempering (salt bath
temperature reduced to 250°C and
viscous flow represented by method 1).

Salt bath temperature
reduced to 250°C,
viscous flow by method I.
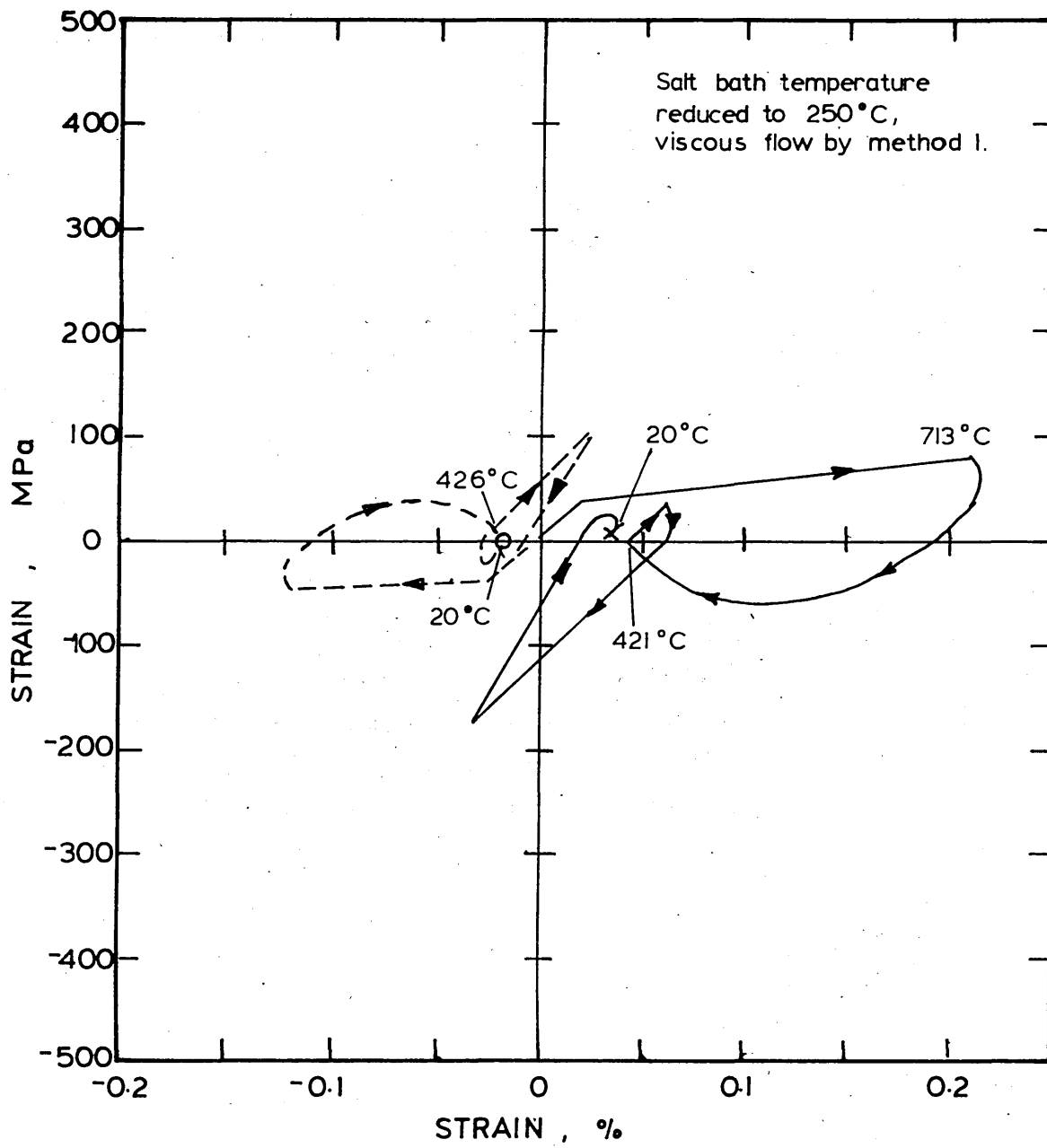
FIGURE 110:   Calculated stress and strain at the
              centre and the surface of a 15mm plate
              during oil quenching (reduction in
              flow stress to simulate transformation
              plasticity and viscous flow represented
              by method 4).

Flow stress reduced below Ms, method 4
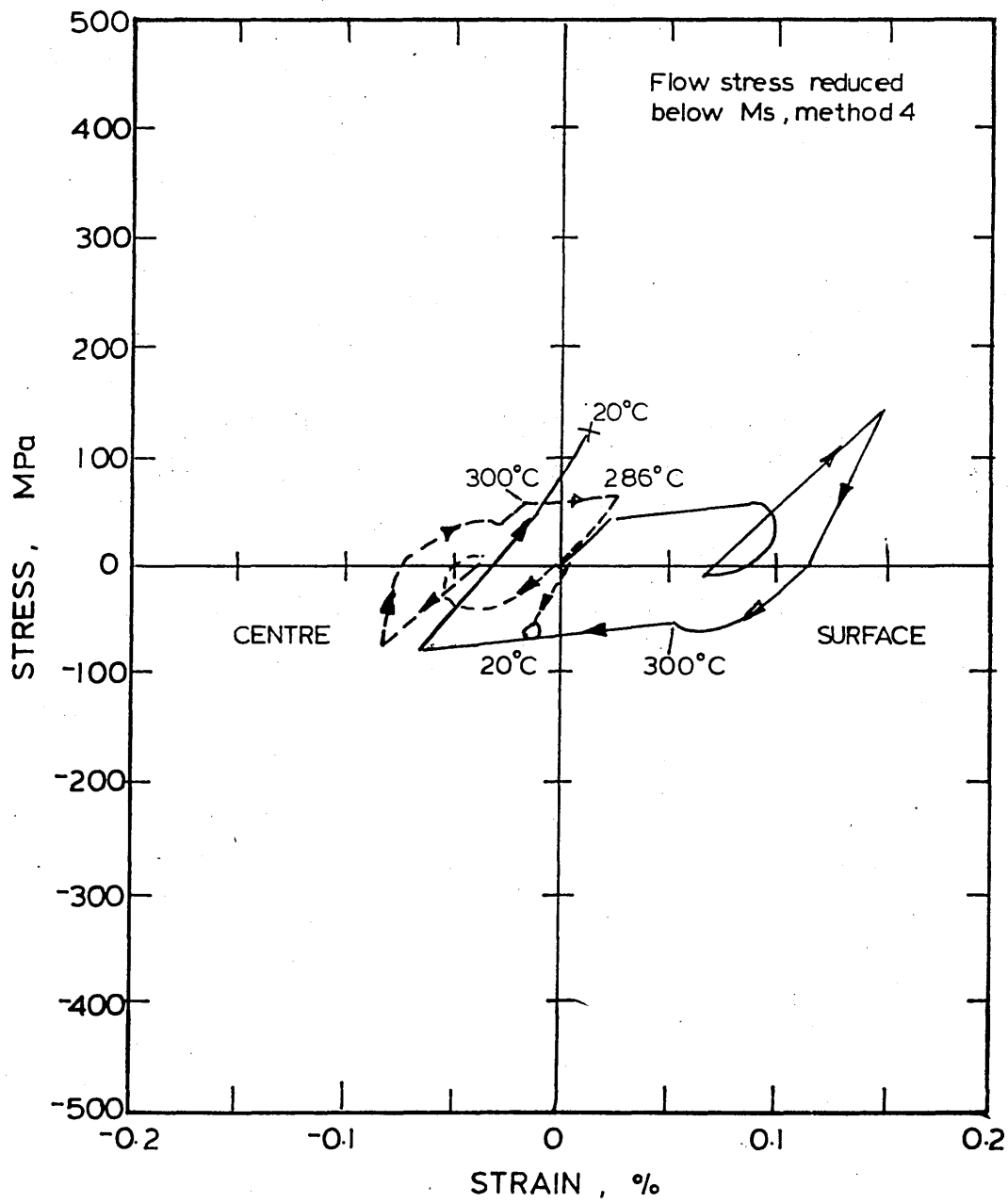
FIGURE 111:   Calculated stress and strain at the
              centre and the surface of a 15mm plate
              during oil quenching with viscous flow
              represented by method 4.

Viscous flow by method 4
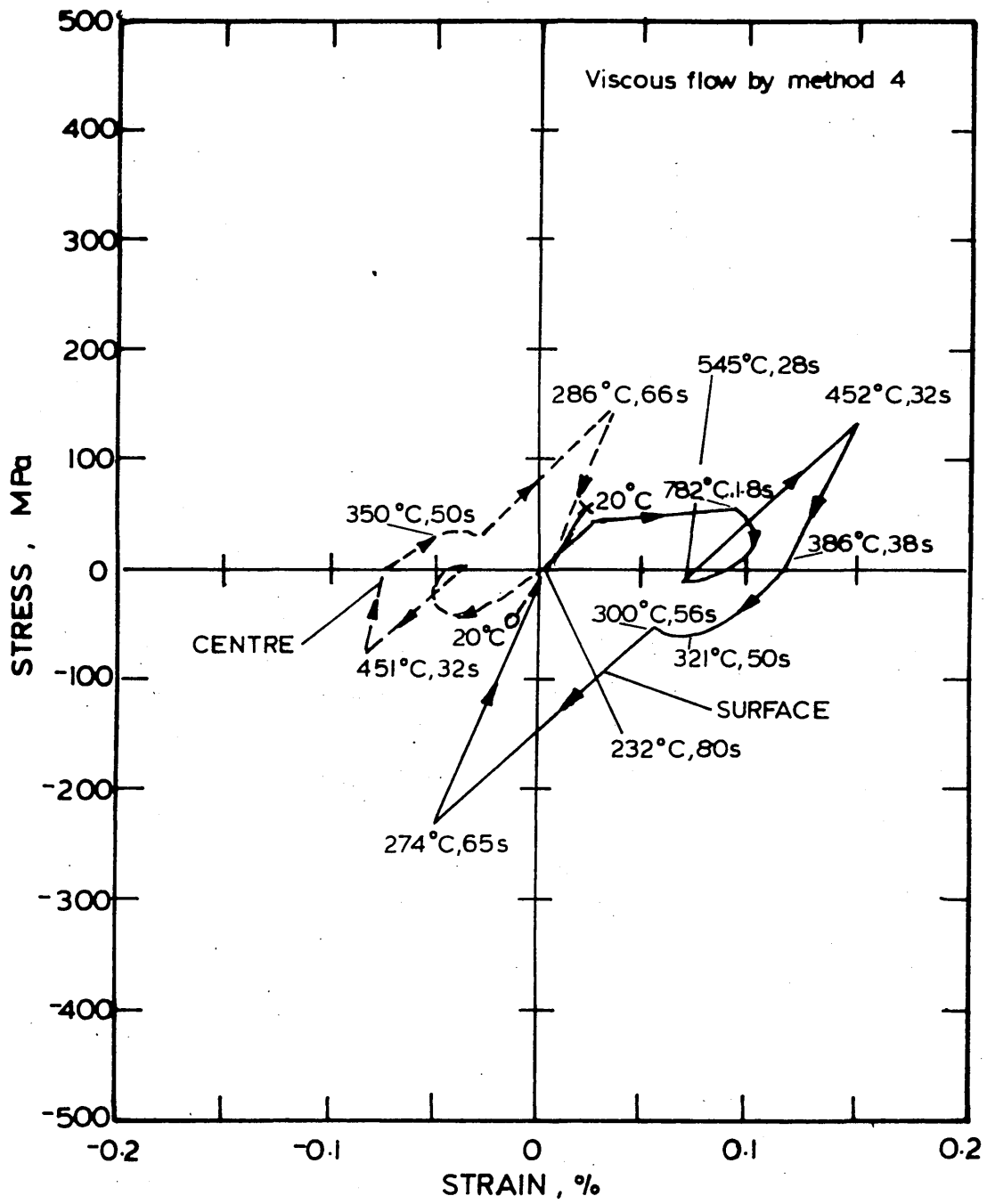
FIGURE 112:   Calculated residual stress distribution
                in a 15mm plate after oil quenching
                (reduction in flow stress to simulate
                transformation plasticity and viscous
   flow represented by method 4).
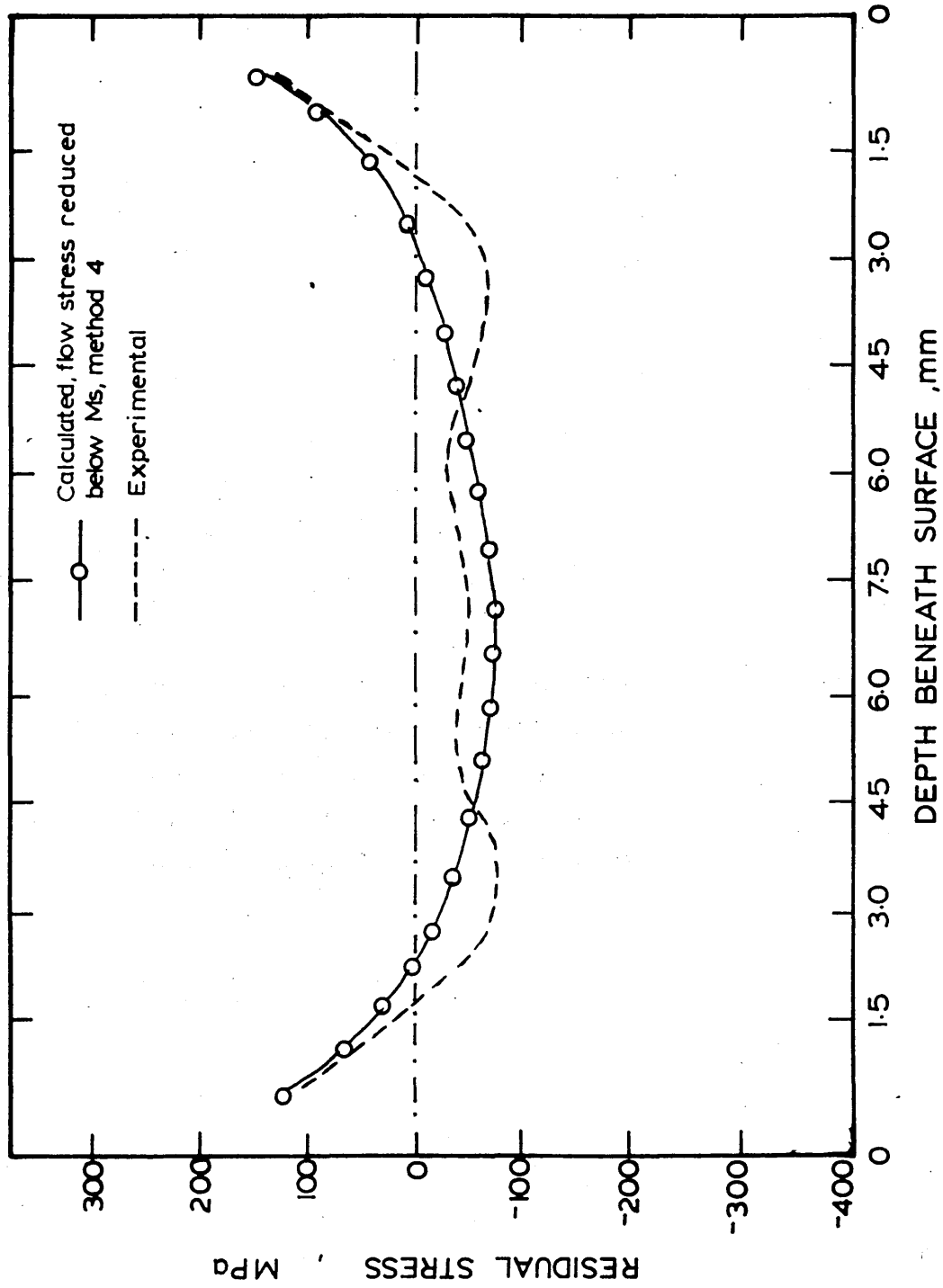
FIGURE 113:   Calculated residual strain distribution
in a 15mm plate after oil quenching with
a reduction in flow stress to simulate
transformation plasticity and viscous
flow represented by method 4.

305.
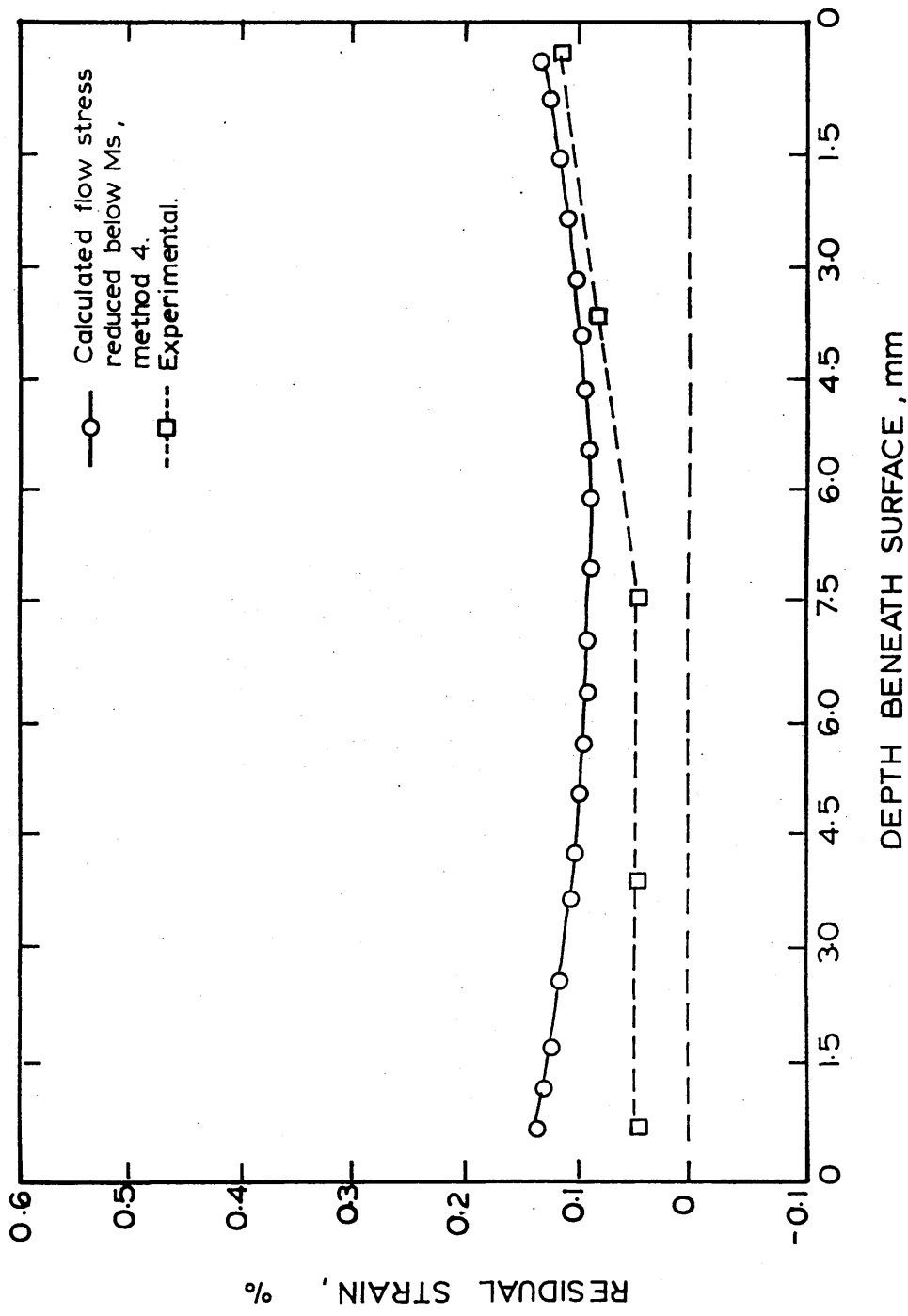
FIGURE 114:   Calculated residual strain distribution
               in a 15mm plate after oil quenching with
   viscous flow represented by method 4.
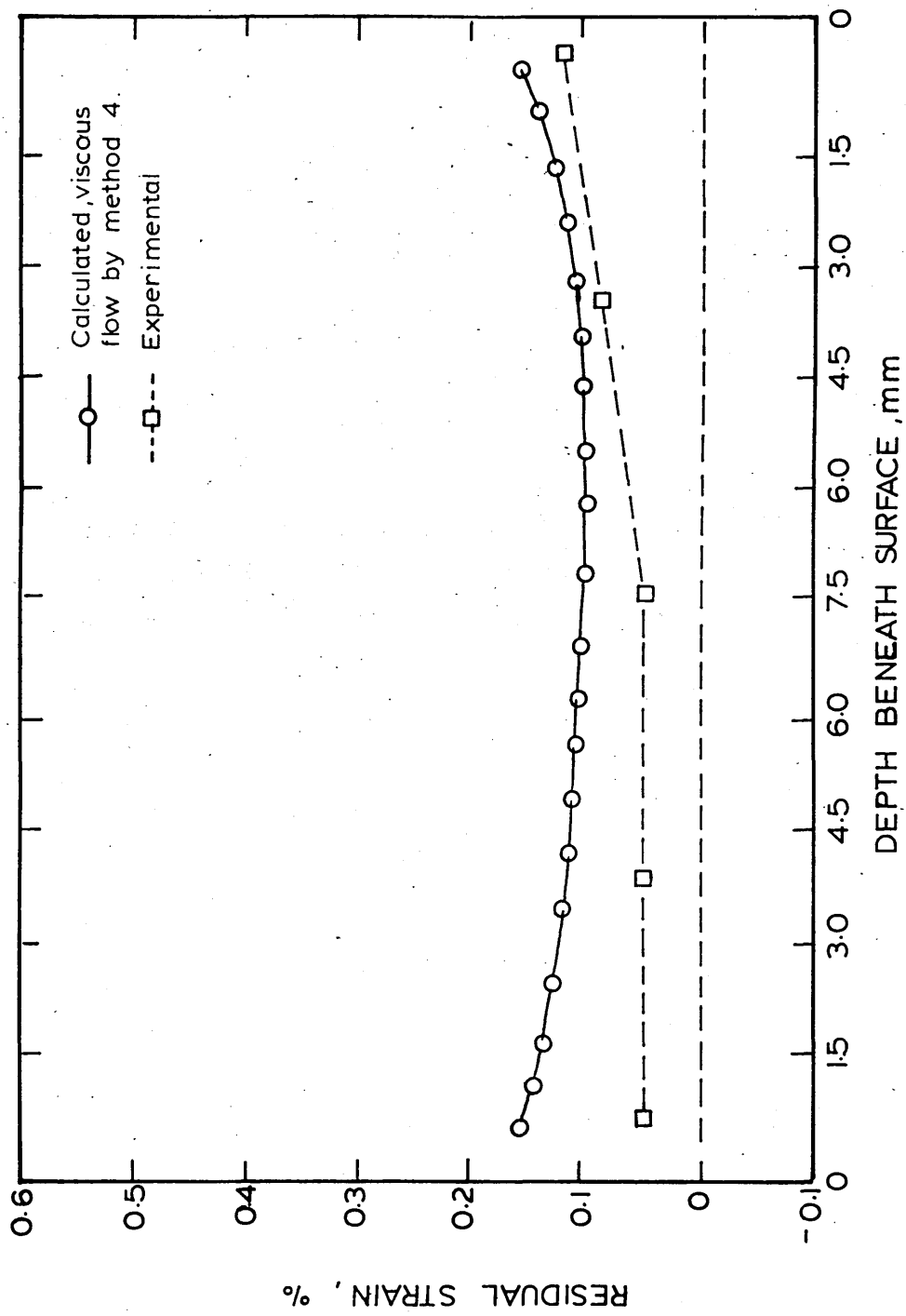
FIGURE 115:   Calculated stress and strain at the
centre and the surface of a 20mm
plate during water quenching with a
reduction in flow stress to simulate
transformation plasticity and viscous
flow represented by method 4.

Flow stress reduced below Ms, method 4

300°C

286°C

273°C

265°C

300°C

SURFACE

20°C

CENTRE

STRAIN, %

STRESS, MPa

500
250
0
-250
-500
-750
-1000
-1250

-0.6 -0.5 -0.4 -0.3 -0.2 -0.1 0 0.1 0.2 0.3 0.4 0.5 0.6

307.
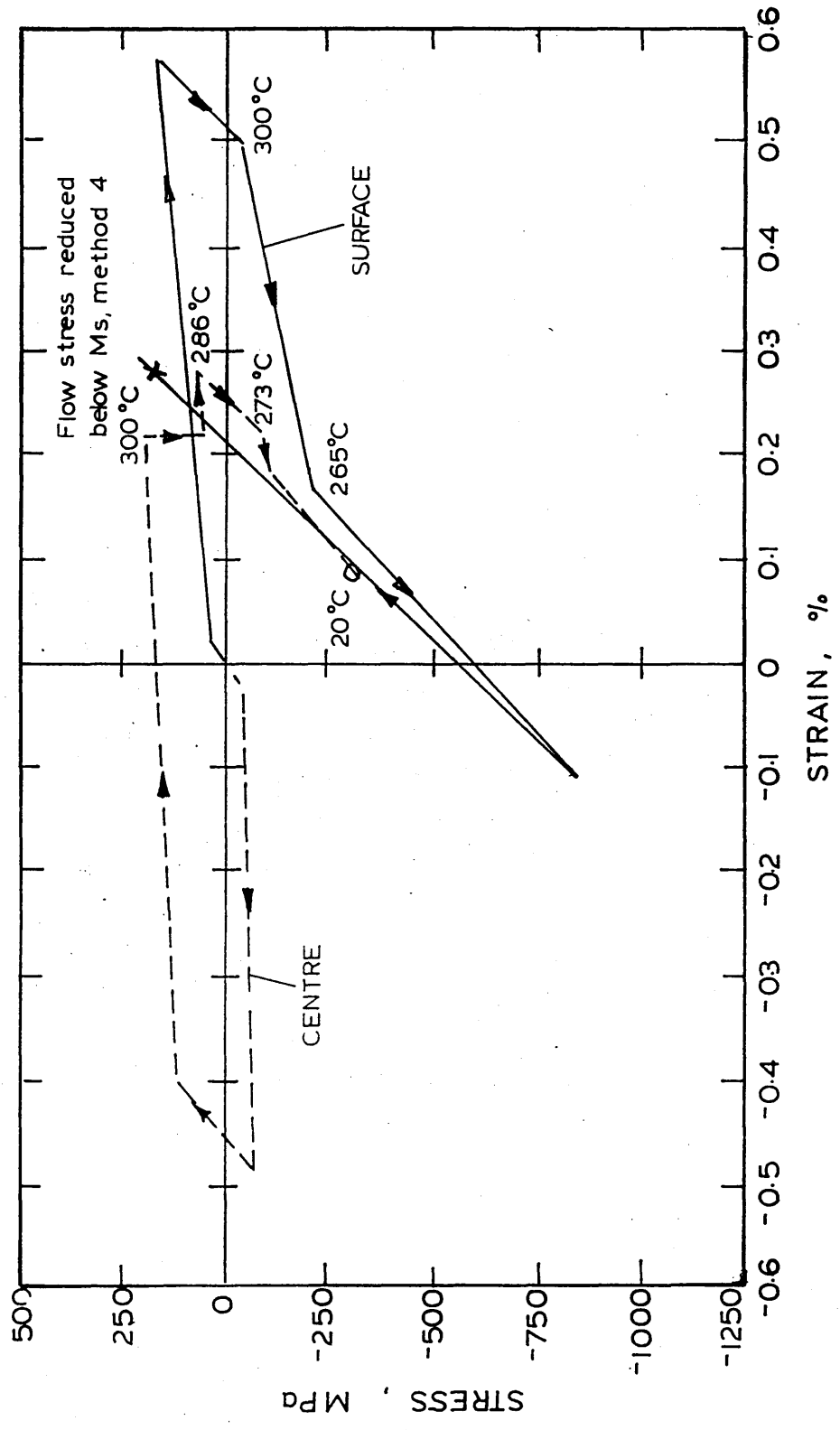
FIGURE 116:   Calculated stress and strain at the
centre and the surface of a 20mm plate
during water quenching with viscous
flow represented by method 4.
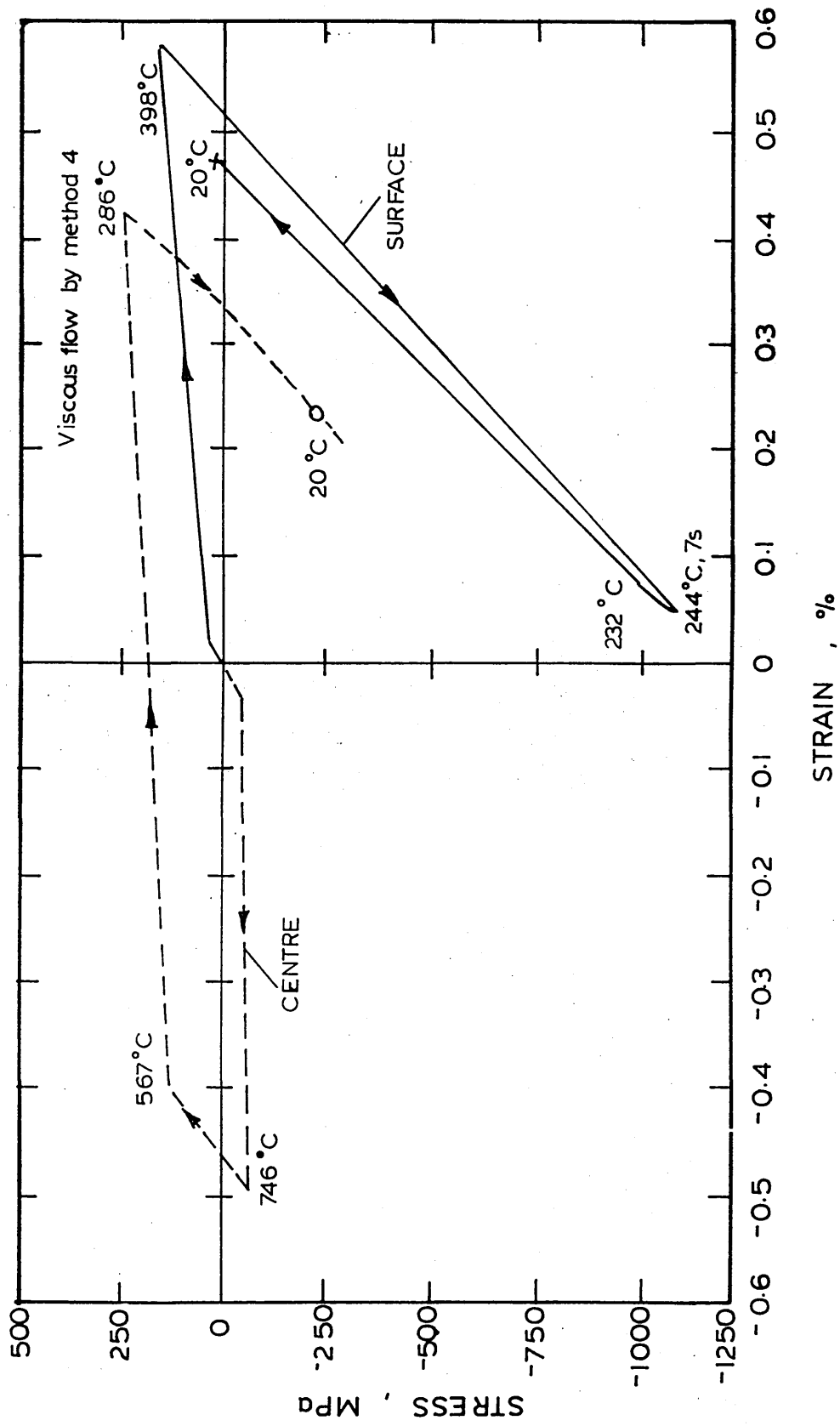
FIGURE 117:   Calculated residual stress distribution
               in a 20mm plate after water quenching
               with flow stress reduced to simulate
               transformation plasticity and viscous
               flow represented by method 4.

309.
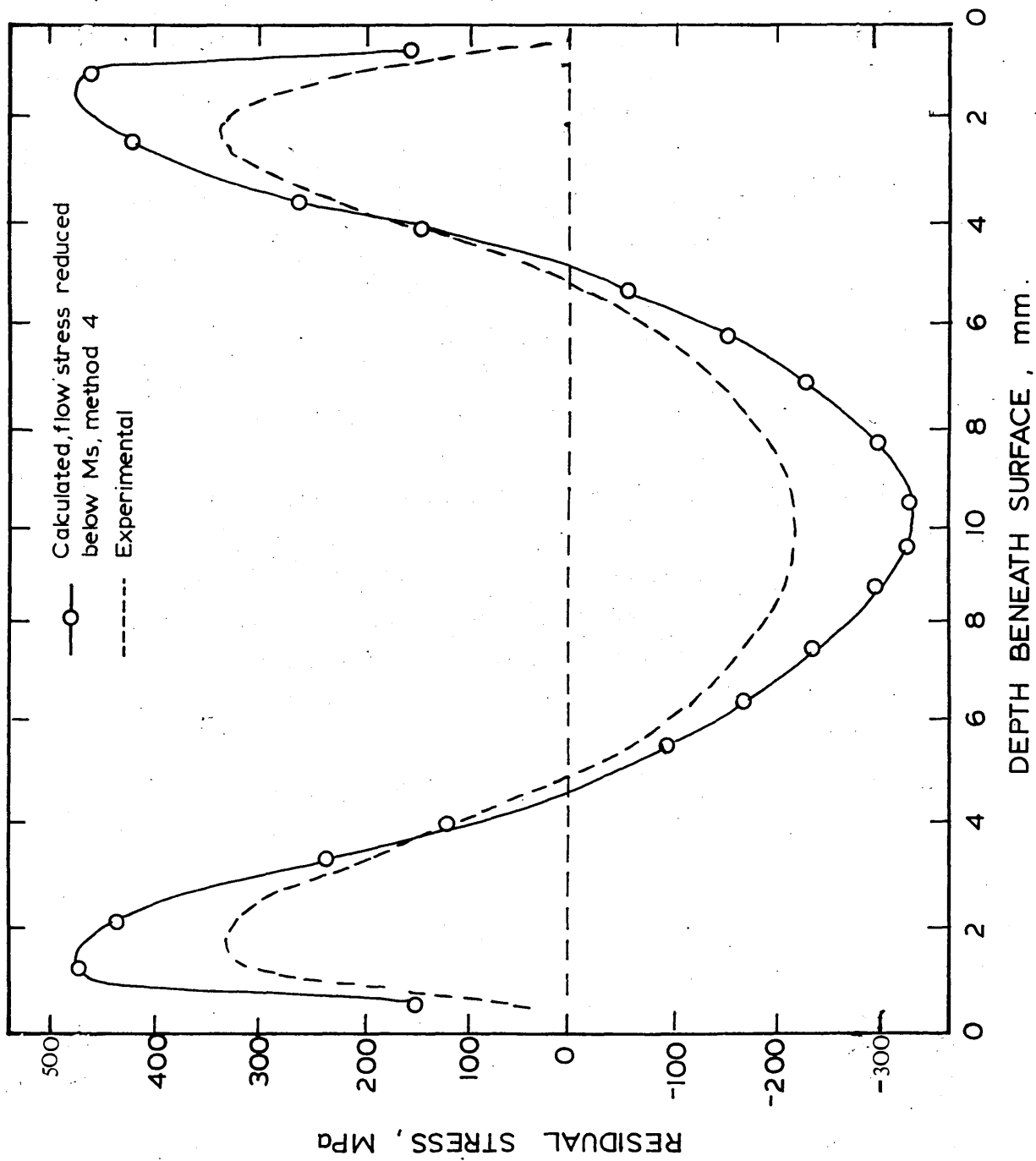
FIGURE 118:   Calculated and experimental residual
strain distribution in a 20mm plate
after water quenching with flow stress
reduced to simulate transformation
plasticity and viscous flow represented
by method 4.

310.
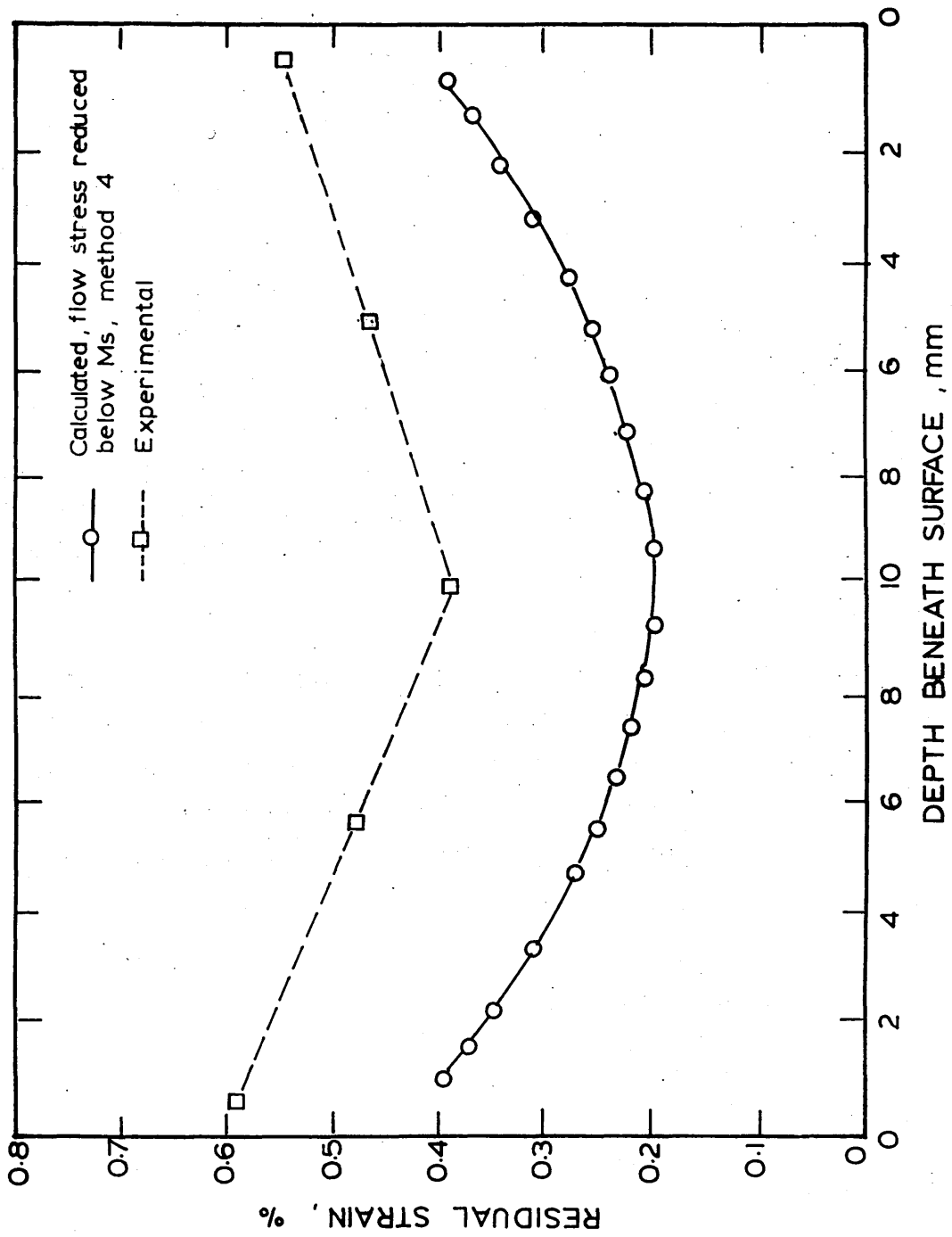
FIGURE 119:   Calculated stress and strain at the
centre and the surface of a 15mm plate
during oil quenching with transformation
plasticity simulated as additional strain
and viscous flow represented by method 4.

TRIP as aditional strain,
viscous flow by method 4

311.
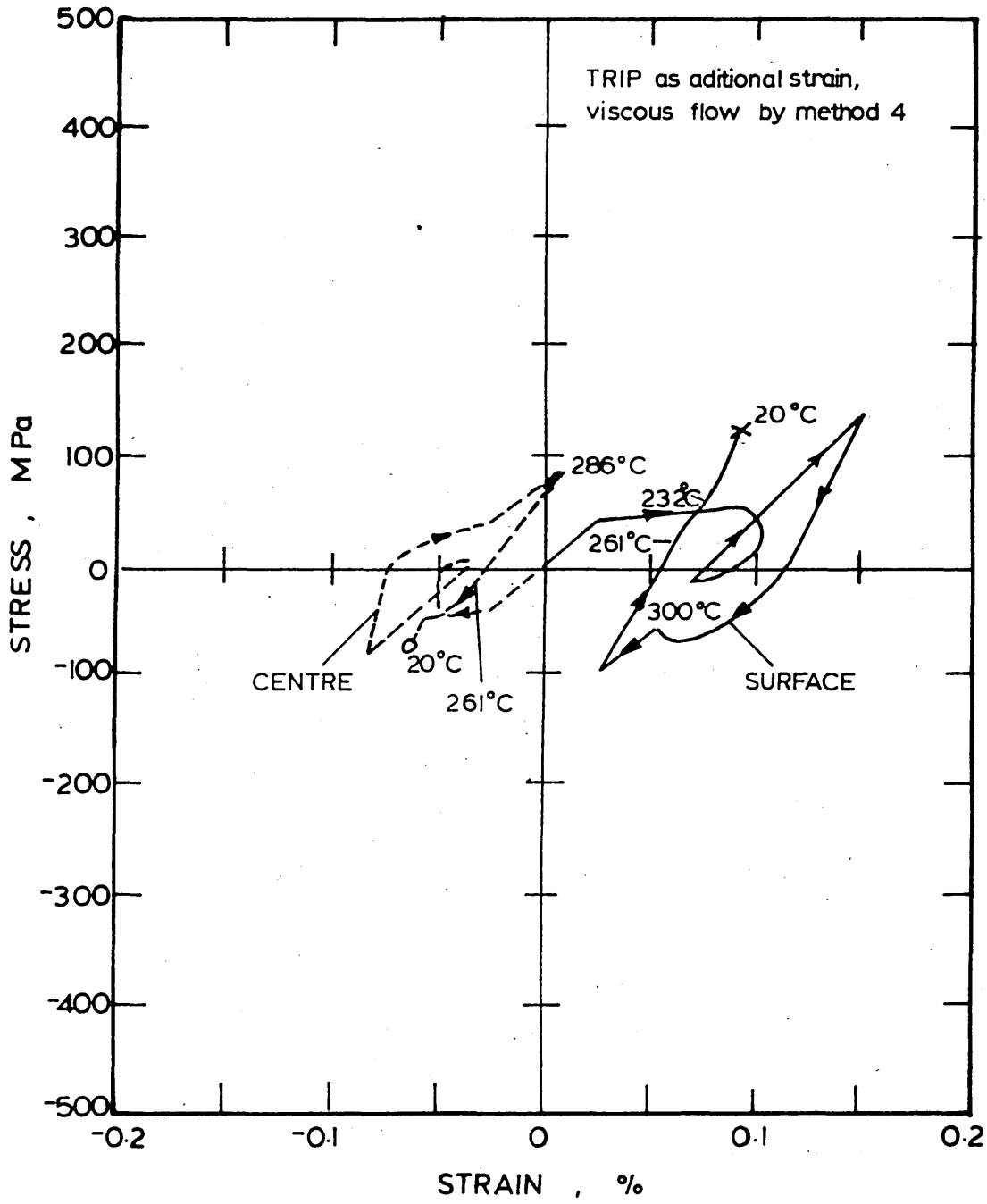
FIGURE 120:   Calculated and experimental residual
              stress distribution in a 15mm plate
              after oil quenching with transformation
              plasticity simulated as additional
              strain and viscous flow represented by
              method 4.

Calculated, TRIP as aditional
strain, viscous flow by method 4

Experimental

DEPTH BENEATH SURFACE, mm

RESIDUAL STRESS, MPa

312.
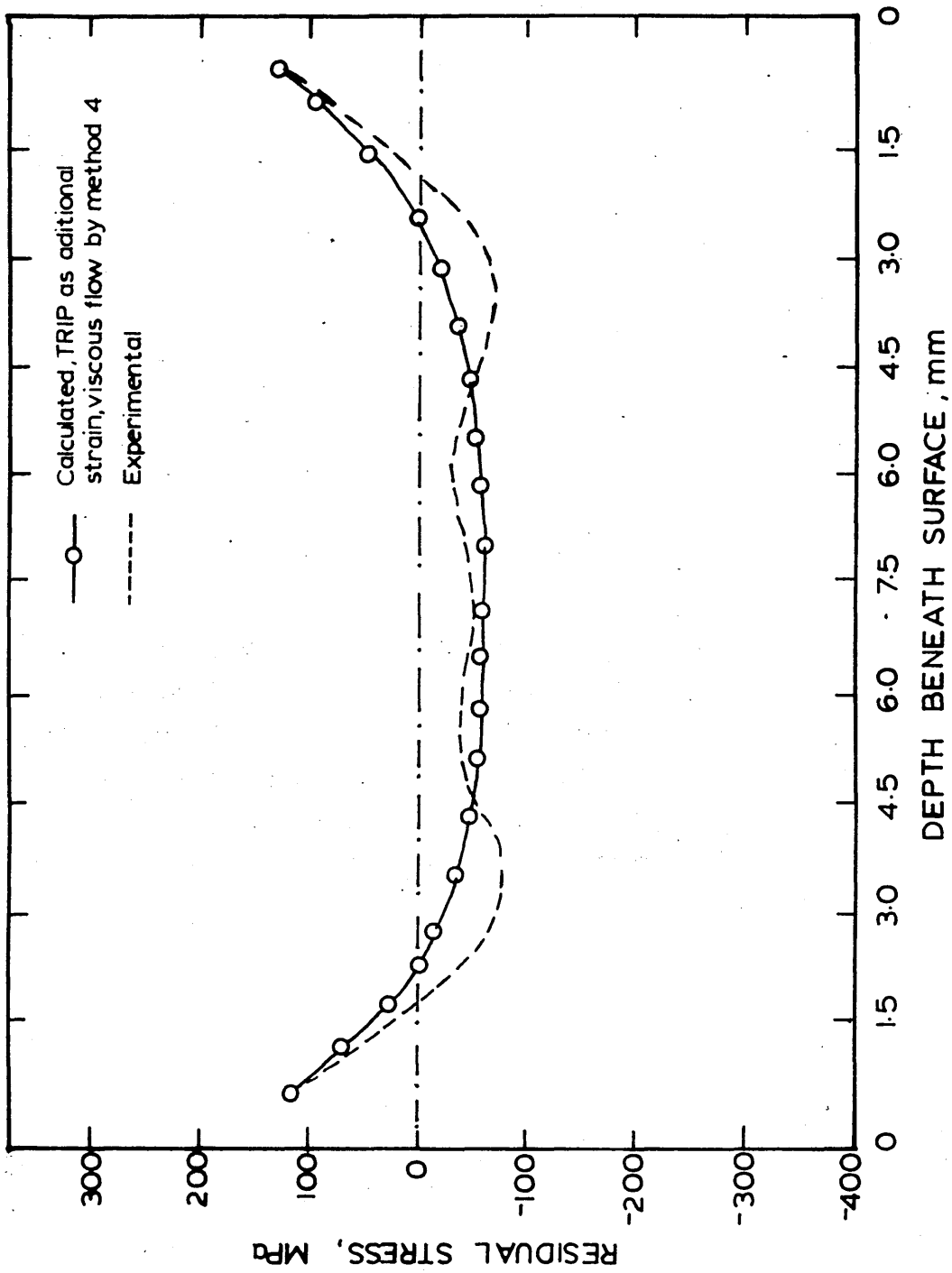
FIGURE 121:   Calculated and experimental residual
               strain distribution in a 15mm plate
               after oil quenching with transformation
               plasticity simulated as additional strain
   and viscous flow represented by method 4.

313a.

313.
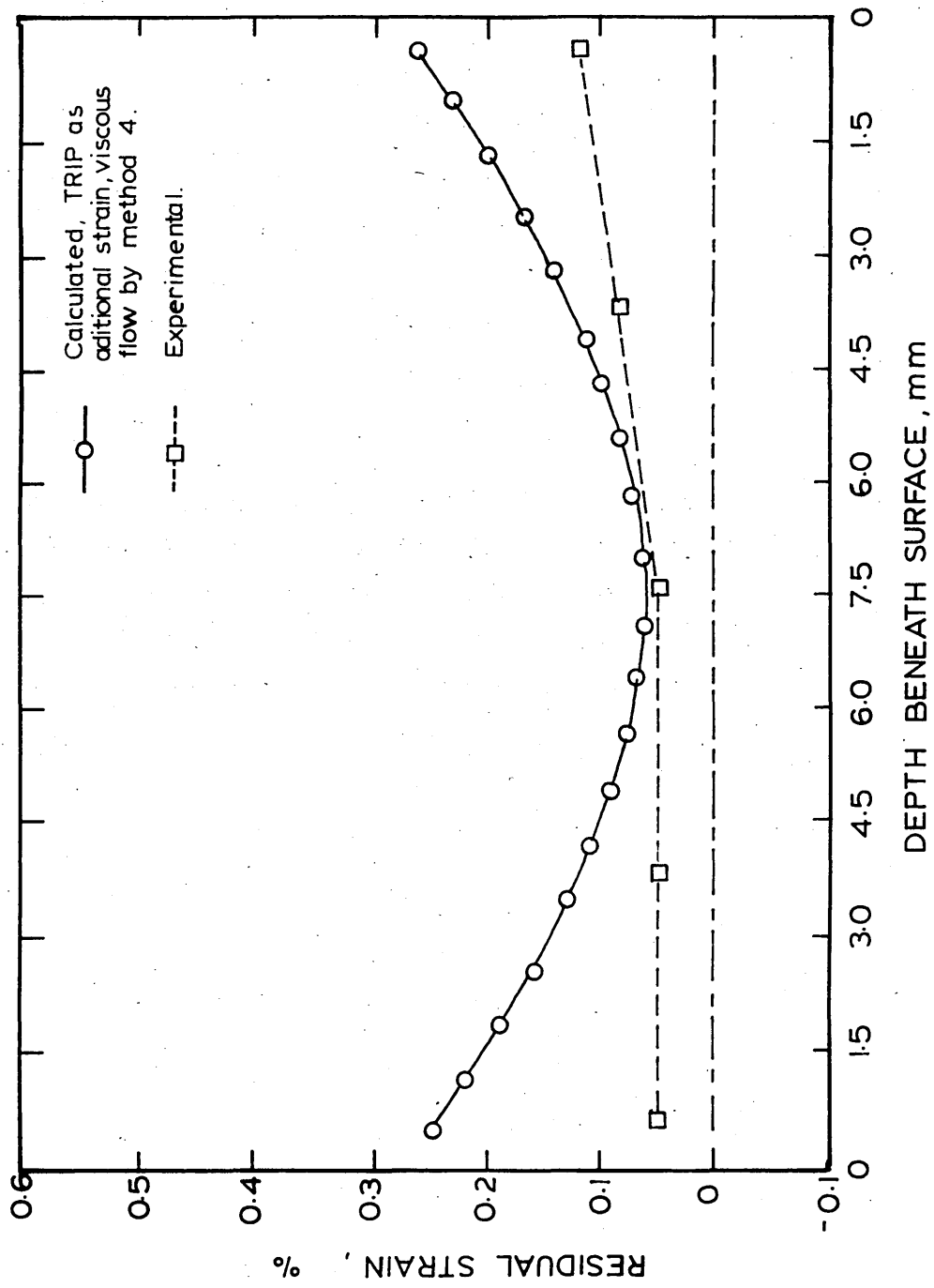
FIGURE 122:   Calculated stress and strain at the
centre and the surface of 20mm plate during
water quenching with transformation
plasticity simulated as additional strain
and viscous flow represented by method 4.

TRIP as aditional strain,
viscous flow by method 4

SURFACE

CENTRE

STRAIN , %

STRESS, MPa

314.
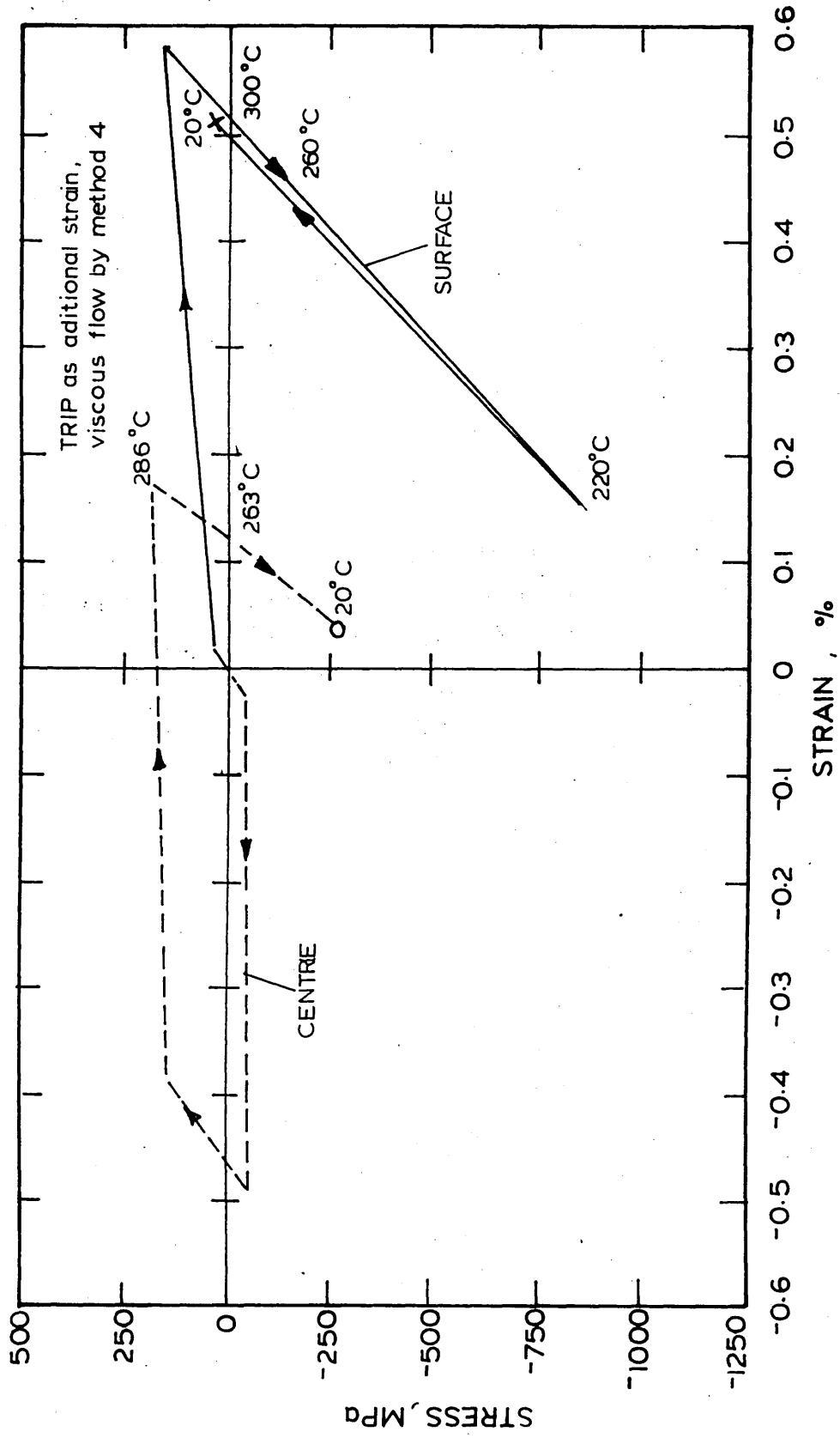
FIGURE 123:   Calculated and experimental residual
               stress distribution in a 20mm plate
               after water quenching with transformation
               plasticity simulated as additional strain
   and viscous flow represented by method 4.
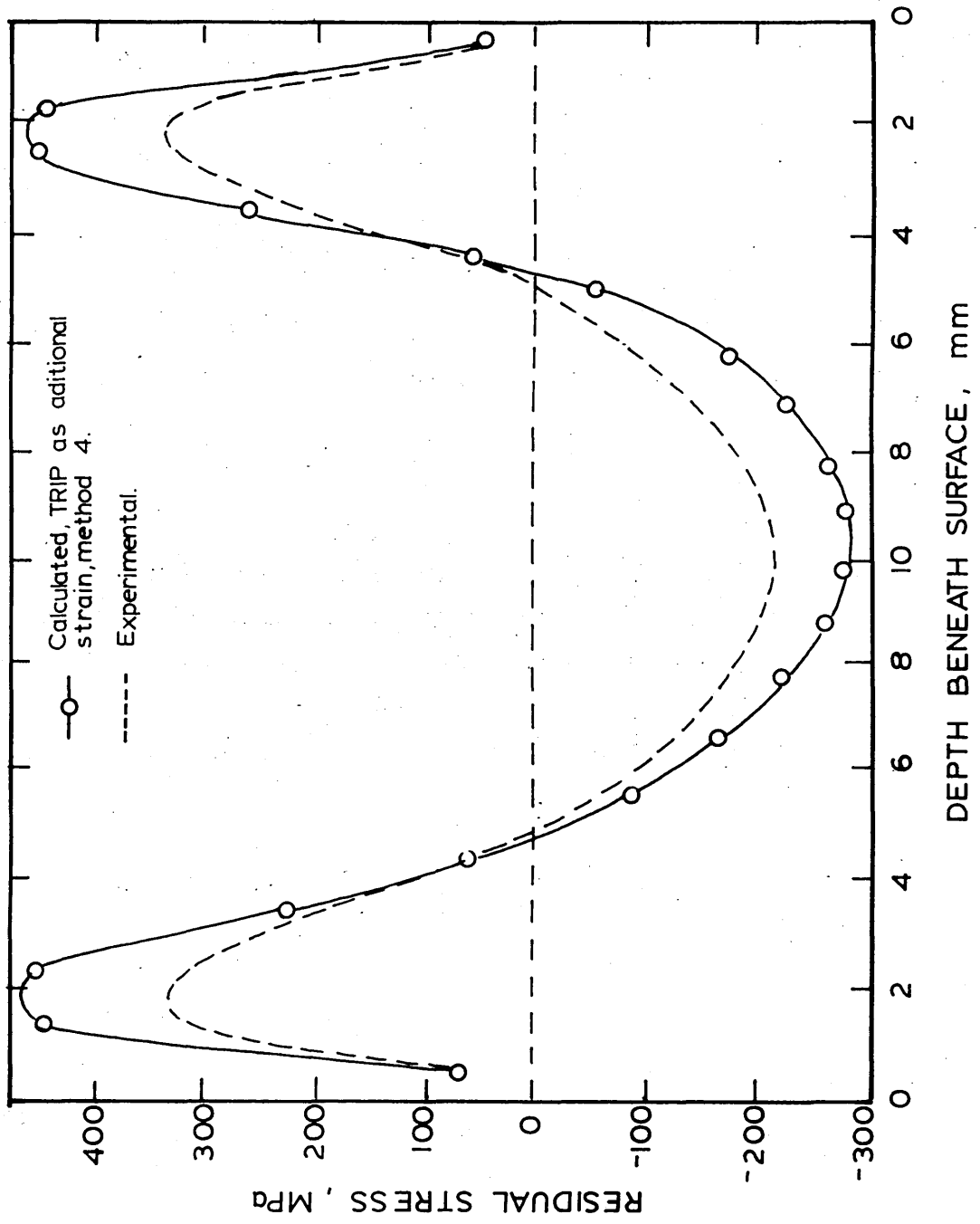
FIGURE 124:   Calculated and experimental residual
               strain distribution in a 20mm plate
               after water quenching with transformation
               plasticity simulated as additional strain
   and viscous flow represented by method 4.
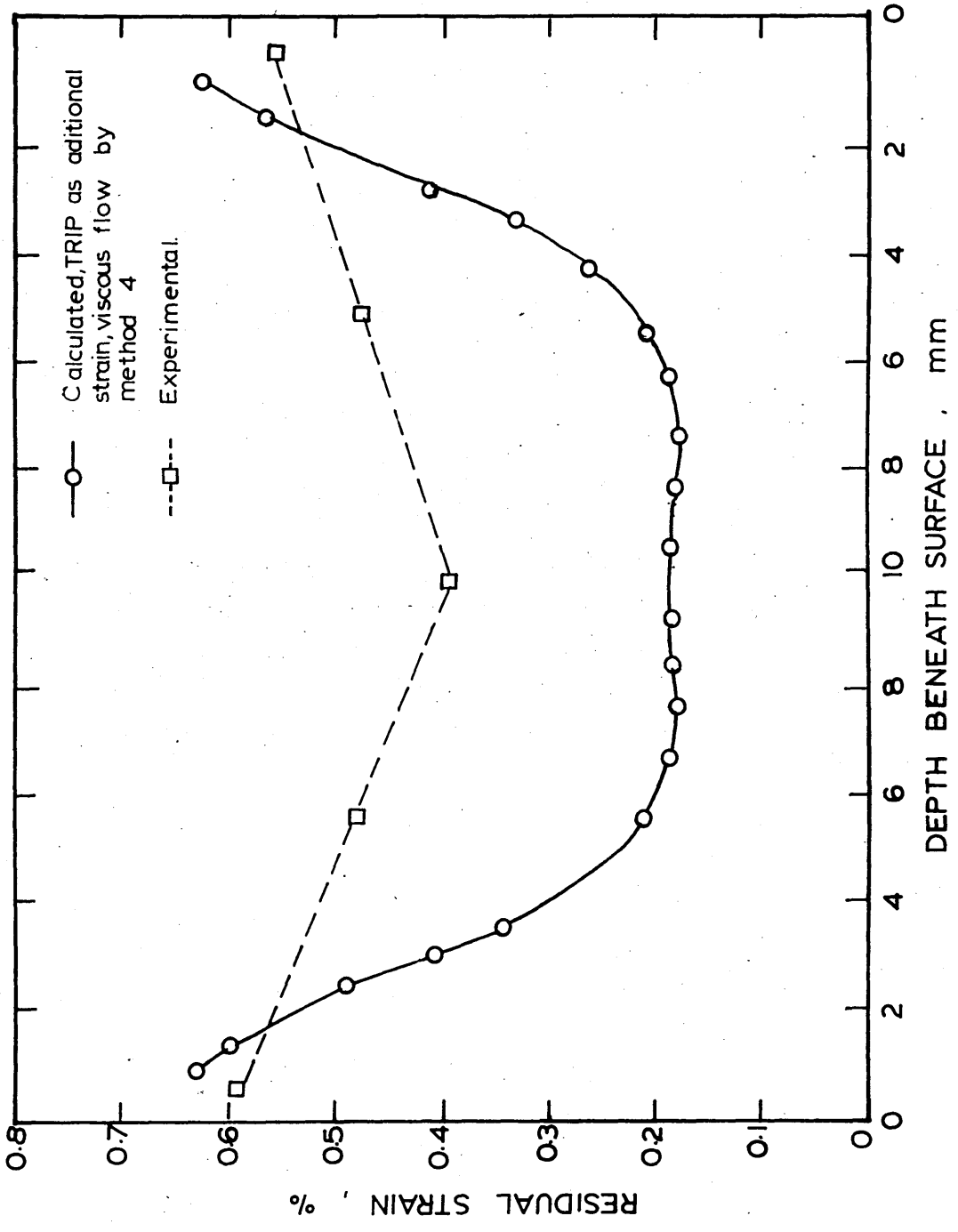
FIGURE 125: Calculated stress and strain at
the centre and surface of a 15mm plate
during martempering (air cool
subsequent to salt bath and viscous
flow represented by method 1).

Air cool subsequent to salt bath.
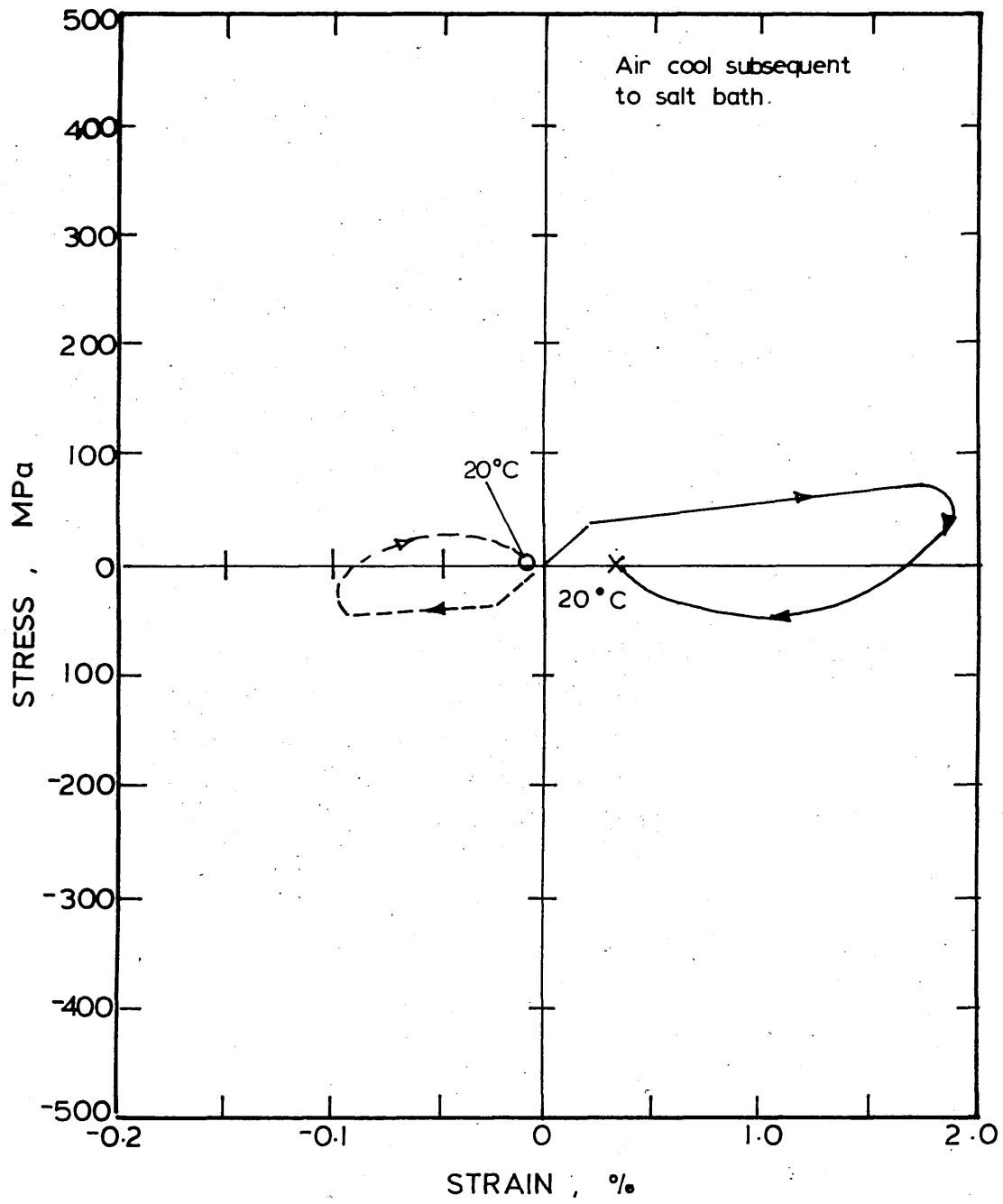
APPENDIX 1

Stress relaxation and creep equations for mechanical models under uniaxial conditions of stress

The deviatoric portions of the stress and strain tensors are given by:

$$s_{IJ} = \sigma_{IJ} - \delta_{IJ}\, \sigma_m \qquad \qquad 1.1$$

$$e_{IJ} = \varepsilon_{IJ} - \delta_{IJ}\, \sigma_m \qquad \qquad 1.2$$

The relationships between stress and strain for mechanical models, under consideration, are given in terms of their deviatoric portions, viz:

Maxwell body

$$\dot{e}_{IJ} = \frac{\dot{s}_{IJ}}{2G} + \frac{s_{IJ}}{2\eta} \qquad \qquad 1.3$$

Kelvin body

$$2\eta\, \dot{e}_{IJ} + 2G\, e_{IJ} = s_{IJ} \qquad \qquad 1.4$$

Standard linear solid

$$\dot{e}_{IJ} + \phi\, e_{IJ} = \frac{\dot{s}_{IJ}}{2G} + \frac{s_{IJ}}{2\eta} \qquad \qquad 1.5$$

The derivations of equations 1.3, 1.4 and 1.5 in the case of uniaxial stress conditions is presented below:

$$\dot{e}_{IJ} = \frac{\dot{s}_{IJ}}{2G} + \frac{s_{IJ}}{2\eta} \qquad \qquad 1.3$$

Substituting the values of s_{IJ} and e_{IJ} from equations 1.1 and 1.2 into equation 1.3

$$\dot{\varepsilon}_{IJ} - \delta_{IJ}\, \dot{\varepsilon}_m = \frac{1}{2G}\left(\dot{\sigma}_{IJ} - \delta_{IJ}\, \dot{\sigma}_m \right) + \frac{1}{2\eta}\left(\sigma_{IJ} - \delta_{IJ}\, \sigma_m \right) \qquad 1.6$$

For uniaxial stress conditions

$$\varepsilon_{IJ} = \varepsilon_{xx}, \quad \varepsilon_{yy} = \varepsilon_{zz} = -\nu \varepsilon_{xx}$$

$$\sigma_{IJ} = \sigma_{xx}, \quad \sigma_{yy} = \sigma_{zz} = 0$$

$$\delta_{IJ} = 1$$

Mean strain $\quad \varepsilon_m = \dfrac{(1-2\nu)}{3} \varepsilon_{xx}$ $\qquad\qquad$ 1.7

Mean stress $\quad \sigma_m = \dfrac{\sigma_{xx}}{3}$ $\qquad\qquad$ 1.8

Substituting from equations 1.7 and 1.8 into equation 1.6

$$\dot{\varepsilon}_{xx} - \frac{(1-2\nu)}{3} \dot{\varepsilon}_{xx} = \frac{1}{2G} \left(\frac{\dot{\sigma}_{xx} - \dfrac{\dot{\sigma}_{xx}}{3}} {} \right) + \frac{1}{2\eta} \left(\frac{\sigma_{xx} - \dfrac{\sigma_{xx}}{3}}{} \right)$$

$$\frac{2(1+\nu)}{3} \dot{\varepsilon}_{xx} = \frac{\dot{\sigma}_{xx}}{3G} + \frac{\sigma_{xx}}{3\eta} \qquad\qquad 1.9$$

Stress relaxation is conducted at constant strain

i.e. $\quad \dot{\varepsilon}_{xx} = 0$

Equation 1.9 reduces to

$$\frac{\dot{\sigma}_{xx}}{3G} + \frac{\sigma_{xx}}{3\eta} = 0$$

$$\frac{d\,\sigma_{xx}}{dt} = -\frac{G}{\eta} \sigma_{xx}$$

$$\frac{d\,\sigma_{xx}}{\sigma_{xx}} = -\frac{G}{\eta} dt$$

Integrating

$$Ln\ \sigma_{xx} = -\frac{G}{\eta} t + constant$$

At time t = 0 $\qquad\qquad \sigma_{xx} = \sigma_{xx}{}^{o}$

Therefore

$$\text{Constant} = \text{Ln } \sigma_{xx}{}^{o}$$

Hence

$$\text{Ln } \sigma_{xx} = -\frac{G}{\eta} t + \text{Ln } \sigma_{xx}{}^{o}$$

$$\text{Ln } \frac{\sigma_{xx}}{\sigma_{xx}{}^{o}} = -\frac{G}{\eta} t$$

$$\frac{\sigma_{xx}}{\sigma_{xx}{}^{o}} = \exp\left(-\frac{Gt}{\eta}\right) \qquad\qquad 1.10$$

Creep is conducted at constant stress

$$\text{i.e.} \quad \dot{\sigma}_{xx} = 0$$

Equation 1.9 reduces to

$$\frac{2(1+\nu)\,\dot{\varepsilon}_{xx}}{3} = \frac{\sigma_{xx}}{3\eta}$$

$$\dot{\varepsilon}_{xx} = \frac{\sigma_{xx}}{2\eta\,(1+\nu)} \qquad\qquad 1.11$$

Equations 1.10 and 1.11 represent the stress relaxation and creep rate for Maxwell body in the uniaxial conditions of stress.

(ii) Kelvin Body

$$2\,\eta\,\dot{e}_{IJ} + 2G\,e_{IJ} = s_{IJ} \qquad\qquad 1.4$$

Substituting the values of e_{IJ} and s_{IJ} from equations 1.1 and 1.2 into equation 1.4

$$2\eta\ (\dot{\varepsilon}_{IJ} - \delta_{IJ}\ \dot{\varepsilon}_m) + 2G(\varepsilon_{IJ} - \delta_{IJ}\ \varepsilon_m) = \sigma_{IJ} - \delta_{IJ}\ \sigma_m \qquad 1.12$$

For uniaxial stress condition, substituting from equations 1.7 and 1.8 into equation 1.12

$$2\eta\ \left\{\dot{\varepsilon}_{xx} - \frac{(1-2\nu)\ \dot{\varepsilon}_{xx}}{3}\right\} + 2G\ \left\{\dot{\varepsilon}_{xx} - \frac{(1-2\nu)\ \varepsilon_{xx}}{3}\right\} = \sigma_{xx} - \frac{\sigma_{xx}}{3}$$

$$2\eta\ (1+\nu)\ \dot{\varepsilon}_{xx} + 2G(1+\nu)\ \varepsilon_{xx} = \sigma_{xx} \qquad 1.13$$

Stress relaxation is conducted at constant strain

i.e. $\qquad \dot{\varepsilon}_{xx} = 0$

Equation 1.13 reduces to

$$\sigma_{xx} = 2G(1+\nu)\ \varepsilon_{xx} \qquad 1.14$$

Creep is conducted at constant stress

i.e. $\qquad \sigma_{xx} = \sigma_{xx}{}^{o}$

substituting in equation 1.13

$$2\eta\ (1+\nu)\ \dot{\varepsilon}_{xx} + 2G(1+\nu)\ \varepsilon_{xx} = \sigma_{xx}{}^{o}$$

Rearranging

$$\frac{d\ \varepsilon_{xx}}{\left(\dfrac{\sigma_{xx}{}^{o}}{2\eta\ (1+\nu)} - \dfrac{G}{\eta}\ \varepsilon_{xx}\right)} = dt$$

321.

Integrating

$$-\frac{\eta}{G} \, Ln \left\{ \frac{\sigma_{xx}{}^{o}}{2\eta(1+\nu)} - \frac{G}{\eta} \, \varepsilon_{xx} \right\} = t + constant$$

at time $t = 0$, $\varepsilon_{xx} = 0$

Therefore

$$Constant = -\frac{\eta}{G} \, Ln \left\{ \frac{\sigma_{xx}{}^{o}}{2\eta(1+\nu)} \right\}$$

Hence

$$Ln \left\{ \frac{ \left\{ \frac{\sigma_{xx}{}^{o}}{2\eta(1+\nu)} - \frac{G}{\eta}\varepsilon_{xx} \right\} }{ \left\{ \frac{\sigma_{xx}{}^{o}}{2\eta(1+\nu)} \right\} } \right\} = -\frac{G}{\eta} \, t$$

Rearranging

$$\varepsilon_{xx} = \frac{\sigma_{xx}{}^{o}}{2G(1+\nu)} \left\{ 1 - exp\left(-\frac{Gt}{\eta}\right) \right\} \qquad 1.15$$

Equations 1.14 and 1.15 represent stress relaxation and creep strain for Kelvin body in the uniaxial conditions of stress.

(iii) Standard linear solid

$$\dot{e}_{IJ} + \phi \, e_{IJ} = \frac{\dot{s}_{IJ}}{2G} + \frac{s_{IJ}}{2\eta} \qquad 1.5$$

Substituting the values of s_{IJ} and e_{IJ} from equations 1.1 and 1.2 into equation 1.5

$$(\dot{\varepsilon}_{IJ} - \delta_{IJ}\dot{\varepsilon}_{m}) + \phi(\varepsilon_{IJ} - \delta_{IJ}\varepsilon_{m}) = \frac{1}{2G}(\dot{\sigma}_{IJ} - \delta_{IJ}\dot{\sigma}_{m})$$

$$+\frac{1}{2\eta}(\sigma_{IJ} - \delta_{IJ}\sigma_{m}) \qquad 1.16$$

322.

For uniaxial stress conditions substituting from equations 1.7 and 1.8 into equation 1.16 and rearranging

$$\frac{2(1+\nu)\ \dot{\varepsilon}_{xx}{}^{o}}{3} + \frac{2\phi\ (1+\nu)\ \varepsilon_{xx}}{3} = \frac{\dot{\sigma}_{xx}}{3G} + \frac{\sigma_{xx}}{3\eta}$$

$$\dot{\varepsilon}_{xx} + \phi\varepsilon_{xx} = \frac{\dot{\sigma}_{xx}}{2G(1+\nu)} + \frac{\sigma_{xx}}{2\eta\ (1+\nu)} \qquad\qquad 1.17$$

Stress relaxation is conducted at constant strain

i.e. $\quad \dot{\varepsilon}_{xx} = 0$ and $\quad \varepsilon_{xx} = \varepsilon_{xx}{}^{o} = \dfrac{\sigma_{xx}{}^{o}}{E}$

Equation 1.17 reduces to

$$\phi\varepsilon_{xx}{}^{o} = \frac{\dot{\sigma}_{xx}}{2G(1+\nu)} + \frac{\sigma_{xx}}{2\eta\ (1+\nu)}$$

Rearranging

$$\frac{d\ \sigma_{xx}}{\left\{ 2G\ \phi\ (1+\nu)\ \varepsilon_{xx}{}^{o} - \dfrac{G}{\eta}\ \sigma_{xx}\right\}} = dt$$

Integrating

$$- \frac{\eta}{G}\ Ln\ \left\{ 2G\ \phi\ (1+\nu)\ \varepsilon_{xx}{}^{o} - \frac{G}{\eta}\ \sigma_{xx}\right\} = t + constant$$

at time $t = 0$, $\sigma_{xx} = \sigma_{xx}{}^{o}$

Therefore

$$constant = - \frac{\eta}{G}\ Ln\ \left\{ 2G\ \phi\ (1+\nu)\ \varepsilon_{xx}{}^{o} - \frac{G}{\eta}\ \sigma_{xx}{}^{o}\right\}$$

Hence

$$- \frac{\eta}{G}\ Ln\ \left\{ 2G\ \phi\ (1+\nu)\ \varepsilon_{xx}{}^{o} - \frac{G}{\eta}\ \sigma_{xx}\right\} = t\ -\frac{\eta}{G}\ Ln\ \left\{ 2G\ \phi\ (1+\nu)\ \varepsilon_{xx}{}^{o}\right.$$

$$\left. - \frac{G}{\eta}\ \sigma_{xx}{}^{o}\right\}$$

Rearranging

$$\frac{2G\,\phi(1+\nu)\,\varepsilon_{xx}{}^{o} - \dfrac{G\,\sigma_{xx}}{\eta}}{2G\,\phi\,(1+\nu)\,\varepsilon_{xx}{}^{o} - \dfrac{G\,\sigma_{xx}{}^{o}}{\eta}} = \exp\left(-\frac{Gt}{\eta}\right)$$

But $\qquad \varepsilon_{xx}{}^{o} = \dfrac{\sigma_{xx}{}^{o}}{E}$

Thus

$$\sigma_{xx} = \frac{2\,\phi\,\eta\,(1+\nu)\,\sigma_{xx}{}^{o}}{E} - \left\{\frac{2\,\phi\,\eta\,(1+\nu)\,\sigma_{xx}{}^{o}}{E} - \sigma_{xx}{}^{o}\right.$$
$$\left.\exp\left(-\frac{Gt}{\eta}\right)\right\}$$

or

$$\frac{\sigma_{xx}}{\sigma_{xx}{}^{o}} = \left\{1 - \frac{2\,\phi\,\eta\,(1+\nu)}{E}\right\}\,\exp\left(-\frac{Gt}{\eta}\right) + \frac{2\,\phi\,\eta\,(1+\nu)}{E}$$

$$1.18$$

Creep is conducted at constant stress

$$\text{i.e.} \qquad \dot{\sigma}_{xx} = 0 \text{ and } \sigma_{xx} = \sigma_{xx}{}^{o}$$

Therefore equation 1.17 reduces to

$$\dot{\varepsilon}_{xx} + \phi\,\varepsilon_{xx} = \frac{\sigma_{xx}}{2\eta\,(1+\nu)}$$

Rearranging

$$\frac{d\,\varepsilon_{xx}}{\left\{\dfrac{\sigma_{xx}{}^{o}}{2\eta\,(1+\nu)} - \phi\,\varepsilon_{xx}\right\}} = dt$$

Integrating

$$-\frac{1}{\phi}\,\mathrm{Ln}\left\{\frac{\sigma_{xx}{}^{o}}{2\eta\,(1+\nu)} - \phi\,\varepsilon_{xx}\right\} = t + \text{constant}$$

324.

at time $t = 0$, $\varepsilon_{xx} = \varepsilon_{xx}{}^{O} = \dfrac{\sigma_{xx}{}^{O}}{E}$

Therefore

constant $= -\dfrac{1}{\phi}$ Ln $\left\{ \dfrac{\sigma_{xx}{}^{O}}{2\eta(1+\nu)} - \dfrac{\phi\sigma_{xx}{}^{O}}{E} \right\}$

Hence

$-\dfrac{1}{\phi}$ Ln $\left\{ \dfrac{\sigma_{xx}{}^{O}}{2\eta(1+\nu)} - \phi\,\varepsilon_{xx} \right\}$ $= t - \dfrac{1}{\phi} Ln\left\{ \dfrac{\sigma_{xx}{}^{O}}{2\eta(1+\nu)} - \dfrac{\phi\sigma_{xx}{}^{O}}{E} \right\}$

Rearranging

$\dfrac{\sigma_{xx}{}^{O}}{2\eta(1+\nu)} - \phi\,\varepsilon_{xx} = \left\{ \dfrac{\sigma_{xx}{}^{O}}{2\eta(1+\nu)} + \dfrac{\phi\sigma_{xx}{}^{O}}{E} \right\}$ $\exp(-\phi t)$

$\varepsilon_{xx} = \dfrac{\sigma_{xx}{}^{O}}{2\phi\eta(1+\nu)} - \left\{ \dfrac{\sigma_{xx}{}^{O}}{2\phi\eta(1+\nu)} - \dfrac{\sigma_{xx}{}^{O}}{E} \right\}$ $\exp(-\phi t)$

Let $A = \dfrac{2\phi\eta(1+\nu)}{E}$

$\varepsilon_{xx} = \dfrac{\sigma_{xx}{}^{O}}{A\,E} - \left\{ \dfrac{\sigma_{xx}{}^{O}}{A\,E} - \dfrac{\sigma_{xx}{}^{O}}{E} \right\}$ $\exp(-\phi t)$

or $\varepsilon_{xx} = \dfrac{\sigma_{xx}{}^{O}}{E}$ $\left\{ \dfrac{1}{A} - \dfrac{\exp(-\phi t)}{A} + \exp(-\phi t) \right\}$ $\quad$ 1.19

From the above condition, that, at $t = 0$, $\varepsilon_{xx}{}^{O} = \dfrac{\sigma_{xx}{}^{O}}{E}$
equation 1.19 has to be readjusted by deducting the elastic
strain introduced.

Thus

$\varepsilon_{xx} = \dfrac{\sigma_{xx}{}^{O}}{E}$ $\left\{ \dfrac{1}{A} - \dfrac{\exp(-\phi t)}{A} + \exp(-\phi t) \right\}$ $- \dfrac{\sigma_{xx}{}^{O}}{E}$

or

$\varepsilon_{xx} = \dfrac{\sigma_{xx}{}^{O}}{E}$ $\dfrac{(1-A)}{A}$ $\{1 - \exp(-\phi t)\}$ $\qquad$ 1.20

Equations 1.18 and 1.20 represent stress relaxation and
creep strain for Standard linear solid in the uniaxial
conditions of stress.

APPENDIX 2

Calculation of residual stresses from the results of changes in strain at the underside of a plate.

The residual stresses across the thickness of the plate shown in figure A2.1 may be determined by the consideration of the equilibrium of forces and moments and from the geometry of the system:

Thus from equilibrium of forces

$$\sigma_1 \ \Delta Z_1 + \frac{1}{2} \ \sigma_b Z_b - \frac{1}{2} \sigma_a \ Z_a = 0 \tag{i}$$

and from equilibrium of moment

$$\sigma_1 \ \Delta Z_1 (Z_a + \frac{\Delta Z_1}{2}) = \frac{1}{2} \ \sigma_a Z_a (\frac{2}{3} Z_a) + \frac{1}{2} \sigma_b Z_b (\frac{2}{3} Z_b)$$

$$= \frac{1}{3} (\ \sigma_a Z_a^2 + \sigma_b Z_b^2) \tag{ii}$$

and from the geometry of the system

$$\frac{\sigma_a}{Z_a} = \frac{\sigma_b}{Z_b} \tag{iii}$$

From (i) and (ii) by eliminating $\sigma_1 \ \Delta Z_1$ first and then substituting in (iii)

$$\frac{3}{2} (Z_a + \frac{\Delta Z_1}{2}) = \frac{\sigma_a Z_a^2 + \sigma_b Z_b^2}{\sigma_a Z_a - \sigma_b Z_b} \tag{iv}$$

$$\text{or} \quad \frac{3}{2} (Z_a + \frac{\Delta Z_1}{2}) = \frac{Z_a^3 + Z_b^3}{Z_a^2 - Z_b^2} \tag{v}$$

$$\text{but} \quad t = Z_a + Z_b + \Delta Z_1 \tag{vi}$$

where t is the original thickness of the plate.

substituting and rearranging

$$Z_a = \frac{(t - \Delta Z_1)(4t - \Delta Z_1)}{6t} \qquad \text{(vii)}$$

and

$$Z_b = t - Z_a - \Delta Z_1 \qquad \text{(viii)}$$

By substituting from equations (vii) and (viii) back
using equations (i) and (iii), the original stress in the
first layer is given by

$$\sigma_1 = \frac{\sigma_b \, (t - \Delta Z_1)^2}{(2t + \Delta Z_1) \, \Delta Z_1} \qquad \text{(ix)}$$

The stress σ_b is determined from the change in strain
measured experimentally from the underside of the plate:

$$\sigma_b = \frac{E}{(1-\nu^2)} \, (\, \Delta \varepsilon_x + \nu \, \Delta \, \varepsilon_y) \qquad \text{(x)}$$

when

$$\sigma_x = \sigma_y$$

$$\varepsilon_x = \varepsilon_y$$

Equation (x) reduces to

$$\sigma_b = \frac{E}{(1-\nu)} \, \Delta \, \varepsilon_b \qquad \text{(xi)}$$

where $\Delta \varepsilon_b$ is the change in strain measured at the
underside of the plate after the removal of the first layer.
When the first layer has been removed, the stresses present
in the underlying layers are modified. In order to achieve
the original stress in each of the underlying layers; the
measured stress as given by equation (ix) is adjusted to

take into account the effect of the preceeding layers. In general the removal of the mth layer affects the stress measured on removing the nth layer ($n \quad m$) by an amount

$$\Delta_n^m = (\frac{\sigma_b}{Z_b})_m \left\{ (Z_a)_m - (n-m) \Delta Z + \frac{\Delta Z}{2} \right\} \qquad \text{(xii)}$$

Thus the total residual stresses originally present in the layers can be obtained by

$$
\begin{aligned}
\sigma(1) &= \sigma_1 \\
\sigma(2) &= \sigma_2 - \Delta_2^1 \\
\sigma(3) &= \sigma_3 - \Delta_3^1 - \Delta_3^2 \\
\sigma(4) &= \sigma_4 - \Delta_4^1 - \Delta_4^2 - \Delta_4^3 \\
\sigma(5) &= \sigma_5 - \Delta_5^1 - \Delta_5^2 - \Delta_5^3 - \Delta_5^4 \\
\sigma(6) &= \sigma_6 \quad \ldots\ldots
\end{aligned}
\qquad \text{(xiii)}
$$

FIGURE A 2.1: Stress distribution induced after
an imaginary layer has been
replaced on the top of the plate
such that the plate is sprung
back into its original shape.
(After Andrews[7]).